Strategic Placement of Viscous Dampers For Seismic Structural Design

A thesis submitted to the
Department of Engineering Science

For the degree of
Doctor of Philosophy (DPhil)

By

Jessica Kaye Whittle
New College

Trinity 2011

Supervised by
Prof M.S. Williams and Prof A. Blakeborough

Acknowledgements

Many people and organisations have made this work not only possible but also a rewarding, learning experience. Firstly, I am indebted to the National Science Foundation for its provision of the Graduate Research Fellowship, as well as New College and the Department of Engineering Science for additional funding for my DPhil and generous support for conferences and training courses. I gratefully acknowledge the guidance of my supervisors, Professor Martin Williams and Professor Tony Blakeborough, without whom this work would not have been possible; I thank them for holding me to high standards, allowing me to shape my own research path and learn from my mistakes, and encouraging me to think for myself. Thank you for taking on an aspiring earthquake engineer and enabling this enriching experience.

The friendship and technical expertise offered by the Structural Dynamics Group, including Suresh, Nacho, Chandra, Sifiso, and Wei – must also be acknowledged, and each is warmly thanked for providing the DCS family. I offer my gratitude to Mobin Ojaghi for patiently teaching me the inner workings of the SDL and being a sounding post for all things earthquake engineering. Additionally, I acknowledge Dr Theodore Karavasilis, for the many hours assisting me in my research and for coming alongside me when I needed it most – including a willingness to challenge and encourage me at the right time. A great thanks is offered to the staff in the engineering department. This includes Clive Baker, for his patience and regular assistance in the SDL. The construction of the device test rigs are acknowledged to him as well as a readiness to answer my questions patiently, brainstorm design ideas, and tirelessly translate American-English confusions (spanners, lab kit, and kips to name a few!). Also, the access to the invaluable computer lab resources is accredited to Tony Gilham and Kevin Corbett, with a particular thanks to Kevin for a friendly face each day and multiple computer processors. Many thanks to Alison May for being the gracious gatekeeper to all things. Without the generous loan of the Jarret and FIP dampers from JRC Ispra and FIP Industriale, respectively, the device testing would not have been possible. I also acknowledge the input and helpful answers to many questions provided by Edmund Booth, Rob Smith, Katherine Coates, Dr Oren Lavan, and Professor Izuru Takewaki – thank you for supporting a young academic exploring a field close to your own. Finally, to the EEFIT team, thank you for giving me the chance to see earthquake engineering in its truest form and for inspiring me in my work.

For those who supported me outside my research, with their encouragement, stability, and reminders of life outside of work, I wholeheartedly thank you. To Dr Lisa Martin, for her friendship, wisdom, and drive as a fellow postgrad engineer, and to the Cranham Crew - Eve, Naomi, Sanne, Andrea, Kira, Emilie, and Päivi - for their loyalty and steadfastness, you are all invaluable Oxford family. In addition, to Dr Chris Ramseyer, Dr Kyran Mish, and Dr Beth Brueggen, thank you for your engineering guidance and mentorship, an invaluable legacy from OU. I am ever grateful for the determined support of my parents, the calming quirkiness of my siblings, the comfort of home offered by grandparents, near and far, and for sisters, Katherine, Melissa, and Subiksha – thank you for believing in me and spurring me on to run the race of faith. Many thanks to Costa Coffee for providing the ideal writing space and for the Impact youth group, for offering a little bit of crazy every Friday that kept me sane.

And to Him who holds all things together and through whom all things have meaning, thank you for 1 Chron. 28:20 and for your great provision and presence throughout the DPhil.

Strategic Placement of Viscous Dampers for Seismic Structural Design

Jessica Whittle
New College

DPhil Engineering Science
Trinity 2011

Abstract

Seismic design with viscous devices is an effective means of dissipating seismic energy and protecting the main structural system from permanent damage. Despite numerous damper placement methods available, there lacks consensus on the best method, thus leaving design engineers without recommended placement strategies.

The purpose of this research is to investigate strategic placement of viscous dampers for seismic design and to offer design recommendations for placing dampers, vertically and horizontally. Five damper placement techniques were selected for investigation, including standard methods, Uniform and Stiffness Proportional damping, and advanced methods, the Simplified Sequential Search Algorithm (SSSA method), the Optimal Damper Placement for Minimum Transfer Functions (Takewaki method), and the Fully-stressed Analysis/Redesign method (Lavan A/R method). Effectiveness of the techniques for distributing linear fluid viscous dampers for two building examples was evaluated under a suite of twenty ground motions, two seismic hazard levels, and in terms of peak interstorey drifts, absolute accelerations, and residual drifts using nonlinear time history analysis. The advanced methods showed comparable performance based on performance indicators. Therefore, usability is recommended as the selection criteria. The Lavan A/R method was found to be the most effective and usable method. It is recommended that multiple design ground motions be used for the SSSA Mode and Lavan A/R methods as well as caution against removal of upper storey damping, which prompts susceptibility to larger roof drifts due to higher-mode effects.

Various brace-damper arrangements were explored to determine strategic horizontal damper placement. It was found that brace-damper arrangements with diagonals and multiple brace-damper sets per floor pose effective means of distributing the axial damper force and protecting the lower-storey columns from overstressing.

Behavioural testing of two nonlinear viscous devices was performed, and results were used to determine analytical models for the nonlinear fluid viscous and fluid spring devices based on fitted parameters. It was found that the stress-relaxation models better captured the nonlinearity of the devices than standard models but yielded only marginally decreased energy dissipation per cycle. Thus, it is recommended that standard models are adequate for analysis of damped structures with these nonlinear viscous devices.

Table of Contents

Chapter 5 – Investigating Optimal Placement Techniques: Shear Frames

Chapter 6 – Investigating Optimal Placement Techniques: Regular and Irregular Buildings

Appendix

Chapter 1

Introduction

Seismic design and retrofit with dampers has been proven repeatedly to be an effective seismic hazard mitigation strategy. Use of dampers for seismic design, also referred to as a supplemental energy dissipative system, is generally more cost-effective than base isolation techniques and conventional seismic design when considering the life-cycle costs of the structure. For example, preliminary analysis of a concrete frame in Palo Alto, California showed a stark level of improvement in performance with dampers than with a conventional retrofit; the conventional retrofit of strengthening members would result in a much higher base shear (and subsequent foundation upgrade) than a retrofit with fluid viscous dampers, which reduced seismic response and base shear by 50% from the original building design (Islam 2001).

Viscous dampers, in particular, are well known for their large energy dissipation capacity and have the quickest rate of growth in application in structures as compared to other devices. The placement of the dampers is critical to the overall level of improvement of a building's seismic response. However, amidst the increase in application of viscous dampers, there is not a consensus for optimising the placement of viscous dampers throughout a building for seismic design. Thus, as damper manufacturers and researchers have suggested, the next important research area for seismic energy dissipation is a generalised method for the strategic implementation of dampers in various building types.

Many optimisation techniques and algorithms for placing dampers in buildings have been proposed in literature over the past fifteen years but none have been adopted by structural

engineering guidelines or commentaries. There exists a wide range of methodologies and necessity for continued research to improve the current methods and provide structural engineering tools for optimal damper selection and placement (Takewaki 2009). Each new damper placement technique is endorsed as an improvement of its predecessor, yet a consensus amongst the seismic design community as well as input from external research parties are needed to obtain standardised guidelines.

The focus of this research is the strategic placement of viscous dampers for seismic structural design. The aims are to offer design recommendations for use of damper placement methods and to provide conclusions regarding placement methods' effectiveness and usability based on thorough comparisons of the methods for realistic scenarios. In addition, the practical concern of the structural capacity of a building with added dampers is addressed.

These aims are achieved first by reviewing the background of supplemental energy dissipative systems, specifically the behaviour and application of viscous dampers, and providing an introduction of the standard practice for damper placement in Chapter 2. Dissipative device placement is explored in further detail in Chapter 3, where the optimisation problem for damper placement is defined, a review of damper placement research is presented, and limitations of the existing methods are addressed. The theory and procedure of three selected advanced techniques, the Simplified Sequential Search Algorithm, the Optimal Damper Placement for Minimum Transfer Functions method, and the Fully-Stressed Analysis/Redesign method, are also presented. The three advanced damper placement techniques were selected to cover a range of methodologies, and with the addition of two standard placement techniques, Uniform and Stiffness Proportional damping, they complete the set of five selected damper placement techniques for investigation and comparison.

An investigation of the behaviour of nonlinear viscous devices is presented in Chapter 4 for the purpose of understanding their operation and to verify the existing damper models through physical testing. This work served as a primer for using viscous devices prior to exploring the damper placement strategies for linear viscous devices in latter chapters. Two nonlinear viscous devices, more easily accessible than linear devices, were experimentally tested to capture the rate effects of the viscous dampers, and analytical models are suggested for both devices based on stress-relaxation models and fitted behavioural parameters.

A verification of the correct application of the damper placement techniques and a preliminary comparison of the damper distribution for shear frames is included in Chapter 5. A framework for analysing and comparing the placement methods is created for the shear frames, and preliminary conclusions based on a set of seven ground motions, including near-fault and far-fault ground motions, lead to improvements for further analysis.

A comparison of the five damper placement methods for two building examples under two seismic hazard scenarios and evaluated for a twenty-ground motion suite represents the main thrust of this work, as presented in Chapter 6. The details of the building designs, ground motion suite, retrofit and damping distribution procedures, and ground motion scaling are presented. The quantitative effectiveness of the damper distributions are compared in terms of three performance indicators: peak interstorey drift, absolute acceleration, and residual drift. Because the damper placement techniques are employed following the procedures presented in literature, comments regarding the usability of the methods may also be offered. Results and conclusions address the synthesized results of the median of the twenty ground motion suite as well as exceptions to the trend with individual ground motions results. General design recommendations for the use of damper placement techniques are also provided.

The consequential design concern is the capacity of the structural system with added viscous dampers, particularly with large expected damper reaction forces resulting from high levels of damping. A strategic damping distribution as addressed in Chapter 5 and 6 is irrelevant if the structural system is unable to support the damper reaction forces. In Chapter 7, the performance of the structural members in supplementally damped frames is investigated in terms of axial loads on columns due to damper reaction forces. Various brace-damper arrangements are explored to strategically reroute the load path of the damper reaction forces and avoid overstressing the lower-storey columns.

Finally, a summary of the conclusions from the individual chapters is presented in Chapter 8, and major conclusions of the thesis are highlighted.

Chapter 2

Background: Supplemental Dissipative Devices for Seismic Design

2.0. Introduction

This chapter presents a brief background of seismic design and highlights the use of supplemental dissipative devices. Focus is placed on the behaviour and application of viscous dampers, one of the most widely-applied types of dissipative devices. Review of supplemental energy dissipation systems leads to the design question of device placement, current guidelines, and common practice. The second literature review chapter explores dissipative device placement in further detail.

2.1. Seismic Design

2.1.1. Background

The intensity and unpredictability of earthquakes makes them formidable natural disasters, with the potential to cause numerous fatalities, extensive structural damage, financial losses, and widespread panic. Kramer (1996) notes that the earliest record of the study of earthquakes dates back 3000 years in China. However, the broad field of earthquake engineering, as Kramer (1996) defines as the "study of the effects of earthquakes on people and their environment and with methods of reducing those effects," is considered a young field, with most major advancements occurring in the second half of the twentieth century until today.

Seismic structural design is the intentional creation and construction of a structural system to respond to earthquake accelerations and forces with the purposes of ensuring life safety and limiting damage to the building and secondary structural elements. Constantinou, Soong, and Dargush (1998) describe the two primary seismic design approaches as: 1. the conventional system of designing structural elements with a balance of strength and ductility to respond favourably to seismic force (eg. moment-resisting steel frames or concrete frames) and 2. the addition of base isolation or supplemental damping devices to the structural system to

divert some of the seismic energy away from the structural elements. Conventional systems rely on energy dissipation via inelastic deformations in the primary structural system, while supplemental and isolation systems may concentrate all energy dissipation in the non-structural devices or a combination of structural and non-structural energy dissipation. Table 2.1 presents examples of the seismic protection systems and distinguishes between supplemental damping and base isolation systems.

Table 2.1. Seismic Protection Systems (Christopoulos & Filiatrault 2006)

Conventional Systems	**Supplemental Damping Systems**		**Isolation Systems**
	Passive Dampers	*Semi-Active & Active Dampers*	
Flexural Plastic Hinges	Metallic	Braces	Elastomeric
Shear Plastic Hinges	Friction	Tuned-Mass	Lead-Rubber
Yielding Braces	Viscoelastic	Variable Stiffness	High-Damping Rubber
	Viscous	Variable Damping	Metallic
	Tuned-Mass	Piezoelectric	Lead-Extrusion
	Self-Centring	Rheological	Friction Pendulum

2.1.2. Eurocode Force-Based Seismic Design

The focus of this research will be moment-resisting steel frame (MRF) building design. Steel MRFs, with their high ductility, and therefore, tendency to exhibit large interstorey drifts, are a common and suitable case for the installation of viscous dampers. Eurocode 3 (BS EN 1993-1-1:2005) presents the criteria for steel building design, and Eurocode 8 (BS EN 1998-1:2004) prescribes the seismic design requirements for a structure. The principle of seismic design is to achieve a balance of strength and ductility. Eurocode 8 categorises structures in terms of behaviour factors, or q-factors. Large q-factors indicate high ductility; therefore, a larger degree of nonlinearity is permitted in the frame to dissipate lateral energy. Linear analysis may be employed for design purposes if a q-factor is incorporated in the building design. The structure is then designed linearly to resist static loads reduced by the q-factor or to respond linearly to the elastic spectrum reduced by the q-factor (the design spectrum).

An elastic response spectrum represents the relationship between the fundamental period and the spectral acceleration of a structure on certain site conditions (soil characteristics and peak

ground acceleration) (Figure 2.1). More generally, the response spectrum is a statistical representation of the performance of single degree-of-freedom structures of varying periods under a large number of realistic ground motions. EC8, 3.2.2.2 describes procedures for creating the elastic response spectrum, and EC8, 3.2.2.5 includes the design response spectrum details. The design response spectrum is approximately equal to the elastic spectrum reduced by the q-factor, with the addition of a lower bound acceleration (β * peak ground acceleration). Additionally, EC3 and EC8 present requirements for MRF design, including a limit of the moment-demand ratio at joints to avoid strong beam and weak column connections.

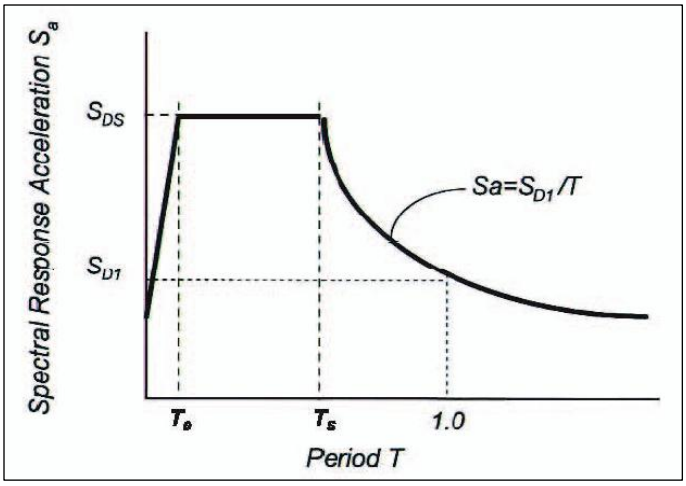

Figure 2.1. Elastic Response Spectrum (FEMA 440, ATC 2005)

The force-based seismic design approach focuses on meeting a single performance objective, typically life safety under a certain seismic hazard level (Christopoulos & Filiatrault 2006). However, with advancements in seismic protection strategies and seismic hazard probability modelling, designers may employ a performance-based seismic design approach, considering the state of the structure under a variety of seismic hazard levels. Supplemental damping systems, where damping and stiffness levels may be controlled by the quantity and size of dissipative devices, are particularly compatible with performance-based seismic design principles.

2.1.3. Performance-Based Seismic Design

Performance-based seismic design (PBSD) provides a framework for seismic design of a structure to meet specific criteria. The principle of PBSD is designing to achieve specific building response objectives under expected earthquake scenarios. Table 2.2 and Table 2.3 display the PBSD seismic hazard levels and performance classifications as presented in FEMA 356 (ASCE 2000). The Basic Safety Objective includes Life Safety requirements under the design based earthquake (DBE, BSE-1) and Near Collapse requirements under the maximum considered earthquake (MCE, BSE-2). The steel MRF drift limits in Table 2.3 are guidelines (not limitations) for what may be expected under the DBE. The Operational performance level drift is not specified in FEMA 356, but it is assumed that Operational performance exhibits drift limits similar to the Immediate Occupancy level and lower absolute accelerations, which influence functioning of internal systems.

Table 2.2. Performance-Based Seismic Design – Seismic Hazard Levels (ASCE 2000)

Seismic Hazard Level	Abbrev.	Probability of Exceedance	Mean Return Period (Years)
Frequently Occurring Earthquake	FOE	50% / 50 years	75 years
Design Based Earthquake (Basic Safety Earthquake – 1)	DBE (BSE-1)	10% / 50 years	500 years
Maximum Considered Earthquake (Basic Safety Earthquake – 2)	MCE (BSE-2)	2% / 50 years	2500 years

Table 2.3.Performance-Based Seismic Design – Performance Levels (ASCE 2000)

Performance Level	Abbrev.	Description (post-earthquake state)	Steel MRFs DBE drifts (%)
Near Collapse	CP	Large permanent drifts, severe degradation of stiffness and strength, on verge of collapse	5% transient or permanent
Life Safety	LS	Some permanent drifts, some residual strength and stiffness, maintains gravity load capacity, possibly beyond economical repair	2.5% transient; 1% permanent
Immediate Occupancy	IO	No permanent drift, safe to occupy, minimal damage to strength-stiffness, minor cracking of structural elements	0.7% transient; negligible permanent
Operational	O	No permanent drift, near original strength and stiffness, all internal systems operational, minor cracking	0.7% transient; negligible permanent

Figure 2.2 illustrates the PBSD classifications of seismically designed structures, with the strictest performance demands represented by the high performance structure. Consider the retrofit of an existing building to improve its performance level. Assuming the building meets Life Safety under the DBE (BSE-1), addition of supplemental damping may be designed to increase the building's performance level from Life Safety to Immediate Occupancy under the DBE. This is a shift from a 'normal structure' to an 'important structure' classification because of the higher performance demands.

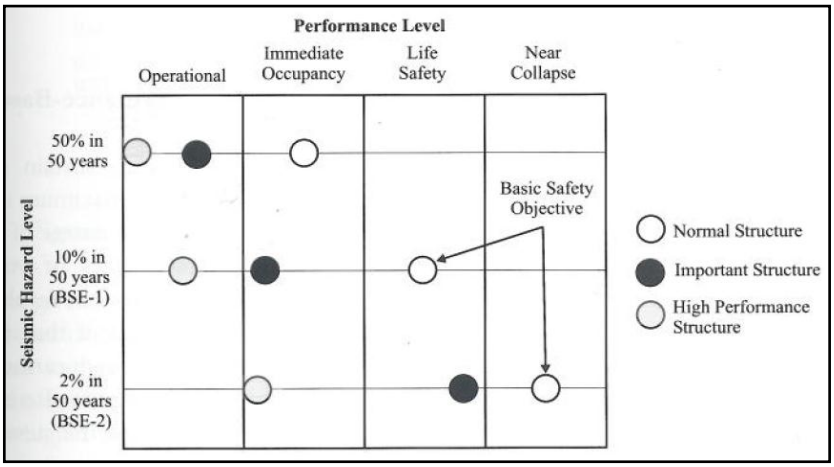

Figure 2.2. Performance-based Seismic Design Framework
(based on SEAOC 1996, ASCE 2000, BSSC 1997) (Christopoulos & Filiatrault 2006)

2.2. Supplemental Energy Dissipative Systems

The disadvantages of conventional seismic design, including the potential of permanent residual drifts, damaged structural members, repair costs, and building downtime, make supplemental energy dissipation an attractive alternative design method. Supplemental energy dissipative systems can be designed to promote linear-elastic or mildly inelastic structural response, thereby eliminating or reducing structural damage. In addition, the discrete devices used in supplemental energy dissipative systems may be replaced more quickly and cost-effectively than primary structural members, thereby reducing structural downtime and repair costs. A brief background of supplemental damping, energy dissipation, damping control systems, and types of dissipative devices is presented.

2.2.1. Background

Base isolation and supplemental damping devices are practical methods of seismic design that are alternative to the seismic design of structural elements only (Key 1988). Base isolation, as defined by Constantinou et. al (1998), "dissipate(s) the seismic energy introduced into the structure during an earthquake" by isolating "the main structural elements from receiving this energy." This is accomplished via isolators typically installed between the foundation and superstructure of a building (Figure 2.3) or between the deck and piers for a bridge.

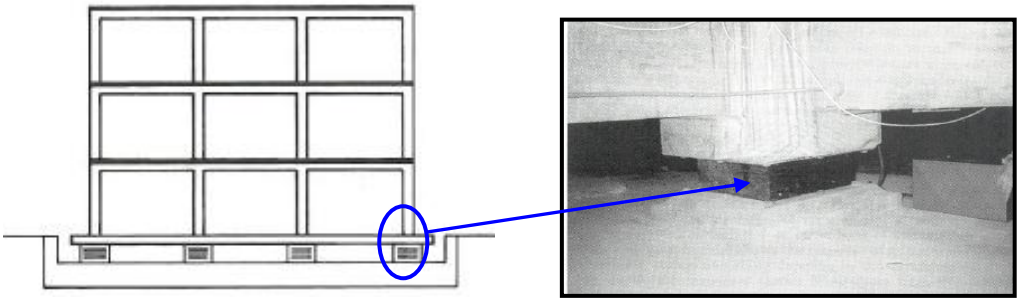

Figure 2.3. Base Isolated Building with Laminated Rubber Bearing Isolators (Key 1988)

Supplemental damping is a more recent seismic design technique that followed on the footsteps of the research and applications of base isolation systems. One of the first applications of metallic dampers (a type of supplemental damping device) occurred in New Zealand in 1981 (Christopoulos & Filiatrault 2006). Supplemental damping has received attention and acceptance over the past twenty years and has been applied to hundreds of buildings worldwide for human-induced, wind, and seismic energy mitigation (Christopoulos & Filiatrault 2006). Some seismic design examples include friction dampers installed in the Canadian Space Agency Complex near Montreal (prior to 1992), viscous damping walls installed in the SUT-Building in Shizuka City, Japan (prior to 1992), and the retrofit of the Wells Fargo Bank building in San Francisco with chevron braces and steel hysteretic dampers after the 1989 Loma Prieta earthquake (Soong & Dargush 1997). Similarly, an early wind-vibration example is the 1969 design of the late World Trade Center twin towers installed with more than 10,000 viscoelastic dampers to reduce accelerations (Soong & Dargush 1997).

2.2.2. Energy Dissipation

Supplemental damping devices, also known as energy absorbers and dissipative devices, dissipate "a portion of the [earthquake] input energy, thereby reducing energy dissipation demand on primary structural members and minimizing possible structural damage" (Constantinou et al. 1998). Using dissipative devices, supplemental damping systems rely on mechanical energy dissipation that is "activated through movements of the main structural systems [and] reduces the overall dynamic response of the structure during a major earthquake" (Christopoulos & Filiatrault 2006). Because supplemental damping devices assume the main energy dissipation role but are not part of the structure's stability and force-resisting system, they may be advantageously replaced after an earthquake (Key 1998).

The energy balance of a supplementally damped structure under seismic forces is found from integrating the relative energy equation with respect to relative displacement *x*. The sum of the relative kinetic energy of the mass E_K, viscous damping energy caused by inherent damping and any viscous dampers E_D, and the strain energy of the structure E_A (denoted "absorbed energy" by Uang and Bertero, 1990) must equal the relative input energy from the seismic event E_I (Uang & Bertero 1990). The strain energy E_A is the sum of the recoverable elastic strain energy of the structure E_S and irrecoverable hysteretic energy E_H, where f_s is the restoring force (Uang & Bertero 1990) and E_H depends on the hysteretic properties of individual structural members and any hysteretic dissipative devices (Christopoulos & Filiatrault 2006). Additional parameters are mass *m*, lateral stiffness *k*, relative velocity $\dot{x}$, relative acceleration $\ddot{x}$, and ground acceleration $\ddot{x}_g$:

$$\int m\ddot{x}dx + \int c\,\dot{x}dx + \int f_s dx = -\int m\ddot{x}_g dx \tag{2.1}$$

$$E_K + E_D + E_A = E_I \tag{2.2}$$

$$E_K = \int m\ddot{x}dx = \int m\dot{x}d\dot{x} = \frac{m\dot{x}^2}{2} \tag{2.3}$$

$$E_D = \int c\dot{x}dx = \int c\dot{x}^2 dt \tag{2.4}$$

$$E_I = -\int m\ddot{x}_g dx \tag{2.5}$$

$$E_A = E_S + E_H = \int f_s dx \tag{2.6}$$

$$E_S = \int kxdx = \frac{kx^2}{2} \tag{2.7}$$

The dissipative energy of the passive supplemental dissipative device, later referred to as E_P, differs depending on the operation mechanism of the device. The energy dissipated by supplemental devices may be considered a component of the hysteretic energy E_H or viscous damping energy E_D. Refer to section 2.3.3 for energy dissipation of viscous devices.

The free vibration of a single degree-of-freedom system with various damping ratios (β), demonstrates that increased damping can dramatically affect the response of a system (Figure 2.4). With an estimated inherent structural damping ratio of 5%, a doubling of the effective damping ratio from 5% to 10% with dissipative devices reduces the displacement by at least half at the third peak (approximately 2.3 seconds) (Figure 2.4). The rate of attenuation of vibration is also quicker for higher damping ratios, as the 50% damping ratio results in negligible displacement after 1.5 seconds while displacement of the structure with 2% damping ratio has been reduced by only half after seven seconds.

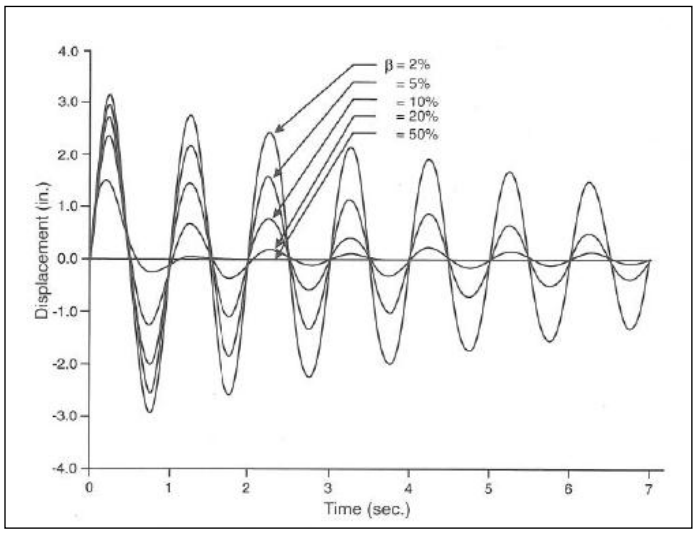

Figure 2.4. Effect of Supplemental Damping on Single Degree-of-Freedom System (Hanson & Soong 2001)

2.2.3. Damping Control Systems

Supplemental damping systems may use passive devices or devices controlled using semi-active, hybrid, or active control systems. Chu, Soong, and Reinhorn (2005) describe active, semi-active, and hybrid control systems as a "natural evolution" of passive dissipative damping systems, where sensors and actuators are employed to monitor the response and excitation of the structure and to supply controlled forces to resist seismic forces. Hybrid control is a combination of active control and passive devices, while semi-active control uses controllable passive devices that do not add energy into the structure (Chu et al. 2005).

Passive dissipative devices are advantageous because they operate independently of external power sources, which may be unreliable in an earthquake. Active, semi-active, and hybrid devices have been employed most notably in numerous structures in Japan, a handful of structures in China and Taiwan, and the U.S. I-35 Highway bridge (Soong & Spencer 2002). On the other hand, passive devices increased in application beginning in the 1990's (Figure 2.5) and continuing through the past decade (Symans et al. 2008). For example, Christopoulos and Filiatrault (2006) cite an increase in the implementation of passive fluid viscous dampers from 1997 to 2006. Various researchers, including Agrawal, Yang, and He (2003) and Ahmadizadeh (2007), have confirmed the effectiveness of passive technologies compared to active control, and the work presented here will be constrained to passive dissipative devices.

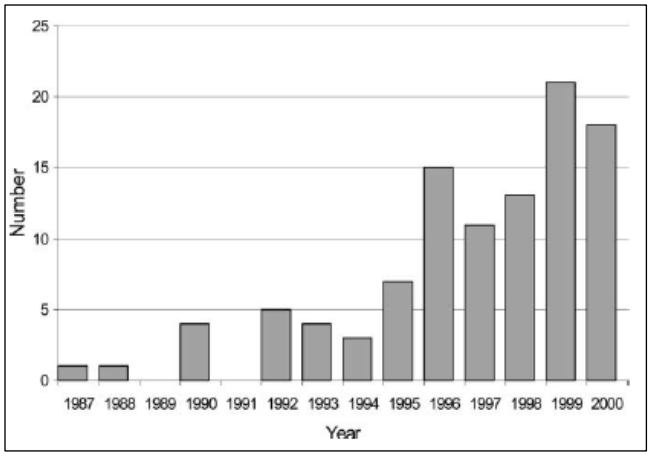

Figure 2.5. Early Growth of Passive Energy Dissipative Device Installations in North America (Soong & Spencer 2002)

2.2.4. Dissipative Devices

Dissipative devices vary in material and damping mechanism, and novel dissipative device design is an active research field. Passive damping devices for seismic applications may be classified into two main categories, hysteretic and viscoelastic (VE). The devices are further distinguished by their dissipation mechanism (Table 2.4).

Table 2.4. Supplemental Energy Dissipation Devices for Seismic Applications (Hanson & Soong 2001)

Type	Device	Principle of Operation
Hysteretic	Metallic yielding	Yielding of metals
	Friction	Frictional sliding
VE	VE solids	Deformation of VE polymers
	Viscous and VE fluids	Deformation of viscous fluids or fluid orificing

2.3. Viscous Devices

Viscous devices have gained recognition as an extremely effective method of seismic energy dissipation for structures. Because of the high energy dissipation potential of viscous devices, the "most rapid growth in the application of supplemental damping systems" for both bridges and buildings has been in the area of viscous devices (Soneji & Jangid 2007). The following section describes the background, application examples, mechanics and design, installation concerns, and advantages and disadvantages of viscous devices. This chapter will use fluid viscous devices as a standard example of a viscous device. The behaviour and modelling of two physical viscous devices, a fluid spring damper and a fluid viscous damper, are explored further in Chapter 4.

2.3.1. Background

A fluid viscous device (FVD) is a type of viscous dissipation device, relying on either the fluid shear forces within a container (viscous damping walls) or on the combination of fluid shearing and forced flow through small orifices within a container (orificed fluid damper) (Hanson & Soong 2001). The orificed fluid damper is the most frequently implemented FVD (Christopoulos & Filiatrault 2006). Figure 2.6 and Figure 2.7 display two FVDs of vastly differing sizes, both manufactured by Taylor Devices, Inc.

Figure 2.6. Taylor FVD – 15 inch (Ojaghi 2008)

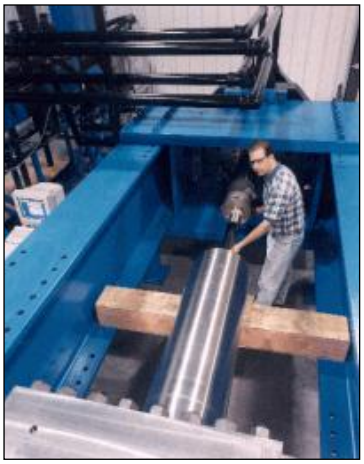

Figure 2.7. FVD for Cartridge Pacific Northwest Baseball Stadium (Taylor 2002a)

2.3.2. Application

FVDs have been historically used for military, defence and aerospace applications, such as the attenuation of ship, spacecraft and aircraft vibrations, and the reduction of weapons grade shock in airburst, water surface and underwater detonations (Constantinou et al. 1998). It was not until the last twenty years that FVDs were applied for civil, structural problems (Hanson & Soong 2001). Taylor (2002a) describes FVDs as "highly advanced product[s]" that "suddenly appeared in the marketplace" in the U.S. after the end of the Cold War in 1990.

Christopoulos and Filiatrault (2006) cite approximately thirty installations of FVDs since 1987. In comparison, twenty installations are recorded by Christopoulos and Filiatrault (2006) for metallic dampers and thirty-six installations for friction dampers, confirming fluid viscous damped structures as a competitive supplementary dissipative system. Examples of structures with viscous damping systems include the 57-storey steel-frame Torre Mayor office building (Figure 2.8) in Mexico City originally constructed with 98 FVDs for seismic energy dissipation (Christopoulos & Filiatrault 2006). The viscous damping system proved effective

for the January 21st, 2003, 7.6 Richter-scale magnitude earthquake outside Mexico City, with the Torre Mayor skyscraper incurring no structural damage and occupants noting motion only in secondary elements, such as chandeliers (Post 2003). Another example is the Millennium Bridge in London, retrofitted in 2002 with 37 FVDs hidden or below the deck and 50 tuned mass oscillators to mitigate human-induced vibrations (Figure 2.9) (Taylor 2002b).

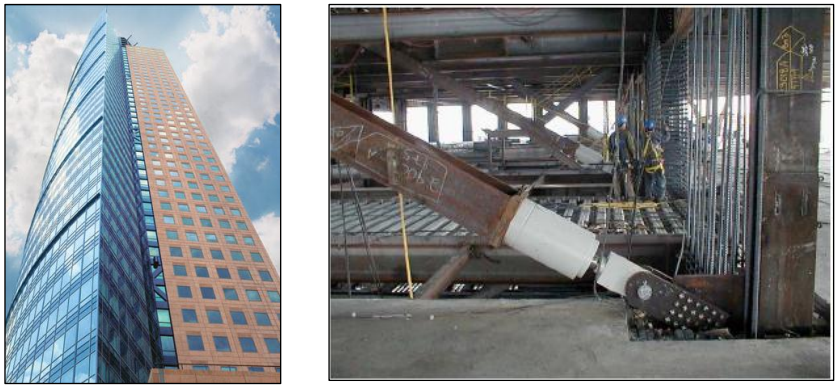

Figure 2.8. Torre Mayor Office Building (Torre Mayor 2011) with FVD (Symans et al. 2008)

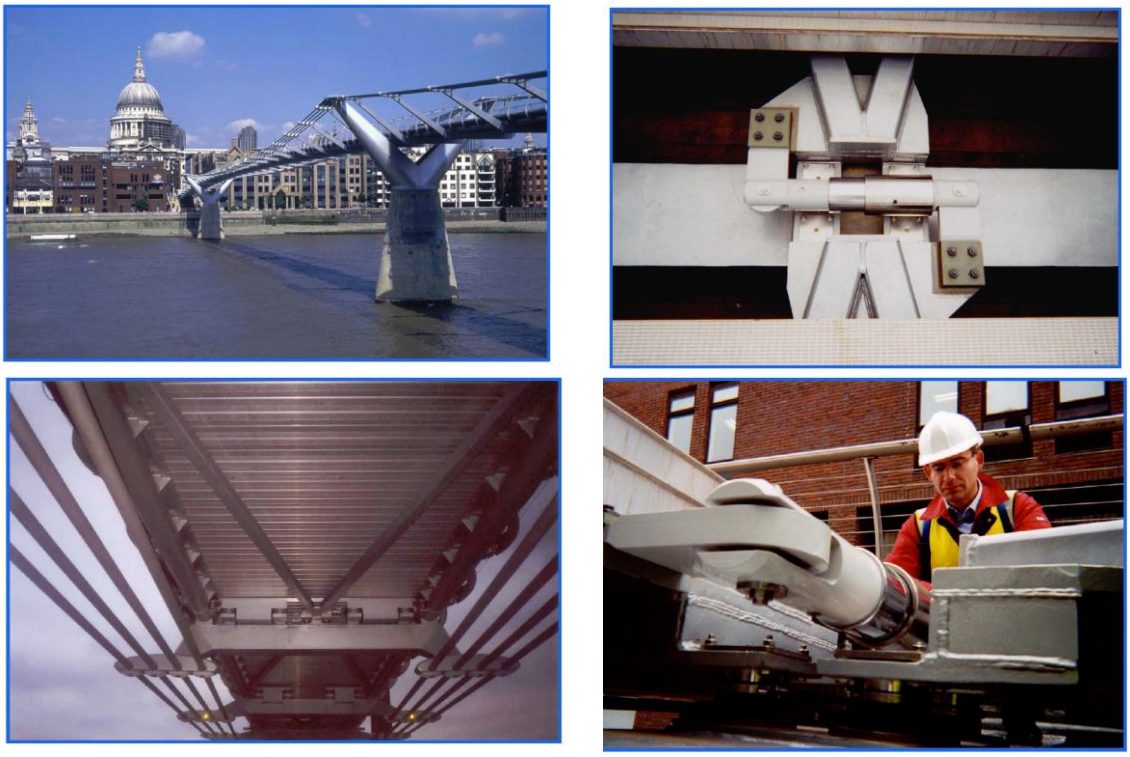

Figure 2.9. Millennium Bridge Retrofit with Frictional, Hermetic FVDs (Taylor 2002b)

2.3.3. Operation and Design

The concept of FVD behaviour for "shock and vibration mitigation is well-known," with the "prominent example…of the automotive shock absorber" (Soong & Dargush 1997). Figure 2.10 displays a conventional orificed FVD whereby the operating principle is the passing of

fluid at high velocities through very small orifices (Constantinou et al. 1998). Forced fluid flow through the orifices in the closed container causes local fluid deformations and resulting energy dissipation (Symans & Constantinou 1998), thus generating the desired damping force (Taylor 2002a).

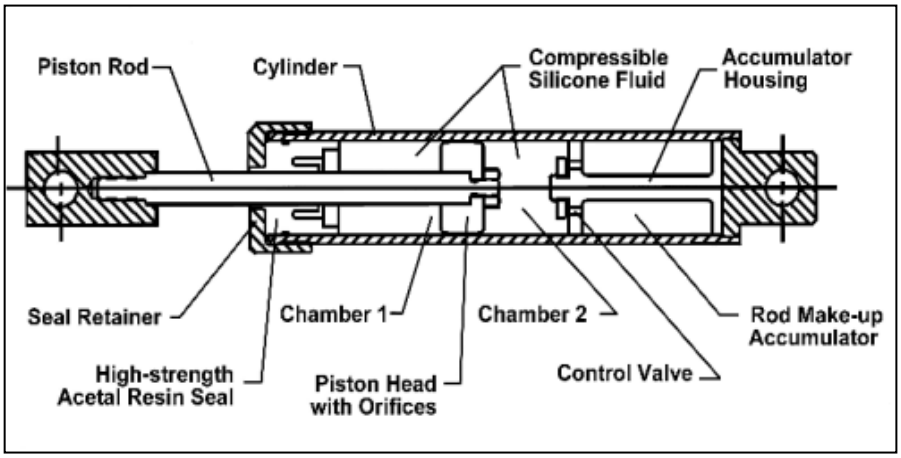

Figure 2.10. Conventional Orificed FVD (Taylor 2002a)

The primary components of a FVD are the piston, the damper housing filled with a relatively incompressible oil (silicone, silicone compound, or similar material), and small orifices in the piston head that allow the fluid to move from one compartment of the device to the other (Hanson & Soong 2001). Alternatively, the fluid may flow through an annular surface between the piston head and outer casing. Each FVD differs slightly depending on the manufacturer. For the conventional orificed FVD in Figure 2.10, more sophisticated components of the device include the piston's material of stainless steel with a bronze head, a "state-of-the-art fluidic control orifice design with a passive bimetallic thermostat to compensate for temperature changes," an accumulator accounting for the change in fluid volume due to the rod's changing position, and high strength seals to ensure closure of the device (Soong & Dargush 1997). Various viscous devices exist, including fluid spring dampers, which contribute a stiffness component to the resistive force, and magneto-rheological devices, with fluid characteristics controllable by magnetic fields.

The resistive force of a linear FVD is represented by a dashpot, where force is the product of the end to end velocity across the element and the damping constant (Taylor 2002a). However, there are advantages of using a nonlinear FVD with a resistive force proportional to an exponential velocity. Because greater amounts of energy can be dissipated with nonlinear FVDs even at low velocities and displacements (Antonucci et al. 2004), nonlinear FVDs are attractive and often quoted as being more commonly implemented than linear devices (Taylor 2002a). However, Soong and Dargush (1997) suggest that linear viscous dampers are more common for seismic applications, implying either increasing application of nonlinear dampers in recent years or debate over which type of damper is most commonly implemented.

The resistive force F_{FVD} of an orificed FVD equals the product of the damping coefficient C and the velocity across the device $\dot{x}(t)$, including the velocity exponent α :

$$F_{FVD}(t) = C|\dot{x}(t)|^{\alpha}\, sgn\big(\dot{x}(t)\big) \tag{2.8}$$

When the velocity-exponent is equal to 1.0, the device is linear. For nonlinear FVDs, the velocity exponent ranges from 0.3 to 2.0, but values ranging from 0.4 to 0.5 are the most popular for seismic building design (Taylor 2002a). Bernoulli dampers with cylindrical orifices and a velocity exponent of 2 were the early fluid viscous dampers (Symans & Constantinou 1998). Since then, manufacturers have improved FVDs via orifice design 'to alter the flow characteristics with fluid speed' and manipulate the velocity-exponent (Burton, Konstantopoulos, Makris, & Antsaklis 1995).

To avoid the restoring force that would develop as a result of nearly incompressible fluid within a closed-container, FVD design includes a rod make-up accumulator and control valve for small dampers, while large damper design typically uses a run-through rod (Symans & Constantinou 1998). The silicon-fluid is "nearly viscous" below a cut-off frequency of approximately 4Hz but exhibits elasticity about this limit (Burton et al. 1995); therefore, it is

suggested that a simple dashpot model is an accurate model of a linear FVD below 4Hz (Soong & Dargush 1997). Symans and Constantinou (1998) present an example of an FVD, with maximum force of 0.45 kN, ± 51mm stroke, 280mm length, piston rod make-up accumulator, and thin silicone oil (100 mm^2/s kinematic viscosity).

The linear FVD energy dissipation E_P of one cycle of harmonic motion is equivalent to the area enclosed by the force-displacement hysteresis curve (blue line of $\alpha = 1$ in Figure 2.11), including parameters of amplitude X_0 and circular frequency ω of motion (Christopoulos & Filiatrault 2006):

$$E_P = \int_0^{2\pi/\omega} F_{FVD}(t)\dot{x}(t)dt = C\omega^2 X_0^2 \int_0^{2\pi/\omega} cos^2(\omega t)dt \tag{2.9}$$

Evaluating the integral yields:

$$E_P = C\,\omega^2 X_0^2 \left[\frac{t}{2} + \frac{1}{4\omega}\sin(2\omega t)\right]\Bigg|_0^{2\pi/\omega} = C\pi\omega X_0^2 \tag{2.10}$$

Similarly, the energy dissipated by nonlinear FVDs of varying velocity-exponents is illustrated in Figure 2.11 as the area enclosed by the curve. It is clear that nonlinear FVDs with velocity-exponents less than one possess greater energy dissipation per cycle than linear devices. The energy dissipation of nonlinear devices is as follows :

$$E_P = \int_0^{2\pi/\omega} F_{FVD}(t)\dot{x}(t)dt = 4C(X_0\omega)^{\alpha+1} \int_0^{\pi/2\omega} \cos^{\alpha+1}(\omega t)\,dt \tag{2.11}$$

Evaluating the integral (Christopoulos & Filiatrault 2006) yields:

$$E_P = 2\sqrt{\pi}\,C\omega^{\alpha}(X_0)^{\alpha+1}\,\frac{\Gamma\left(1+\frac{\alpha}{2}\right)}{\Gamma\left(\frac{3}{2}+\frac{\alpha}{2}\right)} \tag{2.12}$$

The gamma function Γ is defined for positive integers z as:

$$\Gamma = (z-1)! \tag{2.13}$$

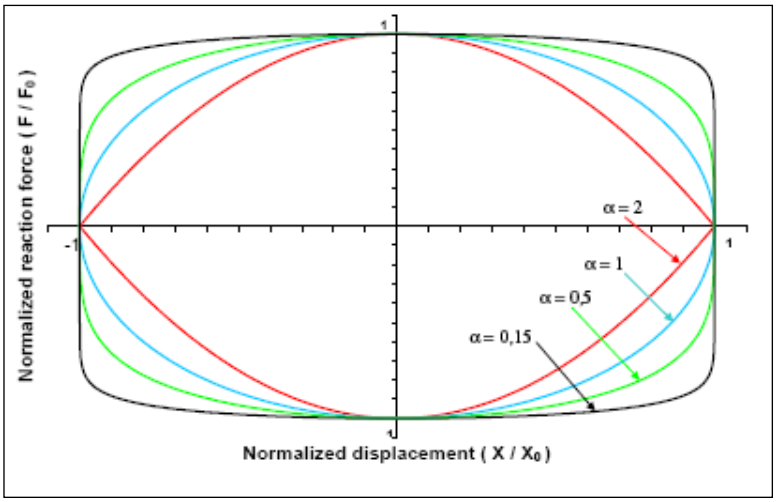

Figure 2.11. Normalised Force-Displacement Curves for Values of α (Antonucci et al. 2004)

2.3.4. Installation

Since FVDs must be located where the devices' resistive forces can be structurally transmitted, the devices are often installed as part of the diagonal bracing (Figure 2.12 and Figure 2.13), at the top of chevron braces and within cross braces (Figure 2.13), and directly between two columns (eliminating pounding effects in Figure 2.14), so that the reaction forces travel from the dissipative device ends into the columns. Novel installation techniques include toggle bracing (Figure 2.15) and scissor-jack systems that amplify the damper displacement and resulting damper reaction force (Christopoulos & Filiatrault 2006). Increased column axial loads are a necessary design consideration with added dampers, as the columns collect the axial component of the damper reaction forces. While staggering dampers can help minimise the column axial loads, strengthening columns may be necessary (Soong & Dargush 1997). This topic is explored in further detail in Chapter 7.

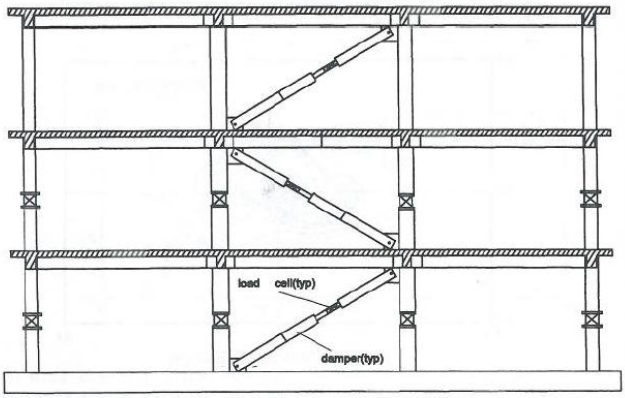

Figure 2.12. Diagonal Braces and FVDs – (Soong & Dargush 1997)

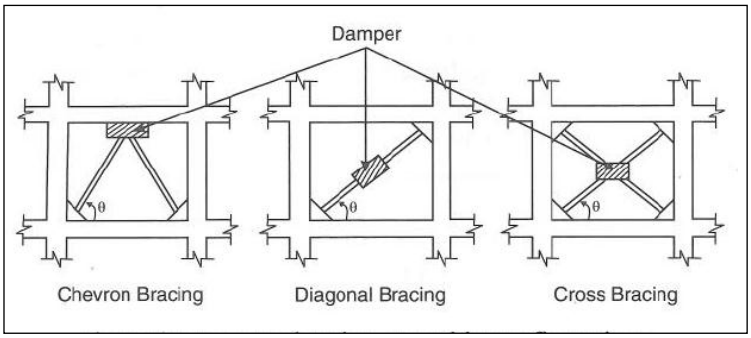

Figure 2.13. FVD Bracing Placement (Hanson & Soong 2001)

Figure 2.14. FVDs Linking Columns of Different Buildings to Eliminate Pounding in the Shanghai Shimao International Plaza (Lu, Gong, Weng, & Ren 2007)

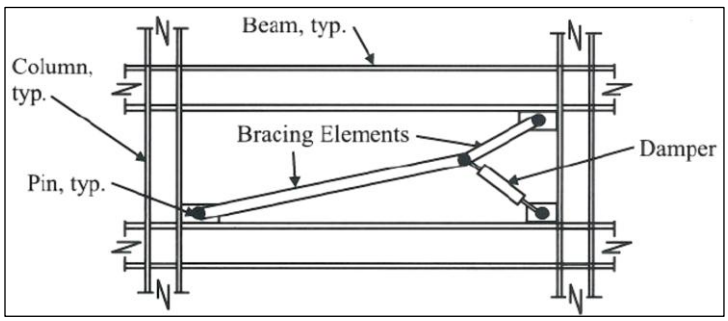

Figure 2.15. Toggle Bracing (Christopoulos & Filiatrault 2006)

2.3.5. Advantages and Disadvantages

Advantages of FVDs include high energy dissipation potential, low maintenance required, out-of-phase damper forces with the structure, possible re-use in multiple earthquakes (Di Paola, La Mendola, & Navarra 2007), and the ease of design for linear FVDs. The forced-fluid orificing of FVDs means the potential for high energy dissipation, yet the manufacture of the internal components requires sophisticated design (Soong & Dargush 1997). If the FVDs are undamaged during an earthquake, they may be re-used in the structure, a clear financial advantage. Another benefit is that the maximum damper forces do not add to the

maximum stressed state of the structure, as the dampers are out-of-phase with structure's elastic forces (Di Paola et al. 2007). The resistive forces in the FVD will be maximum when the structure is experiencing low internal forces (upright, original undeformed position), at maximum velocity. Similarly, when the structure is experiencing maximum forces (full-deflected shape, peaks of the time-history ground motion), the FVD is in its unstressed state, at maximum deflection and zero velocity. This is highly advantageous as many other dampers add forces to the structure's maximum stressed state. The simplicity of the linear FVD force-velocity equation makes design and predictability of linear FVDs easier than other dampers.

The level of sophistication necessary for manufacture, and therefore the cost of FVDs, is an obvious disadvantage. Representatives from Taylor Devices, Inc. suggest damper costs between $2,000 USD to $10,000 USD depending on the force capacity. Di Paola et al. (2007) notes that one of the major challenges of the nonlinear FVDs is their high nonlinear behaviour, making it difficult to apply the response spectrum analysis to the nonlinear differential equations of motions. The durability of the orificed FVD's high strength seals is another design concern (Soong & Dargush 1997). Finally, a challenge for all dissipative devices is strategically placing the devices to maximise their energy dissipation.

2.4. Placement of Dissipative Devices

After the exploration, installation, and acceptance of passive supplementally damped structures as a reliable seismic design strategy, the next design concern for structural engineers is strategic distribution of dampers throughout the structure (Takewaki 2009). This is an important design consideration because the location of devices will influence their effectiveness, and thus, will control the total number of dampers (cost) to achieve the desired structural response (Soong & Dargush 1997). However, structural design codes do not prescribe optimal placement methods for supplemental dissipative energy systems (Liu, Tong,

& Lee 2005). This section presents an overview of the current guidelines for supplemental energy dissipation systems and observations of damper placement in practice.

2.4.1. Guidelines for Damper Placement

Current seismic design guidelines do not include specific suggestions for the strategic placement of dampers along the height of building structures. Review of common structural codes and guidelines, including FEMA 356, FEMA 368 (*2000 NEHRP Provisions*), FEMA 450, BS EN 1998-1, BS EN 1998-3, the International Building Code, and ASCE7-05, reveals the limited code-based information on optimal dissipative device placement. FEMA 356 (ASCE 2000) and FEMA 368 (BSSC 2001) present equations for determining the total viscous damping supplied by the addition of supplemental dampers to meet an effective damping ratio, but do not address the distribution of this damping (Liu et al. 2005). Table 2.5 summarises the content of common building guidelines and device standards. General passive dissipative systems include dissipative bracing as well as dampers.

2.4.2. Common Practice

It is observed that dampers are often distributed in buildings according to rules of thumb or commonly accepted practices. These rules and practices may include damping proportional to storey stiffness, placing dissipative devices at a single storey, and uniform damper distribution. These methods may lead to an uneconomical design with multiple dampers sizes and damper placement configurations that are difficult to verify as optimal. Project-specific limitations, such as architectural constraints, also contribute to the damper placement decisions.

The uniform damper configuration, the same viscous damping added on each floor, is considered a convenient, albeit non-optimal, placement technique (Singh & Moreschi 2002). Examples of uniform damper placement within structural applications include the uniform distribution of the viscoelastic dampers from floor 10 to floor 110 in the late World Trade

Center twin towers and uniform distribution of two equally-sized viscoelastic dampers per building face per floor within the Santa Clara County Building in San Jose, California (Figure 2.16) (Soong & Dargush 1997). An example of single-storey damping is that of the ground floor, equal-bay distribution of 58 friction dampers in the Canadian Space Agency Complex near Montreal (Soong & Dargush 1997).

Table 2.5. Summary of Building Codes and Device Standards

Building Guidelines and Device Standards (Europe and U.S.)		**Source, Date**	**Addresses:**					**Description**
			Passive Dissipative Systems	Base Isolation	Dampers	Design for Total Viscous Damping	Strategic Placement of Dampers	
FEMA 356*	Prestandard and Commentary for the Seismic Rehabilitation of Existing Buildings	ASCE, 2000	X	X	X	X		Includes a section devoted to passive devices (ch. 9): modelling, testing, analysis, and recommendations; supercedes FEMA 273 & 274
FEMA 368 (2000 NEHRP Provisions)	NEHRP Recommended Provisions for Seismic Regulations for New Buildings and Other Structures	BSSC, 2001	X	X	X	X		Presents an appendix on structures with damping systems, recommended for trial use and peer review.
FEMA 450** (2003 NEHRP Provisions)	NEHRP Recommended Provisions for Seismic Regulations for New Buildings and Other Structures	BSSC, 2004	X	X	X	X		Supercedes FEMA 368; Added "Structures with Damping" Chapter
BS EN 1998-1	Eurocode 8. Design of Structures for Earthquake Resistance- Part 1: General Rules, Seismic Actions and Rules for Buildings	BS EN, 2004		X				Presents seismic isolation but specifically does not address distributed passive devices.
BS EN 1998-3	Eurocode 8. Design of Structures for Earthquake Resistance- Part 3: Assessment and Retrofitting of Buildings	BS EN, 2005	X	X				Briefly addresses passive damping as a potential retrofit solution (via base isolation or dissipative bracing).
IBC	International Building Code	ICC, 2006	X	X				Primary building code for the majority of the U.S., only seismic isolation recommendations.
ASCE-7	Minimum Design Loads for Buildings and Other Structures	ASCE, 2006	X	X	X	X		U.S. guidelines for load and design calculations; chapter concerning structures with damping systems
prEN15129	Anti-Seismic Devices Standard	CEN /TC, 2008	X	X	X			Presents guidelines for modelling and testing dissipative devices and base isolators.

* superceded by ASCE 41- Seismic Rehabilitation of Existing Buildings
** superceded by FEMA P-750, the 2009 edition

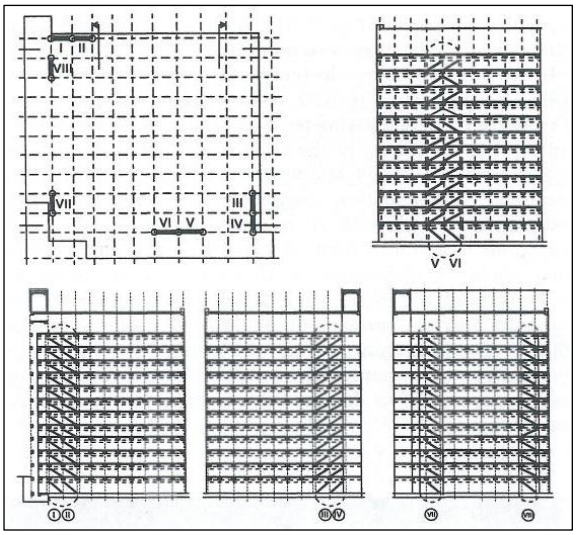

Figure 2.16. Uniform Distribution of VE Dampers in the Santa Clara County Building (Soong & Dargush 1997)

Just as it is more practical and economical for a structural designer to use only a few types of beams and columns for one building, it is likely that one building will ideally use same-size dampers or a very small variety (Hart & Wong 2000). Two examples of FVD applications using equally-sized dampers are 1. the 1995 design of 62 FVDs of 130kN capacity within chevron braces in the three-storey steel-frame Pacific Bell North Area Operations Centre in Sacramento, California and 2. the 1996 addition of 40 FVDs of 670kN capacity within the 35-storey building in Boston, Massachusetts (Soong & Dargush 1997). The distribution scheme of these equally-sized dampers is not specified.

The design approach used by Taylor Devices, Inc. is an example of damper placement based on practice easily replicated but not necessarily optimal. Their design approach initially assumes multiple, same-sized dampers evenly distributed throughout the building and iteratively reduces the number of dampers by trying a larger damper size until the number of dampers is less than 32 pieces (an estimate to limit installation costs), the force rating of the damper exceeds 300 tonnes, or less efficient behaviour of the structure occurs due to sparse damper distribution (Taylor 2002a). The use of an arbitrary number, such as 32 pieces, is an example of a manufacturer's rule of thumb as opposed to an optimised strategy used to

regulate damper placement. Haskell and Lee (2002) demonstrate this procedure for sizing and placing dampers, based on the constraints of total lateral force, velocity, and required stroke. Taylor Devices, Inc., one of the largest manufacturers of dampers, suggests that "generalised solutions for implementing dampers in all the various building types" is the current cutting-edge research focus for passive damping (Taylor 2007).

2.5. Conclusions

Supplemental energy dissipation systems are proven to be effective and reliable means of improving the seismic performance of structures by increasing total damping and reducing undesired structural response. Viscous devices are characterised by high energy dissipation and out-of-phase structural response and have been implemented in structures world-wide. Their advantages and prevailing application compared to other devices justifies focus on damper placement techniques with viscous dampers.

While rules of thumb and common practices exist for determining the number of devices to place at each storey, the optimisation of damper distribution within a multi-storey structure and for various building types is a critical consideration for strategic design. Optimal damper placement promotes maximum device effectiveness and resulting cost-efficiency of the supplementally damped system. The minimal guidelines for damper placement within current standards reveal a need for further research and consensus on strategic damper placement guidelines.

The next chapter reviews existing viscous damper placement methods and prepares the foundation for researching the effectiveness and design issues of optimal damper placement.

Chapter 3

Review of Dissipative Device Placement Methods

3.0. Introduction

The previous chapter established supplemental damping as an increasingly tested and reliable seismic design strategy. Although the placement of dampers is a critical design concern, building codes and guidelines do not prescribe a particular method for optimally placing dampers. However, a rich array of methods asserting optimal damper distribution exists in literature. Takewaki (2009) presents an extensive list of contributions to the field of damper placement and concludes that despite the large quantity of information, structural engineers still lack tools necessary for placing dampers optimally in a structure. The aim of this chapter is to describe the optimisation problem for damper placement, review the history of research achievements in the field, pinpoint the limitations of the existing research, and explain the theory and procedure of selected damper placement methods.

3.1. The Optimisation Problem

The general optimisation problem for damper placement is to minimise the seismic response of the building by strategically placing viscous dampers throughout its floors. Seismic response may be characterised by a variety of performance objectives, such as absolute accelerations, peak interstorey drifts, residual drifts, and base shear. The methodology and objective functions for placing dampers differ amongst the available techniques. The total added damping may be constrained to a certain value or minimised for an optimised location of dampers. The dual aim of minimising total added damping and meeting building performance criteria with an optimal damper placement is often referred to as an optimal sensitivity method (Takewaki 2009). These techniques appear more frequently in recent research. The project scope is limited to methodologies for distributing dampers at specific floors along the building height. An overview of numerical optimisation provides insight into the types of damper placement techniques presented in literature.

3.2. Classification of Optimised Damper Placement Approaches

Press, Teukolsky, Vetterling, and Flannery (2007) state the objective of numerical optimisation as finding the global or local extremum (minimum or maximum) of a function "quickly, cheaply, and in small memory." However, determining the global extremum is a difficult problem. The challenge is to locate the global extremum with assurance that it is not mistakenly the local extremum. Optimisation methods are often categorised as deterministic or stochastic (Press et al. 2007).

Deterministic methods, also referred to as exact methods, aim at finding the precise solution amidst all possible solutions in a one to one mapping between the problem and the solution space. Examples of deterministic methods include computer (enumerative) search strategies, Bayesian search (partition) algorithms, and successive approximation (relaxation) methods (Pintér 2008). Stochastic methods address the problem as having various potential solutions, in a one to many mapping between the problem space and the solution space. The aim is to estimate the best solution with as little indeterminacy as possible without considering every possible solution. Examples of stochastic methods include simulated annealing, stochastic approximation, evolutionary strategies, and other heuristic methods (Weisstein 2008). Deterministic and stochastic approaches are both represented in viscous damper placement optimisation.

Current research efforts in optimising damper configurations for seismic design can be categorised into four optimisation approaches: analytical, heuristic, evolutionary, and parametric (Liu et al. 2005). Analytical approaches optimise a "defined objective function" (also known as fitness or cost function) for the total damping capacity (Liu et al. 2005), and are synonymous with deterministic approaches. Stochastic methods may include heuristic techniques and evolutionary strategies. Parametric studies, while not explicitly optimisation techniques, are most similar to stochastic methods in that they seek potential solutions without

exhaustively mapping the problem space. Figure 3.1 illustrates the classification of damper optimisation approaches.

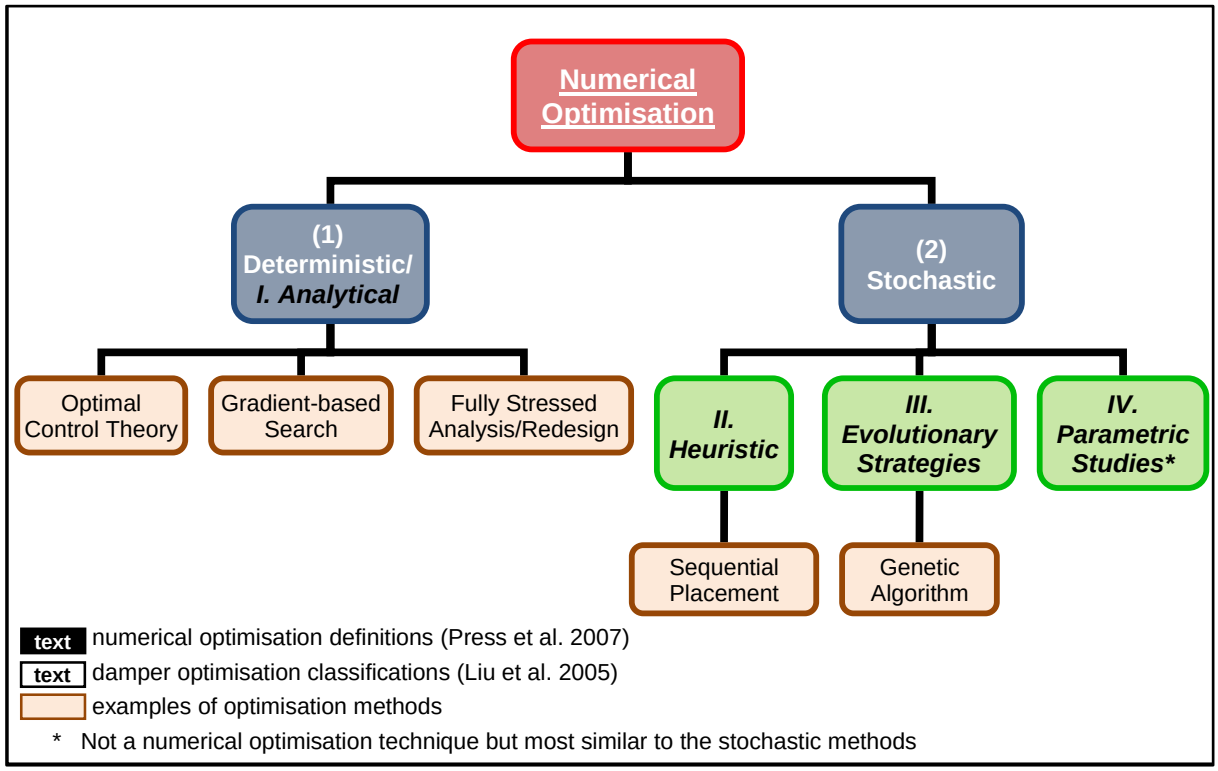

Figure 3.1. Classification of Optimised Damper Placement Approaches

Heuristic approaches are particularly applicable to structural engineering problems because they allow for problem-specific a priori knowledge (Liu et al. 2005). A heuristic method is an informal means of solving a problem, often based on rules of thumb and trial-and-error. Evolutionary algorithms are inspired by evolutionary biology and the survival of the fittest principle, whereby an adaptive search algorithm omits the inferior solutions to the fitness function and continues searching and potentially mutating possible solution combinations (Pintér & Weisstein 2008). Parametric studies compare a discrete number of variables, such as three dissipative device sizes or four distinct damper locations. These studies are limited to simple structures and are not exhaustive of optimal solutions; research of parametric approaches has dwindled since the 1990s.

3.3. Review of Research Achievements

A review of damper placement research achievements is presented in terms of stochastic methods and analytical methods. The large quantity of placement strategies in literature have

been condensed to selected significant efforts.

3.3.1. Stochastic Methods

3.3.1.1. Early Research and Parametric Studies

Some of the earlier research efforts include parametric studies to optimise the first storey damping coefficient of a multi-storey, shear building under white noise excitation (Constantinou & Tadjbakhsh 1983) and deriving the optimum damper distribution to maximise the first mode damping ratio for an idealised multi-storey structure (Ashour & Hanson 1987). Gürgöze and Müller (1992) numerically optimised the placement of a single damper in a linear multi-degree of freedom system using an energy criterion. Hahn and Sathiavageeswaran (1992) conducted parametric studies of viscoelastic dampers concluding that the best response of a uniform stiffness building is obtained by damping the lower floors. In addition, it was concluded that tall structures are more sensitive to the influence of damper distributions than short buildings. Limitations of these early research efforts include, in some cases, the optimising of only one damper, the use of idealised structures, and the exclusion of a full suite of real ground motion records.

3.3.1.2. Heuristic Methods – Sequential Placement

Cheng and Pantelides (1988) present an early study of active control of a multi-storey building using the controllability index to determine optimal actuator locations. A novel heuristic placement method was the adaptation of the controllability index to sequentially place dampers where their effects are maximised (Zhang & Soong 1992). This method, the Sequential Search Algorithm (SSA), was considered an advancement in the field because of its practicality. Zhang and Soong (1992) compared SSA to uniform damping, concluding that with SSA, between two and five dampers were saved for a 10-storey structure with viscoelastic dampers using drift as the performance criterion. Additional performance objectives, such as absolute accelerations, were not considered, and a relatively small amount of damping (10% effective damping ratio) was selected. Other researchers verified the SSA

method for viscoelastic dampers and a shear-frame model (Shukla & Datta 1999) and for torsional effects of a three-dimensional model (Wu, Ou, & Soong 1997).

An evolution of the SSA method was the Simplified Sequential Search Algorithm (SSSA) (Lopez-Garcia 2001), which sought to further simplify the method for passive devices by decreasing the computational-effort of determining optimal locations and simulating stochastic ground motions. It claimed simplicity and practicality over existing methods due to its sequential procedure, use of tools familiar to designers, and inherent consideration of discrete damper sizes. For linear structures with linear viscous dampers, the method was as efficient, in terms of interstorey drifts, as more complex placement methods, such as Takewaki (1997) and N. Gluck, Reinhorn, J. Gluck, and Levy (1996). Lopez-Garcia and Soong (2002) supported the SSSA's efficiency for a recommended number of procedural steps (damper sizes) based on building height.

Limitations of the SSSA study include the use of few ground motions, small unrealistic damping levels (less than 10% effective damping ratio with dampers) for comparing SSSA to other methods, and the use of example structures and damper placement distributions from previous researchers. The last limitation implies that the placement methods compared to SSSA were not followed in full and therefore, usability of the methods could not be adequately compared. The method's dependency on specific ground motions and proven effectiveness limited to linear structures were two inherent limitations of the technique. However, Lopez-Garcia and Soong (2002) confirm that the sensitivity of the SSSA damper distribution to ground motion characteristics decreases with increasing levels of damping. Minor differences were found in SSSA damper distributions for four different ground motions with 18% damping as compared to much larger discrepancies in distribution when using 6% damping for the same structure and ground motions.

3.3.1.3. Evolutionary Strategies – Genetic Algorithms

Computationally-intensive evolutionary methods have most notably included genetic algorithms, such as Movaffaghi and Friberg (2006) and Singh and Moreschi (2002). Genetic algorithms are evolutionary techniques specifically applied to combined global optimisation problems (Pintér 2008). In the case of supplementally damped structures, the problem is a combination problem, since there may be $\boldsymbol{d}$ identical dampers to be placed at $\boldsymbol{n}$ possible stories, $[(\boldsymbol{d}+\boldsymbol{n}-1)! / (\boldsymbol{d}! (\boldsymbol{n}-1)!]$ (Singh & Moreschi 2002). Movaffaghi and Friberg (2006) explain that the genetic algorithm evolves based on user-provided fitness functions whereby new generations "reproduce" "until some termination criterion is satisfied." "The best solution of the successive populations gradually converges to the optimal solution" (Movaffaghi & Friberg 2006). Although the genetic algorithm is a powerful optimisation method, the main disadvantage is high computational time.

The genetic algorithm presented by Movaffaghi and Friberg (2006) proposed optimisation using genetic algorithms with discrete variables (using the IDESIGN software) interfaced with ABAQUS. The objective function for the scenario of a nuclear reactor was the minimisation of the vectorial sum of the three translational floor accelerations. Singh and Moreschi (2002) developed a method to optimally place and size viscous and viscoelastic dampers employing a genetic algorithm. The method was demonstrated for various linear dampers and linear, shear and torsional structures and assessed for interstorey drifts, floor accelerations, and shear forces. Comparing the results of Singh and Moreschi (2002) and Singh and Moreschi (2001) for the same 24-storey building, the genetic algorithm yields accelerations greater than those from the gradient-based search method and less than those from the SSA method, thereby confirming a comparable performance of the genetic algorithm to other placement methods.

Because of the time required for analysis and reliance on complex computational models,

genetic algorithms do not meet the condition of a practical and usable damper placement strategy that could be adopted by design guidelines. Thus, genetic algorithms have not been selected as one of the five damper placement methods for investigation.

3.3.2. Analytical Methods

Many analytical optimal placement methods have been proposed, including methods based on the principles of active control theory (Gluck et al. 1996), gradient-based search methods, including Takewaki (1997, 2000), Singh and Moreschi (2001), and Lavan and Levy (2006), as well as fully-stressed analysis/redesign methods (Levy & Lavan 2006). Three of these analytical methods are explored: optimal control theory, optimal damper placement for minimum transfer functions, and fully-stressed analysis/redesign.

3.3.2.1. Active Control Approaches - Optimal Control Theory

Gluck et al. (1996) adapted optimal control theory (OCT) to the damper placement problem. Similar to active control, whereby sensors are designed to record and generate desired forces in the structure to counteract vibrations, passive control requires the damper design parameters to generate specific forces to counteract vibrations. OCT is used to minimise the performance objective by optimising the location of linear passive devices. Since passive dampers cannot provide feedback in terms of optimal control gains, three methods (response spectrum approach, single mode approach, and truncation approach) are proposed to remove the off-diagonal state interactions within the gain matrix and allow approximation of floor damping coefficients (Gluck et al. 1996). Combination of these methods with OCT and passive devices achieves an equivalent effect compared to active control, but is limited to structures dominated by a single mode response. The OCT approach was demonstrated with passive linear viscous and viscoelastic devices within a braced multi-storey building.

Levy and Lavan (2009) performed quantitative analysis concluding that active control techniques for optimising damper placement are less effective than passive control techniques. Active control was found less effective for minimising interstorey drifts than

fully-stressed analysis/redesign methods using deterministic (time history ground motion records) or stochastic (white noise) ground motions. This is attributed to the standard active control approach of considering "an integral on the sum of a quadratic form of the state variables," as opposed to constraining the maximum performance objective (Levy & Lavan 2009). An additional limitation of this method is that the user must have prior knowledge of active control theory to apply the technique to the optimal placement of dampers.

3.3.2.2. Gradient-based Search Methods – Takewaki Method

The Optimal Damper Placement for Minimum Transfer Functions (Takewaki 1997) technique (abbreviated in this research as the Takewaki method) is a gradient-based optimisation method with the objective of minimising the sum of the interstorey drifts of the transfer function, evaluated at the structure's undamped fundamental frequency. The method has since been developed further for more complex structures, multiple performance objectives, and optimal sensitivity design (Takewaki 2009). Since the damper placement distribution is based on the dynamic behaviour of the structure alone, the Takewaki method claims independence from ground motions. Takewaki (1997) showed the efficiency of the method for two shear buildings and assumed stationary ground motions.

Limitations of the Takewaki technique include the objective of minimising the sum of a performance indicator as opposed to the maximum value, which is a more appropriate damage indicator, and the exclusion of design objectives within the method. The lack of verification of the 1997 method for realistic building designs and ground motion scenarios, the method's status as an early benchmark method for optimal damper placement, and its claimed independence from ground motion characteristics warrants further investigation.

3.3.2.3. Fully-Stressed Analysis/Redesign Method

Another notable analytical placement method is the Fully-stressed Analysis/Redesign procedure (abbreviated in this research as the Lavan A/R method), which uses engineering

knowledge and a simple numerical approach for damper placement (Levy & Lavan 2006). Based on the principle of fully-stressed design of truss members, the Lavan A/R method uses a recurrence relationship to maximise ('fully-stress') the dampers influence on the performance parameter (e.g. drift) of the building and minimise the total added damping necessary (Levy & Lavan 2006). A slight alteration of the original Fully-stressed Analysis/Redesign procedure may be used to constrain the total damping (Lavan & Levy 2009).

The Lavan A/R method has been verified by formal gradient-based optimisation and has been applied to shear-frames, industrial frames (Levy & Lavan 2006), and 3D irregular frames (Lavan & Levy 2006). Levy and Lavan (2006) claimed the method achieves the optimal design, with a desired uniform damage distribution, an inherent consideration of performance based design objectives, and efficiency based on realistic ground motion records and structures. Levy and Lavan (2009) showed the Lavan A/R method to be more effective than active control methods (such as Gluck et al. (1996)) in terms of interstorey drifts for multiple structures and ground motions.

However, to the author's knowledge, the Lavan A/R method has not been compared to any other available advanced damper placement techniques, evaluated in terms of additional performance objectives, nor employed by other researchers from the ground-up to assess usability.

3.3.3. Additional Avenues of Optimal Placement Research

The many studies performed in the past four years alone testify to the prolific research efforts in the field of optimal damper placement. Examples include the reintroduction of older concepts, with slight modifications, such as the minimisation of transfer function amplitude of the *base shear force* (Aydin, Boduroglu, & Guney 2007) as an updated version of the

Takewaki method (1997), which minimises the transfer function amplitude of the *sum of interstorey drifts*. Another example is the improvement of the SSA method (1992) with the SSSA method (2001). Some recent placement methods consider a structural softening incorporated with a strategic damper placement (Cimellaro & Rentamales 2007) as well as multi-objective optimisation (Lavan & Dargush 2009). Note that while the research efforts presented here have highlighted achievements for placing viscous and viscoelastic dampers, research for placing other damper types are also on-going, such as Apostolakis and Dargush (2010) for distributing hysteretic passive dampers.

3.3.4. Comparisons of Damper Placement Strategies

While there is an abundance of techniques claiming optimal damper distribution, few thorough comparisons of placement methods for code-compliant building designs, realistic performance objectives, and seismic hazard levels can be found in literature. In most cases, a new method is highlighted and shown to be more effective than its predecessor for selected examples. However, a notable comparison is the work of Cimellaro and Retamales (2007) comparing adapted advanced methods for dual structural softening and damping. In addition, Zhang and Soong (1992), Lopez-Garcia (2001), Singh and Moreschi (2001), Liu et al. (2005), and Levy and Lavan (2009) provided valuable comparative conclusions about select placement methods for different performance criteria.

Cimellaro and Retamales (2007) offered insight into the performance of many advanced placement methods in a comparison of Uniform, SSSA, Takewaki, and OCT methods. Yet the comparison is conducted for *modified* versions of the SSSA, Takewaki and OCT methods that optimise both structural softening and added damping. Based on the analysis of two shear buildings and use of realistic seismic hazard levels (such as 0.7% drift limit with dampers to achieve an Immediate Occupancy level under the DBE) and 25 synthetic ground motion records, they concluded that the modified SSSA method is best at reducing interstorey drifts

and that the modified OCT and Takewaki methods are best at reducing accelerations. However, all three advanced methods produced comparable results, and Cimellaro and Retamales (2007) suggested using "difficulty in implementation" as part of the selection criteria for damper placement methods.

Results of Levy and Lavan (2009), Zhang and Soong (1992), and Lopez-Garcia (2001) have been noted earlier. Singh and Moreschi (2001) showed their gradient-based search method as 24% more effective at reducing absolute accelerations compared to the SSA method at the worst case floor in a 24-storey shear concrete building example (circa 1961) under stochastic design ground motions represented by the power spectral density function. Similar drift reductions occurred for both the SSA and gradient-based search for the example, and a 15% reduction in drifts compared to uniform damping.

Finally, Liu et al. (2005) compared the effectiveness of a genetic algorithm (GA), the SSA method, uniform damping, and their proposed probabilistic based heuristic optimisation technique (PBHO) for a 10-storey, lumped mass structure under three artificial design ground motions (based on El Centro, Kobe, and Northridge records). The SSA method achieved the same peak drifts as the PBHO and GA methods in the same time; however, accelerations were best reduced (by 22% difference) with PBHO and GA, programmed for reducing accelerations, than with the SSA method.

3.3.5. Limitations of Current Methods

There are reoccurring limitations within existing placement method studies and comparisons, including the lack of nonlinear devices, nonlinear building performance, code-compliant buildings, realistic performance objectives and assessment criteria, real ground motion records, and statistical conclusions. Complexity and time-efficiency are key factors that may filter the methods easily-applied and adopted by the engineering community.

Many of the placement methods are restricted to linear devices. Some suggest usability with nonlinear devices but do not verify this with examples. The SSSA method is described as having the *potential* to optimise nonlinear devices upon further research studies (Lopez-Garcia 2001). For many of these optimisation approaches, the structure is idealised as a simple shear frame, ignoring rotations in the structure or irregularities in geometry. The SAP2000 analysis program (CSI 2009a) is used for a few examples, and it is assumed that the damping is modelled by the basic linear dashpot within SAP2000. ABAQUS is used only once in the literature, interfaced by Movaffaghi and Friberg (2006) with genetic-algorithm software IDESIGN to form a design optimisation tool. Generally, the shear structures are not code-compliant building designs, and to best assess the performance of the placement methods, a realistic, code-compliant building design is needed. A few irregular (setback and 3D torsional) examples are presented in literature, including Wu et al. (1997), Lavan and Levy (2006), and Takewaki (1999).

Similarly, realistic building performance objectives, such as meeting a required drift under a specific seismic hazard level or achieving the desired effective damping ratio, are not regularly employed in the damper placement studies. Multiple, informative performance objectives should be used to assess the methods' effectiveness. Many of the presented studies refer only to drifts as the determining factor for a method's effectiveness.

Nonlinear behaviour of the structure with dampers is not specifically addressed, and many of the methods explicitly state that they are incompatible with nonlinear structural response (Lopez-Garcia 2001; Singh & Moreschi 2001). This assumption may be justified, though, as it is a common design strategy to add damping sufficient to ensure linear building performance under design hazard levels (Smith & Coates 2009). However, examining the performance of damped structures past linear-performance may reveal important

characteristics of the damper distributions for nonlinear building behaviour. The majority of research efforts use steel frame structures, which may be justified by the flexibility and suitability of steel structures for added dampers. Nevertheless, there is a need to investigate the applicability of these methods within concrete frames.

Some of the techniques depend on specific ground motions for creating the damper distribution, while others, such as the Takewaki method, claim independence from ground motion characteristics. In general, ground motions are not scaled to realistic seismic hazard levels (such as DBE or MCE) for many of the presented damper placement studies and may be scaled arbitrarily or not at all. Ground motions suites, in many cases, are very small and therefore, cannot yield statistically-conclusive results. Some placement techniques rely on stochastic ground motion representations (such as the power spectral density function). However, the non-stationary nature of earthquakes (Takewaki 1997) means that neglect of true accelerations time histories may yield unreliable results.

Finally, as noted for individual techniques, complexity and time-expended are two limiting criteria. For an optimal damper placement method to be adopted by practising engineers, it must be usable, practical, efficient, and time-effective. While powerful and effective, evolutionary methods are unattractive solutions because they are time-intensive and require high computational power. Active control approaches are also unappealing, not only because of recent research showing their limitations compared to passive approaches, but also because of their complexity and required knowledge of active control. In addition, methods relying on certain in-house software, do not meet the practical and usable criteria.

3.4. Selected Damper Placement Methods

Based on this review of the research field and its limitations, five damper placement methods were selected for further investigation. Although the research field reveals gaps of using optimisation techniques for nonlinear dampers, the need for thorough conclusions and

investigations of existing linear viscous damper methods justifies the use of linear dampers for this research effort. The standard damper placement methods chosen were the Uniform damping and Stiffness Proportional damping methods, and the advanced damper placement methods were the Simplified Sequential Search Algorithm (SSSA), the Optimal Damper Placement for Minimum Transfer Functions (Takewaki), and the Fully Stressed Analysis/Redesign method (Lavan A/R). The three advanced techniques were selected because of their role as cornerstones in the field, their range in methodology from analytical, gradient-based optimisation to analysis-dependent, heuristic optimisation, and their use of tools familiar to engineers, thereby practical and avoiding the pitfalls of computationally-intensive methods. The following sections present an overview of the theory and procedure of each damper placement method.

3.5. Standard Placement Methods

Both the Uniform damping method and Stiffness Proportional damping method are simple ways of distributing the total damping throughout the building. Singh and Moreschi (2002) concede that Uniform damping may be the most convenient damper placement method but may not be the most effective. Uniform damping equally apportions the total damping to each floor C_i, such that it is equal to the ratio of total damping C_t and number of floors n:

$$C_i = \frac{C_t}{n} \tag{3.1}$$

The Stiffness Proportional damping method distributes damping directly proportional to the lateral stiffness of each floor. An approximate lateral floor stiffness may be determined using a triangular load distribution. The damping per floor is proportional to the ratio of the floor stiffness K_i and the sum of all floor stiffnesses K_t:

$$C_i = C_t \left(\frac{K_i}{K_t}\right) \tag{3.2}$$

3.6. Simplified Sequential Search Algorithm (SSSA)

3.6.1. Fundamentals

The SSSA method (Lopez-Garcia 2001) is a heuristic approach for placing dampers

throughout a structure and evolved from the SSA method (Zhang & Soong 1992). The objective of the SSSA technique is to maximise the 'effectiveness' of the dampers, which, in turn, minimises the seismic response of the structure. Because a viscous damper's behaviour is directly proportional to the interstorey velocity at the damper's installation floor, the optimal location is at the floor with maximum interstorey velocity.

The general SSSA optimal location index γ_i at floor i is defined by the drift coefficient α_1, interstorey drift δ_i, velocity coefficient α_2, and interstorey velocity $\dot{\delta}_i$ (Lopez-Garcia 2001):

$$\gamma_i = \alpha_1 \delta_i + \alpha_2 \dot{\delta}_i \tag{3.3}$$

It is assumed that the units of the drift coefficient α_1 are *1/distance* (e.g. 1/m) and the units of the velocity coefficient α_2 are *time/distance* (e.g. s/m), such that the final optimal location index γ_i is unitless. The optimal location index of a viscoelastic damper would depend on both the drift and velocity components of the index. However, in the case of a fluid viscous damper, the drift coefficient is zero and the velocity coefficient is one, such that the interstorey velocity controls the index:

$$\gamma_i = \alpha_2 \dot{\delta}_i = \dot{\delta}_i \tag{3.4}$$

The constraints are the total added viscous damping and the number of dampers. Dampers are assumed to be equally-sized, and final design may consolidate multiple equally-sized dampers at one floor into fewer, large dampers.

3.6.2. Procedure

3.6.2.1. General Procedure

Application of the method follows a sequential approach: determine total added damping necessary to meet an effective damping ratio objective, analyse the bare frame structure using time history analysis, place discrete damping at a floor based on the optimal location index, analyse the performance of the structure with added damping, locate next optimal location, and repeat until all dampers have been placed. The number of dampers is analogous to the number of iterations of the procedure. Lopez-Garcia and Soong (2002) recommend a number

of iterations n_d that is 2 times greater than the number of storeys of the low-rise structure and 1.5 times greater for a mid-rise structure.

3.6.2.2. Adapted SSSA Mode Procedure

The SSSA technique relies on time history analysis of the structure at each iteration, and is dependent on individual ground motion records. Initial investigation of the SSSA technique led to the conclusion that a sequential damper placement procedure for each ground motion record is not efficient when considering a large ground motion suite. In addition, dependency on a single ground motion record is unrealistic for design. Therefore, an adaptation of the SSSA technique was employed, whereby the conventional SSSA method with 20 iterations was applied to three spectrum-compatible accelerograms. A final SSSA placement scheme was selected based on the most frequently occurring damping value at each floor within the artificial accelerograms set, subject to the constraint of the total added damping value. The advantage of the SSSA Mode adaptation is time-efficiency and a procedure that may be more easily adopted by structural engineers.

3.7. Optimal Damper Placement for Minimum Transfer Functions (Takewaki Method)

3.7.1. Fundamentals

The Takewaki method is a gradient-based search method and categorised as an analytical optimisation approach. The objective of the Takewaki method is to minimise the sum of the amplitudes of the interstorey drifts of the transfer function, evaluated at the undamped fundamental frequency of the structure. The constraint is the total added viscous damping. A brief review of the theory is presented; refer to Takewaki (1997 and 2009) for more details.

The distribution of damping is initially assumed uniform, and the gradient-based search method is applied at each iteration of the script. The optimality index γ_j with respect to the floor damping coefficient is a function of the interstorey drift of the transfer function $\widehat{\delta}_i$, based on the individual floor i and total number of floors n, where the $(\ )_{,\, j+1}$ refers to partial differentiation with respect to the damping coefficient c_{j+1} (Takewaki 1997). Indices j and i both represent the particular floor (i.e. 1 – 10 for a ten-storey building):

$$\gamma_j = \frac{\left(\sum_{i=1}^{n}|\widehat{\delta}_i|\right)_{,j+1}}{\left(\sum_{i=1}^{n}|\widehat{\delta}_i|\right)_{,1}} \tag{3.5}$$

Eq 3.5 was solved in Matlab using symbolic variables for the damping coefficients per floor c_j and symbolic partial differentiation of the sum of interstorey drifts (Appendix A-3). Following this, the optimal index array of the current step γ_o includes all the optimality indices such that:

$$\gamma_o = [\gamma_1;\ \gamma_2;\ \gamma_3; \ldots; \gamma_{n-1}] \tag{3.6}$$

Note that the first optimal index γ_1 is a reflection of the sum of interstorey drifts partially differentiated with respect to the second floor damping. There is not an optimal index corresponding to the first floor, as it is the denominator of the optimal index value γ_j. The step of the gradient search in terms of the optimality index $\Delta\gamma$ is defined as the difference in the final desired optimal location index γ_F (an array of ones) and the optimal location index γ_o of the current step N, divided by the step size N_i:

$$\Delta\gamma = \frac{\gamma_F - \gamma_o}{N_i} \tag{3.7}$$

Defining array B as the sum of the interstorey drifts of all floors differentiated with respect to damping coefficient c_j at floor j:

$$\mathrm{B}_j = \left(\sum_{i=1}^{n}|\widehat{\delta}_i|\right)_{,j} \tag{3.8}$$

The incremental change in the damping array Δc is based on the partial derivatives of array B:

$$\Delta c * \frac{1}{B_1}\left(\frac{dB_{j+1}}{dc} - \frac{dB_1}{dc}\gamma_j\right) = \Delta\gamma \tag{3.9}$$

Finally, the resulting damping array c of the following step $N+1$ is:

$$c_{N+1} = c_N + \Delta c \tag{3.10}$$

Note that the Takewaki script as presented in the Appendix defines array B as the Bj array and the partial derivative terms in Eq. 3.9 as the *B matrix*. Convergence is achieved when the objective function is minimised, and the modified optimality index for each floor is near unity

for floors with positive damping coefficients and less than unity for floors with zero damping. An optimality index of unity could also be described as the state when the rate of change of the sum of interstorey drifts (of the transfer function) of all floors, with respect to the certain floor damping coefficient, is equal to the rate of change of the sum of interstorey drifts (of the transfer function) of all floors, with respect to the first floor damping coefficient. If the first floor damping converges to zero, then the floor with the largest damping coefficient becomes the differentiating value of the denominator of the optimality index.

3.7.2. Procedure

Application of the method was employed with a Matlab script, created specifically for this research based on the procedure presented in Takewaki (1997, 2009). See Appendix A-3 for the full script for the irregular building example. The Takewaki method requires the dynamic properties of an equivalent shear model: degrees of freedom, stiffness matrix *K*, mass matrix *M*, and total added damping value *C*. The step-size and total number of iterations is selected by the user, and in most cases, the step-size was determined by trial-and-error. Convergence is denoted within the script by the near-unity optimal index array γ_j and a plot illustrating minimisation of the objective function versus total iterations.

3.8. Fully-Stressed Analysis/Redesign Method (Lavan A/R Method)

3.8.1. Fundamentals

The Lavan A/R method is categorised as an analytical method. The total added damping is constrained in the Lavan A/R method, a slight alteration from the original method (Lavan & Levy 2009). The objective of the method is to best meet the objective function (performance index) with the allowable total damping. The performance index is specifically recommended as a drift value in Levy and Lavan (2006); for example, the performance index for drifts *pi* at floor *i* is equal to the maximum of the interstorey drift $d_i(t)$ normalised by the allowable interstorey drift $d_{all,i}$ (Lavan & Levy 2009):

$$pi_i = max\left(\frac{|d_i(t)|}{d_{all,i}}\right) \tag{3.11}$$

A performance index of one denotes 'fully-stressed' or optimal design. The recurrence relationship between the damping vector c_d and the performance index is as follows, with parameters including floor damping value $c_{di}^{(k)}$ of the current step *k*, the floor damping value $c_{di}^{(k+1)}$ of the next step *k+1*, the current floor performance index $pi_i^{(k)}$, the exponential convergence parameter *q*, and total added damping *TAD* (Lavan & Levy 2009):

$$c_{di}^{(k+1)} = c_{di}^{(k)} (pi_i^{(k)})^{\frac{1}{q}} \left(\frac{TAD}{\sum_i c_{di}^{(k)} (pi_i^{(k)})^{\frac{1}{q}}} \right) \tag{3.12}$$

Lavan and Levy (2009) recommend a convergence parameter of 0.5 for linear analysis and 5 for nonlinear analysis. The bracketed term in the recurrence relationship limits the floor damping value by the allowable total added damping. Convergence is achieved when the constraint error (max(pi_i)-1) reaches a small value and minor changes occur in the damping array for two subsequent iterations (Levy & Lavan 2006).

3.8.2. Procedure

The Lavan A/R method prescribes an active ground motion to be used for the initial analysis. For linear analysis, this active ground motion is selected amongst a deterministic ground motion set based on the largest spectral displacement S_d at the effective damping ratio, evaluated for an equivalent single degree of freedom structure. Once the performance index, active ground motion, and building model are prepared, the procedure follows these steps, using drift as the performance index: distribute the damping, perform time history analysis, determine peak interstorey drifts, calculate the recurrence relationship and new damping array, and repeat. Continue these steps until the performance index is achieved (i.e. less than or equal to 1) and the constraint error (difference of the performance index from unity) is minimised. The Lavan A/R standard method requires checking the final damping configuration for the next active ground motion, which will be the second most-demanding ground motion in terms of displacement demands (Levy & Lavan 2009). If the maximum performance index exceeds unity under a ground motion, the process is repeated with this new

active ground motion.

The Lavan A/R method was applied using linear time history analysis and a simple Excel program to calculate the recurrence relationship at each step. The Lavan A/R method assumes initial damping to be uniformly distributed. For the standard Lavan A/R method, the reason for selecting an active ground motion with the largest S_d is to minimise the total added damping value for the entire set of ground motions. When total damping is already constrained, the selection of active ground motions is not a critical step as the objective is to best meet the performance index with the limited amount of damping.

3.9. Conclusions

A review of the field of damper placement research reveals not only the quantity and variety of proposed approaches but also the paucity of thorough comparisons and realistic design conclusions about the methods' effectiveness and general usability. If practical and efficient damper placement strategies are to be recommended in building codes and guidelines, it is critical that additional researchers assess existing placement methods to develop conclusions about the methods' usability and effectiveness for multiple performance objectives, building scenarios, and hazard levels. In addition, a fair assessment of the increased performance attained by using the advanced damper placement techniques as compared to using less-complex standard techniques would also be a valuable contribution to the field. It leads to the question – is the additional complexity and time expended by using advanced damper placement methods justified by the improvements in building performance?

The overview of three advanced placement methods and two standard methods presented in this chapter completes the research background and paves the way for comparing the effectiveness and usability of these strategies. Chapter 5 will investigate damper placement methods for the simplest example, shear frames, and simultaneously verify the correct application of the methods. More extensive investigations of the methods will be presented for a regular building and an irregular building in later chapters.

Chapter 4

Understanding Viscous Dampers Through Physical Testing

4.0. Introduction

The purpose of this chapter is two-fold: to understand the operation of viscous dampers and to verify the existing damper models through physical testing. Accurate analytical models of viscous devices are important for numerical analyses of structures with added dampers. Since nonlinear viscous devices are commonly used in practice because of their high energy dissipation capacity, two different nonlinear dissipative devices, a nonlinear fluid viscous damper and a nonlinear fluid spring damper, were investigated. In addition, nonlinear devices were more easily available than linear devices, the type of viscous damper employed in the strategic placement research. Physical experimental testing captures the rate-dependent device behaviour and was used to fit the analytical models of the devices. Descriptions of the viscous devices, test rigs, device performance, analytical models, and energy dissipation calculations are presented.

4.1. Operational Details of Viscous Dampers

Two viscous dampers were acquired from different manufacturers: a fluid spring damper and a fluid viscous damper. Both devices were of small capacity, and it is likely that larger-scaled versions would be installed in full-size buildings for seismic energy dissipation.

4.1.1. Fluid Spring Damper

The fluid spring damper (FSD), also referred to as an elastomeric spring damper or spring-damper pressurized-fluid viscous device, dissipates energy by viscous deformation of a pressurized compressible silicone-based fluid, which is forced to flow between the piston head and inner casing (Figure 4.1). A nonlinear FSD has a viscous damping component *C* and a stiffness component *k*. Its resistive force F_{FSD} is a function of the displacement $x(t)$ and velocity $\dot{x}(t)$ characterised by an exponent α:

$$F_{FSD}(t) = kx(t) + C|\dot{x}(t)|^{\alpha} sgn\big(\dot{x}(t)\big) \tag{4.1}$$

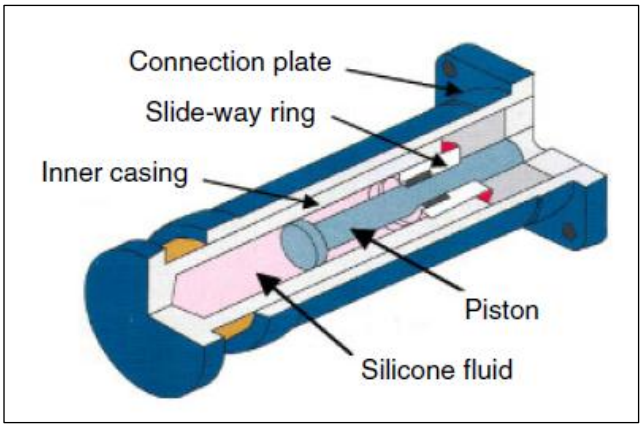

Figure 4.1. FSD (Sorace, Terenzi, Magonette, & Molina 2008)

The operation of the acquired FSD is limited to compression; therefore, installation of these devices in buildings must incorporate two equal and opposite FSDs along the same line of action (Figure 4.2). The device was donated by the Joint Research Centre - Ispra, and was originally manufactured by the Jarret company, a subsidiary of the Enidine corporation. Previous testing on similar devices was conducted by Pekcan, Mander, and Chen (1995), Sorace and Terenzi (2001), Molina, Sorace, Terenzi, Magonette, and Viaccoz (2004), and Blakeborough (2004), within a frequency range of 0.5 Hz to 6 Hz and an amplitude range of 0.5mm to 10mm, while Sorace et al. (2008) explored similar devices of larger capacity. Maximum damper forces within the research of Pekcan et al. (1995) and Blakeborough (2004) did not exceed 20 kN. Therefore, the maximum force of the FSD was estimated as 20 kN, and the stroke as ± 10mm.

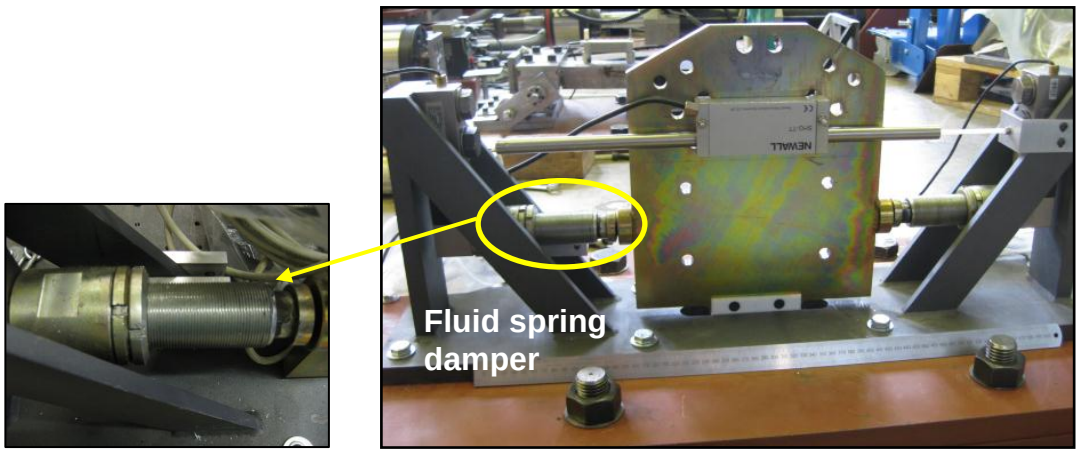

Figure 4.2. Acquired Fluid Spring Damper

4.1.2. Fluid Viscous Damper

The second viscous damper tested was the nonlinear fluid viscous damper (FVD), which dissipates energy through the deformation and shearing of viscous fluids by fluid orificing. An example of an FVD is shown in Figure 4.3, whereby the piston moving through the compartments forces the silicone-based viscous fluid through the piston orifices, shearing the fluid and dissipating energy.

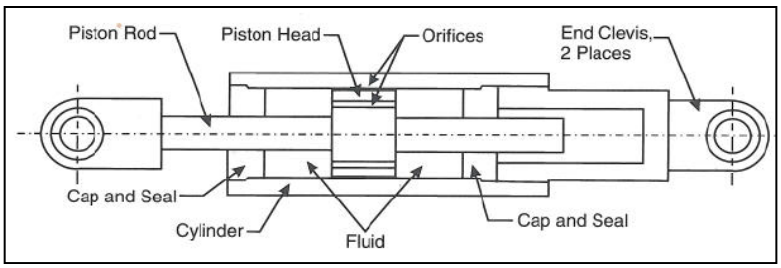

Figure 4.3. Orificed FVD (Hanson & Soong 2001)

The FVD resistive force F_{FVD} is often modelled with a velocity-dependent component $\dot{x}(t)$ and no apparent stiffness, as represented by its constitutive equation where the viscous damping coefficient C and velocity exponent α represent the same properties as for the FSD:

$$F_{FVD}(t) = C|\dot{x}(t)|^{\alpha}\, sgn\big(\dot{x}(t)\big) \tag{4.2}$$

Research by Symans and Constantinou (1998) reveals that there is a stiffness component of the FVD force due to the compressibility of the viscous fluid that is apparent only above a cut-off frequency of about 4 Hz. This stiffness component may be mitigated in device construction with accumulators and run-through rods (Symans & Constantinou 1998). FVDs are categorised as nonlinear and linear, depending on the velocity exponent. Nonlinear FVDs, with a velocity exponent less than 1.0, have a greater energy dissipation potential than linear devices. The manufacturer designated the acquired FVD as nonlinear with a velocity exponent of 0.15 and viscous damping coefficient of 5.1 kN-sec/mm. The maximum force of the FVD was specified as 13.1 kN and the stroke as ±60 mm. The acquired FVD is shown in Figure 4.4. The device was loaned from FIP Industriale, an Italian manufacturer of anti-seismic equipment. FIP Industriale devices have been incorporated into the St Francis Shangri-La

Place in Manila, Philippines and the Taipei 101 skyscraper (formerly Taipei World Financial Center) in Taiwan. A schematic of the device is presented in Appendix A-1.

Figure 4.4. Acquired Fluid Viscous Device

4.2. Methodology

The following section presents the methodology of the testing, including the experimental set-up, behavioural testing, and analytical modelling approach.

4.2.1. Experimental Set-Up

Experimental testing consisted of the general laboratory equipment and software as well as test rigs specifically designed for the dissipative devices. Measuring devices are described within the test rig sections.

4.2.1.1. Structural Dynamics Laboratory

Experimental testing of the dampers was conducted at the University of Oxford's Structural Dynamics Laboratory (SDL). The SDL is equipped with a strong floor and servo-hydraulic actuators. Figure 4.5 displays the hydraulic hardware of the SDL, including hydraulic pumps, accumulators, oil reservoir, substations, actuators, and pump controls. A linear variable displacement transducer (LVDT) and load cell are located inside each actuator. Available actuators are of 10kN, 100kN, and 250 kN maximum capacities and a stroke range of ±75 to ±125 mm. The Instron 8800 controller commands the actuators, and force and displacement data from the actuator and additional sensors are read by the data acquisition dSpace board.

Software necessary for testing includes RS Plus for calibrating and initialising the actuators, Matlab's Simulink for programming the experimental tests, and Control Desk software (dSpace experiment software) for initialising and graphically monitoring the tests and communicating with the dSpace board. Prior to testing, the Simulink test program is created

and compiled for Control Desk; parameter changes to a sinusoidal dynamic test (e.g. amplitude, frequency, ramp time) may be applied within the Control Desk GUI. One computer runs the RS Plus software, and another employs Control Desk and Simulink.

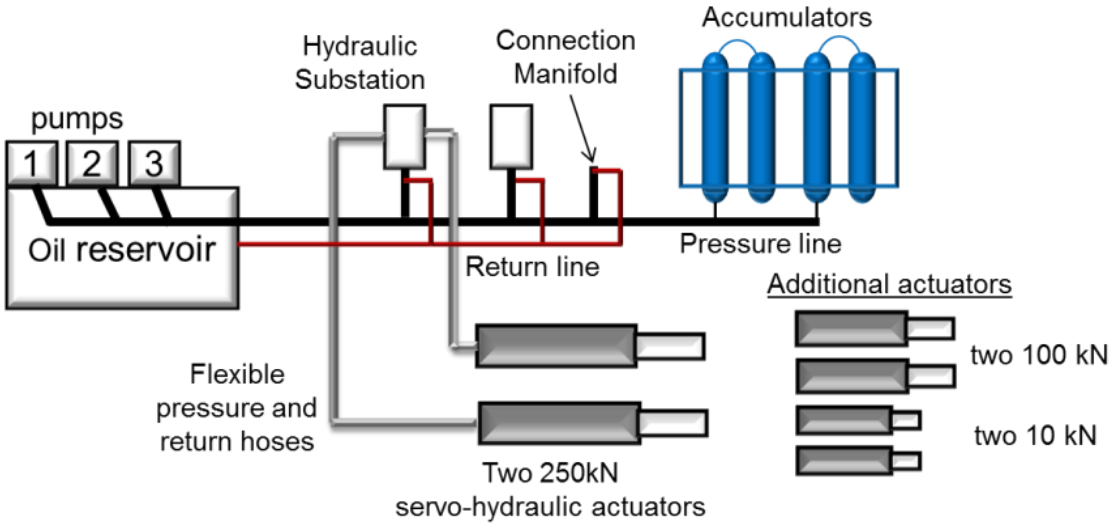

Figure 4.5. Structural Dynamics Lab Equipment
(redrawn based on Blakeborough, M.S. Williams, Darby, & D.M. Williams 2001)

4.2.1.2. Damper Test Rigs

Damper-specific test rigs were designed to secure the devices to the strong floor and ensure that the actuator, damper, and displacement sensors were aligned for axial loading. The FSD and FVD test rigs were designed to be interchanged at the same location in the SDL, using the same sensors, actuator, base plate, and connection between the actuator and test rig.

4.2.1.2.1. Sensors

Force and displacement were measured by the load cell and LVDT within the actuator head. Based on previous research at Oxford suggesting the effectiveness of linear encoders due to their low-noise and high displacement tolerance, a Newall SHG-TT linear encoder with 0.001mm accuracy was selected as the primary displacement sensor. An additional advantage of the linear encoder is portability, enabling it to be placed closer to the damper's relative motion than the fixed actuator LVDT. A thermocouple designed in-house by previous researchers was employed for selected tests to monitor large temperature changes in the outer casing of both dampers.

4.2.1.2.2. Actuator

Based on the expected maximum damper stroke and testing rates, the 100 kN actuator was selected. Figure 4.6 illustrates the manufacturer's performance plot of the 100 kN actuator and the feasibility of tests for the FVD. The blue boundary line indicates the maximum stroke of the damper; the red points show potential sinusoidal tests, and the lower curve is the actuator capacity at full load and upper curve the capacity with no load. A similar capacity check was generated for the FSD.

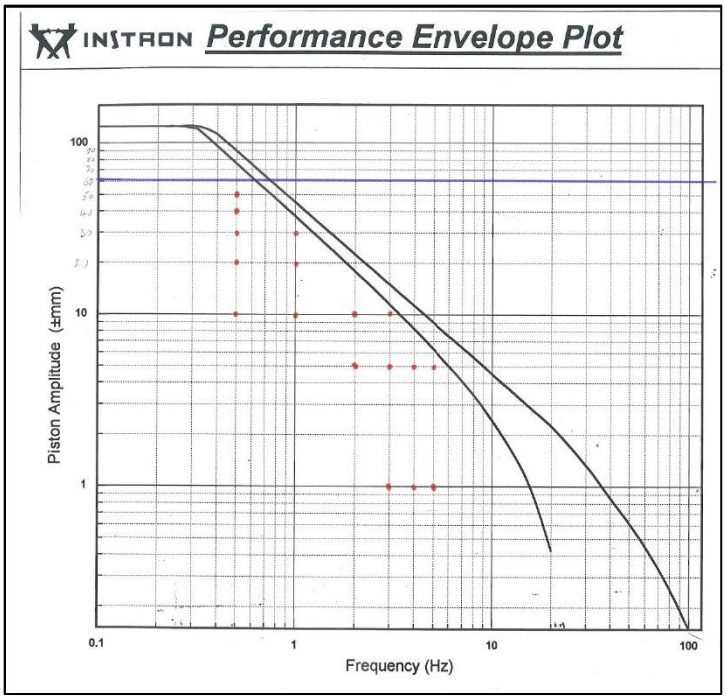

Figure 4.6. 100kN Actuator Performance Plot – FVD Tests
(notations made to original figure, Instron Limited 1997)

4.2.1.2.3. Connections between the Actuator and Test Rigs

The actuator was secured to a permanent steel anchor, adapter plate, and horizontal swivel restraint. The 0.330m by 0.250m by 0.070 m steel adapter plate was designed to connect the actuator swivel restraint to the permanent steel anchor (Figure 4.7). To protect the actuator from any undue out-of-plane forces, a short steel joist section (200mm section UB127x76x13) served as a vertical hinge positioned between the actuator and damper test rig (Figure 4.8). Both test rigs relied on a steel base plate (1.32m by 0.52m by 0.04m) to raise the dampers to the same elevation as the actuator (0.195mm centreline height measured from the strong

floor). The large steel base plate was bolted to the strong floor using M30, 50mm diameter strong floor anchors.

Figure 4.7. Permanent Anchor and Adapter Plate

Figure 4.8. Actuator Mounting (Left) and Hinge (Right)

4.2.1.2.4. FSD Test Rig

The FSD test rig was designed so that the axial force could be applied to the central (gusset) plate of the FSD apparatus. Figure 4.9 shows a schematic of the laboratory layout and FSD test rig in terms of the horizontal and vertical alignment. The small steel base plate (0.8m by 0.18m by 0.02m), angle supports, and gusset plate were included with the acquired FSD apparatus. The gusset plate was not attached to the apparatus' base plate. Instead, the gusset plate's PTFE base slid within a slotted hole (Figure 4.2). The end of each damper was welded to the angle supports.

Previous research (Blakeborough 2004) tested the FSD device within a chevron brace, which revealed a tendency for the gusset plate to rotate with the applied force. A solution to the rotation problem was a stiff 'arm' to apply axial forces along the plate, slide the plate, and transmit the axial forces to the FSD dampers on either side. The arm was constructed of steel 100mm by 100mm by 5mm tube sections. The stiffness of the arm compared to the stiffness of the FSD device was the primary design consideration. Bolt capacity, deflection, and axial and moment capacity of the arm were also considered in the design. Steel plates were welded to either side of the steel arm and corresponding bolt holes drilled into the gusset plate to create a bolted attachment for the arm.

In addition, a smaller, second steel base plate (0.98m by 0.36m by 0.030m) was designed to raise the FSD test rig to the same height as the fixed actuator centreline. The linear encoder box was bolted to the gusset plate, and an M5 threaded, nylon rod was used to attach the linear encode rod end to a fixed point on the FSD angle support (Figure 4.9). This fixed point was an aluminium L-shaped plate, screwed into the FSD angle supports. The nylon rod was designed to protect the linear encoder rod from any out-of-plane rotations of the gusset plate and to secure the rod horizontally during axial testing.

Figure 4.10 illustrates the side-view of the FSD test rig, the actuator head on the right, attached hinge, steel arm, and bolted attachment to the gusset plate of the FSD apparatus. The linear encoder box is attached at the opposite side of the gusset plate (see Figure 4.2), and the linear encoder rod and nylon attachment are visible. The thermocouple, a small wire cable, is attached to the left damper with electric tape. Figure 4.11 shows the plan view of the FSD test rig.

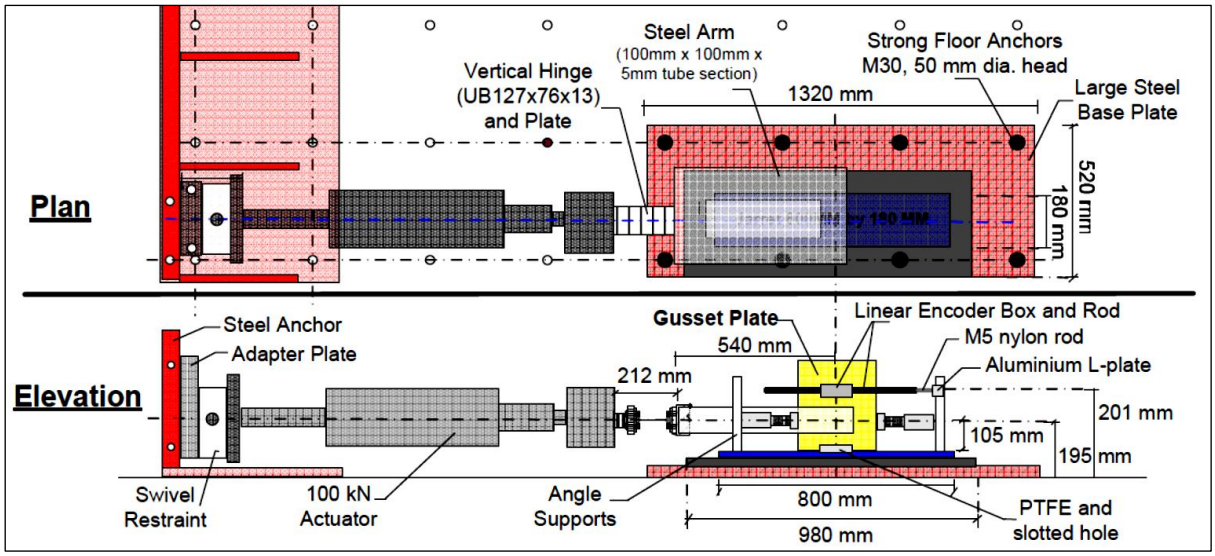

Figure 4.9. FSD Test Rig – SDL Layout

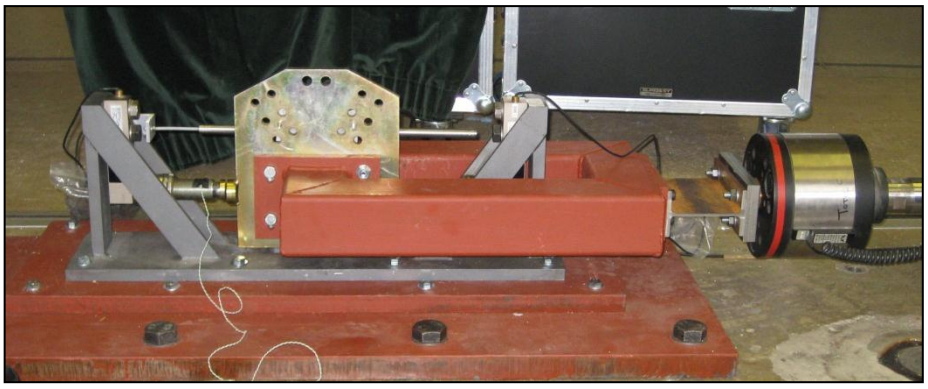

Figure 4.10. FSD Test Rig – Profile View

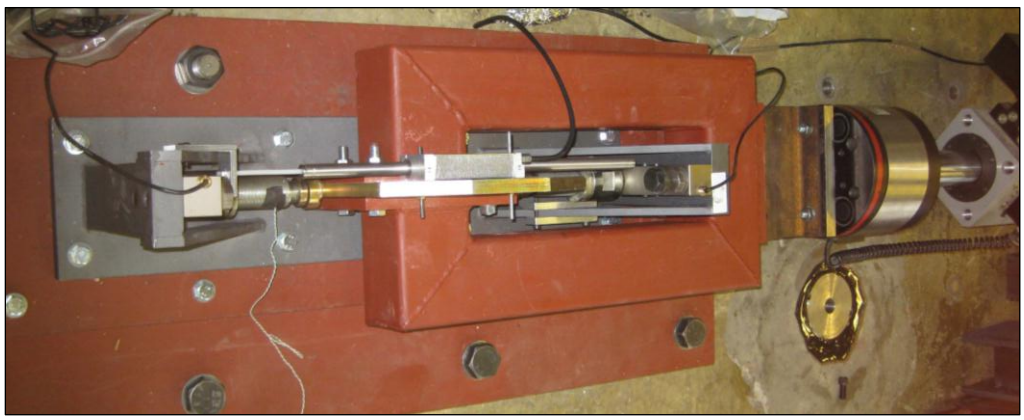

Figure 4.11. FSD Test Rig – Plan View

4.2.1.2.5. FVD Test Rig

The FVD required a test rig with M12 bolt connections at both ends, to attach to the threaded ends of the damper. Figure 4.12 shows a schematic of the laboratory layout and FVD test rig. The ball and socket joints at the ends of the damper enabled attachment and protection of the damper and actuator against out-of-plane forces. The same vertical hinge was used, with the addition of a 0.20m by 0.096m by 0.019m steel plate and an 18mm exposed, welded M12 bolt to attach the FVD at the actuator end. A steel anchor and a 0.26m by 0.090m by 0.019m steel plate with another welded M12 bolt were used as the reaction end opposite the actuator head.

A clamp attachment was designed for the linear encoder and attached to the body of the FVD, such that displacements could be measured directly from the FVD motion. The clamp was attached to the centre of the FVD and tightened with a small threaded screw at the top; the linear encoder reader was secured to base of this clamp (Figure 4.12 elevation schematic). Therefore, the linear encoder reader followed the motion of the FVD and recorded the displacement over the rod, while the linear encoder rod was kept stationary. Similar to the FSD linear encoder rod, a nylon threaded rod secured the encoder rod in the horizontal axis and protected the encoder rod against unforeseen rotations or errors in the applied tests. The nylon rod was secured to a small aluminium plate bolted to the steel anchor.

Figure 4.13 illustrates the side-view of the FVD test rig, and described from left to right, the actuator head is on the left, followed by the attached hinge, steel plate with bolt connection for the FVD, the FVD, and M12 bolt connection, steel plate, and anchor on the opposite end. The clamp for the linear encoder reader, attached the centre of the FVD body, and the linear encoder rod are visible. Figure 4.14 shows the plan view of the FVD test rig, and the attachment of the FVD and linear encoder rod at the anchor end. The thermocouple and power source are also visible.

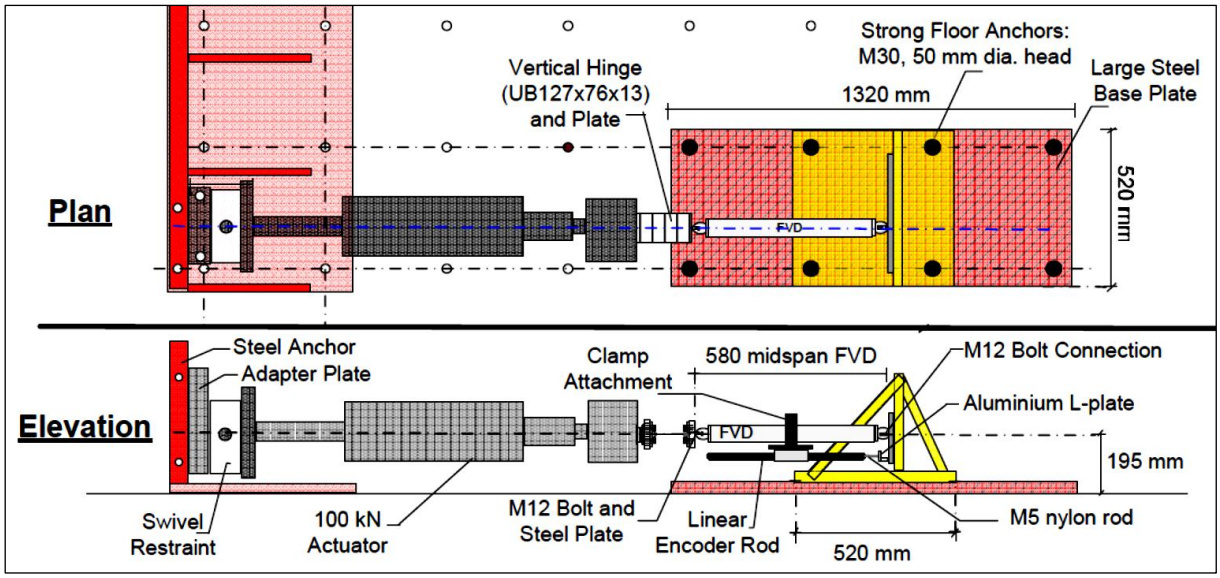

Figure 4.12. FVD Test Rig – SDL Layout

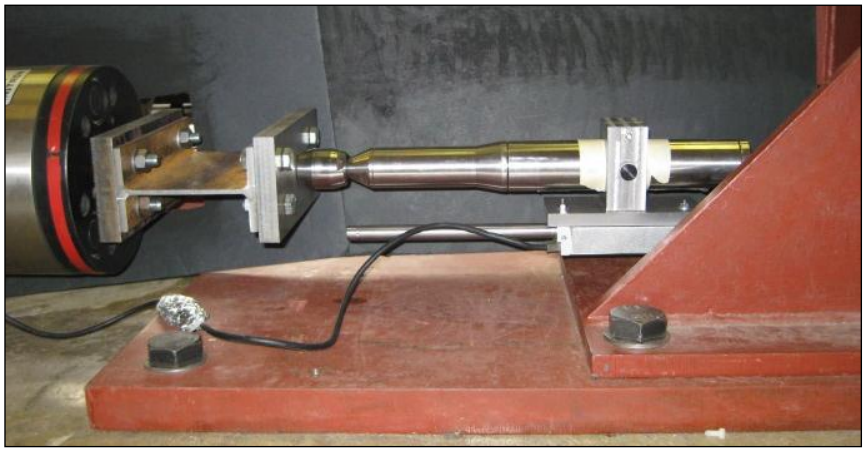

Figure 4.13. FVD Test Rig – Profile View

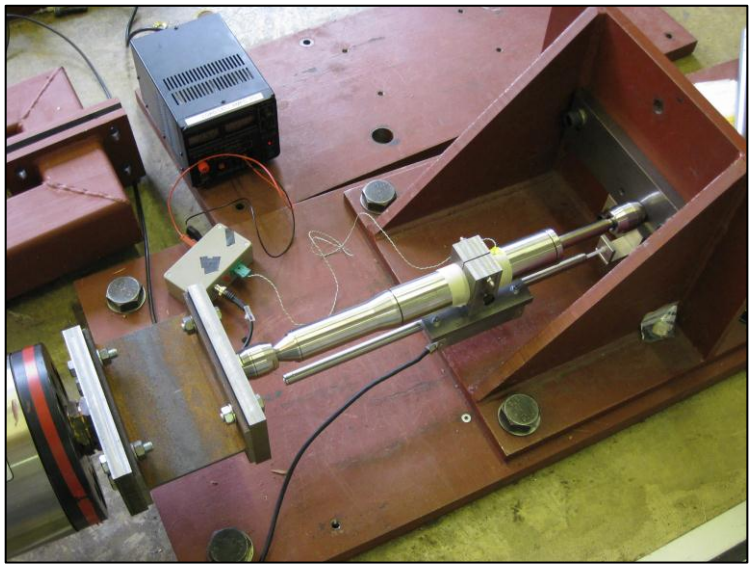

Figure 4.14. FVD Test Rig – Plan View

4.2.2. Behavioural Dynamic Testing

The experimental testing is described in terms of the testing approach, procedure, observations, and data processing methods.

4.2.2.1. Testing Approach

Behavioural testing was conducted with a series of dynamic sinusoidal tests of varying amplitude and frequency. Considering that a medium to high-rise building may have a first mode period of 2.5 sec and a third mode period of 0.3 sec (a range of 0.4Hz to 3Hz), a broad frequency range of 0.2 Hz to 4 Hz was selected for the testing matrix. For the FVD, the manufacturer-provided details of maximum stroke and force were used to create a testing matrix within device performance limits. Previous research was used as a guideline for the FSD performance limits, and actuator performance limitations were also taken into account. Table 4.1 and Table 4.2 display the testing matrices for the dampers, selected to cover a range of the dampers' capacities.

Table 4.1. Testing Matrix – FSD

	Frequency (Hz)					**X = FSD**	
Amplitude (mm)	*0.2*	*0.5*	*1*	*2*	*3*	*4*	*5*
1	X	X	X	X	X	X	X
2			X	X		X	
3						X	
4	X	X	X	X	X	X	X
5			X			X	
6						X	
7			X		X		
9		X	X				
10	X						

Table 4.2. Testing Matrix –FVD

	Frequency (Hz)			**O = FVD**
Amplitude (mm)	*0.1*	*0.2*	*1*	*4*
5	O	O	O	O
10		O	O	
15			O	
20		O	O	
30		O	O	
35			O	

4.2.2.2. Procedure

Preparation for operating the SDL equipment included calibrating the actuators using RS Plus and compiling the sinusoidal testing program in Simulink for the Control Desk application. The behavioural testing procedure included inputting the RS Plus analog output limits and settings, entering the desired testing parameters (e.g. amplitude, frequency, sampling rate) into the Control Desk program, monitoring the test via Control Desk, and exporting captured data to a Matlab data file. For selected tests, a video recording and television screen above the control station enabled close-up monitoring of the device during testing. See Appendix A-2 for notes on testing in the SDL.

A control system was selected to control the cyclic tests based on the linear encoder (LE) displacements, a better gauge of the specimen displacement during testing than the actuator LVDT. An outer control loop was added to the Instron control loop, based on the LE sensor and controlled by the error between the LVDT and LE. The inner loop is the Instron control loop, with parameters input in RS Plus, while the outer loop is a feedforward PID lag controller (FPIDL), with inputs managed in Control Desk (Figure 4.15). This control configuration was selected based on previous success in the SDL; see Ojaghi (2010) for further details on the FPIDL controller for the sinusoidal cyclic testing program.

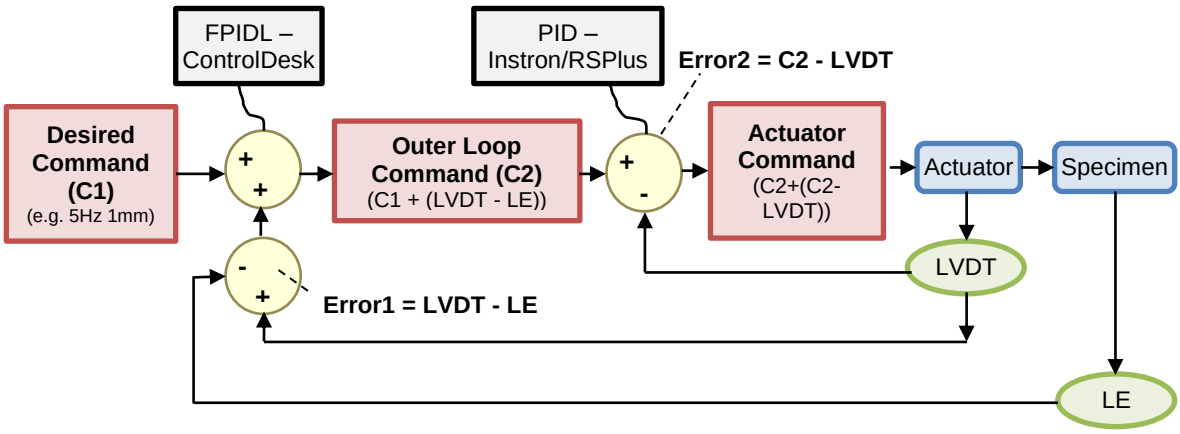

Figure 4.15. Control System for Sinusoidal Cyclic Testing Program (adapted from Ojaghi 2010)

The input parameters for the ControlDesk program included amplitude, testing frequency, sampling frequency, duration for data capture, ramp time, and PID settings. A 1000 Hz sampling frequency was selected for the tests. The PID settings for both devices were determined based on initial testing to improve the overall control of the actuators. These final settings were constant during the testing matrix (Table 4.3), apart from a few exceptions for the FSD. The lag parameter was zero for the majority of tests. For the FSD, low frequency tests were best controlled with a larger proportional gain (PG) and ramp time, while high frequency tests used smaller values of proportional gain and ramp time. The FSD was a more difficult device to control than the FVD, and variation of PG and ramp time were necessary to achieve adequate control for different tests. Note that the Instron PID controller was a constant PI controller for both tests, while the ControlDesk FPIDL controller was used primarily for PG.

Table 4.3. Additional Test Settings

Instron PID Inner Loop Controller	**FSD**	**FVD**
Proportional Gain	33.39	33.39
Integral Gain	1.5	1.5
Derivative Gain	0	0
ControlDesk FPIDL Outer Loop Controller		
Proportional Gain	0.5 – 1.2*	1.10
Integral Gain	0	0
Derivative Gain	0	0
Ramp Time	0.125 – 0.1*	0.025

* depending on frequency of tests

4.2.2.3. Observations

When conducting a series of high-rate tests in succession, the device temperature was monitored to avoid overheating (following manufacturer specifications and prEN15129, CEN/TC 2008), and high-rate tests were limited to a few cycles. Manufacturer's experience suggested that three cycles at maximum amplitude and velocity simulates a large earthquake demand (Infanti 2009). If the temperature of the device rose to more than 5 degrees Celsius over room temperature, testing was stopped until the device returned to room temperature.

Conflicting research exists regarding temperature effects on viscous device performance; however, it was assumed that these devices would be employed for seismic application, where long-duration use and high-temperature effects are less likely than in wind applications, where device temperature may rise to 100 degrees Celsius (Infanti 2009). Therefore, temperature was not monitored for all tests or measured with the aim of correlating temperature to device performance.

Observations were made about the physical behaviour of the devices, noting any unforeseen movement, misalignment, or potential operation or maintenance concerns. The FSD device was found to shift downwards after high-rate tests, such that the gusset plate and reaction points for the dampers were out of alignment (Figure 4.16). This problem was solved with manual resetting of the gusset plate after testing. The shift of the plate indicates the slight rotation of the plate during testing, a trait that could result in the FSDs being detached from the applied lateral force. Few operational problems were noted with the FVD device. However, oil residue at the end of the FVD shaft was visible after high-rate tests (Figure 4.17).

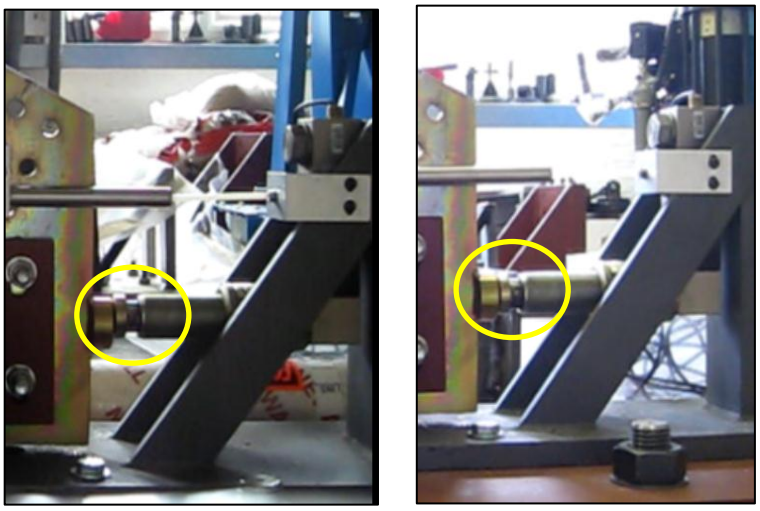

After a 4mm, 1Hz Test *Re-Aligned Manually*

Figure 4.16. Rotation of FSD Gusset Plate

Figure 4.17. FVD Oil Residue

4.2.2.4. Processing Data

The experimental results were processed in Matlab. The linear encoder displacement and force signals were filtered with a second-order Butterworth filter with 20 Hz cut-off frequency to remove noise from the signals. A filtfilt application of the filter was employed to eliminate phase lag in the filtering process. In addition, experimental velocity was approximated as the rate of change in filtered displacement over each time step.

4.2.3. Analytical Modelling

A main objective of physical testing was the verification of existing behavioural models for dampers, which included fitting analytical models based on the experimental data. The damper models, governing equations, and processing details are presented.

4.2.3.1. Damper Models

The Kelvin-Voigt model, where the damper output force is the sum of the restoring force in the device and the viscous damping force, is often selected as the simplest means of modelling both the restoring and viscous force in the FSD viscoelastic material (Figure 4.18 (A)). In the case of the FVD, the restoring force is the result of slight compressibility of the fluid, and can be greatly reduced with the use of an accumulator in the damper housing or a run-through rod (Hou 2008). Research has found that the restoring force in an FVD is negligible below a cut-off frequency (under 4 Hz) (Symans & Constantinou 1998), suggesting the adequacy of a dashpot model for FVDs as opposed to a Kelvin-Voigt model as there is negligible parallel stiffness (Figure 4.18 (B)).

Although the silicone fluid within viscous dampers is often idealised as a purely viscous fluid, the elastic behaviour of the silicone fluid at high shear strains requires a slightly more complex model than the simple dashpot (Hou 2008). First proposed by Bird, Armstrong, and Hassager (1987), the classical Maxwell model for viscoelasticity has been suggested as an effective means of capturing the shear stress relaxation in the silicone fluid at sudden shear strains (Figure 4.19 (B)). The shear stress relaxation may be exhibited in the output force relaxation at constant displacement on the hysteresis curve. Symans and Constantinou (1998) found the relaxation time to be 0.006 seconds for low rates of damper force for a 450 N, ± 51mm linear FVD; this very small relaxation time suggests that the FVD behaved as a linear viscous dashpot below the cut-off frequency. The research presented here will explore the presence of the stress relaxation for nonlinear FVDs.

Two phases of analytical damper modelling were considered based on available damper models. The first phase of damper modelling used the general constitutive models for the devices (Equations 4.1 and 4.2), represented in Figure 4.18 as a simple dashpot model for the FVD and a Kelvin-Voigt (KV) model for the FSD. The second phase of analytical models considered the elasticity of the silicone fluid at constant shear strain by employing a Maxwell model, as recommended by prEN 15129 (CEN/TC 2008). Therefore, the FVD behaviour is modelled with a Maxwell model (spring and damper in series) and the FSD as a combined Kelvin-Voigt Maxwell (KVM) model, with a spring and damper in parallel coupled with a spring in series (Figure 4.19). Results will compare the fit of the general models to the stress-relaxation models (Maxwell and KVM models).

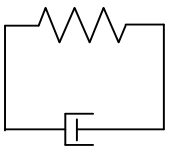

Kelvin-Voigt Model (FSD)
(A)

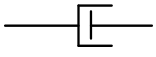

Dashpot Model (FVD, below 4Hz)
(B)

Figure 4.18. General Constitutive Damper Models

Kelvin-Voigt + Maxwell (KVM) Model (FSD) (A)

Maxwell Model (FVD) (B)

Figure 4.19. Improved Stress-Relaxation Models – Spring in Series with General Models

4.2.3.2. Governing Equation – FVD Maxwell Model

First consider the Maxwell model for a nonlinear FVD, where parameters are the Maxwell element output force $F_M(t)$, force in the dashpot $F_d(t)$, force in the spring $F_s(t)$, displacement in the spring $x_s(t)$ and dashpot $x_d(t)$, and total displacement across the element $x(t)$ (Figure 4.20).

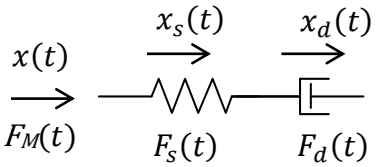

Figure 4.20. Maxwell Model (FVD) – Annotated

The known properties of a Maxwell element are:

$$F_M(t) = F_s(t) = F_d(t) \tag{4.3}$$

$$x(t) = x_s(t) + x_d(t) \tag{4.4}$$

Assuming a linear spring in series with stiffness k_s and a nonlinear dashpot with viscous damping C and velocity exponent α for the nonlinear FVD Maxwell model:

$$F_M(t) = F_s(t) = k_s x_s(t) \tag{4.5}$$

$$F_M(t) = F_d(t) = C|\dot{x}_d(t)|^{\alpha} sgn\big(\dot{x}_d(t)\big) \tag{4.6}$$

Differentiating the displacements yields velocity across the element:

$$\dot{x}(t) = \dot{x}_s(t) + \dot{x}_d(t) \tag{4.7}$$

Substituting the constitutive equations for the spring velocity and dashpot velocity:

$$\dot{x}(t) = \frac{\dot{F}_M(t)}{k_s} + \left|\frac{F_M(t)}{C}\right|^{1/\alpha} sgn\big(F_M(t)\big) \tag{4.8}$$

While this equation will not be explicitly solved here, an estimation of the nonlinear FVD behaviour based on this equation is presented. The rate of change of force for a highly

nonlinear damper is predominantly either zero (damper behaves as a dashpot) or approaching very large values (when highest shear strains occur) due to the almost rectangular-shaped hysteresis curve. This applies for a velocity exponent of 0.15, and based on Figure 2.11, this simplification would apply to highly nonlinear FVDs with velocity exponents less than 0.5 due to their rectangular-shaped hysteresis curves. Therefore, the nonlinear FVD behaviour in Equation 4.8 can be simplified as a dashpot when the rate of change of force is zero:

$$F_M(t) = C|\dot{x}(t)|^{\alpha} sgn\big(\dot{x}(t)\big) \tag{4.9}$$

Similarly, when the rate of change of force is large, velocity is nearly zero, and thus, Equation 4.8 can be rearranged as follows:

$$F_M(t) + \frac{C}{{k_s}^{\alpha}}\left|\dot{F}_M(t)\right|^{\alpha} sgn\left(\dot{F}_M(t)\right) = 0 \tag{4.10}$$

Therefore, the simplified behaviour of a highly nonlinear FVD may be expressed as follows:

$$F_M(t) + \frac{C}{{k_s}^{\alpha}}\left|\dot{F}_M(t)\right|^{\alpha} sgn\left(\dot{F}_M(t)\right) = C|\dot{x}(t)|^{\alpha} sgn\big(\dot{x}(t)\big) \tag{4.11}$$

Because of the second derivative of force term, raised to a fractional exponent, this nonlinear Maxwell equation is more difficult to solve than the linear Maxwell equation, an ordinary differential equation (ODE) as follows:

$$F_M(t) + \frac{C}{k_s}\dot{F}_M(t) = C\big(\dot{x}(t)\big) \tag{4.12}$$

The linear Maxwell equation is simplified by substituting the linear stress-relaxation factor λ_L:

$$F_M(t) + \lambda_L \dot{F}_M(t) = C\big(\dot{x}(t)\big) \tag{4.13}$$

Returning to the nonlinear Maxwell equation, consider a highly nonlinear damper with velocity exponent of 0.15, and further simplify the equation by substituting the nonlinear stress-relaxation factor λ_{NL}:

$$\lambda_{NL} = \frac{C}{{k_s}^{\alpha}} \quad \text{and} \quad \alpha = 0.15 \tag{4.14}$$

$$F_M(t) + [\lambda_{NL}\left|\dot{F}_M(t)\right|^{-0.85} sgn(\dot{F}_M(t))]\dot{F}_M(t) = C|\dot{x}(t)|^{\alpha} sgn\big(\dot{x}(t)\big) \tag{4.15}$$

A first attempt at solving the nonlinear Maxwell equation used the fractional derivative Maxwell model (Makris & Constantinou 1991), yet the high nonlinearity of this FVD was poorly modelled. An alternative method is proposed, using an approximate stress-relaxation factor λ, to simplify the nonlinear Maxwell equation and allow for a similar solution to the linear Maxwell equation. The resulting negative fractional exponent value of the rate of change of force (e.g. $\dot{F}_M{}^{-0.85}(t)$) is very small and nearly constant when the rate of change of force is nonzero and approaching large values. An approximate stress-relaxation factor λ may represent the nonlinear stress-relaxation factor and the very small negative fractional component of the force rate:

$$\lambda = [\lambda_{NL}\left|\dot{F}_M(t)\right|^{\alpha-1} sgn(\dot{F}_M(t))] \tag{4.16}$$

$$F_M(t) + \lambda \dot{F}_M(t) = C|\dot{x}(t)|^{\alpha} sgn\big(\dot{x}(t)\big) \tag{4.17}$$

This approximation is appropriate for square-shaped hysteresis curves, as defined by the velocity exponent. If the initial force occurs when displacement is maximum and velocity is zero, the resulting initial output force is zero. Using the initial condition of zero force at zero time and solving this ODE in terms of the Maxwell element force and time *t* yields the solution for the nonlinear FVD force. The values to the right of the equal sign in Eq. 4.17 are assumed to be constant, such that the Maxwell model FVD force will be calculated at each time step for a particular velocity and displacement:

$$F_{M,FVD}(t) = C|\dot{x}(t)|^{\alpha} sgn\big(\dot{x}(t)\big)(1 - e^{-t/\lambda}) \tag{4.18}$$

This may also be written as:

$$F_{M,FVD}(t) = (F_{FVD}(t))(1 - e^{-t/\lambda}) \tag{4.19}$$

4.2.3.3. Governing Equation – FSD Kelvin-Voigt-Maxwell Model

Recall that the forces of elements in series are equivalent. Thus, the force in the Kelvin-Voigt model $F_{KV}(t)$ is equal to the spring force in series in the Kelvin-Voigt-Maxwell model (Figure 4.21). A similar derivation in terms of the KV element and spring in series is performed to

acquire a governing equation for the force in the KVM model.

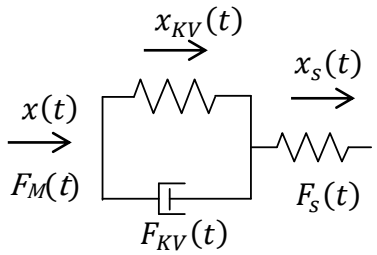

Figure 4.21. KVM Model (FSD) – Annotated

Substituting the nonlinear constitutive equations for the velocity of the spring in series and the KV element, in terms of the stiffness of the spring in series k_s, stiffness of the spring in parallel k, displacement of the KV element x_{KV}, and previously defined terms, produces:

$$\dot{x}(t) = \frac{\dot{F}_M(t)}{k_s} + sgn\big(F_M(t)\big)\left|\frac{F_M(t) - kx_{KV}(t)}{C}\right|^{1/\alpha} \tag{4.20}$$

Using the same estimation as presented for the highly nonlinear FVD, the FSD behaves as a Kelvin-Voigt model when the rate of change of force is zero:

$$F_M(t) = C|\dot{x}(t)|^{\alpha} sgn\big(\dot{x}(t)\big) + kx_{KV}(t) \tag{4.21}$$

When the rate of change of force is large (when highest shear strains occur) due to the almost rectangular-shaped hysteresis curve, the velocity is zero, and the restoring force from the spring in parallel is constant:

$$F_M(t) + \frac{C}{{k_s}^{\alpha}}\left|\dot{F}_M(t)\right|^{\alpha} sgn\left(\dot{F}_M(t)\right) = kx_{KV}(t) \tag{4.22}$$

Therefore, the nonlinear KVM equation is an estimation of the behaviour of the nonlinear FSD when both phases are considered:

$$F_M(t) + \frac{C}{{k_s}^{\alpha}}\left|\dot{F}_M(t)\right|^{\alpha} sgn\left(\dot{F}_M(t)\right) = C|\dot{x}(t)|^{\alpha} sgn\big(\dot{x}(t)\big) + kx_{KV}(t) \tag{4.23}$$

If the approximate stress-relaxation factor is assumed, the nonlinear KVM equation can be solved as an ODE, where the values to the right of the equal sign in Eq. 4.23 are assumed constant at each time step. If the initial force occurs when displacement is maximum and velocity is zero, then the initial force of the FSD is the maximum force from the spring in

parallel *kA*, based on the amplitude *A*. This differs from the FVD, where a zero initial velocity leads to zero initial force. The displacement of the KV element x_{KV} is assumed to be much greater than the displacement of the spring in series and, therefore, approximated as the displacement across the entire element $x(t)$. Solving the ODE with this initial condition leads to the theoretical FSD force considering stress relaxation $F_{KVM,\,FSD}$:

$$F_{KVM,FSD}(t) = \left[kx(t) + C|\dot{x}(t)|^{\alpha} sgn\left(\dot{x}(t)\right)\right] - \left[kx(t) + C|\dot{x}(t)|^{\alpha} sgn\left(\dot{x}(t)\right) - kA\right]e^{-t/\lambda} \quad (4.24)$$

This may also be written as:

$$F_{KVM,FSD}(t) = F_{FSD}(t) - \left[\left(e^{-t/\lambda}\right)\left(F_{FSD}(t) - kA\right)\right] \quad (4.25)$$

4.2.3.4. Processing Analytical Models

The analytical models were processed in Matlab. Desired displacements and velocities were calculated based on amplitude *A*, cyclic frequency ω, and time *t* of the tests, such that desired displacement was $A\sin(\omega t)$ and velocity $A\omega\cos(\omega t)$. The desired displacement and desired velocity were used to calculate the analytical damper forces independently of the tested damper performance. Because the viscous devices are largely controlled by the velocity, it was assumed that the desired velocity would provide a better representation of the analytical model's effectiveness, than the experimental velocity, which is not directly measured during testing and approximated from the experimental displacement.

To compare the experimental and analytical damper behaviour, phase lag between the analytical and experimental responses was taken into account when plotting the analytical response. Experimental data was plotted as recorded. Two phase lags were observed, including the phase lag between experimental and analytical applied displacements, attributed to the ramp-up time of the actuators to achieve commanded experimental displacements, and the phase lag between the experimental displacement and experimental force, possibly attributed to friction in the device. The second phase lag was negligible for the FSD tests greater than 1Hz and diminished with increasing frequency for all FVD tests.

Parameters of the analytical model for each test were determined visually using engineering judgment and trial and error fitting to achieve an understanding of how each parameter contributed to the device behaviour. For the FVD, the manufacturer-provided damping coefficient and velocity exponent were initially assumed accurate and adjusted when necessary to better fit the experimental data. Based on the experimental results, it was determined that the stress-relaxation parameter varied within the cycle depending on the rate of change of absolute velocity (i.e. the device acceleration). As the FVD approached zero force (decelerating), one stress relaxation rate was observed, and as the FVD approached maximum force (accelerating), another stress-relaxation rate was observed. Figure 4.22 highlights the varying behaviour of the FVD, depending on the acceleration. In the first part (~0 sec - 0.25 sec, neglecting ramp-up time) and the third part (0.5 sec - 0.75 sec) of the FVD cycle, the device is decelerating and experiences a larger stress relaxation at the plateau of the curve, which transitions smoothly into the linear region of the curve. In the second (0.25 sec - 0.50 sec) and fourth (0.75 sec - 1 sec) parts of the cycle, the FVD is accelerating to peak force, and experiences less stress relaxation at the force plateau and a sharper transition from the linear curve section to the plateau (Figure 4.22, gold boxes).

To approximately model this behaviour, two stress-relaxation parameters were used for the FVD model, one stress-relaxation rate λ_1 for the acceleration time segments and another relaxation rate λ_2 for the deceleration time segments. Further details of the stress-relaxation modelling are included in the FVD results section. For the FSD, key modelling parameters were similar to the FVD with the addition of the parallel stiffness k. A single stress-relaxation parameter λ was found to be adequate for modelling the behaviour of the FSD. Experimental results of the FSD showed noticeable stress relaxation to occur only in the deceleration quarter-cycles. Therefore, the FSD stress-relaxation parameter λ is similar to the FVD deceleration stress-relaxation parameter λ_2.

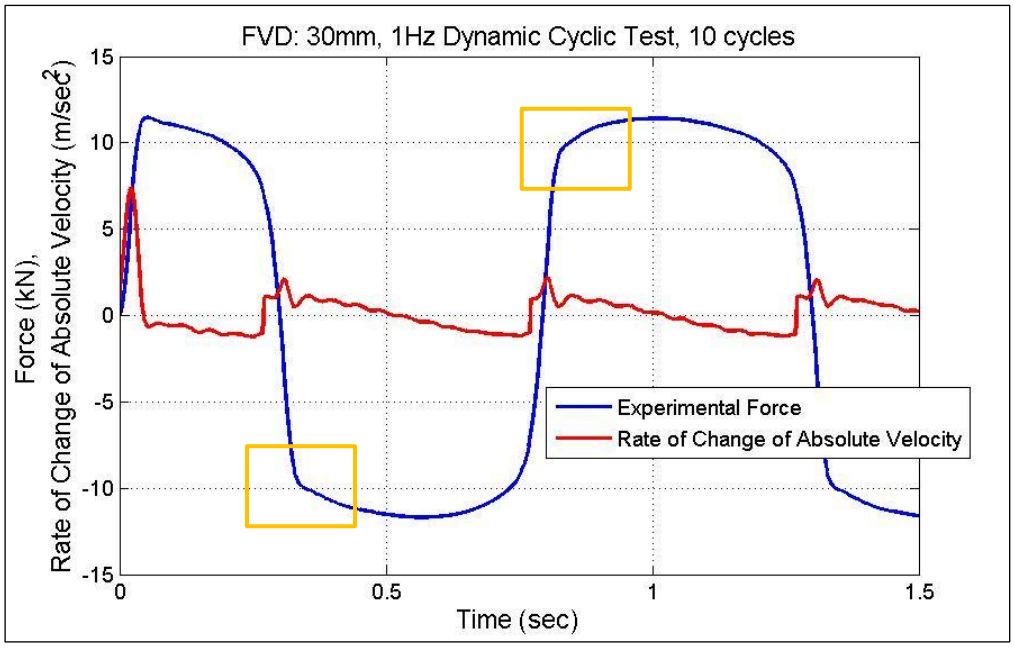

Figure 4.22. Variation in FVD Stress-Relaxation Rates (gold boxes)

4.3. Results and Discussion

4.3.1. Fluid Spring Damper

The results of the FSD include a description of the specific device model, performance in terms of experimental and analytical results, fitted model parameters, and trends based on experimental data.

4.3.1.1. FSD Force Output Model

The combined KVM model for the FSD was designed for each test quarter-cycle *T/4*, based on the cyclic period *T*. Table 4.4 illustrates the force equation for each quarter-cycle and the device position at the start of the quarter-cycle. The FSD is at its centred position and produces zero output force at the start of the cycle (*t=0*), neglecting the short ramp-up time to achieve the peak velocity (*t~0*). At the end of the first quarter-cycle (*t=T/4 sec*), the FSD is at the maximum amplitude of the cycle. Forces of the second quarter-cycle are based on the KVM model. At the end of the second quarter-cycle (*t=T/2 sec*), the FSD returns to its initial position. The same process continues for displacements in the opposite direction, with the FSD returning to its initial position at the end of the cycle (*t=T sec*). Note that cyclic amplitude *A* is negative in the fourth quarter-cycle.

Table 4.4. FSD Output Force over Time

Time, t (sec)	FSD Output Force (kN)	FSD Position at Initial Time
0 :(T/4)	$\left(kx(t) + C\lvert\dot{x}(t)\rvert^{\alpha} sgn\left(\dot{x}(t)\right)\right)$	
(T/4) : (T/2)	$\left(kx(t) + C\lvert\dot{x}(t)\rvert^{\alpha} sgn\left(\dot{x}(t)\right)\right) - \left[\left(e^{-t/\lambda}\right)\left(kx(t) + C\lvert\dot{x}(t)\rvert^{\alpha} sgn\left(\dot{x}(t)\right) - kA\right)\right]$	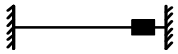
(T/2) : (3T/4)	$\left(kx(t) + C\lvert\dot{x}(t)\rvert^{\alpha} sgn\left(\dot{x}(t)\right)\right)$	
(3T/4) : T	$\left(kx(t) + C\lvert\dot{x}(t)\rvert^{\alpha} sgn\left(\dot{x}(t)\right)\right) - \left[\left(e^{-t/\lambda}\right)\left(kx(t) + C\lvert\dot{x}(t)\rvert^{\alpha} sgn\left(\dot{x}(t)\right) - kA\right)\right]$	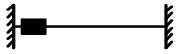

Figure 4.23 shows the force time history of the FSD, in terms of the experimental results F_{exp} and the constitutive components of damping $F_{KV,d}$ and stiffness $F_{KV,s}$. The addition of the stiffness and damping force curves yield the analytical model, without stress relaxation (Figure 4.24). The analytical KVM model incorporates the stress relaxation and better predicts the experimental results, as shown in Figure 4.24 for two different tests.

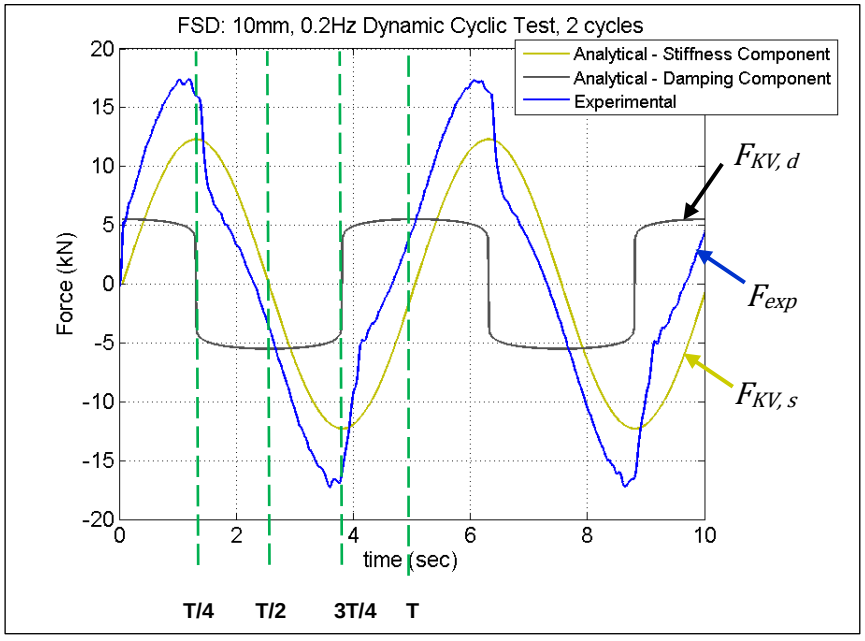

Figure 4.23. FSD Force Time History – Contribution of Stiffness and Damping Components

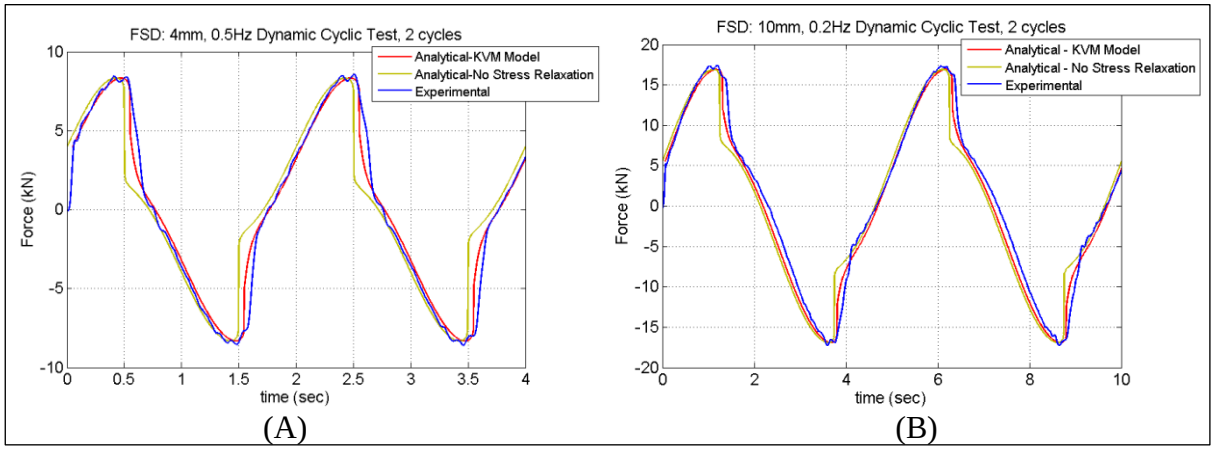

Figure 4.24. FSD Force Time History
KVM Model vs. KV Model (No Stress Relaxation) vs. Experimental

Returning to Figure 4.23, the green dashed lines denote the quarter-cycle divisions. Experimental results show that substantial stress relaxation occurs only in the second and fourth quarter-cycles, where the parallel spring and damper are of opposite signs (FSD force deceleration occurring). Note that because the FSD force output is a combination of the spring and damper force, peak force output occurs slightly before *T/4* and *3T/4*, as opposed to a lone spring or damper that would achieve peak forces in phase with peak displacements or velocities at multiples of *T/4*.

4.3.1.2. FSD Performance

The performance of the FSD is presented in terms of force and displacement hysteresis curves and the force and velocity relationship for a variety of tests. The analytical KVM model captures the rate of change of force at the peak displacements, as displayed in Figure 4.25 for 4mm amplitude low frequency and high frequency tests. The standard Kelvin-Voigt model without stress relaxation, noted as 'Analytical-No Stress Relaxation' overestimates the energy dissipation in the constant strain region and predicts a vertical force-displacement curve at the peak amplitude. This is more prominent in the high-frequency, 5 Hz test. While the KVM model is an improvement over the standard model, it still fails to capture all of the stress relaxation in the 5Hz test.

The FSD experimental results showed unequal positive and negative forces (the upper portion compared to the lower portion of the hysteresis curve) for some of the tests; this is noticeable in Figure 4.25 for the 0.5 Hz test, where the experimental negative forces are greater than the positive forces, and inversely for the 5Hz test. This characteristic of the FSD may be attributed to the two FSD devices having slightly different behavioural parameters.

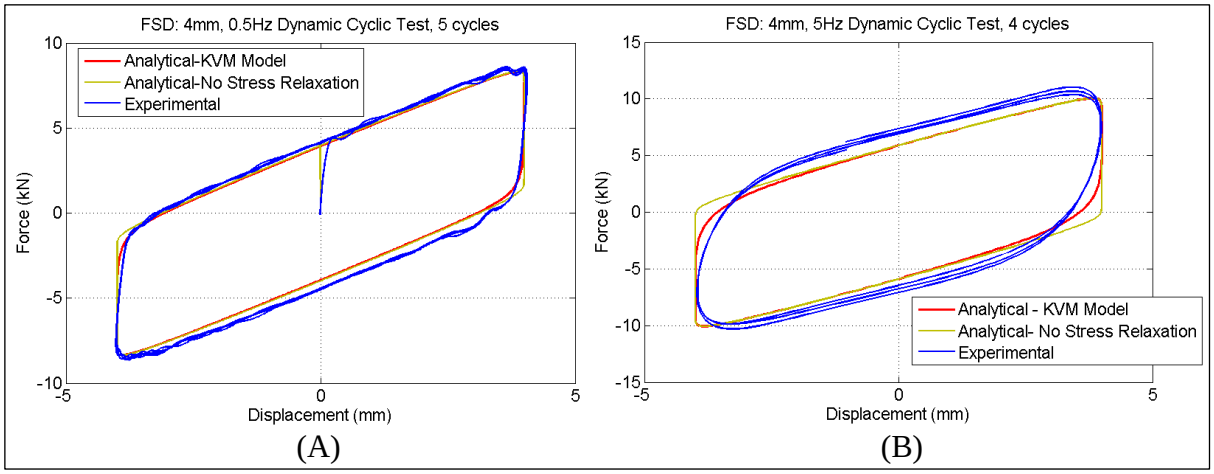

Figure 4.25. FSD Force and Displacement Relationship
KVM Model vs. KV Model (No Stress Relaxation) vs. Experimental

A series of varying amplitude and constant frequency tests are plotted in Figure 4.26 and Figure 4.27 to display the frequency-dependency in FSD hysteresis curves and the fit of the analytical models. At large amplitudes and low-frequency (Figure 4.26), the FSD exhibits a pinched shape, yielding smaller forces at small displacements and larger forces at large displacements than are predicted by the analytical model. However, the analytical stress relaxation at constant displacement fits reasonably well with the experimental data for all three 0.2 Hz tests, and the force output fits well for the 1mm and 4mm amplitude tests.

Slightly visible in Figure 4.27 is the decrease in experimental force with each cycle of the tests. The analytical model predicts the correct FSD forces in the lower part of the curve but under-predicts the upper curve forces, as indicated by all six tests at 1 Hz (Figure 4.27). Again, this difference can be attributed to the analytical model assuming equal behaviour of the two aligned FSDs, where in fact, the FSD device producing the positive forces in the

upper-portion of the curve may possess a slightly larger damping coefficient. The pinched shape in the hysteresis curve under 0.2 Hz and 10mm is also observed in the upper portion of the 9mm, 1Hz test.

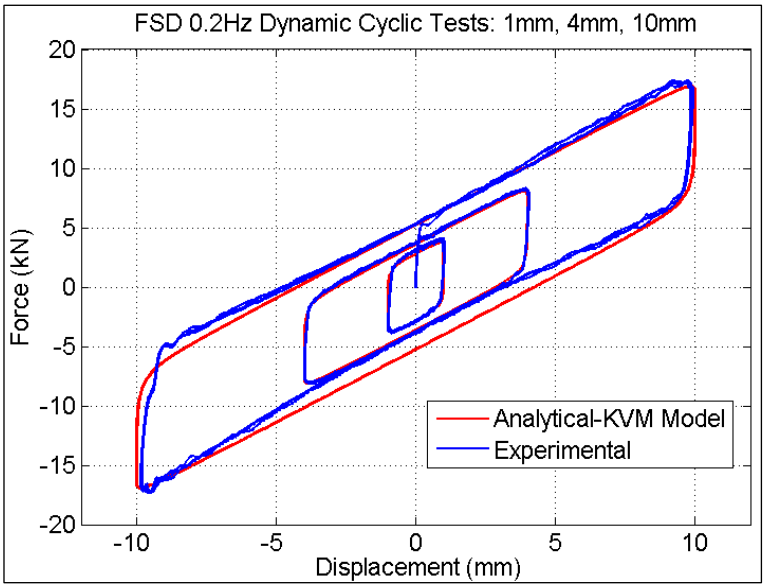

Figure 4.26. FSD - Dynamic 0.2 Hz Tests

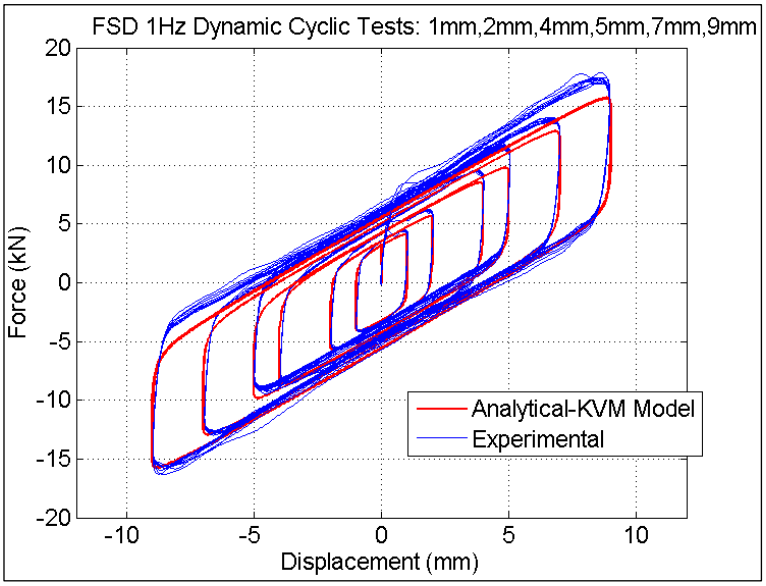

Figure 4.27. FSD - Dynamic 1Hz Tests

Finally, the performance of the FSD in terms of force and velocity is plotted in Figure 4.28 and Figure 4.29. Figure 4.28 (A) illustrates the experimental force versus the experimental velocity compared to the analytical force and desired velocity. Good correlation is shown between the analytical model and experimental results. Since experimental velocity is calculated based on the measured displacement signal, it is a more erratic signal than the

desired velocity. Figure 4.28 (B) compares the experimental force and analytical force plotted against the experimental velocity for the same 10mm, 0.2 Hz test, confirming that the jagged curve is a product of the experimental velocity signal. Additional force and experimental velocity curves are presented in Figure 4.29 for 0.5Hz and 1 Hz tests. Figure 4.29(B) reveals the maximum experimental force larger than the minimum experimental force as well as the analytical model better capturing the lower portion than the upper portion of the force-velocity curve.

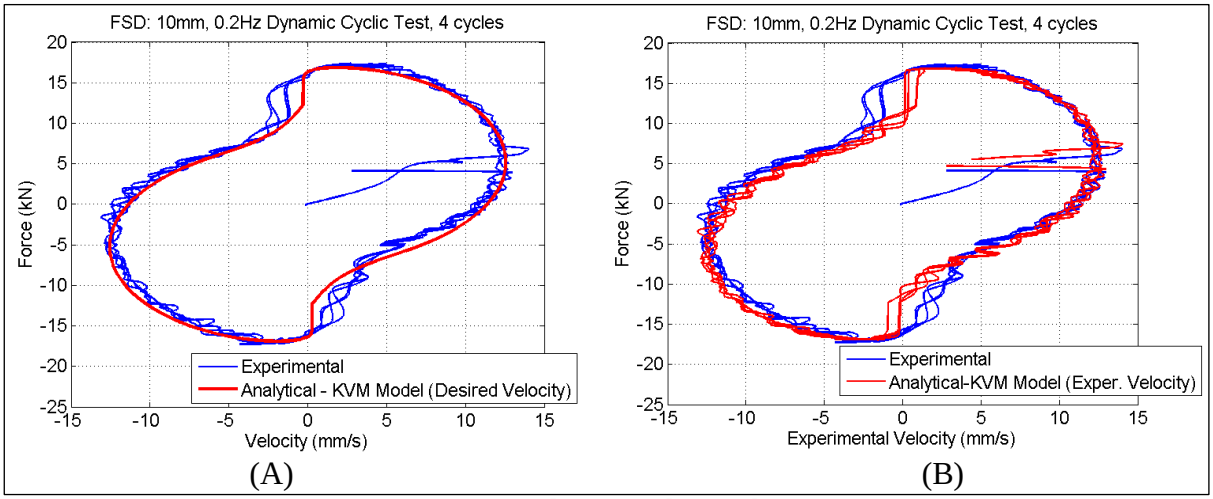

(A) (B)

Figure 4.28. FSD Force-Velocity Relationship, 0.2 Hz at 10mm
(A) KVM Model (Desired Vel.) vs. Experimental; (B) KVM Model (Exper. Vel.) vs. Experimental

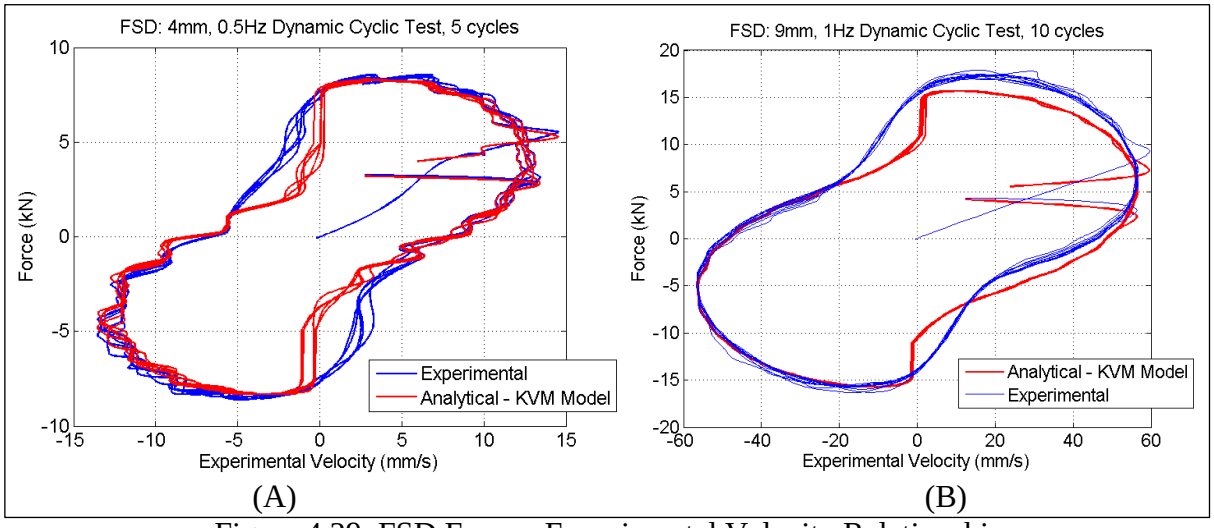

(A) (B)

Figure 4.29. FSD Force - Experimental Velocity Relationship
KVM Model (Experimental Velocity) vs. Experimental at (A) 4mm, 0.5Hz and (B) 9mm,1Hz

4.3.1.3. FSD Model Parameters

The stiffness *k* of the spring in parallel represents the slope of the force versus displacement curve; a constant value of 1.23 kN/mm was found to best model consistently the experimental

results. The velocity exponent α of the damper, which is exponentially proportional to the output force, characterises the shape of the force-displacement hysteresis curve. A constant value of 0.08 fit the experimental results for all tests. Table 4.5 provides details of the additional fitted parameters for the analytical model. The damping coefficient *C* was used to adjust the maximum damper output force; this parameter was found to gradually increase with increasing maximum velocity, roughly following a linear trendline (Figure 4.30). Another approach to fitting the model would be changing the velocity exponent and controlling the damping coefficient. Since the velocity exponent is primarily controlled by the orifice or annular flow design (Symans and Constantinou 1998) and not the properties of the fluid, it is justified that the damping coefficient may vary and the velocity exponent remains relatively constant.

Table 4.5. Parameters for FSD Analytical Model

Test Name	Frequency (Hz)	Amplitude (mm)	Maximum Velocity (mm/sec)	λ (sec)	C (kN-sec/mm)
j_1mm_02hz	0.2	1	1	0.150	2.75
j_4mm_02hz	0.2	4	5	0.110	3.25
j_10mm_02hz	0.2	10	13	0.100	4.50
j_1mm_05hz	0.5	1	3	0.080	3.25
j_4mm_05hz	0.5	4	13	0.045	3.25
j_9mm_05hz	0.5	9	28	0.045	3.25
j_1mm_1hz	1	1	6	0.030	2.75
j_2mm_1hz	1	2	13	0.030	3.00
j_4mm_1hz	1	4	25	0.030	3.25
j_5mm_1hz	1	5	31	0.030	3.25
j_7mm_1hz	1	7	44	0.023	3.75
j_9mm_1hz	1	9	57	0.022	4.00
j_1mm_2hz	2	1	13	0.028	3.00
j_2mm_2hz	2	2	25	0.020	2.90
j_4mm_2hz	2	4	50	0.018	3.50
j_1mm_3hz	3	1	19	0.030	3.25
j_4mm_3hz	3	4	75	0.014	3.40
j_7mm_3hz	3	7	132	0.014	4.00
j_1mm_4hz	4	1	25	0.018	3.50
j_2mm_4hz	4	2	50	0.015	4.00
j_3mm_4hz	4	3	75	0.015	4.10
j_4mm_4hz	4	4	101	0.012	4.50
j_5mm_4hz	4	5	126	0.010	4.75
j_6mm_4hz	4	6	151	0.010	5.00
j_1mm_5hz	5	1	31	0.012	3.50
j_4mm_5hz	5	4	126	0.009	4.00

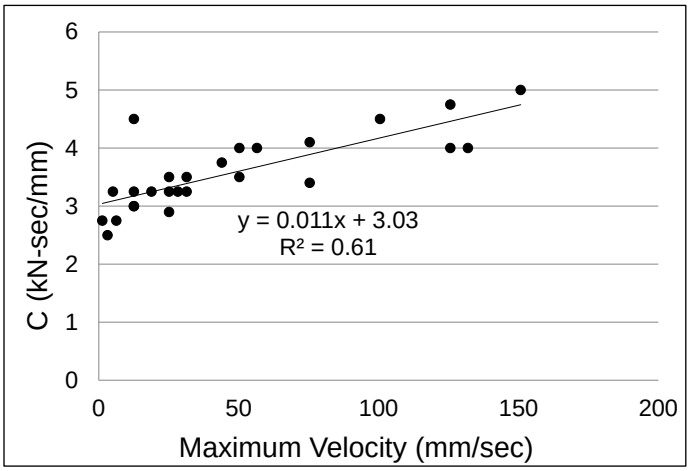

Figure 4.30. FSD Analytical Damping Coefficient vs. Maximum Velocity

The stress-relaxation parameter λ controls the force relaxation rate and varies inversely with the frequency of the tests, best modelled with a power function. For twenty-six data points, a best-fit trendline for stress-relaxation rate versus frequency has an R-squared value (coefficient of determination) of 0.89 and an equation displayed in Figure 4.31(A). Considering only 4mm amplitude tests, seven data points yield a similar trend between λ and frequency, and an R-squared value of 0.99 (Figure 4.31 (B)).

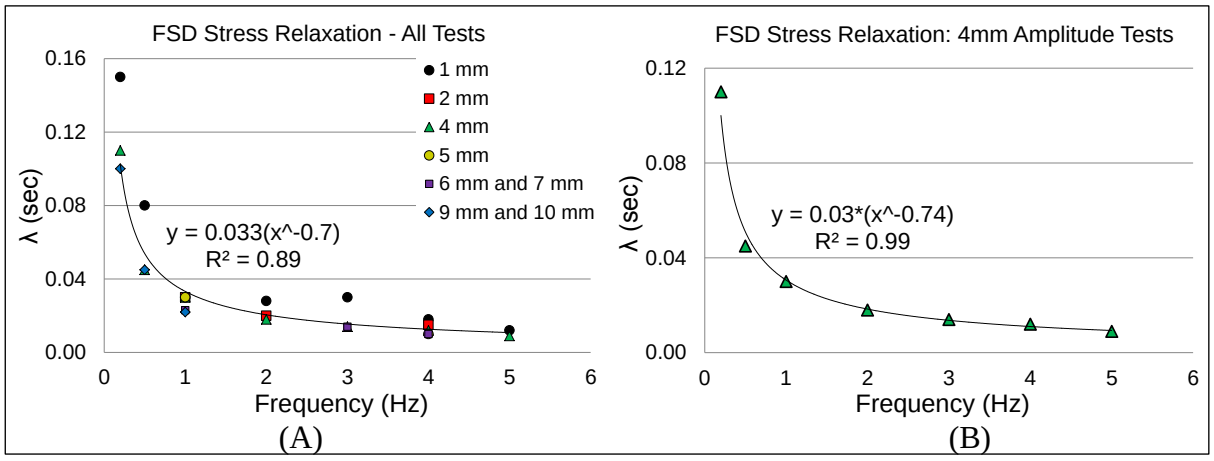

Figure 4.31. FSD Analytical Stress Relaxation Trends
Stress-Relaxation Factors for (A) All FSD Tests; (B) FSD 4mm Amplitude Tests

Finally, the trendlines from the experimental tests may be used to define the force in the FSD. Recall the FSD KVM governing equations for the acceleration phase (A) and the deceleration phase (D), where the FSD approximate stress-relaxation factor λ occurs only in the deceleration phase:

$$A)\ F_{KVM,FSD,A}(t) = kx(t) + C|\dot{x}(t)|^{\alpha} sgn(\dot{x}(t)) \quad (4.26)$$

$$D)\ F_{KVM,FSD,D}(t) = \left(kx(t) + C|\dot{x}(t)|^{\alpha} sgn(\dot{x}(t))\right) - \left[\left(e^{-t/\lambda}\right)\left(kx(t) + C|\dot{x}(t)|^{\alpha} sgn(\dot{x}(t)) - kA\right)\right] \quad (4.27)$$

The damping coefficient and stress-relaxation factor may be defined as function of amplitude and cyclic frequency ω based on the experimental cyclic test results:

$$C = 0.011\omega A + 3.03 \quad (4.28)$$

$$\lambda = 0.033\left(\frac{\omega}{2\pi}\right)^{-0.7} = 0.033(2\pi)^{0.7}\omega^{-0.7} \quad (4.29)$$

Substituting the damping coefficient and stress-relaxation factor equations, the known constants of stiffness and the velocity exponent, and the equations for displacement and velocity yields the force of the FSD under cyclic loading in terms of time, cyclic frequency, and amplitude:

$$A)\ F_{KVM,FSD,A}(t) = (0.011\omega A + 3.03)|\omega A cos(\omega \boldsymbol{t})|^{0.08} sgn\left(\omega A cos(\omega \boldsymbol{t})\right) + 1.23 A sin(\omega \boldsymbol{t}) \quad (4.30)$$

$$D)\ F_{KVM,FSD,D}(t) = \left(F_{KVM,FSD,A}(t)\right) - \left[\left(e^{-30.30(2\pi)^{-0.7}\omega^{0.7}\boldsymbol{t}}\right)\left(F_{KVM,FSD,A}(t) - 1.23A\right)\right] \quad (4.31)$$

4.3.2. Fluid Viscous Damper

The results of the FVD include a description of the specific device model, performance in terms of experimental and analytical results, and model parameters and trends based on experimental data.

4.3.2.1. FVD Force Output Model

The Maxwell model for the FVD was designed for each quarter-cycle *T/4* of the test, based on the cyclic period *T*. Table 4.6 illustrates the force equation for each quarter-cycle and the device position at the start of the quarter-cycle. While the position of the FVD is identical to that of FSD throughout the cycle, the force output differs, with stress relaxation applied via the Maxwell model at every quarter-cycle. As described previously, two stress-relaxation parameters are used. Firstly, λ_1 is the stress relaxation of the acceleration sections (the second and fourth quarter-cycles) in a traditional Maxwell model. Secondly, λ_2 is the stress-relaxation of the deceleration sections (the first and third quarter-cycles) where the current time *t* is

subtracted from the duration of the quarter-cycle *tf* (i.e. 0.25 sec for a 1Hz cycle). This alteration of the time range accounts for the initial condition of the ODE for the deceleration sections, where the initial force is the maximum dashpot force.

Table 4.6. FVD Output Force over Time

Time (sec)	FSD Output Force (kN)	FVD Position at Initial Time
0 : (T/4)	$C\lvert\dot{x}(t)\rvert^{\alpha} sgn\big(\dot{x}(t)\big)(1-e^{-tf+t/\lambda_2})$	
(T/4) : (T/2)	$C\lvert\dot{x}(t)\rvert^{\alpha} sgn\big(\dot{x}(t)\big)(1-e^{-t/\lambda_1})$	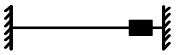
(T/2) : (3T/4)	$C\lvert\dot{x}(t)\rvert^{\alpha} sgn\big(\dot{x}(t)\big)(1-e^{-tf+t/\lambda_2})$	
(3T/4) : T	$C\lvert\dot{x}(t)\rvert^{\alpha} sgn\big(\dot{x}(t)\big)(1-e^{-t/\lambda_1})$	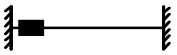

Figure 4.32 illustrates the force time history of the FVD in terms of the experimental results, analytical Maxwell model, and the analytical dashpot model. Peak forces occur at the peak velocities (0 sec, *T/2* sec, and *T* sec). As to be expected, the dashpot model characterises the peak force well, but assumes a sudden change occurs between the maximum and minimum FVD force, apparent in its prediction of a nearly vertical slope between the two peak forces. The analytical Maxwell model better captures the rate of change of force, particularly in the first and third quarter-cycles (deceleration), as seen in the negative slope of force in the first half-cycle of Figure 4.32.

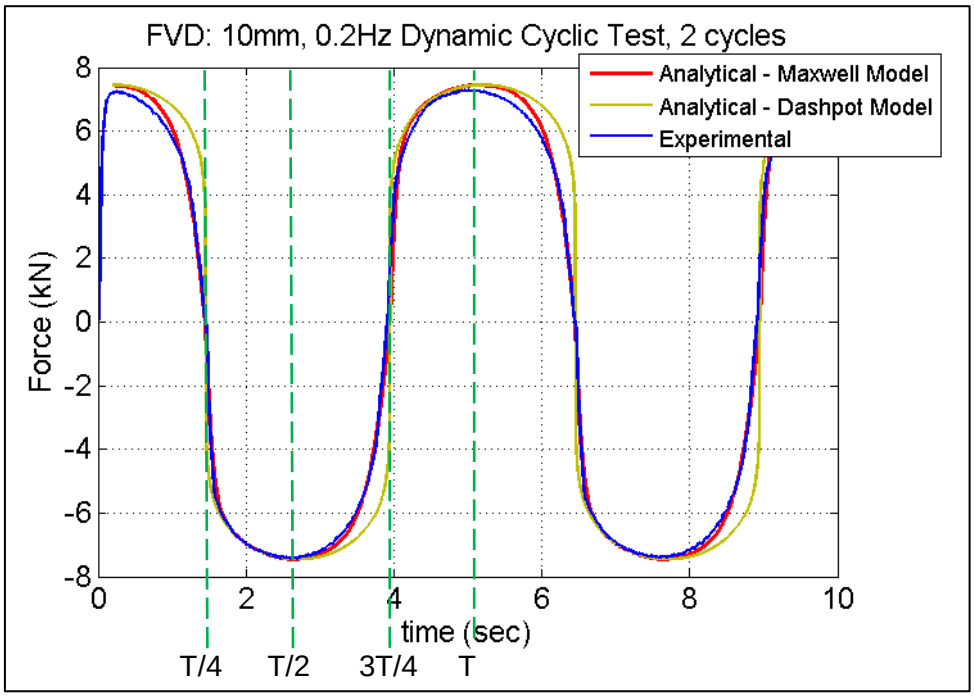

Figure 4.32. FVD Force Time History
Maxwell Model vs. Dashpot Model (No Stress Relaxation) vs. Experimental

4.3.2.2. FVD Performance

The performance of the FVD is presented in terms of force and displacement hysteresis curves and the force and velocity relationship for a variety of tests. Figure 4.33 displays the force-displacement hysteresis curves for four tests of varying frequency (0.1 Hz, 0.2 Hz, 1 Hz, 4 Hz) and two amplitudes (5mm and 20 mm), comparing the analytical Maxwell model, analytical dashpot model (no stress relaxation), and experimental results. The stress relaxation is more apparent in the 1Hz and 4Hz frequency tests and more noticeable in the 5mm, 0.1Hz test than the 20 mm, 0.2 Hz test, where the dashpot model is not far from the actual behaviour. The jagged peaks in the analytical Maxwell model for the 5mm, 4 Hz test are a result of the discrete quarter-cycle time period designating when one stress-relaxation equation ends and the next begins. Any errors in selecting the quarter-cycle times are exaggerated at high rates, a limitation of this model. Although there are some discrepancies between the analytical Maxwell model and the experimental curve, such as the analytical model slightly overestimating the peak force in the 0.1Hz, the analytical Maxwell model predicts the behaviour of the FSD more accurately than the dashpot model.

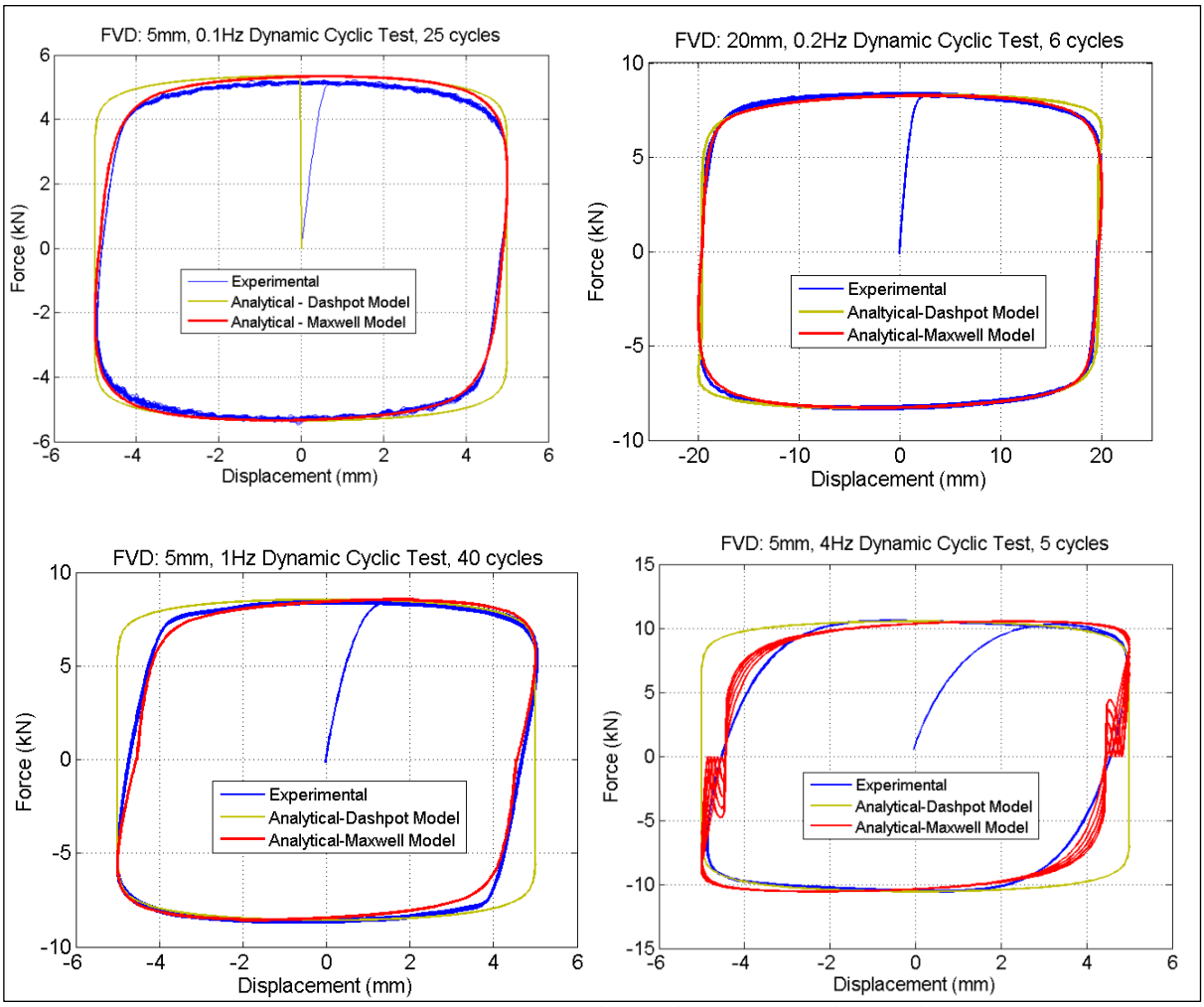

Figure 4.33. FVD Force and Displacement Relationship
Maxwell Model vs. Dashpot Model (No Stress Relaxation) vs. Experimental

Figure 4.34 and Figure 4.35 show the force versus displacement curves at 0.2 Hz and 1 Hz for varying amplitudes. The analytical model hysteresis curves roughly fit the experimental data. However, the analytical model does not fit the peak experimental forces in the negative displacement region (left portion of the curves) in the 30mm, 0.2Hz test in Figure 4.34 and all the tests greater than 5mm in Figure 4.35. This suggests that the FVD has slightly different damping coefficient or velocity exponent values depending on the direction of the motion. Note that the force differences are most noticeable in the tests with larger maximum velocities.

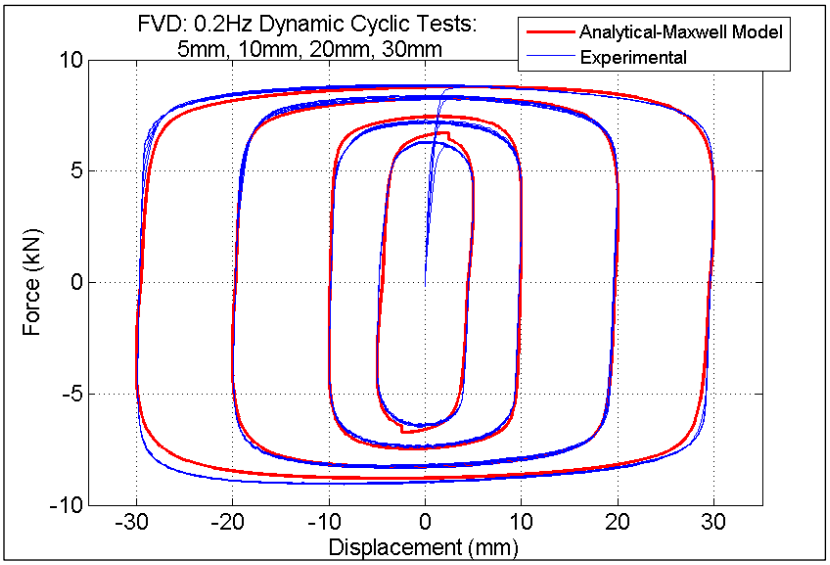

Figure 4.34. FVD - Dynamic 0.2 Hz Tests

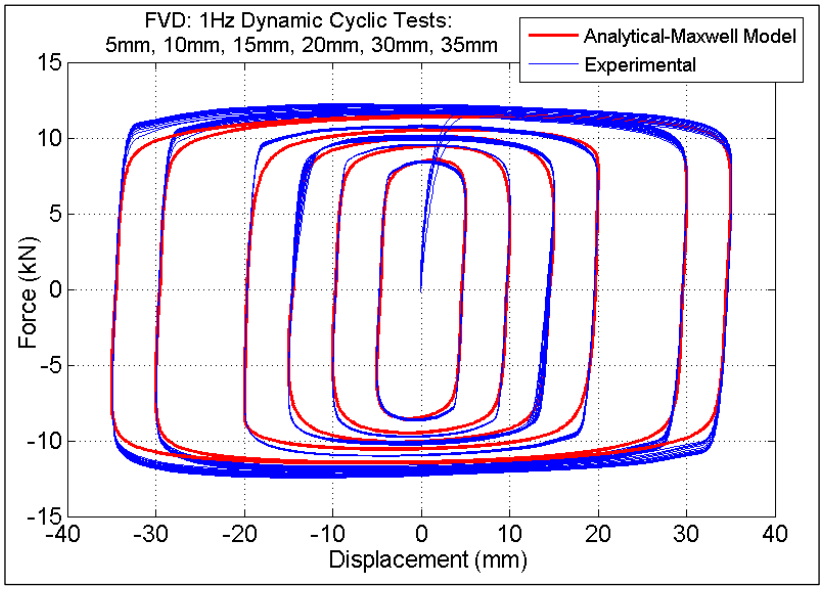

Figure 4.35. FVD - Dynamic 1Hz Tests

The force versus velocity response of the Maxwell model is comparable to the experimental data and captures the peak forces and slope of the force-velocity curve, as seen in Figure 4.36 (A), where analytical force and analytical velocity are plotted against experimental force and experimental velocity. Because the experimental velocity signal is more erratic than the desired velocity signal, plotting the analytical model versus the experimental velocity provides further verification of the fit of the model (Figure 4.36 (B)).

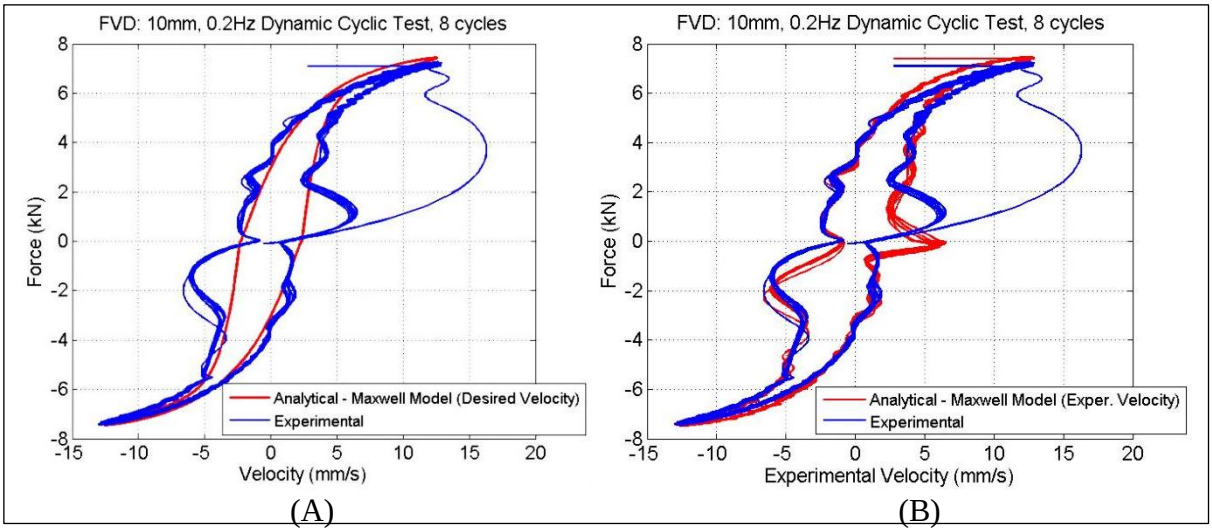

(A) (B)

Figure 4.36. FVD Force and Velocity Relationship, 0.2 Hz at 10mm
(A) Maxwell Model (Desired Vel.) vs. Experimental; (B) Maxwell Model (Exper. Vel.) vs. Experimental

4.3.2.3. FVD Model Parameters

Table 4.7 provides details of the fitted parameters for the analytical model. In the cases of the FVD exhibiting a larger damper force in one direction than the other, such as the minimum peak force slightly larger than the maximum peak force in Figure 4.37, the model was fit to the smaller absolute peak force. The manufacturer-provided parameters of C and α were adequate for the majority of the tests. The damping coefficient C is directly proportional to the output force, and for 1Hz longer-stroke tests (20mm, 30mm, and 35 mm amplitudes), a marginally larger damping coefficient of 5.2 kN-sec/mm better fit the experimental data. Similarly, a 4.5 kN-sec/mm damping coefficient more accurately modelled the low-frequency 0.1Hz test, but represents an outlier in the test data of consistent 5.1 or 5.2 kN-sec/mm damping coefficients.

Table 4.7. Parameters for FVD Analytical Model

Test Name	Frequency (Hz)	Amplitude (mm)	Maximum Velocity (mm/sec)	λ_1 (sec)	λ_2 (sec)
fip_5mm_0_1hz	0.1	5	3	0.250	0.40
fip_5mm_02hz	0.2	5	6	0.100	0.40
fip_10mm_02hz	0.2	10	13	0.060	0.20
fip_20mm_02hz	0.2	20	25	0.060	0.20
fip_30mm_02hz	0.2	30	38	0.060	0.20
fip_5mm_1hz	1	5	31	0.015	0.05
fip_10mm_1hz	1	10	63	0.015	0.05
fip_15mm_1hz	1	15	94	0.015	0.05
fip_20mm_1hz	1	20	126	0.008	0.02
fip_30mm_1hz	1	30	188	0.008	0.02
fip_35mm_1hz	1	35	220	0.008	0.02
fip_5mm_4hz	4	5	126	0.008	0.013

The velocity exponent α is exponentially proportional to the output force and controls the shape of the force versus displacement curve; lower velocity exponents correspond to more square-shaped hysteresis curves. The manufacturer's velocity exponent of 0.15 was found to best characterise the shape of the hysteresis curve for all tests.

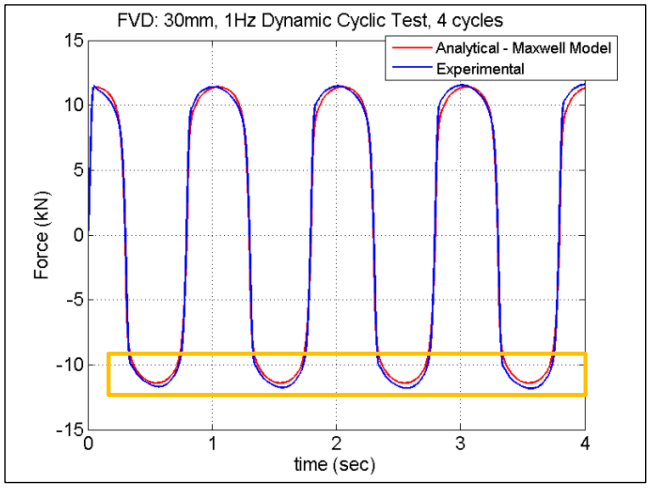

Figure 4.37. FVD Peak Force Variation

Similar to the FSD results, the stress-relaxation parameters λ_1 and λ_2 of the FVD model vary inversely with the frequency of the tests. Figure 4.38 shows the correlation between these parameters and frequency. A best-fit trendline was an inverse function with an R-squared value of 0.86 for λ_1 and an inverse power function with an R-squared value of 0.88 for λ_2, both based on 12 tests. Apart from the 1Hz long-stroke tests and 4Hz test, the stress-relaxation parameters are much larger than the 0.006 seconds discovered by Symans and Constantinou (1998) for linear FVDs, which is to be expected for a nonlinear FVD with such a low velocity-exponent.

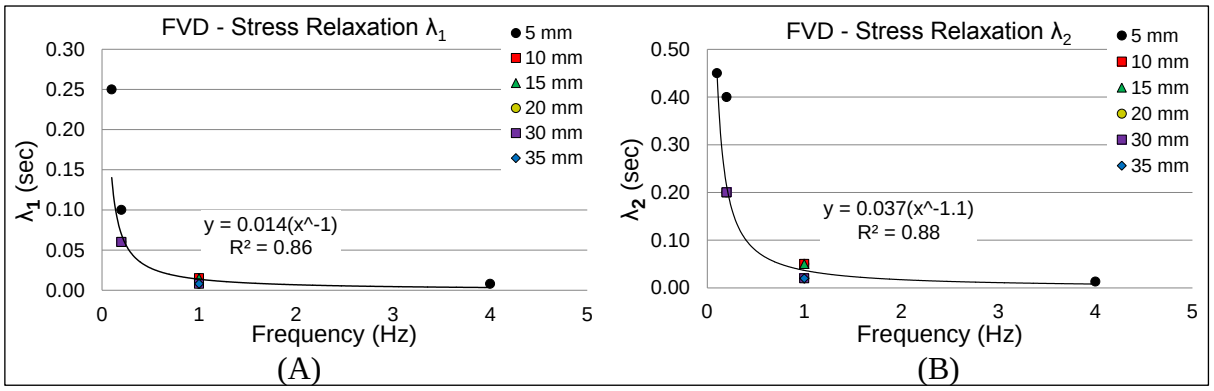

Figure 4.38. FVD Parameter Trends
Stress-Relaxation Factors: (A) λ_1 (Acceleration Phase); (B) λ_2 (Deceleration Phase)

The trendlines from the experimental tests may be used to define the force in the FVD. Recall the FVD Maxwell model governing equation, with approximate stress-relaxation factors for the acceleration phase (A) λ_1 and for the deceleration phase (D) λ_2:

$$A)\ F_{M,FVD,A}(t) = C|\dot{x}(t)|^{\alpha} sgn\big(\dot{x}(t)\big)(1 - e^{-t/\lambda_1}) \tag{4.32}$$

$$D)\ F_{M,FVD,D}(t) = C|\dot{x}(t)|^{\alpha} sgn\big(\dot{x}(t)\big)(1 - e^{-tf+t/\lambda_2}) \tag{4.33}$$

The stress-relaxation factors are defined as function of cyclic frequency based on the experimental test results:

$$\lambda_1 = 0.014\left(\frac{\omega}{2\pi}\right)^{-1} = 0.028\pi\omega^{-1} \tag{4.34}$$

$$\lambda_2 = 0.037\left(\frac{\omega}{2\pi}\right)^{-1.1} = 0.037(2\pi)^{1.1}\omega^{-1.1} = 0.0793\pi^{1.1}\omega^{-1.1} \tag{4.35}$$

Substituting the equations for stress-relaxation factors, the known constants of damping coefficient and velocity exponent, and the equations for cyclic velocity yields the force of the FVD as a function of time and cyclic frequency, where final quarter-cycle time *tf* is a function of cyclic frequency:

$$tf = \frac{T}{4} = \frac{\pi}{2\omega} \tag{4.36}$$

$$\text{A)}\ F_{M,FVD,A}(t) = 5.1|\omega A cos(\omega \boldsymbol{t})|^{0.15} sgn\big(\omega A cos(\omega \boldsymbol{t})\big)(1 - e^{-35.71\pi^{-1}\omega \boldsymbol{t}}) \tag{4.37}$$

$$D)\ F_{M,FVD,D}(t) = 5.1|\omega A cos(\omega \boldsymbol{t})|^{0.15} sgn\big(\omega A cos(\omega \boldsymbol{t})\big)(1 - e^{12.61\pi^{-1.1}\omega^{1.1}(\boldsymbol{t}-0.5\pi\omega^{-1})}) \tag{4.38}$$

4.3.3. Energy Dissipation

The previous sections present the analytical force output models incorporating stress relaxation to better capture the behaviour of the FSD and FVD. Adequacy of the models is assessed by their ability to capture the stress relaxation at constant strain and approximately model the overall force-displacement hysteresis curve. Limitations of the analytical force models include discrepancies in predicting the actual peak damper forces, likely due to the fitted behavioural parameters and particularly apparent in the FSD (Figure 4.25). Hence, total energy dissipation of both the standard and stress-relaxation models compared to the actual

device energy dissipation may be underestimated in some of the tests, a direct result of the fitted parameters and not the analytical model formulation.

In general, the significance of the stress-relaxation models may be evaluated by their influence on the energy dissipation of the devices. Thus, this may suggest if stress-relaxation models as opposed to standard models are critical for analysis of damped structures using these types of nonlinear viscous devices. The objective of this section is to compare the energy dissipated by the standard and stress-relaxation models to determine what influence the stress-relaxation component of the curve has on the total energy dissipation of the device. Since the dashpot and Kelvin-Voigt models are the standard models in baseline practice, for the comparison it is assumed that the model parameters accurately reflect the peak force output of the devices. For additional insight, the actual device energy dissipation is presented.

The energy dissipation per cycle of the stress relaxation FVD model has been calculated using the following equation, where the energy in the deceleration and acceleration sections are calculated separately using the analytical force output model in Eq. 4.37 and Eq. 4.38, as follows:

$$E_{FVD,M} = 2\left(\int_0^{\frac{T}{4}} F_{FVD,M,D}(t)\dot{x}(t)dt\right) + 2\left(\int_{\frac{T}{4}}^{\frac{T}{2}} F_{FVD,M,A}(t)\dot{x}(t)dt\right) \tag{4.39}$$

Similarly, the energy dissipated per cycle of the FSD stress-relaxation model is based on the analytical model in Eq. 4.30 and Eq. 4.31, as follows:

$$E_{FSD,KVM} = 2\left(\int_0^{\frac{T}{4}} F_{FSD,KVM,A}(t)\dot{x}(t)dt\right) + 2\left(\int_{\frac{T}{4}}^{\frac{T}{2}} F_{FSD,KVM,D}(t)\dot{x}(t)dt\right) \tag{4.40}$$

The energy dissipation per cycle of the standard models, the dashpot for the FVD and the Kelvin-Voigt model for the FSD, are presented in detail in Chapter 2 for the FVD and may be similarly applied for the FSD. Finally, the actual energy dissipation of the device was

approximated as the area under the force-displacement hysteresis experimental curve. A trapezoidal area method was employed in Matlab to evaluate the integrals.

Table 4.8 presents the energy dissipation of the FVD models for a range of tests, where the energy calculation uses the generalised expression for the stress-relaxation parameters. Note that the force versus displacement hysteresis curves of four tests in Table 4.8 are presented in Figure 4.33. The ratio of the energy dissipated by the Maxwell model and dashpot model (ratio of stress relaxation and standard models, $E_{SR}/E_{STD,}$ within highlighted column) indicates that the standard model overestimates the energy dissipated by the stress-relaxation model by 4% in the worst case. Overall, the energy dissipation of the standard dashpot model is consistently within 2% to 4% of the stress-relaxation model, regardless of frequency or amplitude. The energy dissipation ratios based on the individual fitted parameters for the models are included in parentheses to show the close correlation of the energy ratios.

Table 4.8. Energy Dissipation of the FVD Models

Frequency (Hz)	**Amplitude (mm)**	**Energy Dissipation (kN-mm)**			**E_{SR} / E_{STD} * (%)**	E_A / E_{SR} * (%)
		FVD Actual E_A	Maxwell E_{SR}*	Dashpot E_{STD}*		
0.1	5	94	111 (98)	116 (102)	96% (96%)	85% (96%)
0.2	10	267	276 (277)	285 (285)	97% (97%)	97% (96%)
0.2	20	618	612 (615)	633 (633)	97% (97%)	101% (104%)
1	5	152	159 (156)	164 (164)	97% (95%)	96% (97%)
1	30	1314	1252 (1300)	1285 (1310)	97% (99%)	105% (101%)
4	5	174	197 (197)	202 (202)	98% (98%)	88% (88%)

*values in parentheses are based on individual fitted parameters (Table 4.7)

The actual energy dissipation of the FVD is modelled well by the stress-relaxation model for the 0.2 Hz tests and 1 Hz tests. The Maxwell model slightly underestimates the energy dissipated in the 1 Hz, 30 mm test, which is expected due to the larger peak forces achieved in the experimental hysteresis curve than the Maxwell model curve (Figure 4.35). The 12-15% overestimation of dissipated energy by the Maxwell model for the 0.1Hz and 4 Hz tests is due to an overestimated peak force (Figure 4.33). With the exception of the 1 Hz, 30 mm test, the stress-relaxation model more closely predicts the actual energy dissipation than the standard

model.

Table 4.9 reflects the energy dissipation of the FSD models for a range of tests. Force displacement hysteresis curves of the 0.5 Hz and 5 Hz tests at 4mm amplitude are presented in Figure 4.25. The standard Kelvin-Voigt model yields energy dissipation per cycle that is 4% to 1% greater than the Kelvin-Voigt-Maxwell (KVM) model. The energy dissipation ratios based on the individual fitted parameters for analytical models are presented in parentheses, showing similar correlation to the energy dissipation ratios based on generalised parameters.

Table 4.9. Energy Dissipation of the FSD Models

Frequency (Hz)	**Amplitude (mm)**	**Energy Dissipation (kN-mm)**			**E_{SR} / E_{STD} * (%)**	E_A / E_{SR} * (%)
		FSD Actual E_A	KVM E_{SR} *	Kelvin-Voigt E_{STD} *		
0.2	1	10.6	12.0 (10.8)	12.1 (11)	99% (98%)	88% (98%)
0.2	10	187	150 (214)	151 (215)	99% (99%)	125% (87%)
0.5	4	66	59.8 (62)	60.6 (62)	99% (100%)	110% (106%)
2	4	83	74 (73)	77 (75)	96% (97%)	112% (114%)
4	1	16	16.0 (16.5)	16.7 (17.9)	96% (92%)	100% (97%)
5	4	98	97 (88)	101 (92)	97% (96%)	101% (111%)

*values in parentheses are based on individual fitted parameters (Table 4.5)

Due to the low peak forces predicted by the analytical models in many of the FSD tests (i.e. 0.5 Hz, 4mm test, Figure 4.25(A)), both the stress-relaxation and standard models may underestimate the total energy dissipation as compared to the actual device performance. Interestingly, the KVM model based on individually fitted parameters (in parentheses) for the 0.2 Hz test at 10mm over-predicts total energy dissipation (Figure 4.26, due to low peak forces and pinched hysteresis shape in the actual test), while the KVM model based on the generalised parameters under-predicts the total energy dissipation compared to the actual device. The very similar energy dissipation values for the KVM and Kelvin-Voigt models suggest that neither is more effective at modelling the energy dissipation of the actual device. Instead, it is clear that effective modelling of the peak forces in the hysteresis curve is critical to achieving an accurate estimation of total energy dissipated per cycle.

Returning to the importance of stress-relaxation towards the total energy dissipation, the

results from the FVD and FSD indicate that the standard models will adequately model the energy dissipation potential of the nonlinear devices within 5% of the energy per cycle of stress-relaxation models. Therefore, while the analytical models with stress relaxation have been shown to capture the effect of high shear strains in these nonlinear devices, the overall effect of the stress relaxation on total energy dissipation potential is minor. Standard nonlinear viscous models should be adequate for numerical analysis of damped structures, and an additional factor of safety could include a 5% increase in the damper energy capacity design to account for the energy dissipation reduction due to stress relaxation at high shear strains. In addition, the parameters of the analytical models should achieve true peak damper forces in the hysteresis curve to accurately model the total energy dissipation.

4.4. Conclusions

The test approach and experimental set-up capture the FSD and FVD behaviour over a range of frequencies and amplitudes and may be employed for future tests of the devices. The Maxwell model for the FVD and the Kelvin-Voigt-Maxwell (KVM) model for the FSD using the approximate stress-relaxation factor better predict the stress relaxation of the devices compared to the standard dashpot model and Kelvin-Voigt model. Damper force equations are proposed for both the FVD and FSD in terms of amplitude and cyclic frequency based on fitted parameters of the damping coefficient, approximate stress-relaxation factor, stiffness, and the velocity exponent.

Overall, the analytical force output models are shown to predict the behaviour of the devices well in terms of stress-relaxation at constant strain and approximate fit of the force-displacement hysteresis curves. Exceptions include discrepancies within the higher frequency tests (i.e. 4Hz FVD and FSD) and neglecting the inequality of positive and negative forces of the experimental hysteresis curves, which prompt discrepancies in peak forces and may be

attributed to differences in the FSD individual device properties and sensitivity of the FVD properties to the displacement direction of high-rate tests.

Based on experimental data, an estimated analytical model with fitted parameters is suggested for the FSD. Stiffness and the velocity exponent remain constant over the range of frequencies, while the stress-relaxation parameter varies inversely with the frequency, best predicted by a power function. The damping coefficient gradually increases with increasing maximum velocity. The FSD was tested to its displacement limit (10mm) and to a force of approximately 17kN, near its previously tested force limit of 20kN.

For the FVD, manufacturer-provided details of damping coefficient and velocity exponent were adequate for the majority of tests. The FVD results also reveal that stress relaxation parameters differ depending on device acceleration, where deceleration prompts a larger stress-relaxation parameter and acceleration yields a smaller stress-relaxation parameter. Both stress-relaxation parameters are approximately inversely proportional to frequency. The FVD does not exhibit a restoring force within the frequency range, confirming the cut-off frequency limit (Hou 2008) and indicating the presence of an accumulator in the FVD design. The FVD was tested to near its force limit (13.1kN) at the 1Hz, 35mm test but only within half its displacement limit of ±60mm.

Further improvements of the analytical models could include redefining the stress relaxation duration, such that it better predicts the FVD and FSD high frequency tests, and adjusting the model to consider variable device parameters in each direction (i.e. the parameters of the two FSD devices and possible directionally-dependent FVD parameters). Although it can be justified that a 35mm amplitude tests represents realistic interstorey drift of a supplementally damped building (i.e. 1% interstorey drift under DBE, see Chapter 6), investigation of the FVD at its operational limits of ±60mm would better characterise its performance. Closely

monitoring the change in device parameters with temperature poses another means of improving the models. Finally, optimally fitting the modelling parameters, particularly in regards to achieving peak damper forces, would provide a better fit of the experimental data.

The purpose of this research to understand the behaviour and verify the analytical models for nonlinear dissipative devices has been achieved. In addition, previously unknown behaviours, such as two stress-relaxation parameters for the FVD and the necessity of the spring in series for the FSD, have been discovered. A comparison of the energy dissipation potential of the stress-relaxation models and standard models for the viscous devices revealed only a 5% maximum difference in total energy dissipated per cycle for a range of tests. Therefore, it is proposed that the standard dashpot and Kelvin-Voigt models would adequately simulate the energy dissipation of the devices for numerical analysis of damped structures. Also, it is essential that the peak force output be accurately modelled by the fitted parameters to ensure true energy dissipation of the device model.

Finally, the application of these conclusions for linear viscous dampers is briefly addressed. The steep rate of change of force with time prompting the square-shaped hysteresis curve for nonlinear viscous dampers is not exhibited in the oval-shaped hysteresis of the linear viscous device. Therefore, based on this hysteresis shape (due to a lack of high shear stress zones) and effectiveness of standard models for representing energy dissipation potential of nonlinear devices, it is justified that a standard dashpot adequately models a linear viscous damper. Thus, the linear dashpot is selected as the analytical model for linear viscous dampers in Chapters 5, 6, and 7.

Chapter 5

Investigating Optimal Placement Techniques: Shear Frames

5.0. Introduction

The purpose of this chapter is to explore the potential of the selected optimal placement techniques through a preliminary investigation of shear frame structures. A shear frame provides the simplest example for comparing the damper placement methods and familiarising the user with the placement procedures. The objectives are to verify the correct application of the methods, to formalise a framework for analysing and comparing the placement methods, and to perform a preliminary comparison of some of the methods. The standard placement methods examined are the Uniform and Stiffness Proportional methods, and the advanced placement methods are the SSSA method, the Takewaki method, and the Lavan A/R method.

The investigation is divided in two parts: 1. application verification of the Takewaki, SSSA, and Lavan A/R methods and 2. comparison of the Takewaki and SSSA Mode methods to standard methods. The Lavan A/R investigation is limited to verifying the method's application because the Lavan A/R method was incorporated as an advanced placement method later in the research stages. The comparative data in literature lends itself to a dual verification and comparison of the Takewaki and SSSA methods to the Uniform, and Stiffness Proportional methods. To verify the correct application of the methods, the shear frames from literature are reproduced and the calculated distribution schemes and performance results compared to the original results.

In the comparison of the methods, the quantity and type of ground motions are expanded to assess the Takewaki and SSSA methods' impacts on peak interstorey drifts. Since a key characteristic of the Takewaki method is its independence from ground motion characteristics

and for the SSSA method, its dependence on ground motion characteristics, a variety of ground motions, both near-fault and far-fault, were selected for the ground motion set. Preliminary findings assess the methods' effectiveness for reducing peak interstorey drifts for two different frames under a set of ground motions. These results suggest the need for comprehensive studies, which lead to the regular and irregular building investigations presented Chapter 6.

5.1. Methodology – Takewaki and SSSA Mode Methods

The following section presents the shear frames and methodology for verifying the application and comparing Takewaki and SSSA methods to standard placement methods. Two shear frames from literature were reproduced and examined. One frame was of spatially varying stiffness and the other with uniform stiffness. A preliminary investigation was conducted on the effectiveness of the Takewaki, SSSA, Uniform, and Stiffness Proportional methods, which provides a framework for comparing the techniques applied to complex structures. This section describes the shear frames, the mechanism for applying the damper placement techniques, and the assessment criteria for the effectiveness of the techniques.

5.1.1. Frame Properties

The two test cases used as a basis for comparison included: frame 1, an irregular building with a soft storey at the roof and varying stiffness throughout, and frame 2, a uniform stiffness building. Without supplemental damping, frame 1 would normally be expected to produce a peak interstorey drift distribution that increased from the base to roof, while frame 2 would be expected to produce inverse shape of peak interstorey drifts from base to roof. Both frames were taken from examples proposed by Takewaki (1997). The Takewaki method and SSSA method were shown to be comparable solutions for minimising the *sum* of interstorey drifts by Lopez-Garcia (2001) for frame 1, the varying stiffness shear frame, under four ground motions, El Centro S00E, Kobe EW, Taft N21E, and Rinaldi Northridge 318.

Both six-storey frames were represented by shear frame models with lumped masses (Figure 5.1. (A)) A Rayleigh damping formulation providing 3% damping in the 1st and 5th modal frequencies was used to model the inherent damping in the bare frame. Inherent damping is disregarded in the Takewaki method, and therefore, it was not included in the frames with dampers to provide a fair comparison to previous test results (Lopez-Garcia 2001). Figure 5.1(B), Table 5.1 and Table 5.2 present the structural properties of the frames, while Figure 5.2 illustrates the first three mode shapes and modal participating mass ratios. The modal participating mass ratio in the lateral direction r_{xn} for a particular mode n is a function of the total unrestrained mass in the lateral direction M_x and the modal participation factor f_{xn}, which is a function of the unit acceleration load a_x and the normalised mode shape Φ_n (CSI 2009a):

$$r_{xn} = \frac{(f_{xn})^2}{M_x} = \frac{(\Phi_n^T a_x)^2}{M_x} \tag{5.1}$$

Refer to Appendix A-7 for additional modal details for both frames. The stiffness distributions differed greatly between the frames, but the total stiffness and total mass were similar, resulting in an identical fundamental period and similar first mode shape (Figure 5.2). Frame 1 has a larger modal contribution of the second mode and third mode than frame 2. Takewaki (1997) designed frame 1 (variable stiffness) to have a uniform distribution of amplitudes of the interstorey drifts of the transfer function, such that Uniform damping would be a nearly optimal damping solution.

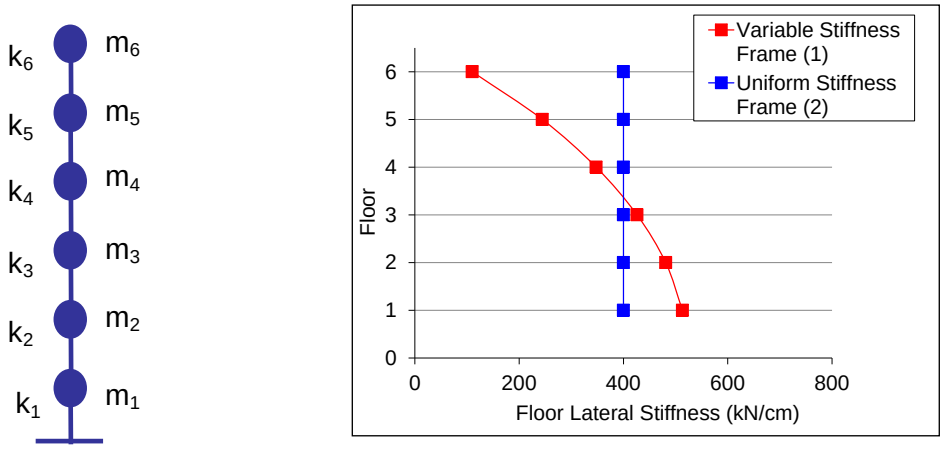

(A) (B)

Figure 5.1. Frame Lateral Floor Stiffness and Shear Model

Table 5.1. Frame Properties

	Frame 1		Frame 2	
Floor	Stiffness (kN/cm)	Mass (kg)	Stiffness (kN/cm)	Mass (kg)
1	513.1	80000	400	80000
2	481.0	80000	400	80000
3	426.0	80000	400	80000
4	347.6	80000	400	80000
5	244.4	80000	400	80000
6	110.0	80000	400	80000

Table 5.2. Frame Natural Periods

	Frame 1	Frame 2
Mode	Period (sec)	
1	1.17	1.17
2	0.50	0.40
3	0.31	0.25
4	0.22	0.19
5	0.17	0.16
6	0.14	0.14

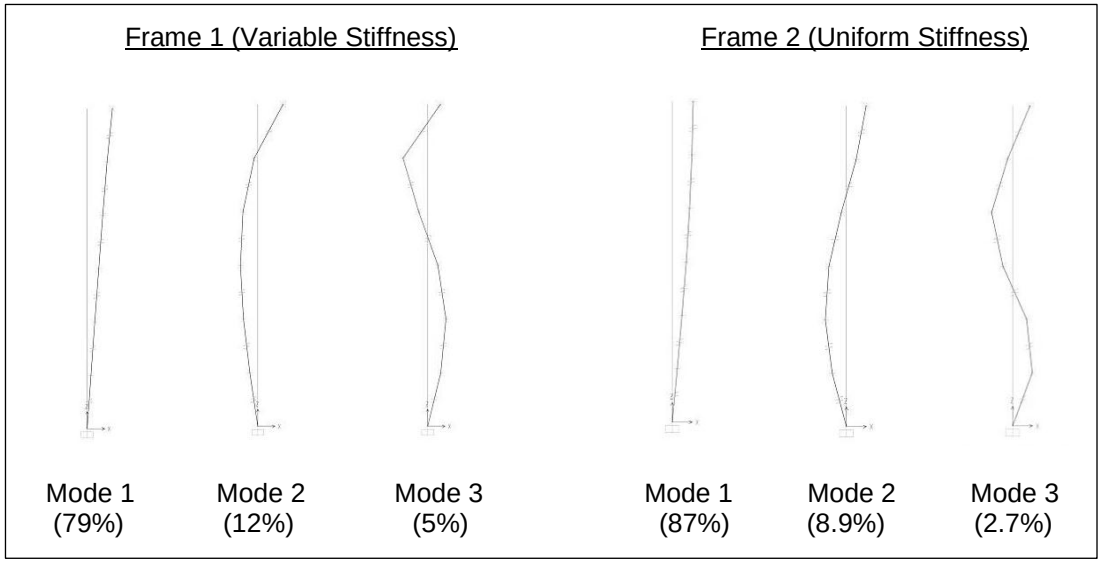

Figure 5.2. Mode Shapes and Mode Participating Mass Ratios: Frame 1 (left) and Frame 2 (right)

5.1.2. Mechanics of Optimisation

For a fair comparison of the three damper placement techniques, the same total added damping (90 kN-sec/cm) was used for each placement method in both frames, based on Takewaki (1997). The relationship between total damping and effective damping ratio as well as the application of the damper placement methods are presented.

5.1.2.1. Effective Damping Ratio

Using the strain energy method presented in the *2000 NEHRP provisions* (BSSC 2001), the total added viscous damping coefficient was translated into the total effective damping ratio required for the building retrofit. The total effective damping ratio ξ is equivalent to the ratio of the energy dissipated in one cycle of the viscous devices E_P and the maximum strain energy dissipated by the structural system E_S at the fundamental period T:

$$\xi = \frac{E_P}{4\pi E_S} \tag{5.2}$$

Considering the number of dampers n_d, single damper coefficient c, damper incline angle θ, interstorey drift δ_i at floor i, total number of floors n, and individual floor stiffness K_i:

$$\xi = \frac{\sum_{i=1}^{n_d} \frac{2\pi^2 c(cos^2\theta)\delta_i^2}{T}}{4\pi \sum_i^n \frac{1}{2} K_i \delta_i^2} \tag{5.3}$$

Further simplification occurs if the following assumptions are made: damper incline angle is zero; floor heights are assumed equal; first mode interstorey drifts are assumed equivalent; dampers sizes are equivalent, and finally, incorporating sum of the damping coefficients C and sum of the floor stiffness K_t (Lopez-Garcia 2001):

$$\xi = \frac{\frac{2\pi^2 C}{Tn^2}}{\frac{4\pi}{2n^2} K_t} = \frac{C\pi}{K_t T} \tag{5.4}$$

Whittaker, Constantinou, Ramirez, Johnson, and Chrysostomou (2003) present the same equation, using mass-based strain energy, which incorporates mode shapes and mass of the structure. The simplification presented here will be referred to as the stiffness-based strain energy equation; note that in order to calculate the total viscous damping for an effective damping ratio, a conservative assumption of uniform damping is applied. Using this equation, the total added damping of 90 kN-sec/cm is approximately equivalent to an 11% effective damping ratio for frame 1 at the fundamental period of vibration and 10% for frame 2.

5.1.2.2. Application of Damper Placement Methods

The application of the Uniform damping technique was performed by dividing the total added damping by the number of stories. Equivalent damping values were placed at each floor. Stiffness Proportional damping follows the principle that the damping at each floor is directly proportional to the floor's lateral stiffness, and the sum of the damping for all floors is constrained by the total added damping value. In the case of frame 2, uniform damping was

equivalent to Stiffness Proportional damping. Both of these methods were easily applied to the frames.

Application of the Takewaki method was executed with a Matlab script to produce the array of optimal added damping per floor. The performances of frame 1 and frame 2 with the Takewaki damper schemes were analysed for all seven ground motion cases. Application of the SSSA method was performed using the SSSA Mode procedure for frame 2 only for a preliminary comparison. An SSSA placement scheme was determined individually for the El Centro (IELC180), Erzincan, and Tabas ground motions (Table 5.5), selected to cover a range of near-fault and far-fault characteristics within the ground motion set, using nine procedural steps (9 dampers). The SSSA Mode scheme was selected as the most frequently occurring damper configuration between the three ground motions (Table 5.3). The performance of frame 2 with the SSSA Mode scheme was analysed for all seven ground motion cases. See Chapter 3 for additional details of the procedures for the damper placement methods.

Table 5.3. SSSA Mode Configuration – Frame 2

	SSSA Method - Added Damping per Floor (kN-sec/cm)			
Floors	*Erzincan (EZ)*	*Tabas (TA)*	*El Centro (EC)*	***SSSA Mode***
6	0	0	0	**0**
5	0	10	0	**0**
4	0	10	10	**10**
3	20	10	20	**20**
2	30	20	20	**20**
1	40	40	40	**40**

The final damping configuration schemes for the frames are presented in Table 5.4 and Figure 5.3. The advanced methods, SSSA and Takewaki, yield damping in the lower half of frame 2, confirming the conclusions of Hahn and Sathiavageeswaran (1992) that optimal damping of a uniform stiffness structure should be placed in the lower half. Note that the final Takewaki

distribution for frame 2 in Table 5.4 differs marginally from the distribution in Table 5.10, a result of using a different step size.

Table 5.4. Damping Configuration Schemes – Shear Frames 1 and 2

Added Damping (kN-sec/cm)						
	Frame 1 (Varying Stiffness)			*Frame 2 (Uniform Stiffness)*		
Floors	**Uniform**	**Stiffness Proportional**	**Takewaki**	**Uniform/ Stiffness Proportional**	**Takewaki**	**SSSA Mode**
6	15.00	4.67	13.73	15.00	0.00	0.00
5	15.00	10.37	16.82	15.00	0.00	0.00
4	15.00	14.74	18.51	15.00	0.00	10.00
3	15.00	18.07	19.19	15.00	0.00	20.00
2	15.00	20.40	8.77	15.00	42.35	20.00
1	15.00	21.76	12.98	15.00	47.65	40.00

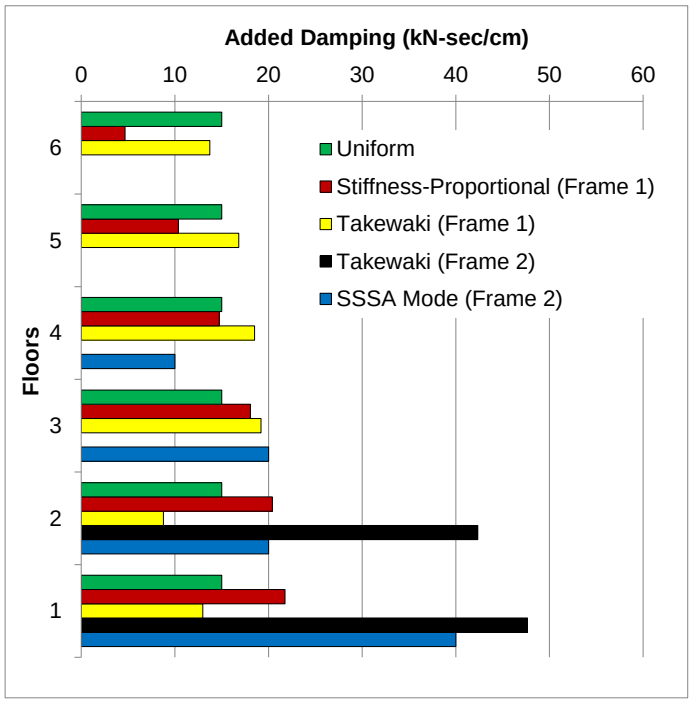

Figure 5.3. Damper Configuration Schemes – Frames 1 and 2

5.1.3. Assessment of Performance

Simulation of the damped frames was conducted with SAP2000 (CSI 2009a) using horizontal lumped masses, fixed foundation restraints, linear link elements for the spring and linear viscous damper elements, and linear time history analysis with 0.01 sec time steps. A set of seven unscaled ground motions acquired from the Pacific Earthquake Engineering Research Center Next-Generation Attenuation Relationships strong-motion database (PEER NGA,

PEER 2005) including both non-pulse-like far-fault and pulse-like near-fault excitations was used for this investigation. The peak interstorey drift at each floor was chosen as the performance index since it can indicate both structural and non-structural damage. Table 5.5 presents the peak ground acceleration (pga) of the ground motions, while Table 5.6 and Table 5.7 present the spectral displacements $S_d(T)$ of the frames with 3% damping (bare frame scenario) and 11% damping (damped frame scenario), evaluated at the frames' first three modes. See Appendix A-4 for the acceleration time histories, pseudo-spectral acceleration (PSA) plots, spectral displacement plots, and frequency content of the ground motion set.

Table 5.5. Ground Motion Set

	Ground Motions	Abbrev.	pga (m/sec^2)
Near Fault	Erzincan	EZ	5.05
	Tabas	TA	8.36
	Aigion	AI	5.33
Far Fault	El Centro (IELC180)	EC	3.07
	Brentwood - Northridge	BN	1.61
	Wadsworth - Northridge	WN	2.97
	Canoga Park / Santa Susana - Northridge	CN	2.28

Table 5.6. Frame 1 - Spectral Displacements

Frame 1	**Mode 1 (T_1)**		**Mode 2 (T_2)**		**Mode 3 (T_3)**	
Ground Motions	S_d (T_1) (m) (3% damping)	S_d (T_1) (m) (11% damping)	S_d (T_2) (m) (3% damping)	S_d (T_2) (m) (11% damping)	S_d (T_3) (m) (3% damping)	S_d (T_3) (m) (11% damping)
EZ	0.298	0.218	0.040	0.040	0.023	0.018
TA	0.232	0.138	0.128	0.084	0.047	0.034
AI	0.071	0.056	0.104	0.071	0.021	0.018
EC	0.137	0.078	0.046	0.034	0.017	0.011
BN	0.056	0.049	0.051	0.026	0.008	0.005
WN	0.125	0.077	0.025	0.018	0.012	0.011
CN	0.063	0.038	0.036	0.020	0.020	0.010

Table 5.7. Frame 2 - Spectral Displacements

Frame 2	**Mode 1 (T_1)**		**Mode 2 (T_2)**		**Mode 3 (T_3)**	
Ground Motions	S_d (T_1) (m) (3% damping)	S_d (T_1) (m) (11% damping)	S_d (T_2) (m) (3% damping)	S_d (T_2) (m) (11% damping)	S_d (T_3) (m) (3% damping)	S_d (T_3) (m) (11% damping)
EZ	0.298	0.218	0.032	0.029	0.015	0.013
TA	0.232	0.138	0.065	0.052	0.045	0.029
AI	0.071	0.056	0.050	0.037	0.017	0.014
EC	0.137	0.078	0.029	0.018	0.012	0.008
BN	0.056	0.049	0.023	0.016	0.006	0.004
WN	0.125	0.077	0.019	0.015	0.013	0.009
CN	0.063	0.038	0.032	0.016	0.014	0.008

5.2. Verification of Placement Method Application

5.2.1. Takewaki Method

The values produced by the Matlab script were verified with the results presented in Takewaki (1997). Nearly identical values were produced for frame 2 (uniform stiffness), while the results for frame 1 (varying stiffness) were not as similar. Takewaki (1997) does not include the prescribed step size but does include the total number of iterations, final objective function, and damper configurations for both shear frame examples.

5.2.1.1. Frame 1

An attempted verification of frame 1 produced a damper distribution within a 24% difference from the distribution in Takewaki (1997) (Table 5.8). Because the initial uniformly damped frame is a near-optimal solution, convergence for this frame was difficult to achieve (Figure 5.4). Using the Matlab script and final damping configuration from Takewaki (1997), the final optimal location indices were calculated (Table 5.8, column 7). The frame 1 verification results as compared to the Takewaki (1997) results have slightly smaller final optimal location indices γ_F and a marginally reduced final objective function V_f using a small step size (Ni = 30), indicating that the verification solution is nearer to optimal than the Takewaki (1997) solution.

Table 5.8. Verification of Takewaki Method for Frame 1

Takewaki Configuration Added Damping (kN-sec/cm)				Optimal Location Index ($\gamma_{F,i}$)		
Floors	Takewaki (1997)	Verification	Percent Difference (%)	$\gamma_{F,i}$	Takewaki (1997)	Verification
6	13.73	13.97	1.7%	5	1.0261	1.0183
5	16.82	17.33	3.0%	4	1.0246	1.0205
4	18.51	19.54	5.4%	3	1.0223	1.0177
3	19.19	21.24	10.1%	2	1.0206	1.0142
2	8.77	6.95	23.2%	1	1.0130	1.0079
1	12.98	10.97	16.8%		-	-
Sum	90	90			NT = 500	NT=100
					Ni=?	Ni=30
					V_i = 0.2033	V_i = 0.2033
					V_f = 0.2027	V_f = 0.2025

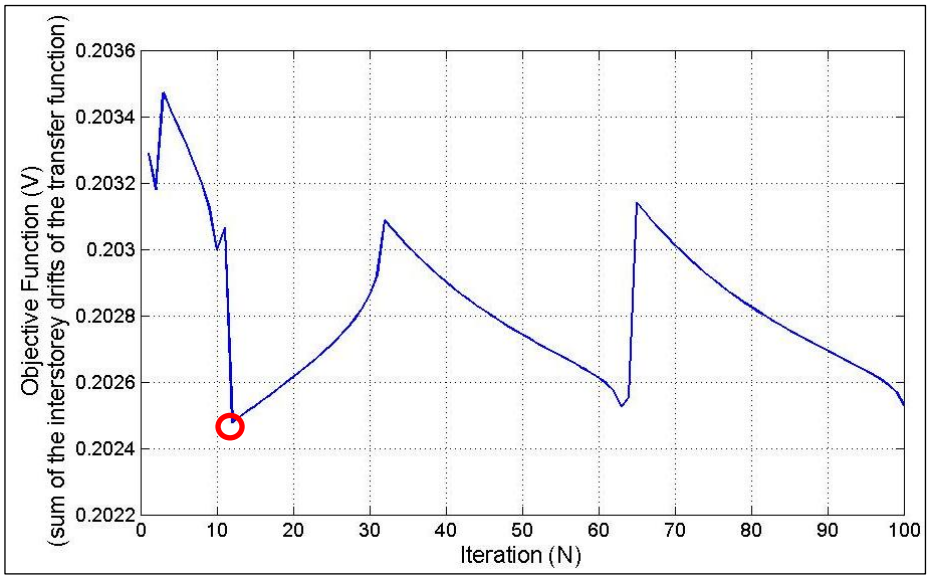

Figure 5.4. Takewaki Objective Function – Frame 1 (red circle denotes N=12)

The Takewaki method incrementally adjusts the damping array based on the difference in the optimality index from unity $\Delta\gamma$ and the second order sensitivity of the sum of interstorey drifts of the transfer function (partial derivative of array *B*, see Eq 3.8 and 3.9). Because the uniform damping distribution is already near optimal, the step of the gradient search in terms of the optimality index $\Delta\gamma$ is very small, resulting in minor changes to the damping array and resulting objective function with each step. Note that although the Takewaki method was carried out for a total of 100 iterations *NT* (Figure 5.4), the minimum objective function value occurred at step 12 but was not maintained.

The first small dip in the objective function curve indicates the change in the damping distribution from uniform damping (V_i = 0.2033) to the second iteration of the Takewaki method (V= 0.2032), where the damping at floors 1 and 6 decrease, damping at the remaining floors increase, and the objective function is marginally reduced. The increase in the objective function at step 3 is the result of searching in the wrong direction, increasing damping at floor 1 by too large an increment; therefore, the method compensates in steps 4-12 by decreasing the first floor and sixth floor damping and gradually reducing the objective function.

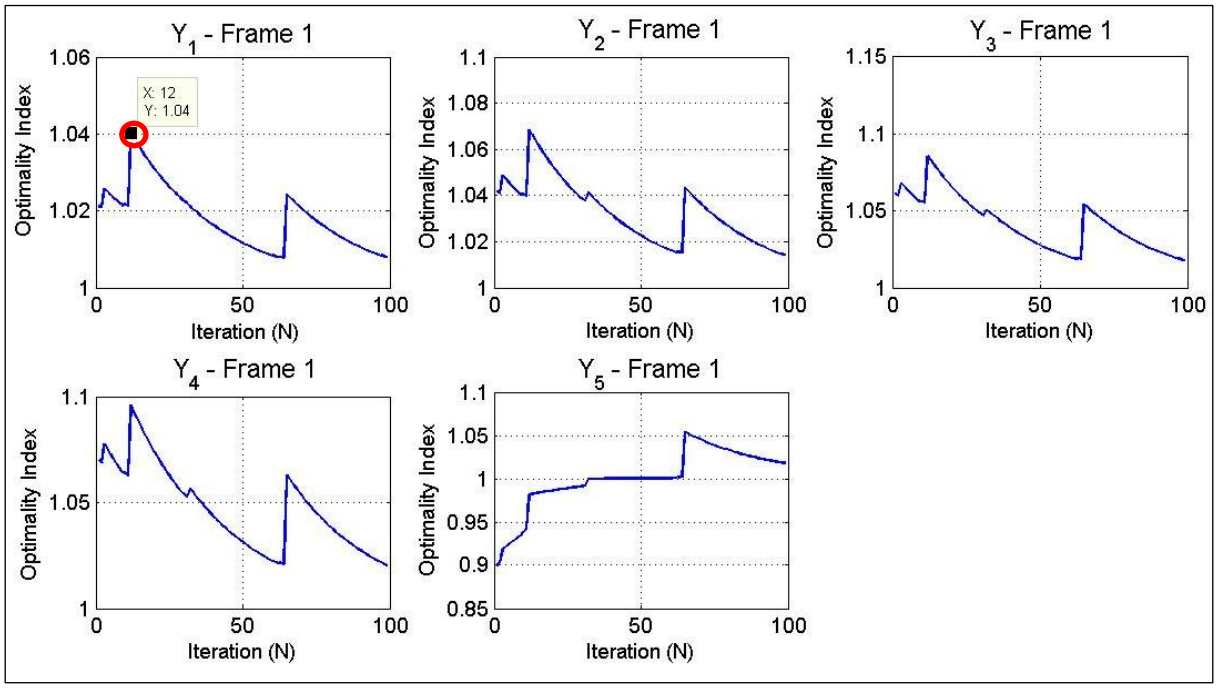

Figure 5.5. Floor Optimality Indices per Step of the Takewaki Method – Frame 1

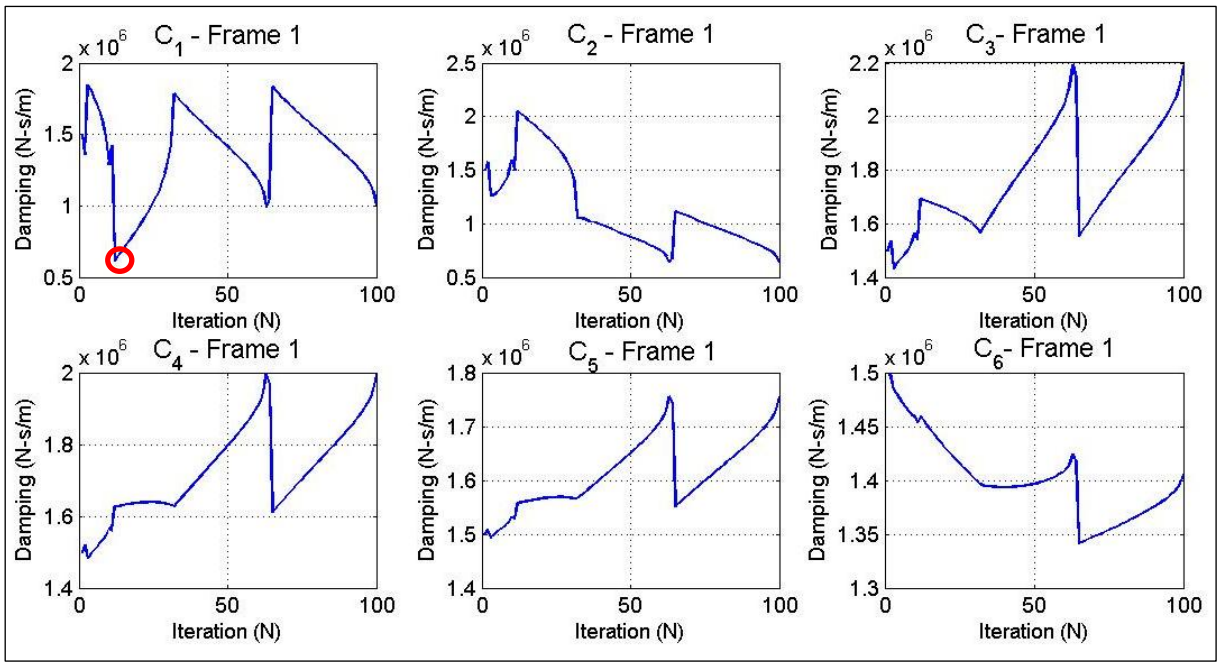

Figure 5.6. Floor Damping per Step of the Takewaki Method – Frame 1

At step 12, the objective function curve increases in response to the undesired increase in the optimality index corresponding to floors 2 (γ_1) through 6 (γ_5) (Figure 5.5). The curve continues in a similar trend due to the competing parameters of minimising the objective function of the sum of interstorey drifts and achieving an optimality index of one for each floor. Recall the optimum damping array is achieved when the objective function is minimised *and* the optimality index equals one for all nonzero damping terms. The change in

individual floor damping per step of the method (Figure 5.6) reveals that the shape of the objective function curve is a reflection of the variation in first floor damping. This is justified because the first derivative of the sum of the interstorey drifts (first order sensitivity) with respect to the first floor damping coefficient is the denominator of the optimal location index and therefore, the controlling factor for the shape of the curve.

Takewaki (1997) notes that for this unique frame, possessing a uniform distribution of the amplitudes of the interstorey drift of the transfer function, only minor improvement in damper distribution can be made (i.e. objective function minimally reduced from 0.2033 (V_i) to 0.2027 (V_f), as noted in Figure 5.4, where the initial damping is near optimal). If carried out for the 500 steps, as Takewaki suggests, the final objective function becomes greater than the initial value and damping is removed from all but three floors. Because of this disparity between the original Takewaki and verification damper schemes, the original Takewaki (1997) damper distribution was used as the Takewaki frame 1 damper scheme for all seven ground motion analyses.

Results of the frame 1 analysis of the Takewaki scheme under the El Centro (IELC180) ground motion are within 7% of the value presented in Lopez-Garcia (2001) for the El Centro S00E ground motion, scaled to the same pga (0.313g) (Table 5.9). Dashes in Table 5.9 and Table 5.11 indicate a lack of data, as Lopez-Garcia (2001) presents only the sum of interstorey drifts for this frame. Both IELC180 and S00E are the N-S components of the Imperial Valley 1940 El Centro ground motion, and therefore, have the same frequency components and different pga values. The results in Lopez-Garcia (2001) are based on a scaled El Centro S00E ground motion with a 0.369g scaled pga, while El Centro IELC180 has an unscaled pga of 0.313g.

Table 5.9. Verification of Takewaki Scheme Performance - Frame 1

	Peak Interstorey Drifts under El Centro (m)	
Floors	Lopez-Garcia (2001)	Verification
6	-	0.019
5	-	0.018
4	-	0.018
3	-	0.018
2	-	0.018
1	-	0.017
Sum	0.102*	0.109

*based on El Centro S00E scaled to pga=0.313g as per El Centro IELC180, and approximated graphically from Lopez-Garcia (2001)

5.2.1.2. Frame 2

Verification of frame 2 produced a damper distribution equal to the distribution in Takewaki (1997) (Table 5.10). The frame 2 verification results achieve nearly identical final optimal location indices γ_F and the same final objective function V_f of 0.1351 using a large step size *Ni* of 4 and 50 total steps *NT*. Figure 5.7 illustrates the minimisation of the objective function near step 8 for frame 2, but optimality is officially achieved at step 32 when the optimality index considering floor 2 (γ_1) is equal to one and the optimality index of zero-damped floors is less than 1 (Figure 5.8).

Table 5.10. Verification of Takewaki Method for Frame 2

Takewaki Configuration Added Damping (kN-sec/cm)				Optimal Location Index ($\gamma_{F,i}$)		
Floors	Takewaki (1997)	Verification	Percent Difference (%)	$\gamma_{F,i}$	Takewaki (1997)	Verification
6	0	0	0	5	0.0723	0.0722
5	0	0	0	4	0.2726	0.2722
4	0	0	0	3	0.5550	0.5543
3	0	0	0	2	0.8548	0.8538
2	42.000*	42.005	0.01 %	1	1.001	1.000
1	48.000*	47.995	0.01 %	-	-	-
Sum	90	90			NT = 50	NT=50
					Ni=?	Ni=4
					V_i = 0.2139	V_i = 0.2139
					V_f = 0.1351	V_f = 0.1351

* determined graphically from Takewaki (1997)

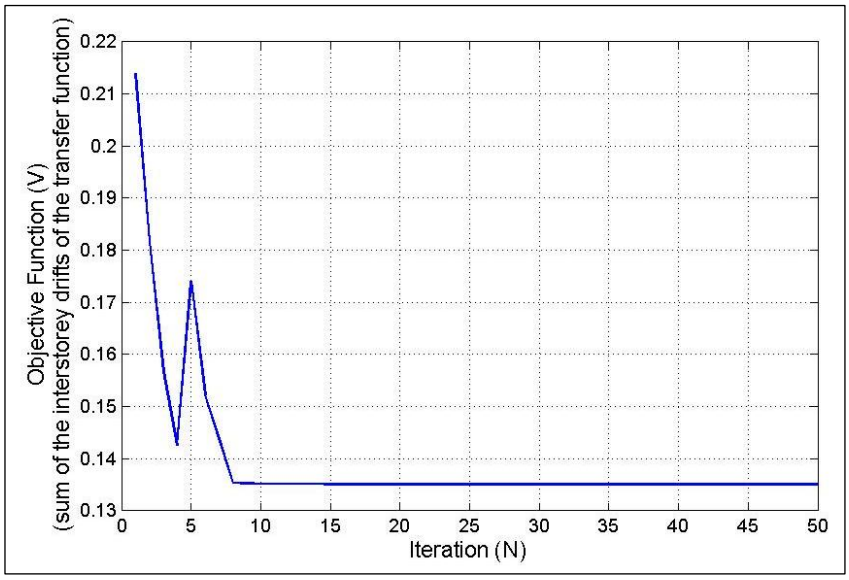

Figure 5.7. Minimisation of the Takewaki Objective Function – Frame 2

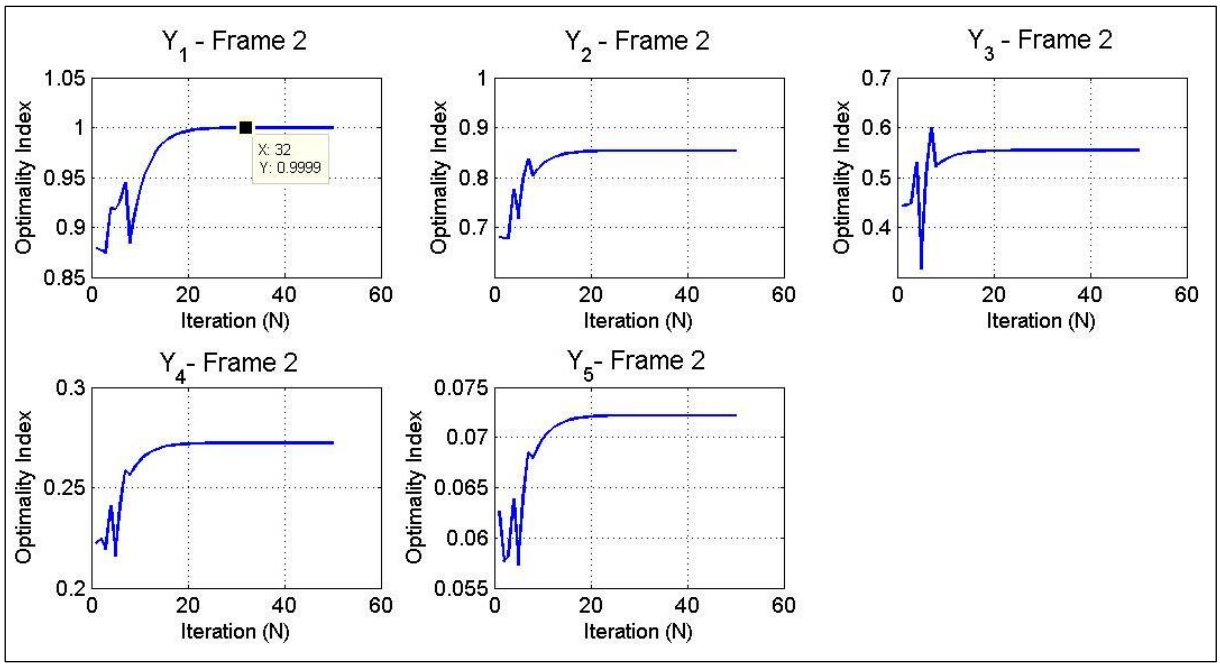

Figure 5.8. Floor Optimality Indices per Step of the Takewaki Method – Frame 2

The process of minimising the objective function for frame 2 is less complex than that of frame 1. The change in floor damping per step is presented in Figure 5.9. At the first step, damping is uniform, and the second step results in the removal of damping at floor six and further reduction of the objective function (Figure 5.7). Damping at floor five is removed at step three, and the damping is redistributed amongst floors 1-4. However, redistribution is approached in the wrong direction (decreasing damping at 1 and 2), thus causing the spike in the objective function at step 5. In response to this, damping at floor three and four are

reduced in steps 6 to 7, and finally damping is removed from both floors three and four at step 8 (Figure 5.7). The individual optimality indices per step (Figure 5.8) confirms that an optimality index of one has been achieved for the second floor and optimality indices less than one for the floors with zero damping.

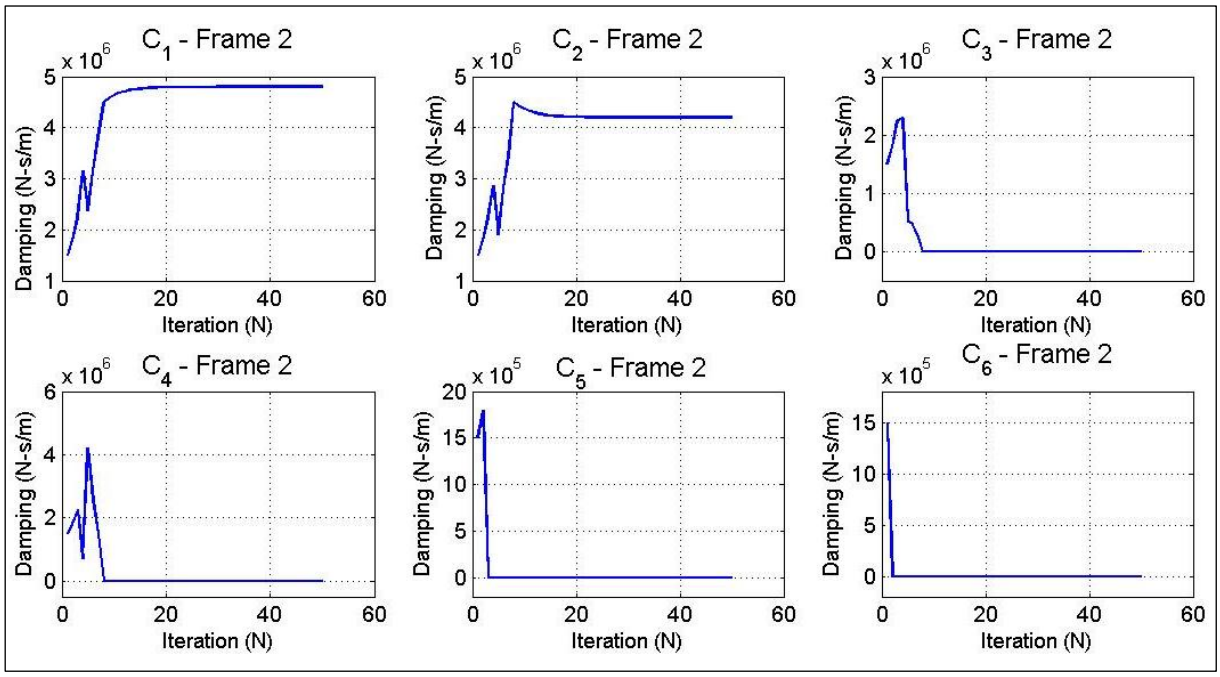

Figure 5.9. Floor Damping per Step of the Takewaki Method – Frame 2

5.2.2. SSSA Method

As a verification of the SSSA application, the SSSA configuration was also calculated for frame 1 (varying stiffness) under the El Centro IELC180 ground motion and various damper quantities. The sum of interstorey drifts and SSSA scheme for six dampers presented in Lopez-Garcia (2001) agrees with the SSSA scheme and drifts (within 10% difference) achieved for frame 1 (Table 5.11), verifying the correct implementation of the method. The SSSA configuration for frame 1 was not included in the ground motion analysis, but was selected here for the verification since Lopez-Garcia (2001) does not present a SSSA configuration for frame 2.

Table 5.11. Verification of SSSA Method (9 dampers) for Frame 1

	SSSA Configuration Added Damping (kN-sec/cm)		Peak Interstorey Drifts under El Centro (m)	
Floors	Lopez-Garcia (2001)	Verification	Lopez-Garcia (2001)	Verification
6	15	15	-	0.019
5	30	30	-	0.017
4	15	15	-	0.020
3	15	15	-	0.020
2	15	15	-	0.020
1	0	0	-	0.021
Sum	90	90	0.106*	0.117

*based on El Centro S00E scaled to pga=0.313g as per El Centro IELC180, and approximated graphically from Lopez-Garcia (2001)

The number of procedural steps (dampers) affects the efficiency of the SSSA method. As an amendment to the 2001 paper, Lopez-Garcia and Soong (2002) recommend the minimum damper number to be equivalent to the number of floors multiplied by 1.5, for medium-rise buildings, and the number of floors multiplied by 2 for low-rise buildings. Table 5.12 includes the different damper distributions and drifts of frame 1 with varying number of dampers under the El Centro IELC180 ground motion. For this particular ground motion and frame, doubling the number of dampers yields only a 6% improvement in reduction of the sum of interstorey drifts. Therefore, based on these results and the goal of balancing performance reduction and time expended, nine dampers were selected for applying SSSA Mode for frame 2.

Table 5.12. Varying the Number of Dampers in the SSSA Method – Frame 1

	SSSA Configuration Added Damping (kN-sec/cm)			Peak Interstorey Drifts under NS El Centro (m)		
Floors	6 dampers	9 dampers	12 dampers	6 dampers	9 dampers	12 dampers
6	15	20	15	0.019	0.017	0.019
5	30	20	22.5	0.017	0.019	0.018
4	15	20	15	0.020	0.020	0.019
3	15	20	15	0.020	0.020	0.019
2	15	10	15	0.020	0.021	0.018
1	0	0	7.5	0.021	0.021	0.018
Sum	90	90	90	0.117	0.116	0.110

5.2.3. Lavan A/R Method

Prior to applying the Lavan A/R method to new structures, it was essential to verify to correct application of the method for a simple example. The two-storey shear frame presented in

Levy and Lavan (2006) was selected, and the calculated Lavan A/R damper configuration scheme, performance index, and constraint error compared to the results in the same paper. The results were very similar, confirming correct application of the method. The frame and ground motion properties, mechanics of optimisation, and verification assessment of the damper configuration are described in detail.

5.2.3.1. Frame and Ground Motion Properties

The shear frame from Levy and Lavan (2006) was a two-storey structure, assumed to behave linearly under the ground motion, with dampers installed horizontally within chevron braces at each floor (Table 5.13). Rayleigh damping was 5% in modes 1 and 2. The active ground motion selected was the same prescribed by Levy and Lavan (2006), the N-S component of the 1940 Imperial Valley, El Centro ground motion, with a scaled pga of 663 cm/sec^2 (LA02 10% in 50 years, Somerville et al. 1997).

Table 5.13. Lavan A/R – Shear Frame Properties

Floor / Mode	Mass (ton)	Stiffness (kN/m)	Period (sec)
1	25	37500	0.281
2	25	25000	0.115

5.2.3.2. Mechanics of Optimisation

SAP2000 was employed to model the frame with the same modelling assumptions used for Takewaki shear frames 1 and 2. It is assumed that the example presented in Levy and Lavan (2006) used a numerical package (such as Matlab) to analyse the basic shear frame. However, the verification presented here used linear time history analysis with SAP200, since SAP2000 will be an essential tool for future application of the Lavan A/R method in complex structures.

Application of Lavan A/R method followed the procedures described in Chapter 3. A convergence parameter of 0.5, an allowable interstorey drift d_{all} of 0.009m (50% reduction of the bare frame interstorey drifts), and an initial uniform damping distribution were selected as per the example in Levy and Lavan (2006). The steps of the Lavan A/R procedure are

presented in Table 5.14 and Figure 5.10, including damping distribution per floor C_i, maximum interstorey drifts per floor over the time history $d_{i,max}$, performance indices pi_i, and the maximum constraint error of the two floors. Note that the method simultaneously optimises the performance index at all floors at each step; the maximum constraint error is provided here as an indication of convergence.

Table 5.14. Lavan A/R Procedure for a Two-Storey Shear Frame

Step	C_1 (kN-sec/m)	C_2 (kN-sec/m)	$d_{1,max}$ (m)	$d_{2,max}$ (m)	C_{total} (kN-sec/m)	max pi_1 = $d_{1,max}/d_{all}$	max pi_2 = $d_{2,max}/d_{all}$	max constraint error = max(pi_i)-1
0	0	0	0.0186	0.0171	0	2.07	1.90	-
1	2795	2795	0.0069	0.0043	5590	0.77	0.48	-0.2303
2	1656	644	0.0084	0.0075	2300	0.94	0.83	-0.0634
3	1452	445	0.0087	0.0074	1897	0.97	0.82	-0.0318
4	1361	297	0.0089	0.0082	1659	0.99	0.91	-0.0144
5	1322	244	0.0089	0.0086	1567	0.99	0.96	-0.0067
6	1305	223	0.0090	0.0088	1528	1.00	0.98	-0.0032
7	1296	213	0.0090	0.0089	1510	1.00	0.99	-0.0016
8	1292	208	0.0090	0.0089	1501	1.00	0.99	-0.0008
9	1290	205	0.0090	0.0090	1496	1.00	1.00	-0.0003
10	1290	203	0.0090	0.0090	1493	1.00	1.00	-0.0001
11	1289	202	0.0090	0.0090	1492	1.00	1.00	0.0000
12	1289	202	0.0090	0.0090	1491	1.00	1.00	0.0001

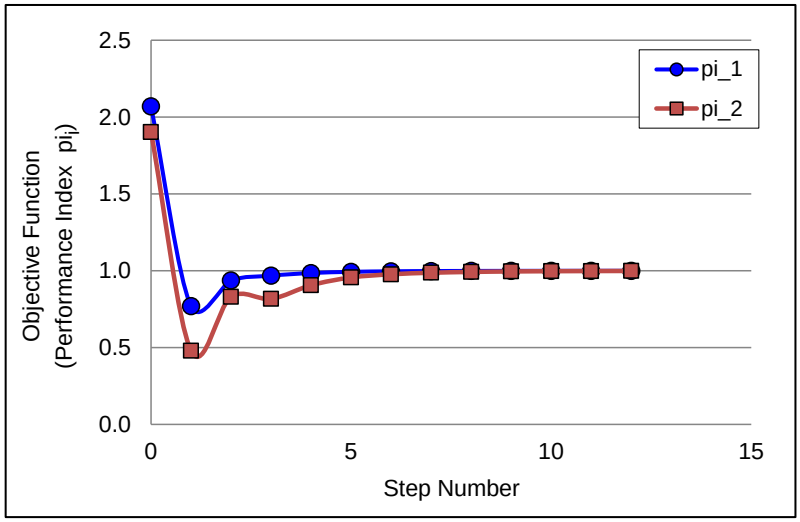

Figure 5.10. Minimisation of the Lavan A/R Objective Function

5.2.3.3. Verification of the Placement Scheme

The first step was to verify the bare shear frame model in SAP2000 with the model in Levy and Lavan (2006). The natural periods and peak interstorey drifts of the bare frame were confirmed with the SAP2000 shear frame. The final Lavan A/R damper distribution calculated here assigns 1289 kN-sec/m damping at the first floor and 202 kN-sec/m damping

at the second floor, for a total of 1491 kN-sec/m damping and a 27% damping ratio due to viscous dampers (Table 5.15). The viscous damping ratio due to dampers is calculated using the strain energy method, using the approximated stiffness-based equation (Eq. 5.4).

The total damping calculated in this example (Table 5.15, row 2) is less than 1% greater than the fully-stressed analysis/redesign damping (Table 5.15, row 5) and less than 3% greater than the traditional gradient-based optimisation from Levy and Lavan (2006) (Table 5.15, row 6). The distribution of damping between floors 1 and 2 slightly differs from the literature results. The damper configuration from Levy and Lavan (2006) was analysed in SAP2000, using the current model, to investigate the source of the distribution discrepancy (Table 5.15, row 3). The resulting allowable drift, maximum performance index, and constraint error, do not match exactly the values presented in Levy and Lavan (2006) (row 3 vs. row 5, Table 5.15), which leads to the conclusion that the discrepancy is likely caused by minor modelling inconsistencies between the SAP2000 model and the numerical model in Levy and Lavan (such as modelling of Rayleigh damping or size of dynamic analysis time steps). However, the achievement of the maximum performance index and minimisation of the maximum constraint error for the same total damping value in this shear frame confirms the correct implementation of the Lavan A/R method.

Table 5.15. Verification and Comparison of Lavan A/R Results

Approach	C_1 (kN-sec/m)	C_2 (kN-sec/m)	C_{total} (kN-sec/m)	$\xi_{dampers}$	$d_{i,max}$ (m)	max $pi_i = d_{i,max}/d_{all}$	max constraint error = (max(pi_i)-1)
Verification of C_1 and C_2 using procedure in Levy and Lavan (2006)	1289	202	1491	27%	0.0090	1.000	0.0001
Analysis with C_1 and C_2 values from Levy and Lavan (2006)	1300	181	1482	27%	0.0091	1.016	0.0160
Results from Levy and Lavan (2006)							
1. Analysis and Redesign Method	1300	181	1482	27%	0.009002	1.000	0.0002
2. Gradient-based Optimisation	-	-	1454	26%	0.009036	1.004	0.0040

5.3. Preliminary Comparison of Placement Methods: Results and Discussion

The analyses results for frames under the seven ground motions and various damper placement schemes are presented. The interstorey drifts (plots (A)-(G), Figure 5.11 and Figure

5.12) are represented as a ratio of peak interstorey drift per floor normalised by the spectral displacement at the fundamental frequency S_d (T_1) for the 'no dampers' case. In addition, the ratio of the fundamental period T_1 to the pulse period of the earthquake T_p is denoted in each near-fault earthquake case. Finally, Figure 5.11 (H) and Figure 5.12 (H) indicate the capacity of each damper placement technique to reduce the maximum interstorey drift ratio (maximum peak interstorey drift amongst all the floors). Floor heights are assumed to be uniformly 3 m and are used to provide a more meaningful indication of peak interstorey drift reductions.

5.3.1. Takewaki Method– Frame 1

The results shown in Figure 5.11, particularly for the AI and BN ground motions, reveal the extreme storey demands at the roof of frame 1. Despite this, all damper placement techniques effectively reduce peak interstorey drifts under both near-fault and far-fault ground motions. Both the Takewaki and Uniform method result in a more uniform drift distribution along the frame height, while the Stiffness Proportional method yields higher roof interstorey drifts compared to the other placement methods, which is to be expected due to the soft-storey roof.

The addition of dampers for frame 1 under the BN ground motion does not significantly reduce peak interstorey drifts at floors 2, 3, and 4. The spectral displacement value (Table 5.6) at the fundamental mode is minimally improved with the 11% effective damping ratio. Considering the 50% reduction in spectral displacements with added damping in the second mode (Table 5.6) as well as the mode shape of the bare frame comparable to the second mode shape for frame 1 under the BN ground motion (Figure 5.2), it can be concluded that the BN ground motion excites the second mode of bare frame 1. The largest frequency component of the BN ground motion is 2.04 Hz (0.49 sec) which is the very near the second modal frequency of frame 1 and suggests the high second mode contribution. Thus, the interstorey drifts at the middle storeys are less influenced by damping in the second mode shape and show a minimal improvement compared to the bare frame.

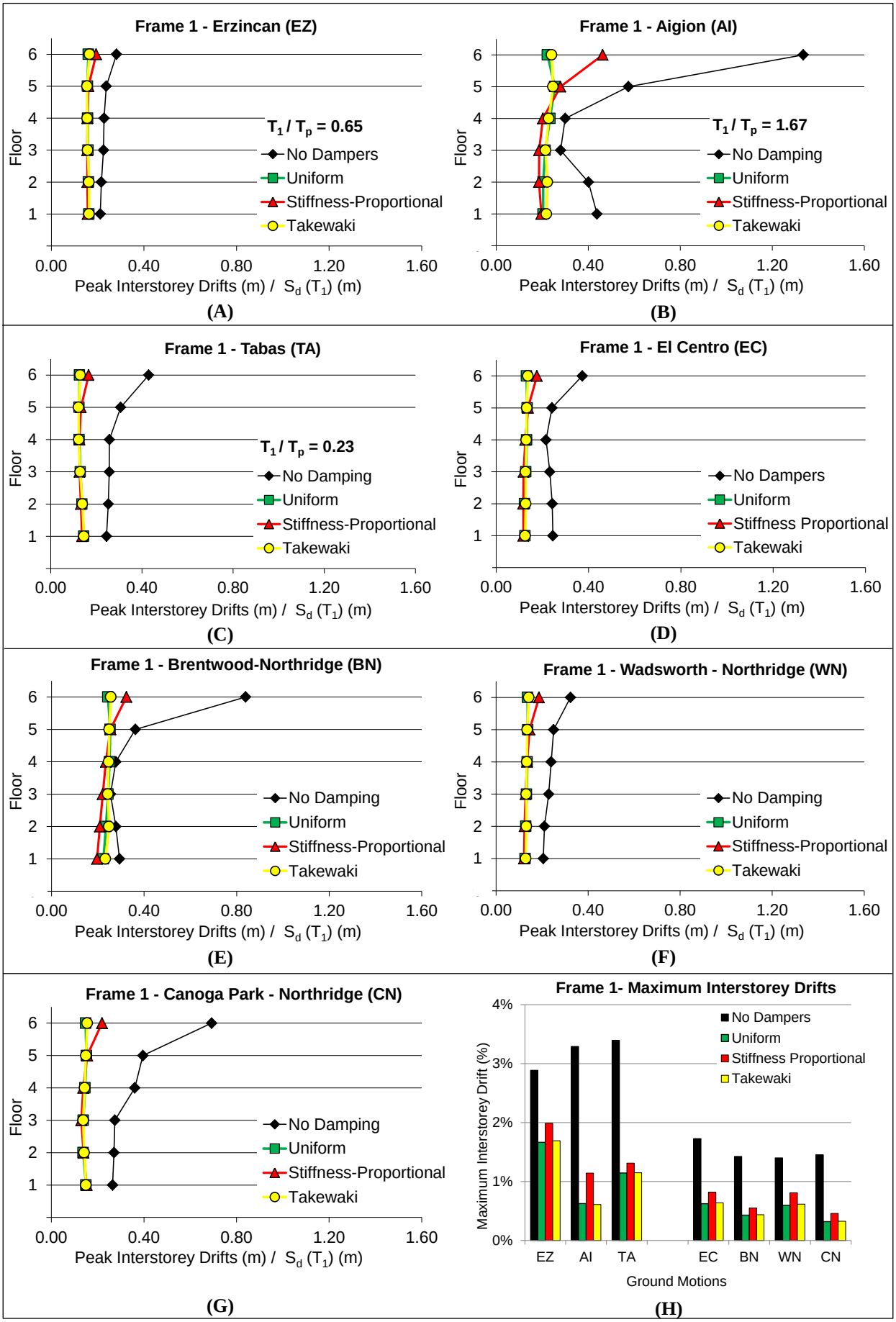

Figure 5.11. Frame 1 – Distribution of Peak Interstorey Drifts

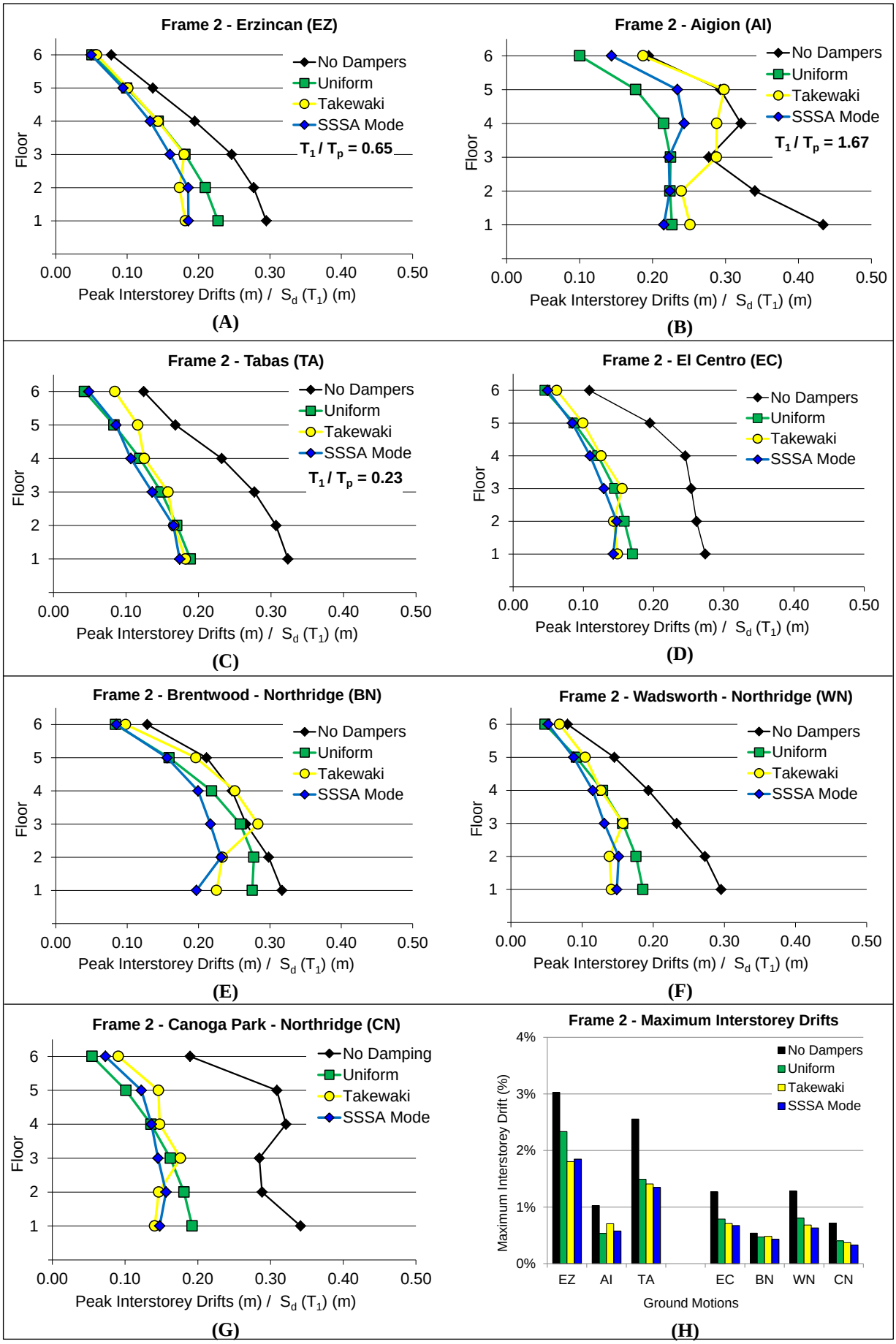

Figure 5.12. Frame 2 – Distribution of Peak Interstorey Drifts

The AI and CN ground motions also exhibit a second mode shape response for the bare frame 1, with a disproportionately large roof drift compared to the other floor drifts. Review of the ground motion frequency content based on the power spectral density (Figure 5.13 (A)) reveals the dominant frequency of the single-pulse AI ground motion as 2.08 Hz (0.48 sec), very near the 0.50 second modal period of frame 1. The AI ground motion results in a greater spectral displacement and greater reduction in displacement due to added dampers in the second mode the compared to the first mode (Figure 5.14). The frequency components of the CN ground motion include a large 2.30 Hz component (0.43 sec) near the second mode of frame 1 and a 4.38 Hz component (0.23 sec), approximately the fourth mode of frame 1 (Figure 5.13 (B)), suggesting the presence of higher mode effects.

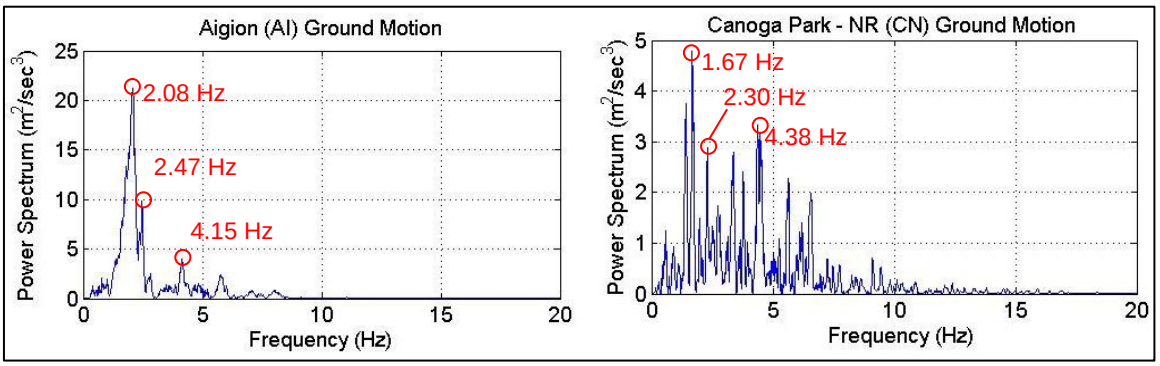

Figure 5.13. Frequency Components of Ground Motions: (A) AI; (B) CN

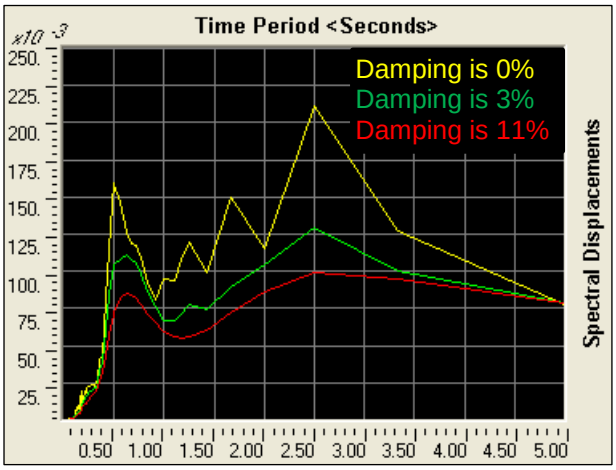

Figure 5.14. Spectral Displacement Curves for AI Ground Motion - S_D (m)

Plot (H) in Figure 5.11 displays the reduction in maximum interstorey drift for each ground motion and damper placement scheme. The Uniform and Takewaki methods produce very similar results, and both can be considered the most optimal damping method of the three

presented. Due to the frame's stiffness irregularities, the Stiffness Proportional method is not as effective; the soft roof and subsequent low stiffness results in minimal damping at the roof that is not adequate for the high interstorey drifts occurring at the roof.

5.3.2. Takewaki and SSSA Mode – Frame 2

Frame 2 represents a very different structural response than frame 1; peak interstorey drifts occur at the base, and the stiffness is uniform. SSSA Mode results have been included in these analyses. Based on the results in Figure 5.12, the Uniform, Takewaki, SSSA Mode methods all successfully reduce peak interstorey drifts, the Takewaki and SSSA mode methods reducing the maximum interstorey drift (plot (H) in Figure 5.12) more than the Uniform method in all but one ground motion case. Results of the four far-fault ground motions reveal a trend in the reduction of maximum interstorey drifts; SSSA Mode scheme is the most effective, followed closely by the Takewaki scheme, and lastly by the Uniform scheme. All maximum interstorey drifts of the placement methods under far-fault ground motions are within a small range (maximum range of 0.20% drift for the Wadsworth – Northridge ground motion).

The near-fault ground motions show a larger disparity in the effectiveness of the methods. In the case of the EZ ground motion (plots (A) and (H), Figure 5.12), the Takewaki scheme is the most effective at reducing the peak interstorey drift and distribution, followed closely by the SSSA Mode scheme. SSSA Mode best reduces drifts under the TA ground motion (plots (C) and (H), Figure 5.12), and Uniform damping best reduces drifts under the AI ground motion (plots (B) and (H), Figure 5.12). The peak drift distributions of the near-fault ground motions illustrate the effectiveness of the Uniform method for damping the upper floors of the shear frame, particular for the AI ground motion.

While the maximum interstorey drifts in plot (H) in Figure 5.12 indicate that the 'no dampers' case achieves the highest maximum interstorey drifts, the interstorey drift profiles yield

interesting results regarding individual floor drifts. For two ground motions cases, BN and AI, the Takewaki damper scheme results in peak interstorey drifts at certain floors that exceed those in the 'no dampers' case. Plots (E) and (H) in Figure 5.12 show that neither the Takewaki nor Uniform method substantially reduces the peak interstorey drift ratio or distribution for BN, while SSSA Mode achieves a reduction. The results for the Takewaki distribution in the BN case may be explained by the spectral displacement values; only marginal changes occur in the spectral displacements with the addition of dampers in the first mode, a 12% reduction (Table 5.5). It may be concluded that this damping quantity for frame 2 is not very influential for the first mode under the BN ground motion. SSSA Mode reduces the middle storeys' interstorey drifts by strategically placing damping at floors 3 and 4 in the frame, whereas the Takewaki method places no damping here and achieves the highest peak interstorey drifts at these internal floors (3, 4, and 5) under the BN and AI ground motions.

Interestingly, the AI and CN ground motions are the only cases to produce an S-shaped distribution of peak interstorey drifts in the bare frame, suggesting the presence of the second or third mode shape of bare frame 2 (Figure 5.2). The second largest frequency component of the AI ground motion is 2.47 Hz, equal to the second mode of bare frame 2, while the third largest frequency is 4.15 Hz, near the third mode of bare frame 2 (Figure 5.13 (A)). The CN ground motion has a large 4.38 Hz component, also near the third modal frequency of frame 2 (Figure 5.13 (B)). In the case of the CN ground motion, a far-fault ground motion, there is adequate damping to reduce the drifts with all three damper placement schemes. However, in the case of the more demanding near-fault AI ground motion, the shape of the damped frame's drift distributions (i.e. C-shaped in the Uniform scheme and S-shaped in the Takewaki scheme) contribute more to a damper scheme's ability to reduce drifts in the bare frame.

It can also be concluded that AI is the only ground motion case where the Uniform scheme

performs substantially better than the Takewaki or SSSA Mode schemes. Both the Takewaki and SSSA Mode damping distributions have concentrated damping at the lower storeys. Therefore, the large interstorey drifts at floors four and five under the AI ground motion and excited third mode shape, are not adequately damped by the Takewaki and SSSA Mode distributions. These results may be indicate the sensitivity of the advanced placement methods to near-fault earthquakes with one dominant pulse and to ground motions with a higher mode contribution (considering the fact that both advanced methods are based on the first modal response of the frame).

Additional analyses were conducted to compare the reduction of the sum of the peak interstorey drifts, which is more representative of the Takewaki method's objective function. These results do not confirm the results presented in Takewaki (1997) for all seven ground motions, which suggest the Takewaki method as more effective than the Uniform for frame 2. The sums of the peak interstorey drifts of the Takewaki method are larger than the Uniform method for both the AI and TA ground motions.

5.4 Conclusions

The investigation of optimal placement techniques for shear frames leads to conclusions about the correct application of the methods, the framework for analysing the damped frames, and preliminary conclusions about the effectiveness of the placement methods. In addition, this investigation yields important findings for further research.

5.4.1. Verification Assessment

By reproducing examples and comparing results to those produced in literature, the methodology for applying the SSSA Mode, Takewaki, and Lavan A/R methods to structures has been verified as correct. Small differences between the results have been justified, and the procedure and tools used for applying the methods are sufficient for application in additional structures and deemed fair representations of the methods. A framework for applying the

damper placement methods to structures, analysing the structures, and comparing the performance of the placement methods has been created and may be used for larger ground motion suites, additional performance objectives, and complex structures.

5.4.2. Preliminary Comparison of Damper Placement Methods

The Takewaki, SSSA Mode, and Uniform damper placement methods effectively reduced the peak interstorey drifts for both frames under the majority of the ground motion cases. The Takewaki and Uniform methods were equally effective at minimising peak interstorey drifts for the variable stiffness frame (1). This confirms conclusions provided in previous literature. The Stiffness Proportional method for frame 1 substantially reduced peak interstorey drifts but was inherently limited in the case of peak drifts occurring at soft-stories.

For far-fault motions and the uniform stiffness frame (2), the effectiveness of the advanced placement methods was similar, with SSSA Mode slightly more effective than the Takewaki method. For near-fault ground motions and the uniform stiffness frame (2), discrepancies between the Uniform, SSSA Mode, and Takewaki results (particularly, Uniform being more effective than advanced methods for the AI case) indicates potential sensitivities of the advanced methods to the ground motion characteristics, which is of particular interest considering the Takewaki method's ground-motion independent approach. The BN ground motion for both frame cases presents an example of when optimal placement methods may have little benefit if the structure is not influenced by added damping.

5.4.3. Lessons Learned for Further Research

The more easily implemented damper placement scheme, the Uniform distribution, yields effective results (equal to or slightly less effective than the advanced methods) for most of the test cases presented. Additional research is needed to determine if the SSSA Mode and Takewaki methods' more complex procedures produce enough improved building performance to make them worthwhile and practical techniques. Also, further work is needed

to investigate the Takewaki method's sensitivity to ground motion characteristics (i.e. near-fault ground motions with varying T_1/T_p ratios or ground motions capable of exciting higher structural modes). However, concentrating on a larger set of far-fault ground motions is recommended as the first step in achieving statistical conclusions about the placement methods, without incorporating the extreme values present in near-fault ground motions. Ground motions should be selected with a broad range of characteristics, which excite expected contributions of modal responses (i.e. likely to be dominated by first mode response but second and third mode contributions may exist), to best assess the performance of the damper placement schemes under typical building response. In addition, a comparison including the Lavan A/R distribution is essential as the technique was selected for investigation after conducting this preliminary comparison.

Many of the limitations of this work are a result of replicating the methodologies presented in the literature, a necessity for verifying the correct applications of the methods. These limitations included the lack of ground motion scaling, the lack of design objectives, unrealistic added damping ratios and frame characteristics. While linear damped frame performance without scaling the ground motions is acceptable for a preliminary test and verification of the methods, it cannot yield realistic building performance results. No design objectives (such as a specified quantity of added damping to achieve a desired result) were included in the examples, which led to the use of the arbitrary value of total damping corresponding to a very small effective damping ratio. Neither frame represents a realistic structure, as uniform stiffness or irregular bare frame drift distributions (as seen in Figure 5.11 and Figure 5.12) would not be acceptable in real-world design.

Further work presented in Chapter 6 will encompass a variety of ground motion records, building characteristics, and performance objectives, which lead to definitive statistical conclusions about the potential for these viscous damper placement methods.

Chapter 6

Investigating Optimal Placement Techniques: Regular and Irregular Buildings

---

6.0. Introduction

The purpose of this chapter is to investigate the effectiveness and usability of five damper placement techniques for two building examples under realistic seismic hazard levels and performance objectives. The five damper placement methods include two standard methods, Uniform damping and Stiffness Proportional damping, and three advanced placement methods, SSSA Mode, Takewaki, and Lavan A/R. A regular building model, irregular building model, and a suite of ground motions were developed. The motivation for analysing an irregular building in addition to the regular building is two-fold: to test the robustness of the individual methods for a more complex structure (variable mass and irregular elevation) and to attain and compare damper placement configurations possessing greater variation.

Each damper placement method was applied to the building examples, and the performance of the buildings with the various damper configurations was analysed using nonlinear time history analysis under the design based earthquake and maximum considered earthquake. The performance of the placement techniques are evaluated statistically with peak interstorey drifts, absolute accelerations, and residual drifts. In addition, the usability and time efficiency of each damper placement method is assessed.

6.1. Methodology

The following section presents a framework for the building designs, ground motion suite details, the application of the damper placement methods, the numerical analysis assumptions, and the selected building performance indicators. Lastly, the final damper configurations for each method are presented.

6.1.1. Building Design

Two steel MRF buildings, one regular and another irregular in elevation, were designed according to the Eurocode (EC3 [BS EN 1993-1-1, 2005], EC8 [BS EN 1998-1, 2004]). A building regular in plan and elevation provides the simplest example of a baseline structure, while a building irregular in elevation (i.e. setback structure) provides additional insight into the application of the damper placement schemes for non-uniform mass distribution and non-conventional stiffness distribution. In addition, designing from scratch, as opposed to using an existing benchmark structure, ensured that the buildings were code-compliant, simple, met realistic performance objectives, and followed a design process from the perspective of a structural engineer.

6.1.1.1. Geometry

First, a reasonable plan and profile were selected based on typical MRFs. Both ten-storey buildings had floor heights of 3.2 m and the same first floor plan (Figure 6.1(B)), with a lateral force resisting system of MRFs in the north-south direction and braced frames in the east-west direction. The regular building was regular in both plan and profile (Figure 6.1(A)), while the irregular building was irregular in elevation, with geometric changes occurring in elevation at floors 2 and 7, with an upper tower comprised of floors 7-10 (Figure 6.1(C)). The single MRF in the north-south direction was designed (gold MRF in Figure 6.1) neglecting the plan irregularities of the irregular building that would otherwise require a three-dimensional analysis. A total height of ten storeys allowed for a large variation in damper locations for a realistic mid-rise building, and a bay width of 8m, although demanding, is common in U.K. or U.S. construction.

6.1.1.2. Loads

Typical gravity loads were chosen for an office building (4 kN/m^2 dead load and 2 kN/m^2 live load), and the tributary area method used to distribute frame loads. It was assumed that seismic loads controlled the design of this frame; however, the final design was also checked for gravity load capacity. The seismic weight was calculated as the sum of dead load and

one-third of live load and was distributed as forces to the interior and exterior columns and as lateral seismic mass to each floor. Table 6.1 includes the load calculations.

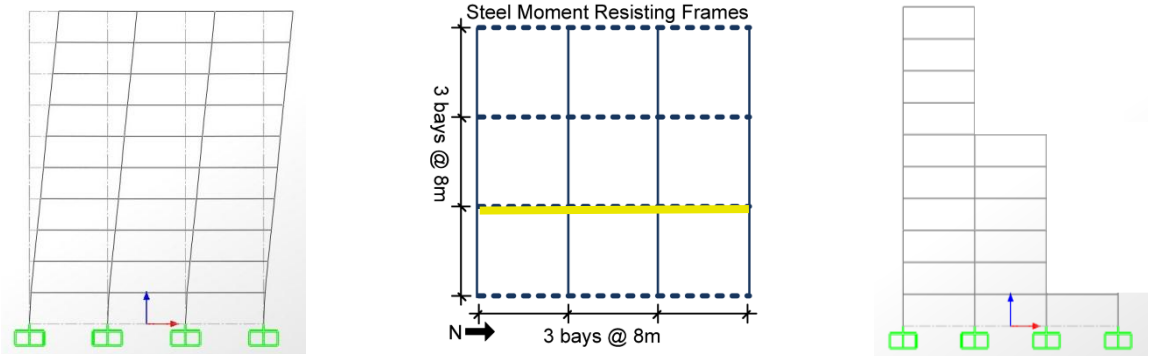

(A) Regular Building– Profile
10 stories @ 3.2m each

(B) Building – Plan
24 m x 24 m plan

(C) Irregular Building – Profile
10 stories @ 3.2m each

Figure 6.1. Building Dimensions

Table 6.1. Seismic Loads

W = (G + 0.3Q) * A Seismic Weight per Floor (W) = [Dead Load (G) + (0.3 * Live Load (Q))] * Floor Area (A)						
Regular Building Loads:						
	A (m^2)	(G+0.3Q) (kN/m^2)	W (kN)	Mass (kg)	W $_{interior\ columns}$ (kN)	W $_{exterior\ columns}$ (kN)
Per Floor	192	4.6	883	90031	294	147
Irregular Building Loads:						
10 – 7	64	4.6	294	30010	-	147
6 – 2	128	4.6	589	60020	294	147
1	192	4.6	883	90031	294	147

6.1.1.3. Response Spectrum

The MRFs were designed using response spectrum analysis, and a 0.3g pga and Eurocode soil B site conditions were chosen to represent a highly seismic area. A high behaviour factor (or strength reduction factor) of 6.5 was selected for the regular building, and a reduced behaviour factor of 5.2 for the irregular building, to account for vertical irregularities (BS EN 1998 4.3.2.1 (7)). Inherent damping of 5% was assumed. The resulting elastic and design response spectrums are presented in Figure 6.2. Because of the lower-bound on the design spectrum, it is more conservative for long period structures to use the 'Design * q' spectrum

(a pseudo-elastic spectrum) for calculation of the expected elastic response; this is specified as the 'displacement of the design seismic action' in EC8, section 4.3.4. Although the different q-factors for the regular and irregular buildings influence the short-period portion of the design response spectrum ('Regular Building – Design Spectrum' and 'Irregular Building – Design Spectrum'), the irregular and regular buildings have identical long-period design spectral responses.

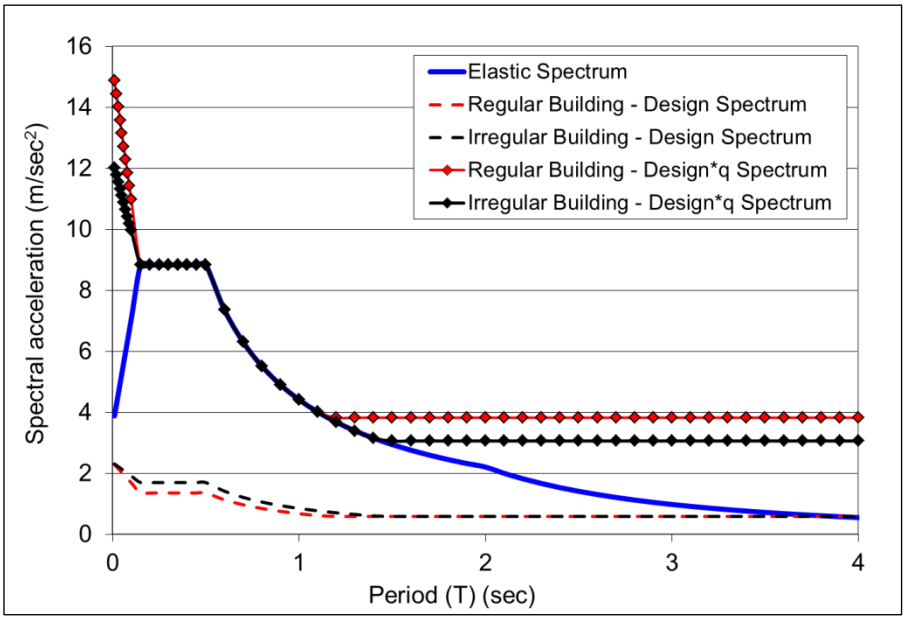

Figure 6.2. Response Spectrum for the Buildings, pga=0.3g, Soil B, 5% damping

6.1.1.4. Serviceability Limitations

Seismic performance levels selected include the frequently occurring earthquake (FOE), which is 40% of the design basis earthquake (DBE), the DBE (10% probability of exceedance in 50 years), and the maximum considered earthquake (MCE) (2% probability of exceedance in 50 years), which is 150% of the DBE (Somerville et al. 1997). A serviceability limit of 1% peak interstorey drift under the FOE was selected as a realistic serviceability criterion for a normal building performance (EC8, 4.4.3.2). This achieves the Immediate Occupancy performance based design level for the FOE and Life Safety for the DBE (FEMA 356, ASCE 2000). For a serviceability limit of 1% peak interstorey drift, the drift limitation is defined in terms of the design interstorey drift d, the behaviour factor q, reduction factor for seismic hazard levels v (e.g. 0.4 for the FOE), and the storey height h (e.g. 3.2 m):

$$\frac{d * q * v}{h} \leq 0.01 \qquad (6.1)$$

6.1.1.5. Analysis-Design Procedure

After the geometry, load, and dynamic criteria were specified, the last step of the overall design procedure was the iterative analysis and design step. SAP2000 (CSI 2009a) was used for modelling the frame, analysing its performance under the response spectrum and static loads, and assisting in the design process. The seismic weights were applied as gravity joint forces on the columns, while the seismic masses were assigned to each floor diaphragm (see section 6.1.4.1 for additional frame modelling details). The design response spectrum was the primary design load case. After each analysis, a member capacity check was conducted using EC3 and SAP2000's steel design package. New member sizes were suggested for failed members or overly conservative members. Then the next analysis was performed, followed by an updated capacity check and new design recommendations. After only a few iterations, a strength-based building design was achieved that met the EC3 capacity requirements. The strength design steps are shown in blue boxes in Figure 6.3.

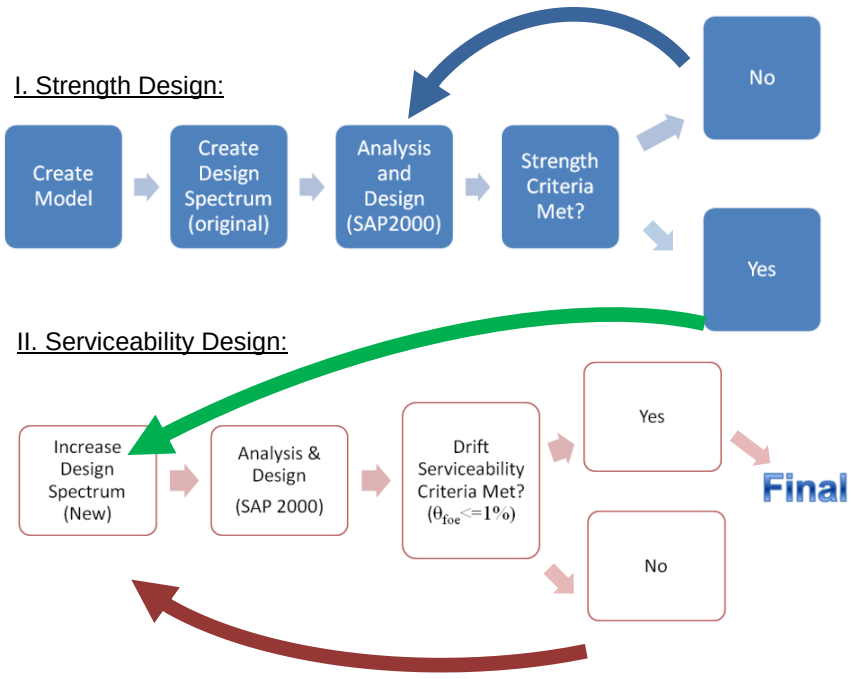

Figure 6.3. Analysis-Design Process

Serviceability limitations were next considered, in terms of drift under a particular seismic hazard level. If the strength design failed to meet the drift limit, it indicated that the building was drift-controlled due to the strict drift limitation imposed by EC8. Following similar steps as the strength analysis-design procedure, a more demanding design response spectrum (smaller q-factor) was used for the design checks, which prompted larger steel members, greater stiffness, and reduced drift values. This process (as shown in the red boxes in Figure 6.3) was followed until a building design met both strength and serviceability requirements. The final design capacity was checked under the seismic gravity loads.

6.1.1.6. Final Building Design

The building designs were based on multiple iterations and improve deficiencies of preliminary building designs. The final building properties are presented in Figure 6.4 and Table 6.2, where the peak drift is based on the response spectrum. The first three mode shapes and corresponding modal participating mass ratios are presented in Figure 6.5 and Figure 6.6. Refer to Appendix A-8 and A-9 for additional modal details. Figure 6.7 shows the peak drift distribution of the buildings under the FOE. The irregular building was designed to achieve a uniform drift distribution under the FOE-scaled response spectrum (Figure 6.7 (B)), yet through this process, the expected drift irregularities due to the stiffness irregularities in elevation were ‘designed out’ of the building.

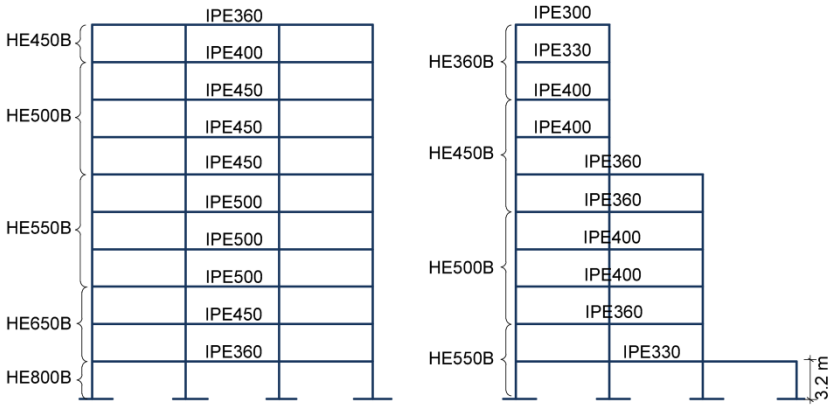

(A) (B)

Figure 6.4. Final Building Designs A) Regular B) Irregular

Table 6.2. Building Properties

Building	FOE Peak Interstorey Drift (%)	DBE Peak Interstorey Drift (%)	1st Natural Period (s)	2nd Natural Period (s)	3rd Natural Period (s)
Regular	0.88 %	2.20 %	2.05	0.70	0.38
Irregular	0.99 %	2.47 %	2.31	0.93	0.47

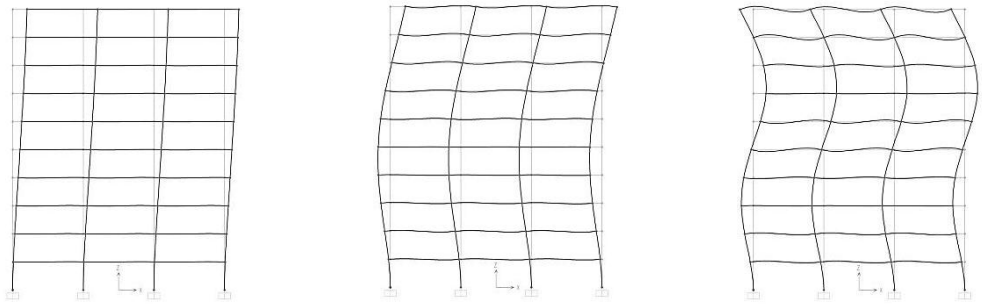

Mode 1 (75%) **Mode 2** (11%) **Mode 3** (4.5%)

Figure 6.5. Regular Building – Mode Shapes and Modal Participation Mass Ratios

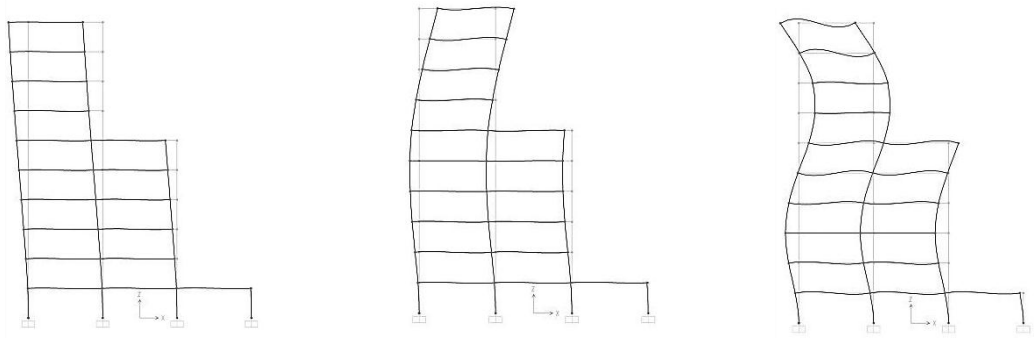

Mode 1 (65%) **Mode 2** (13%) **Mode 3** (7.3%)

Figure 6.6. Irregular Building – Mode Shapes and Modal Participation Mass Ratios

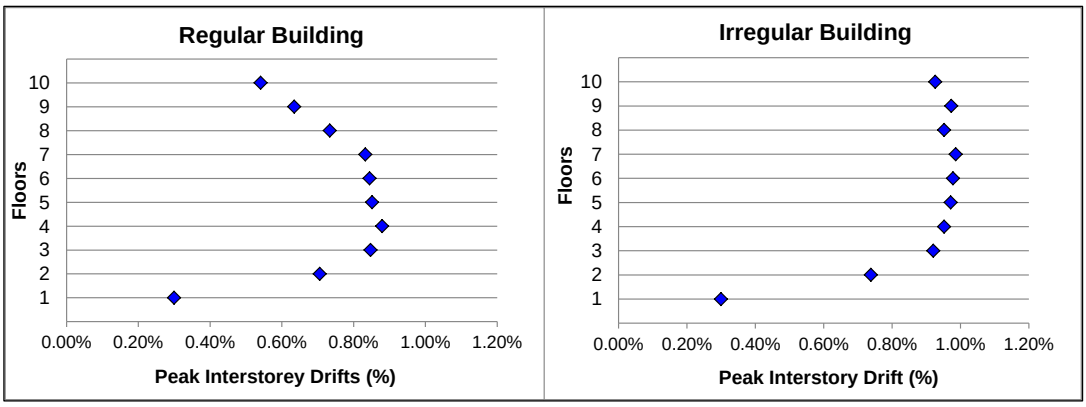

(A) (B)

Figure 6.7. FOE Peak Interstorey Drift Distribution for A) Regular and B) Irregular Buildings

The stiffness matrix was an essential component for applying the optimisation placement methods. An approximate stiffness matrix was obtained by applying a triangular lateral load

distribution along the height of the frame; floor stiffness per floor K_j was approximated as the quotient of the sum of the shear forces V_i in the columns (4 columns per floor) and the lateral displacement of the entire floor δ_j:

$$K_j = \frac{\sum_{i=1}^{4} V_i}{\delta_j} \tag{6.2}$$

Note that the floor slab is assumed rigid, and the columns per floor are restrained by a diaphragm constraint. Table 6.3 highlights the similarities in the regular and irregular building floor stiffnesses, best exhibited in the floor stiffnesses normalised by first floor stiffness of each building. Despite the stiffness similarities, a product of identical loading and uniform-drift objectives, the irregular and regular buildings differ greatly in mass distribution due to the vertical setbacks.

Table 6.3. Floor Stiffnesses

	Regular Building		**Irregular Building**	
Floor	Stiffness (kN/cm)	Normalised Stiffness	Stiffness (kN/cm)	Normalised Stiffness
10	132	0.11	26	0.06
9	206	0.18	44	0.09
8	244	0.21	61	0.13
7	265	0.23	73	0.16
6	303	0.26	90	0.19
5	336	0.29	106	0.23
4	354	0.30	121	0.26
3	391	0.33	137	0.29
2	488	0.42	182	0.39
1	1172	1.00	469	1.00

6.1.2. Ground Motion Records

A set of twenty ground motion records were selected and scaled to best model realistic seismic hazard demands on the buildings using time history analyses. In addition, a set of three artificial accelerograms were created specifically for applying the SSSA Mode method. Details of the ground motion suite and accelerogram set are presented.

6.1.2.1. Ground Motion Suite - Source and Selection Criteria

A set of twenty ground motion records were selected from the PEER-NGA (PEER 2005) and scaled to model realistic seismic hazard demands on the buildings (Table 6.5). The absence of

near-fault characteristics and Eurocode soil B classification (exhibiting shear wave velocities 360 – 800 m/sec) were the primary selection criteria. Two exceptions include the Imperial Valley 1940 ground motion, which was selected because of its common use as a benchmark ground motion record, and the Kobe-Abeno ground motion, which is near the Eurocode Soil B classification limit. The absence of near-fault characteristics, such as long period velocity pulses, was an additional selection criterion. Refer to Appendix A-5 for acceleration and velocity time history plots for each ground motion record.

6.1.2.2. Ground Motion Suite - Scaling

The ground motions were normalised to the same hazard level (i.e. DBE or MCE), so that performance objectives at a specific hazard level could be evaluated from the ground motions. This was performed by scaling the ground motions to the same pseudo-spectral acceleration (PSA) at the building's fundamental frequency and 5% inherent damping (Table 6.4). Because the dynamic properties of the buildings differ, the PSA scale factors differ between the regular and irregular buildings.

Table 6.4. PSAs under Seismic Hazard Levels

	PSA at T_1 (m/sec^2)	PSA at T_1 (m/sec^2)
Seismic Hazard Level	*DBE*	*MCE*
Regular Building	3.83	5.75
Irregular Building	3.06	4.59

For the case of the regular building under the DBE, all twenty ground motions were scaled to 3.83 m/sec^2, the PSA from the design*q spectrum at the fundamental frequency of the building. Simulating the MCE hazard level required increasing the DBE scale factor by 50%. Properties of the ground motion records, including station name, peak ground accelerations, and DBE and MCE scale factors, are presented in Table 6.5.

Table 6.5. Properties of the Ground Motion Suite

	From PEER-NGA (2005)						Regular Building		Irregular Building	
	Ground Motion (GM)	Station Name	Component	Location	pga (g)	Duration (sec)	DBE Scale Factor	MCE Scale Factor	DBE Scale Factor	MCE Scale Factor
1	Imperial Valley 1979	Cerro Prieto	H-CPE237	USA	0.157	63.74	4.31	6.46	5.64	8.45
2	Loma Prieta 1989	Hollister - S & P	HSP000	USA	0.371	59.96	1.13	1.70	1.14	1.71
3	Loma Prieta 1989	Woodside	WDS000	USA	0.080	39.95	4.77	7.15	4.29	6.43
4	Manjil 1990	Abbar	ABBAR--T	Iran	0.496	46.00	0.88	1.32	0.88	1.32
5	Cape Mendocino 1992	Fortuna - Fortuna Blvd	FOR000	USA	0.116	44.00	2.66	1.44	2.17	3.25
6	Landers 1992	Desert – Hot Springs	LD-DSP000	USA	0.171	50.00	5.17	7.76	5.87	8.81
7	Northridge 1994	LA - W 15th St	W15090	USA	0.104	39.99	3.56	5.34	3.57	5.36
8	Northridge 1994	Moorpark - Fire Sta	MRP180	USA	0.292	40.00	4.02	6.03	4.19	6.28
9	Northridge 1994	N Hollywood - Cw	CWC270	USA	0.271	21.92	1.92	2.88	1.40	2.11
10	Northridge 1994	Santa Susana Ground	5108-360	USA	0.232	57.25	3.56	5.34	4.08	6.13
11	Northridge 1994	LA - Brentwood VA	0638-285	USA	0.164	44.83	4.60	6.90	3.57	5.35
12	Northridge 1994	LA - Wadsworth VA	5082-235	USA	0.303	55.17	3.09	4.64	3.09	4.64
13	Kobe 1995	Nishi-Akashi	NIS090	Japan	0.503	40.96	2.25	3.37	1.93	2.89
14	Kobe 1995	Abeno	ABN090	Japan	0.235	140.00	4.22	6.33	2.44	3.65
15	ChiChi 1999	TCU105	TCU105-E	Taiwan	0.112	90.00	2.40	3.59	2.25	3.37
16	ChiChi 1999	CHY029	CHY029-N	Taiwan	0.238	90.00	2.34	3.51	1.74	2.61
17	Hector 1999	Hector	HEC090	USA	0.337	45.31	1.90	2.84	2.06	3.10
18	Imperial Valley 1940	USGS 117 El Centro Array #9	I-ELC180	USA	0.313	40.00	2.11	3.16	1.77	2.66
19	New Zealand 02 1987	99999 Matahina Dam	A-MAT083	NZ	0.256	27.00	4.05	6.07	4.80	7.20
20	Nahinni Canada 1985	Site 3	S3270	Canada	0.148	19.09	13.93	20.75	14.61	21.92
21*	Victoria Mexico 1980	UNAMUCSD 6604 Cerro Prieto	CPE045	Mexico	0.621	24.45	4.10	6.14	3.44	5.16

* Not included in the final ground motion suite; used as the active ground motion for regular building Lavan A/R placement method.

6.1.2.3. Artificial Accelerogram Set

A modified application of the SSSA technique, the SSSA Mode method, required a set of three spectrum-compatible accelerograms. Various programs to create artificial accelerograms were considered, and the Seismic Record Processing (SRP) software by Karabalis, Cokkinides, and Rizos (1992) was selected. Unlike other programs that create accelerograms from noise with frequency modifications, SRP uses existing ground motions as a baseline template and iteratively alters these accelerograms to meet the frequency characteristics of the provided elastic response spectrum (Karabalis, Cokkinides, Rizos, & Mulliken 2000).

Three spectrum-compatible accelerograms were created in SRP based on the elastic response spectrum of the buildings. These accelerograms met the requirements for artificial earthquakes provided in EC 8 (3.2.3.1.2) (BS EN 2004), which specifies that an artificial earthquake suite has a minimum of three accelerograms and that "no value of the mean 5% damping elastic spectrum should be less than 90% of the corresponding value of the 5% damping elastic spectrum." The same spectrum-compatible accelerogram set for the SSSA Mode method was used for both the regular and irregular buildings, and this is justified by the identical elastic response spectrum (0.3g pga and Eurocode B soil). Figure 6.8 displays the response spectrums of the accelerograms, the elastic spectrum of the buildings, and indicates the buildings' first three natural periods. Plots of the accelerograms' time histories are included in Appendix A-6.

6.1.3. Application of Optimisation Placement Schemes

After a realistic building and ground motion suite were developed, the optimisation placement schemes were applied to the bare buildings (without dampers). The retrofit scenario for added damping, the damper typology, and the details of each damper placement method are presented.

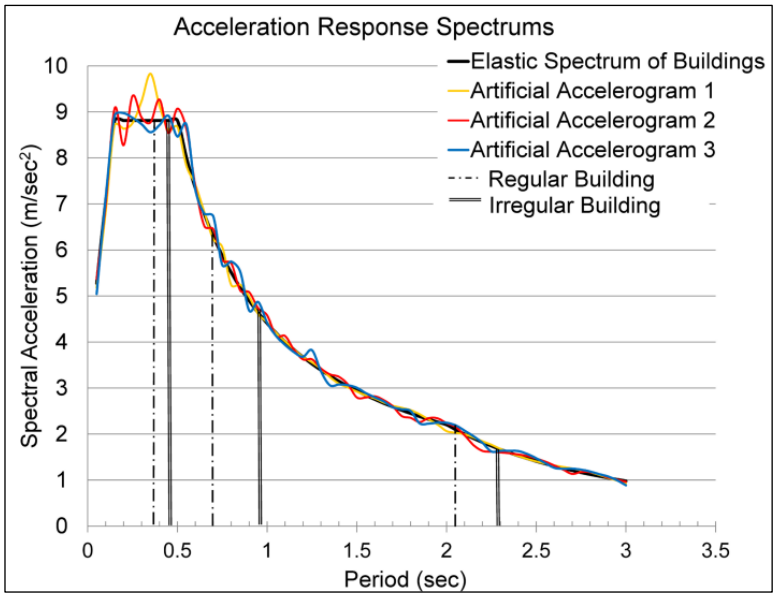

Figure 6.8. Acceleration Response Spectrums of the Artificial Accelerogram Set

6.1.3.1. Retrofit Scenario

A strategic amount of added damping in the form of linear viscous dampers was calculated to improve the performance of the buildings. The objective was to add dampers to achieve a linear elastic building performance under the DBE, causing no permanent damage to structural members, and thereby increasing the building performance from a Life Safety level to an Immediate Occupancy level under the DBE.

The buildings without dampers met the Life Safety (LS) performance level under the DBE and the Immediate Occupancy (IO) level under the FOE. The IO performance under the FOE for both buildings is indicated by peak interstorey drifts less than 1% under the FOE implying no permanent deformations in the structure (Table 6.2). For important structures with sensitive contents, such as hospitals or museums, a more stringent performance requirement, such as IO performance level under the DBE, may be desired, both to ensure the full-functioning of the structural members after the DBE and to reduce accelerations, which may damage sensitive contents.

Using the equal displacement approximation, the *2000 NEHRP provisions* (BSSC 2001), and the strain energy method used in the previous chapter, a total amount of viscous damping was calculated, such that the buildings with dampers would achieve near 1% peak interstorey drift under the DBE. The equal displacement approximation permits the assumption that a linear relationship exists between drift and structural response in both the elastic and plastic range (Figure 6.9).

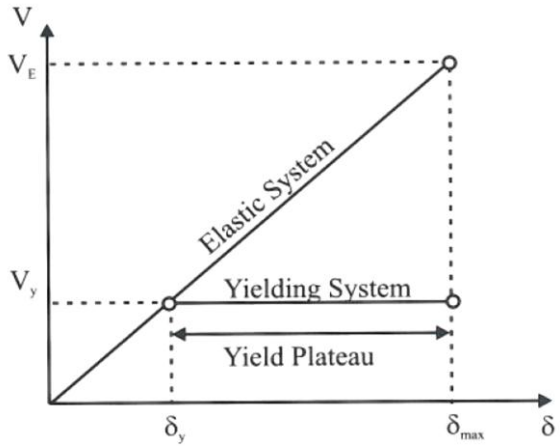

Figure 6.9. Equal Displacement Approximation (Christopoulos & Filiatrault 2006)

The *2000 NEHRP provisions* (BSSC 2001, Table 13.A.3.1) presents the relationship between damping B-values and total effective damping ratios for damped systems. The damping value *B* may represent the ratio between two pseudo-spectral acceleration responses *PSA* and two drift values δ_{DBE} at the same effective damping ratios (Ramirez, Constantinou, Whittaker, Kircher, & Chrysostomou 2002). This may be written as follows, assuming a 5% inherent effective damping ratio ξ of the bare frame and total damping ξ_{total} as the sum of the effective damping from viscous dampers and inherent structural damping:

$$B = \frac{PSA\ (\xi = 5\%)}{PSA\ (\xi = \xi_{total})} = \frac{\delta_{DBE}\ (\xi = 5\%)}{\delta_{DBE}(\xi = \xi_{total})} = \frac{\delta_{DBE,bare}}{\delta_{DBE,added\ dampers}} \tag{6.3}$$

For the regular building, a B-value of two (corresponding to a 37% total effective damping ratio) reduces the interstorey drift by a factor of two, achieving expected peak drift responses near 1% for the DBE (Table 6.6). The total damping is comprised of 32% effective damping from viscous dampers and 5% from inherent structural damping. Effective damping of 37%

is comparable to typical values, as approximately 30% of critical damping of the first mode is considered practical (Lavan & Levy 2009). For the irregular building, a B-value of 2.1 (corresponding to a 40% total effective damping ratio) reduces the expected peak drift of the frame with dampers to 1.18% under the DBE (Table 6.6). These damping values was selected as a realistic compromise between total damping quantity and desired response (near 1% peak interstorey drift under the DBE).

Table 6.6. Building Properties with Added Dampers

		Estimated Peak Interstorey Drifts (%)				**Total Damping**	**Damping from Viscous Dampers**	
		DBE		*MCE*				
Building	B -value	Bare frame	Frame with dampers	Bare Frame	Frame with dampers	ξ total (%)	ξ dampers (%)	C (kN-s/cm)
Regular	2.0	2.20 %	1.10 %	3.30 %	1.65 %	37 %	32%	812
Irregular	2.1	2.47 %	1.18 %	3.71 %	1.77 %	40 %	35%	337

The effective damping ratio from viscous dampers was translated into a total viscous damping coefficient *C*, which corresponds to damper sizes. This was calculated using the strain energy method (BSSC 2001), whereby the effective damping ratio $\xi_{dampers}$ is equivalent to the ratio of the energy dissipated in one cycle of the viscous damping system and the maximum strain energy dissipated by the structural system at its fundamental period (see Chapter 5). Lateral floor stiffnesses were used to approximate the structure's maximum strain energy. As an additional check, similar values for strain energy dissipation of the structure were calculated in terms of mass-based strain energy (Whittaker et al. 2003). The design properties of the buildings with added dampers are presented in Table 6.6.

6.1.3.2. Damper Typology

The investigation of damper placement schemes was limited to the total added viscous damping per floor of the structure. While various work has been conducted on damper typologies within a frame, such as diagonal, horizontal, and toggled positions, this chapter focuses on total damping values and a consistent typology because it represents the simplest comparison case for the optimisation techniques. A damper typology of a chevron-braced

frame with two horizontal dampers, one on either side of the brace apex, was selected as a common installation position that maximises the effectiveness of the damper for lateral forces (i.e. the velocity and reaction force of the damper aligned parallel to the ground motion) (Figure 6.10).

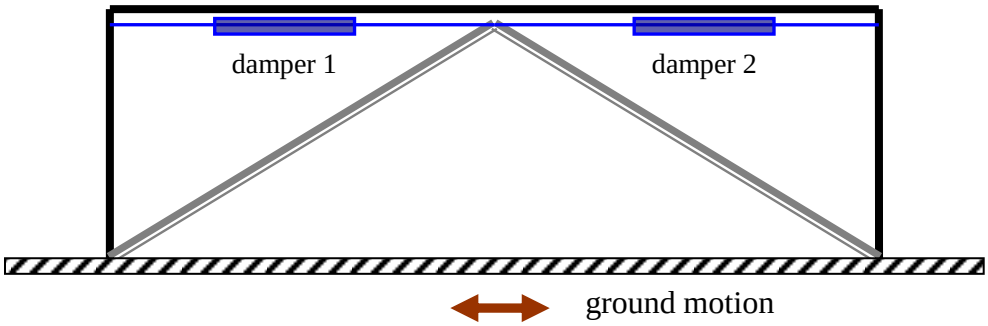

Figure 6.10. Damper Typology

The purpose of the chevron braces was to assist in the installation of the dampers in the building without affecting the building's dynamic response. The braces were unconnected to the top beam and were limited by a very low mass to avoid contributing to the building's stiffness and dynamic performance. The chevron braces were designed approximately ten times stiffer than the floors. The result was a method for adding horizontal dampers to the structure without adding stiffness or mass. Time history analyses with and without the chevron braces in the bare structure confirmed that the braces had no effect on the performance of the building. It is acknowledged that general brace design and influence on the structure is not addressed in this work, and that primary focus is on the added dampers' influence on the building response.

6.1.3.3. Uniform Damping and Stiffness Proportional Damping

Both the Uniform damping method and Stiffness Proportional damping method were applied following the procedure in Chapter 3. For Stiffness Proportional damping, the approximate lateral floor stiffnesses (Table 6.3) were utilised.

6.1.3.4. SSSA Mode Damping

Twenty dampers (i.e. twenty procedural steps) were selected for the SSSA Mode application in the 10 storey buildings. A linear time history analysis with SAP2000 was run for each step

of the SSSA Mode method and for three separate artificial accelerograms to determine the final SSSA Mode configuration. The building and dampers were modelled and analysed with the same assumptions as the final building model using linear time history analysis. Maximum interstorey velocities were determined over the entire ground motion duration using the tabular output option in SAP2000 and post-processing with Excel and Visual Basic macros. The SSSA Mode method was employed whereby the conventional SSSA method with 20 iterations was applied to three spectrum-compatible accelerograms; the SSSA Mode placement scheme was selected based on the most frequently occurring damping value (mode) at each floor within the artificial accelerograms set subject to the constraint of the total added damping value. For example, at floor seven, the most frequently occurring damping value amongst the three artificial accelerograms is 121.8 kN-sec/cm. In the unlikely case of no frequently occurring value amongst the three accelerograms at a certain floor, an average value would be taken, and total damping would be constrained using engineering judgement. SSSA Mode results are presented Table 6.7 and Table 6.8.

Table 6.7. Regular Building: SSSA Mode Configuration for the Artificial Accelerogram Set

	SSSA Method - Added Damping per Floor (kN-sec/cm)			
Floor	*Artificial Accelerogram **1***	*Artificial Accelerogram **2***	*Artificial Accelerogram **3***	***SSSA MODE***
10	40.6	40.6	40.6	40.6
9	40.6	40.6	40.6	40.6
8	81.2	81.2	81.2	81.2
7	121.8	81.2	121.8	121.8
6	121.8	81.2	81.2	81.2
5	121.8	81.2	81.2	81.2
4	81.2	121.8	121.8	121.8
3	121.8	162.4	121.8	121.8
2	81.2	121.8	121.8	121.8
1	0	0	0	0

This SSSA Mode damper placement scheme (final columns of Table 6.7 and Table 6.8) was used when analysing the buildings under the full ground motion suite. Because the damper placement scheme varies only slightly for each artificial accelerogram, it can be concluded that this alteration of the SSSA technique is consistent with SSSA method's original placement objectives.

Table 6.8. Irregular Building: SSSA Mode Configuration for the Artificial Accelerogram Set

SSSA Method - Added Damping per Floor (kN-sec/cm)				
Floor	*Artificial Accelerogram **1***	*Artificial Accelerogram **2***	*Artificial Accelerogram **3***	***SSSA MODE***
10	16.85	16.85	16.85	16.85
9	16.85	16.85	16.85	16.85
8	16.85	16.85	16.85	16.85
7	33.70	16.85	33.70	33.70
6	33.70	33.70	33.70	33.70
5	33.70	33.70	33.70	33.70
4	50.55	50.55	50.55	50.55
3	67.40	67.40	67.40	67.40
2	67.40	84.25	67.40	67.40
1	0	0	0	0

The application of the SSSA Mode method for a single ground motion was a time-intensive task with twenty iterations of placing a damper, analysing, and determining the next optimal location. However, the sequential application was uncomplicated and used analysis tools familiar to a structural engineer. The sequential placement procedure resulted in a damping configuration not optimised as an array, but instead, inherently limited by the number of steps selected for the procedure. In other words, the damping applied to a floor in each step was immutable and could only increase or remain constant with each procedural step. In addition, there is no clear indication that maximising dampers' effectiveness will satisfactorily minimise the structural response. Using performance based objectives of drift enabled the user to check if the objective function was eventually met.

6.1.3.5. Takewaki Damping

Application of the Takewaki method followed the procedure presented in Chapter 3 and used the Matlab script with input values of the equivalent shear model: degrees of freedom, stiffness, mass, and total added damping. See Appendix A-3 for the Takewaki script used for the irregular building. The distribution of damping is initially assumed uniform, and the gradient-based search method is applied iteratively. Recall that the guidelines for selecting the step size are not provided by the Takewaki method. In both buildings, the step size is selected by trial-and-error based on the existence of a solution and rate of convergence.

For the regular building, a step size of 7 led to convergence, indicated by near unity values for the optimality index, for all non-zero damping terms, and the objective function (sum of the interstorey drifts of the transfer function) was reduced from 0.196 to 0.167. The final damping configuration for the regular building is presented in Table 6.9, and Figure 6.11 shows the objective function with each step. The optimal solution occurs when the objective function is minimised (Figure 6.11, achieved near step 45) and when the optimal location indices equal one at all floors except the zero-damped floors (Figure 6.12, achieved near step 94). After a gradual approach, unity is finally achieved at step 94 for the ninth floor optimality index γ_8 (Figure 6.12), and this combined with the minimised objective function marks the optimal solution.

Table 6.9. Regular Building: Takewaki Damper Placement Configuration

Floor	*C (kN-sec/cm)*	γ_o *(step size = 7)*
10	0	0.369
9	46.32	1.000
8	70.14	1.000
7	89.44	1.000
6	102.22	1.000
5	114.02	1.000
4	126.16	1.000
3	134.80	1.000
2	128.90	0.999
1	0	-

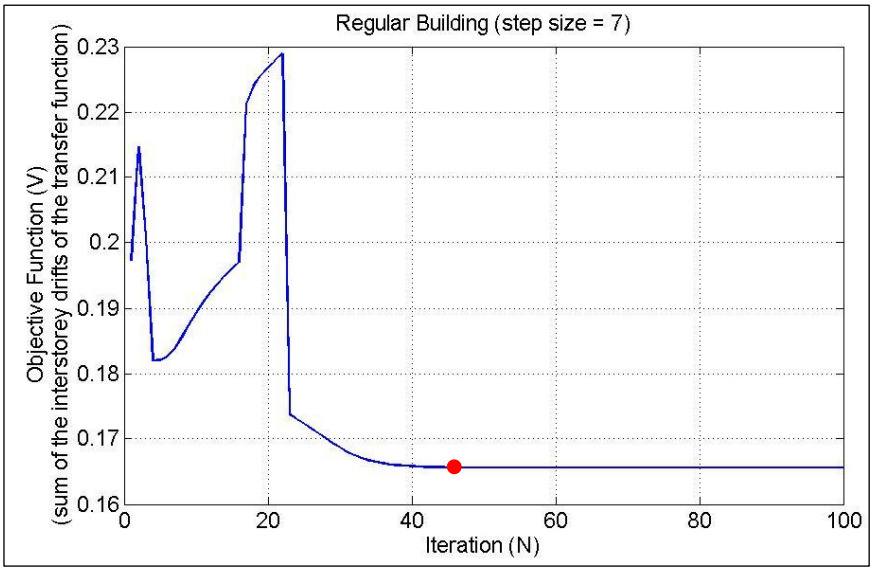

Figure 6.11. Regular Building: Minimisation of the Objective Function – Takewaki Method

The initial spike in the objective function curve is a result of redistributing the initial uniform damping in an ineffective direction. The third step corrects for this by reducing damping at floor one until the eventual removal of floor one damping at step 4 (first trough of the curve), causing a reduction in the objective function and optimality indices (Figure 6.12). Once the first floor damping is removed (Figure 6.13), the second largest first-order sensitivity value *B*, which occurs at floor 3, is selected for the denominator of the optimality index step. The second peak of the objective function curve at step 22 is sharply reduced when the damping at floor ten is removed at step 23. When damping at a floor is removed, the damping is distributed uniformly to the remaining floors and often causes a steep change in the damping curves as the floors are reset to the uniform damping values. Note that the roof optimality index converges to a number less than one (Figure 6.12), which is the desired convergence value for floors without damping.

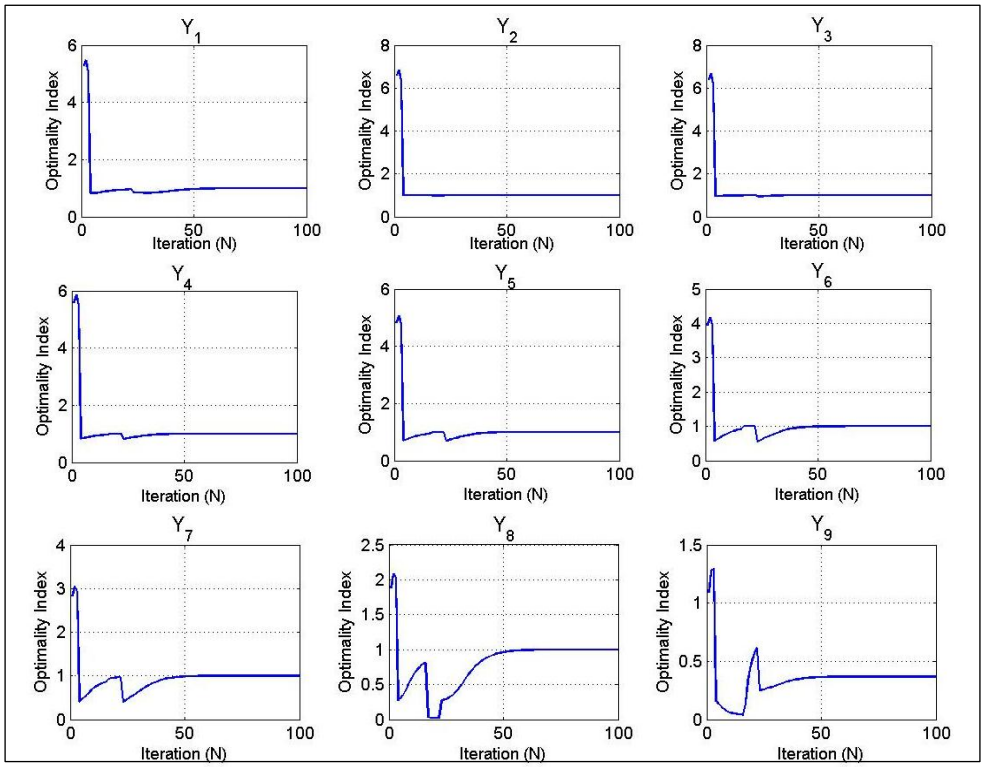

Figure 6.12. Regular Building – Floor Optimality Index per Step of Takewaki Method

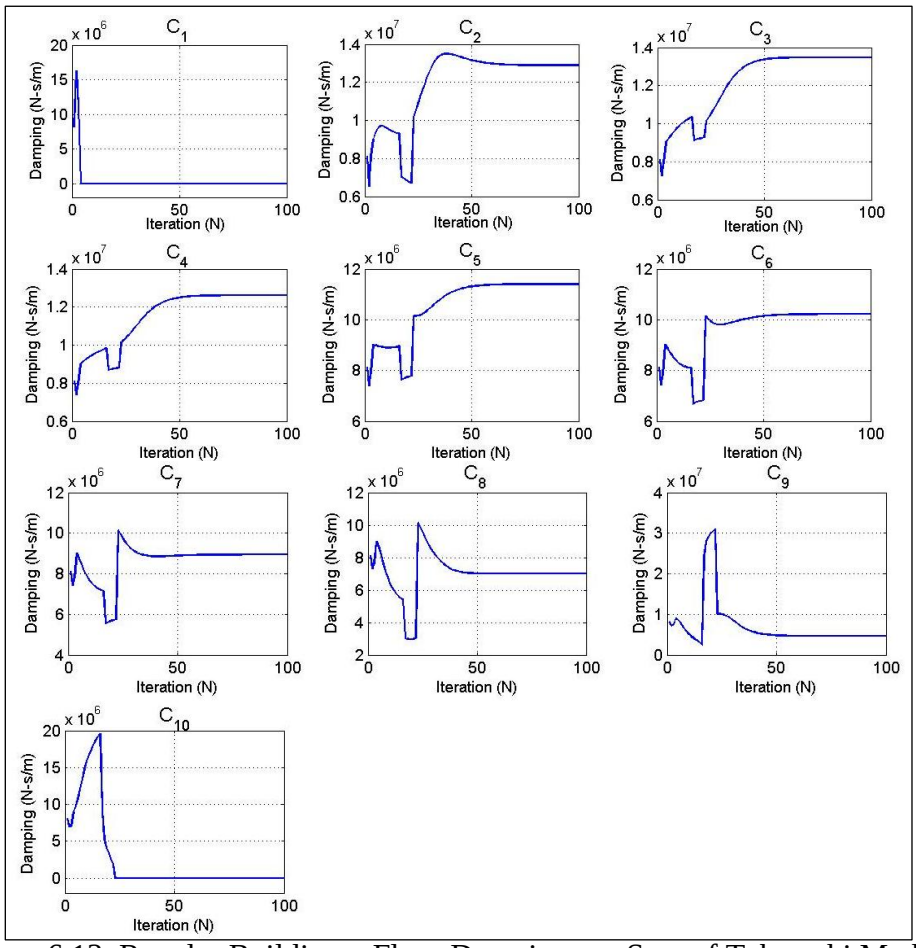

Figure 6.13. Regular Building – Floor Damping per Step of Takewaki Method

For the irregular building, a step size of three converged, and the objective function reduced from 0.230 to 0.190, with unity values of the optimality index for all non-zero damping terms. The final damping configuration for the irregular building is presented in Table 6.10, while Figure 6.14 shows the change of the objective function with each step. The optimal solution was achieved at step 200, when the tenth floor optimality index γ_9 reached unity (Figure 6.15), which occurred shortly after the objective function reached a minimum value at step 198.

Table 6.10. Irregular Building: Takewaki Damper Placement Configuration

Floor	*C (kN-sec/cm)*	γ_o *(step size = 3)*
10	15.3	1.000
9	20.9	1.000
8	25.1	1.000
7	29.6	1.000
6	38.2	1.000
5	45.5	1.000
4	51.8	1.000
3	57.2	1.000
2	53.5	1.000
1	0	-

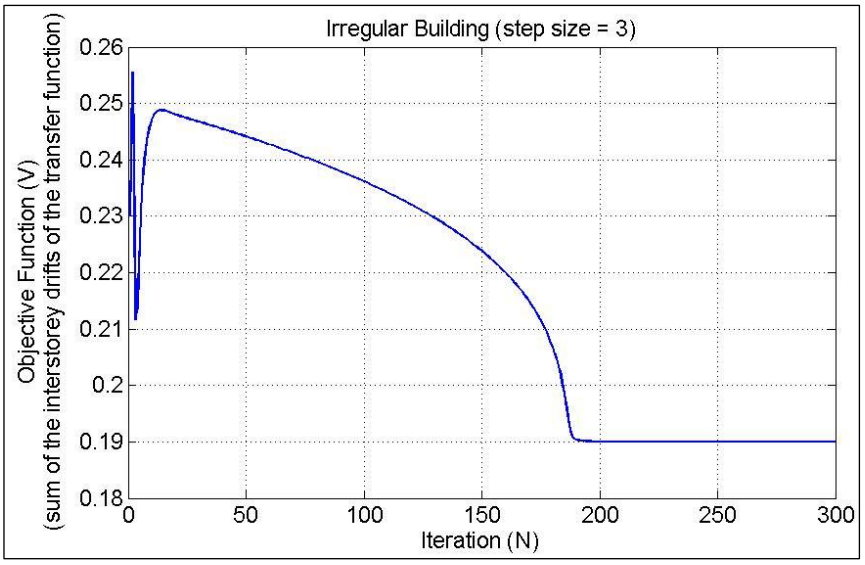

Figure 6.14. Irregular Building: Minimisation of the Objective Function – Takewaki Method

The initial spike in the irregular building curve is a result of the first damping distribution adjustment in the second step, where damping is incrementally changed by relatively large values, in an ineffective direction. Damping is removed at the first floor in step 3 causing a decrease in the objective function and shifting the optimality indices at most floors closer towards unity (Figure 6.15). The method steeply reduces the damping at floor 10 (Figure 6.16) from steps 175 to 185 as it attempts to achieve unity for the floor 10 optimality index γ_9.

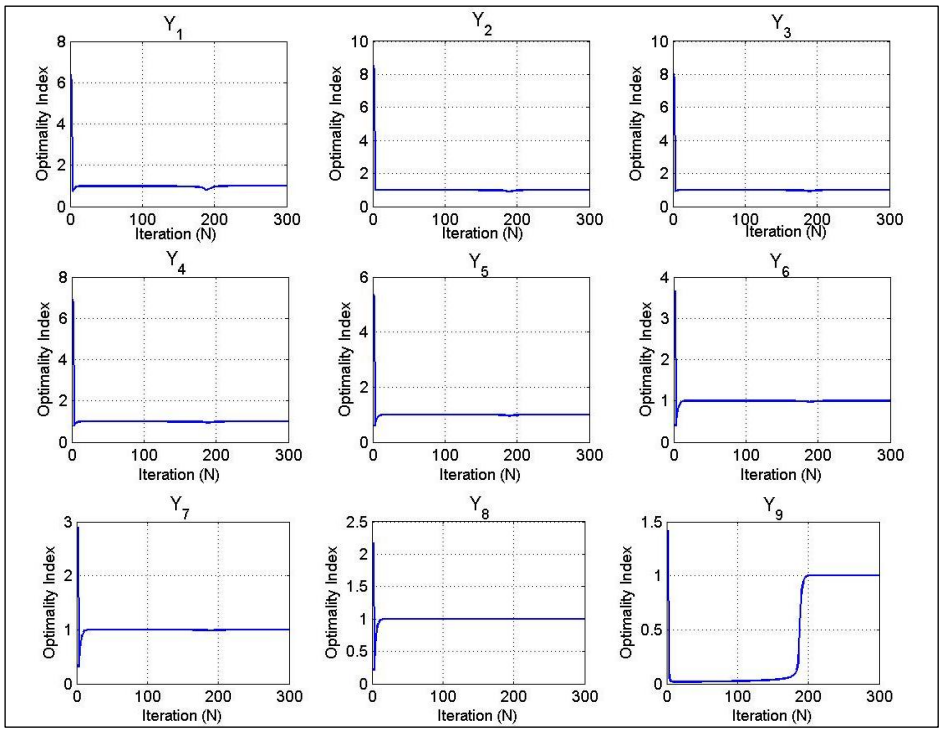

Figure 6.15. Irregular Building – Floor Optimality Index per Step of Takewaki Method

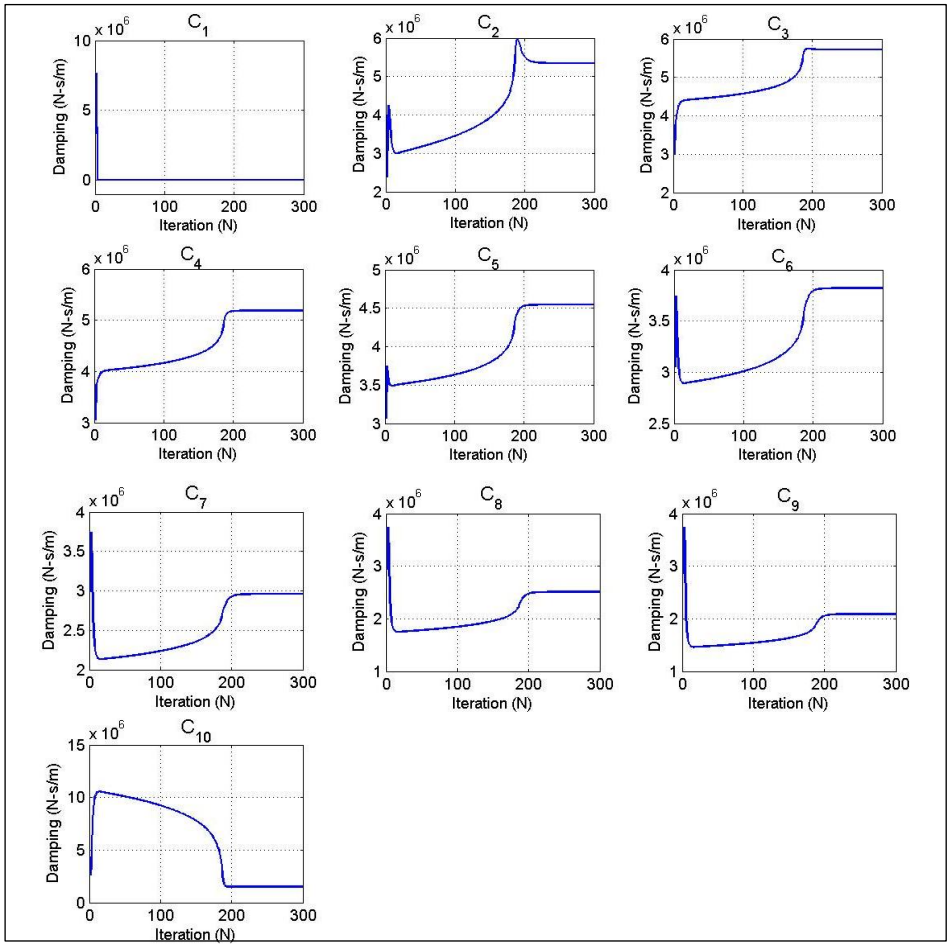

Figure 6.16. Irregular Building – Floor Damping per Step of Takewaki Method

The application of the Takewaki method depends on a reliable script for executing the gradient-based search. Creating the script is a potentially time-consuming task and may require programming tools not familiar to all engineers. However, applying the Takewaki method to a building with the finalised script was a quick, efficient process. Because the method is based on the dynamic properties of the structure, and therefore, ground-motion independent, a single damper placement scheme was calculated for the building and used for all of the ground motion records. The Takewaki method resulted in a damping configuration that was optimised as an array; with each step, the damper configuration at every floor (except zero-damped floors) was revised until the optimality criteria were achieved. Similar to the SSSA method, there is no specific building performance objective inherently included in the Takewaki procedure, and even more so, no suggestions for determining the total added damping value. However, performance based objectives can be incorporated into the

procedure and final checks of the objective function conducted. Finally, the objective function of minimising the sum of drifts has the potential to be disadvantageous for structures with irregular drift distributions.

6.1.3.6. Lavan A/R Damping

Application of Lavan A/R followed the procedure presented in Levy and Lavan (2006) and the constrained damping recurrence relationship equation in Lavan and Levy (2009). The Lavan A/R method was applied to the building frames using linear time history analysis and an Excel program to calculate the recurrence relationship at each step, with an assumed convergence parameter of 0.5 (see procedure in Chapter 3). The building and dampers were modelled and analysed with the same assumptions as the final building model.

The Victoria Mexico ground motion was selected as the Lavan A/R active ground motion for the regular building because it produced the largest interstorey drifts in the bare frame structure. A 50% reduction of peak interstorey drifts under the active ground motion was used as the performance index, more suitable than a fixed drift objective when considering a single ground motion and fixed total damping. For example, for the regular building, the peak drift of the bare frame under the active ground motion was 3.29%; therefore, the allowable peak drift with dampers was 1.65%.

The Lavan A/R method converged in less than 6 iterations, as shown by the small change in the performance index near step 5 (Figure 6.17) for all floors and the minimisation of the constraint error (difference of the maximum performance index from unity) (Figure 6.18 (A)). All floors achieve a performance index near one, with the exception of the first floor. This is a result of the first floor's high stiffness, such that it achieves much lower drift performance than the other floors, even with zero damping at the first floor. The desired drift limit was achieved and further reduced for all floors under the active ground motion (Figure 6.18 (B)), yielding a uniform drift distribution with the exception of the first floor. The final damping

configuration is presented in Table 6.11.

Table 6.11. Regular Building: Lavan A/R Damper Placement Configuration

Floor	C (kN-sec/cm)		$d_{i,max}$ (%)		$pi_i = d_i / d_{all,i}$
10	9.10		1.56%		0.95
9	39.94		1.56%		0.95
8	60.70		1.56%		0.95
7	92.08		1.56%		0.95
6	96.77		1.56%		0.95
5	101.30		1.56%		0.95
4	133.50		1.56%		0.95
3	155.23		1.56%		0.95
2	123.38		1.56%		0.95
1	0.00		0.89%		0.54
Sum:	812	*Peak:*	1.56%	*Max:*	0.95

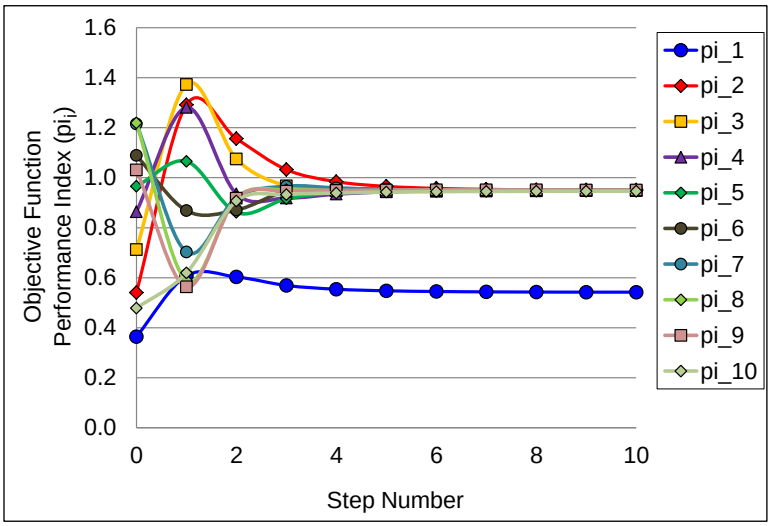

Figure 6.17. Regular Building: Lavan A/R - Objective Function for Each Floor

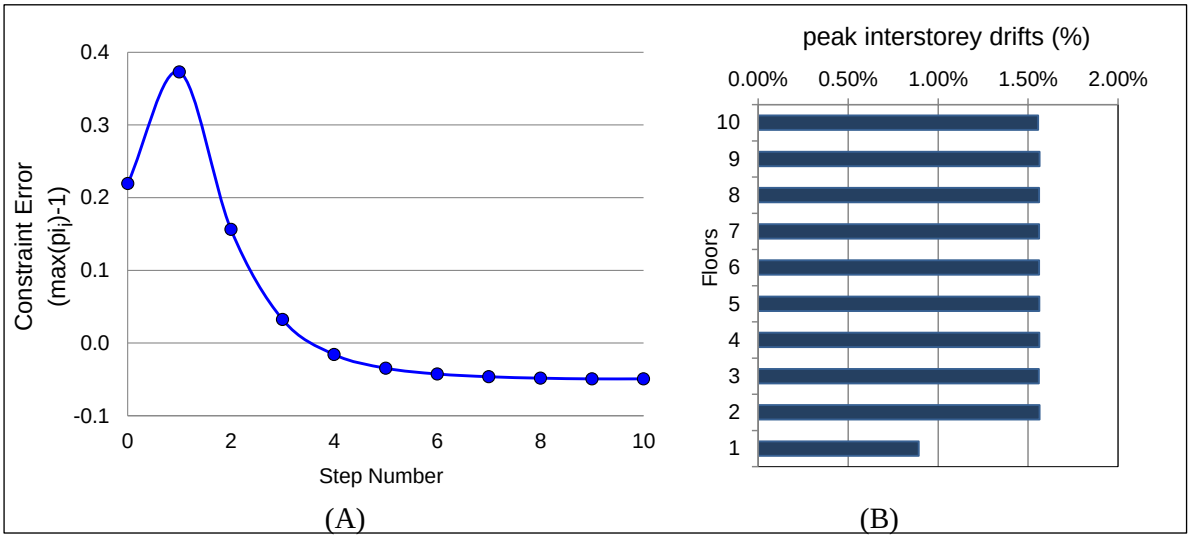

Figure 6.18. Regular Building: Lavan A/R
A) Maximum Constraint Error; B) Peak Interstorey Drift Profile under Active Ground Motion

The New Zealand 02 was selected as the active ground motion for the irregular building, as it produced the highest bare frame peak interstorey drifts. A peak interstorey drift of 1.18% with dampers under the active ground motion, as opposed to percent reduction, was selected as the objective value due to the unreasonably high peak drifts experienced by the bare frame under this ground motion. The Lavan A/R method converged in about 4 iterations, based on the performance indices reaching a stable value (1.2) for all floors (Figure 6.19) and the constraint error being minimised (Figure 6.20 (A)). Similar to the regular building damping distribution, the high stiffness of the first floor yields zero damping and a much lower drift value and performance index compared to the other floors.

The desired drift limit was not achieved (*pi* is greater than 1) for this ground motion and total damping quantity, which was to be expected for this extreme ground motion case and a limited reserve of total damping. However, the achieved damping distribution was justified as best for this quantity of total damping, since the objective function was minimised and damping achieved a uniform drift distribution under the active ground motion (Figure 6.20(B)). The final damping configuration is presented in Table 6.12.

Table 6.12. Irregular Building: Lavan A/R Damper Placement Configuration

Floor	C (kN-sec/cm)		$d_{i,\,max}$ (%)		$pi_i = d_i / d_{all,i}$
10	3.92		1.38%		1.17
9	15.61		1.41%		1.19
8	17.24		1.39%		1.18
7	29.67		1.40%		1.19
6	35.19		1.40%		1.18
5	45.28		1.40%		1.19
4	53.42		1.39%		1.18
3	82.55		1.40%		1.19
2	54.11		1.40%		1.18
1	0.00		0.99%		0.84
Sum:	337	*Peak:*	1.41%	*Max:*	1.19

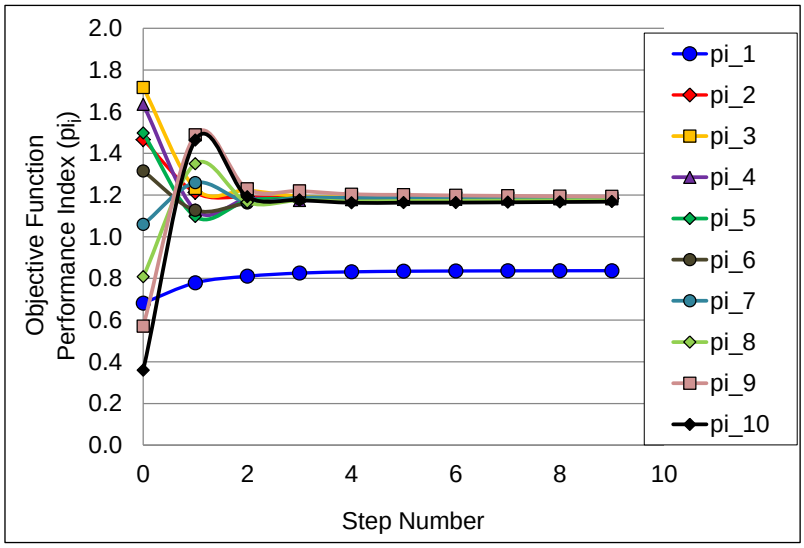

Figure 6.19. Irregular Building: Lavan A/R –Objective Function for Each Floor

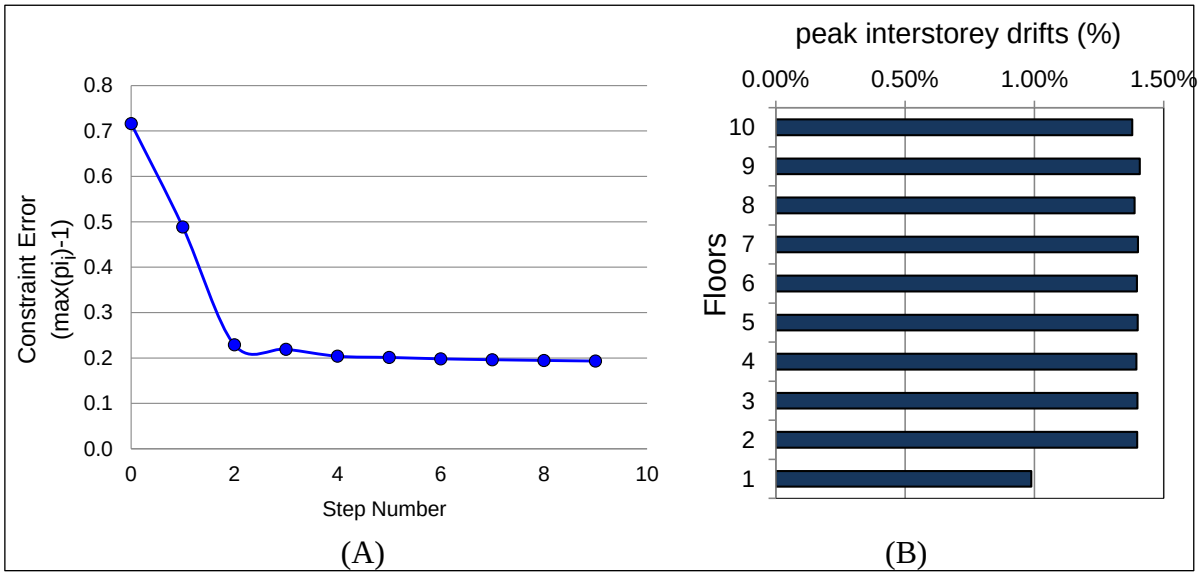

Figure 6.20. Irregular Building: Lavan A/R

A) Maximum Constraint Error; B) Peak Interstorey Drift Profile under Active Ground Motion

The application of the Lavan A/R method relies on analysis tools and concepts familiar to structural engineers. A solution is achieved very quickly (less than 10 iterations), and the method is heuristic in its design-oriented objectives and logical redistribution of dampers at each step. It is similar to SSSA in its dependence on individual ground motions to determine a damper configuration; although, it does provide rationale for the selection of the active ground motion and a further check with high-demand ground motions. In addition, it is similar to the Takewaki method with its optimisation of the floor damping as an array, which is improved with each step of the procedure. Once a user has verified the correct procedure

for the Lavan A/R method, the time-expended for this method depends on the number of steps, speed of the time history analysis, and selected number of active ground motions.

6.1.4. Dynamic Time History Analysis

Direct integration, dynamic time history analysis was selected as the best option for simulating the ground motion shaking and capturing the performance of the building with velocity-dependent viscous dampers. The numerical modelling details for SAP2000 (CSI 2009a) and nonlinear analysis parameters are presented.

6.1.4.1. Numerical Modelling Details

The building frames were modelled in SAP2000 using frame elements of S355 steel material, diaphragm constraints to model rigid floor behaviour, and fixed foundation joint constraints. Linear link elements were used for the linear viscous dampers, whereby a damping value and zero stiffness value could be specified. Initial analysis confirmed that a linear damper element (with an exponent of 1) was identical to a linear link element with only damping. Also, the linear link element substantially reduced computation time for nonlinear analysis. The SAP2000 Refer manual (CSI 2009a) confirmed that linear link elements are suitable for linear and nonlinear direct integration time history analysis.

6.1.4.2. Time History Analysis

Nonlinear time history analysis of the buildings with added dampers was used to evaluate the damper placement configurations effect on building performance. Nonlinear analysis was selected as the primary analysis tool because of the high performance demands on the buildings. Although linear performance is expected for the buildings under the DBE, nonlinear analysis justified this assumption and captured any unexpected nonlinearities. In addition, a few linear analyses were conducted to confirm that the linear building performance was the same under linear or nonlinear dynamic analysis.

Material nonlinearity and geometric nonlinearity (p-delta) were included in the nonlinear analysis, and lumped plasticity at the ends of all the frame elements was modelled with bilinear plastic hinges. The plastic hinges, based on the FEMA 356 plastic hinge for beams (M3, strong-axis moment) and columns (P-M2-M3, interacting axial force and moment), were created and applied to the respective beam and column members. Rayleigh damping was modelled within the time history analysis, using 5% damping in the first and second modes of the buildings. A time step of 0.005 seconds was utilised for each ground motion time history, and approximately 20 seconds were added to the end of the ground motion records to capture the unforced, building response decay and a true residual drift. Finally, each ground motion time history was applied after the nonlinear static gravity loads from the controlling load combination (G+0.3Q), such that the earthquake scenarios were run on a realistic stressed building state under the gravity loads.

6.1.5. Performance Indicators and Comparison

Peak interstorey drift, absolute acceleration, and residual interstorey drift were selected as key performance indicators. Interstorey drift indicates potential damage to primary structural members, while absolute floor acceleration corresponds to damage of building contents and sensitive equipment. Residual interstorey drift indicates the permanent damage to the structural members and feasibility of economic repair of the building after the earthquake. Peak interstorey drift is calculated as the maximum drift of adjacent floors over the entire time history, represented as a percentage of the total floor height. Absolute floor acceleration is taken as the maximum absolute value of the total floor acceleration over the entire time history, and residual interstorey drift is measured as the final, stationary peak interstorey drift, measured at least 20 seconds after the end of the ground motion record.

6.1.6. Final Damper Configurations

The final damping configurations are presented in Table 6.13 and Figure 6.21. The damping value is presented per floor; therefore, the damping for a single damper within the chevron

brace is half the floor value. The total added damping for each configuration scheme is 812 kN-sec/cm for the regular building and 337 kN-sec/cm for the irregular building.

Table 6.13. Damping Configuration Schemes

Added Damping (kN-s/cm)										
	Regular Building (812 kN-s/cm)					*Irregular Building (337 kN-s/cm)*				
Floor	Uniform	Stiffness Proportional	SSSA mode	Takewaki	Lavan A/R	Uniform	Stiffness Proportional	SSSA mode	Takewaki	Lavan A/R
10	81.20	27.60	40.60	0.00	9.10	33.70	6.73	16.85	15.26	3.92
9	81.20	42.90	40.60	46.32	39.94	33.70	11.31	16.85	20.89	15.61
8	81.20	51.00	81.20	70.14	60.70	33.70	15.59	16.85	25.09	17.24
7	81.20	55.30	121.80	89.44	92.08	33.70	18.81	33.70	29.59	29.67
6	81.20	63.30	81.20	102.22	96.77	33.70	23.26	33.70	38.20	35.19
5	81.20	70.10	81.20	114.02	101.30	33.70	27.30	33.70	45.46	45.28
4	81.20	73.80	121.80	126.16	133.50	33.70	31.21	50.55	51.84	53.42
3	81.20	81.50	121.80	134.80	155.23	33.70	35.29	67.40	57.20	82.55
2	81.20	101.90	121.80	128.90	123.38	33.70	46.89	67.40	53.47	54.11
1	81.20	244.50	0.00	0.00	0.00	33.70	120.61	0.00	0.00	0.00

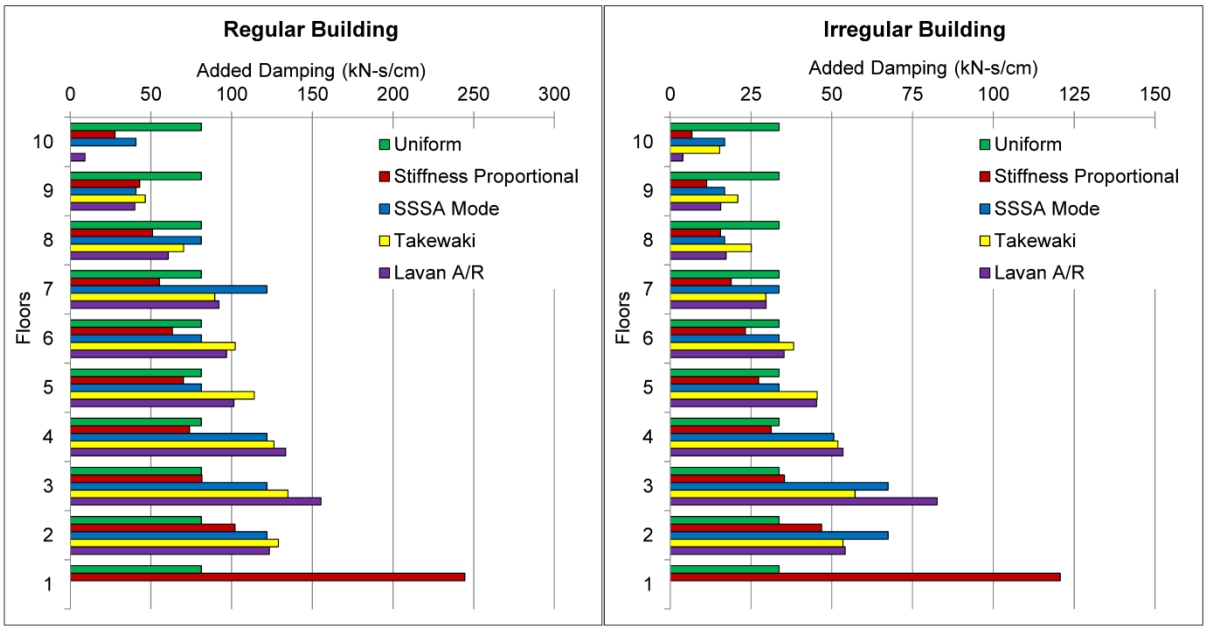

Figure 6.21. Final Damping Configuration Schemes:
Regular Building (left), Irregular Building (right)

6.2. Results and Discussion: Modal Damping Ratios

The contribution of the damping distributions to modal damping is presented in Table 6.14 for each damper scheme and the first three building modes. The damping ratios were calculated using undamped eigenvector analysis and an energy-based equation for effective damping (Whittaker et al. 2003). All five damper placement methods achieve greater first mode

damping than the design value (Table 6.14, row 2), with the exception of the Stiffness Proportional method for the irregular building, which produces a lower fundamental damping ratio than desired. The advanced techniques produce similar fundamental damping ratios, over 30% greater than the design damping ratios. Table 6.14 reveals that there is less damping in modes two and three in the irregular building than the regular building, and the lowest modal damping ratios occur with the Stiffness Proportional scheme. The total added damping generally overdamps mode 4 and higher for both buildings (indicated by dashes), which suggests that there is no dynamic response for higher modes. However, results in the next sections show the influence of higher mode effects in selected ground motions.

Table 6.14. Damper Schemes Contribution to Modal Damping

	Modal Damping Ratios ($\xi_{dampers}$)					
	Regular Building			*Irregular Building*		
Damper Schemes	*Mode 1*	*Mode 2*	*Mode 3*	*Mode 1*	*Mode 2*	*Mode 3*
Design with dampers	32%	-	-	35%	-	-
Uniform	39%	-	-	43%	-	-
Stiffness Proportional	33%	81%	-	32%	54%	80%
SSSA Mode	46%	-	-	48%	83%	83%
Takewaki	48%	93%	-	49%	86%	-
Lavan A/R	48%	93%	-	49%	68%	94%

The potential for creating damping distributions that are ineffective for higher mode responses is an important concern. Takewaki is limited to the first mode response in its calculation of interstorey drifts under the undamped fundamental frequency. While SSSA Mode and Lavan A/R consider higher mode responses because of the time history analyses required in their approaches, they depend on the modal strain energy equation for total damping based on first mode response (SSSA Mode and Lavan A/R recommendation) or depend on active ground motions selected with the highest spectral displacement under the fundamental mode (Lavan A/R guideline). Therefore, all three advanced methods specifically mitigate against the first mode response. Since Table 6.14 confirms the overdamping of the majority of the higher modes for most of the damping distributions, it is justified that the placement techniques

approach the damping design with focus on a dominant first mode response. The extent of the methods' effectiveness for higher mode contributions will be investigated for individual ground motions in the following sections.

6.3. Results and Discussion: Regular Building

The regular building performance with the various damper placement schemes is compared in terms of peak interstorey drifts, absolute accelerations, and residual interstorey drifts. All values presented are the median results of the twenty-ground motion suite, unless otherwise noted.

6.3.1. Peak Interstorey Drifts

Figure 6.22 compares the added damper placement schemes in terms of the median peak interstorey drift distributions under the DBE. The drift design objective of the bare frame under the DBE ($\delta_{DBE,\ bare}$) and the frame with dampers ($\delta_{DBE,\ dampers}$) is noted with dashed lines in Figure 6.22. All the damper schemes achieve less than 1.10% peak interstorey drift, thereby meeting the DBE design objective and reducing the bare frame drifts by more than half. Both the Takewaki and Lavan A/R schemes result in peak interstorey drifts best approaching a desirable, uniform drift distribution. Stiffness Proportional and Uniform produce the least uniform drift distributions, with Uniform overdamping the upper floors and Stiffness Proportional overdamping the first floor such that floors three and four are not effectively damped. Figure 6.23 compares the distributions under the MCE, with the solid lines representing the measured median of the peak interstorey drifts and the dashed lines representing the expected drift profile if the DBE peak interstorey drifts are scaled by 150%. The MCE drift distributions mirror the DBE results scaled by 150%, as to be expected for a predominantly linear building response. Under the MCE, the design objective for added dampers (1.65% interstorey drift) is met by all of the damper placement schemes.

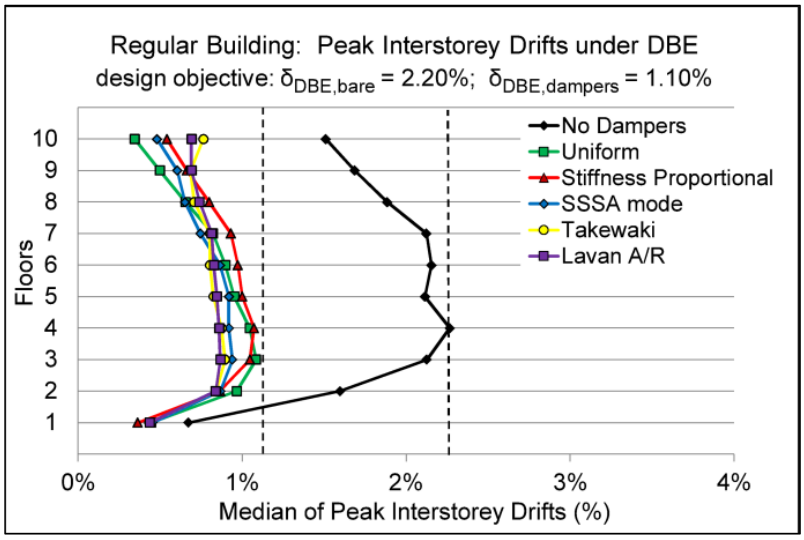

Figure 6.22. Regular Building – Median of Peak Interstorey Drifts under the DBE

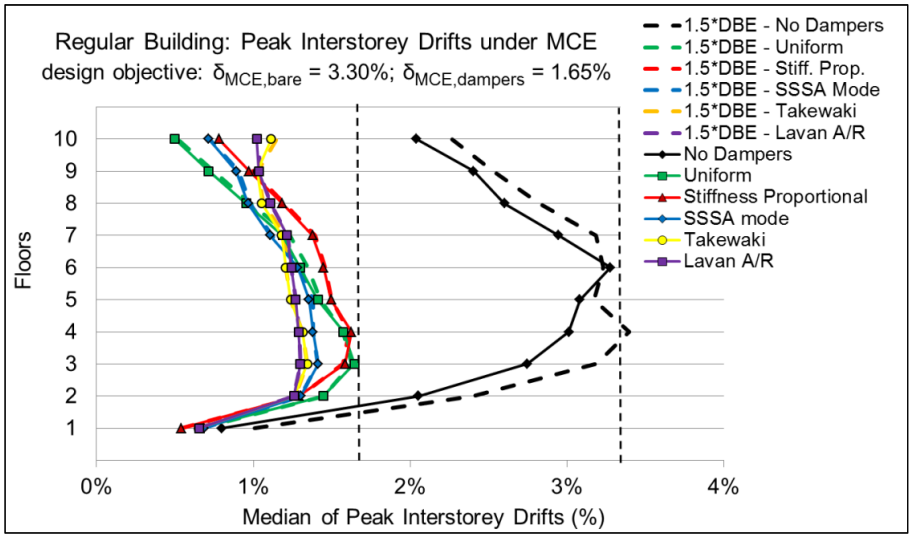

Figure 6.23. Regular Building – Median of Peak Interstorey Drifts under the MCE

Table 6.15 presents the maximum peak interstorey drifts of all floors, represented as maximum value of the median of the peak interstorey drifts of the ground motion suite. The maximum peak interstorey drift value may occur at different floors for each damper placement scheme (e.g. maximum drift with the Uniform distribution occurs at floor 3, Figure 6.22). Parameters for maximum floor drift include interstorey drift δ taken over the ground motion time t and evaluated for 20 ground motions gm and at every floor (1-10):

$$\text{max floor drift} = \max\left(\text{median}\left[\max\{\delta(t)\}\right]\Big|_{1\text{st gm}}^{20\text{th gm}}\right)\Big|_{1\text{st floor}}^{10\text{th floor}} \tag{6.4}$$

Table 6.15. Regular Building – Maximum of Peak Interstorey Drifts

	DBE Ground Motion Suite $\delta_{DBE, bare}$ = 2.20% $\delta_{DBE, dampers}$ = 1.10%	MCE Ground Motion Suite $\delta_{MCE, bare}$ = 3.30% $\delta_{MCE, dampers}$ = 1.65%
	% (mm)	% (mm)
No Dampers	2.27% (72.5)	3.28% (104.9)
Uniform	1.08% (34.7)	1.64% (52.6)
Stiffness Proportional	1.07% (34.3)	1.62% (52.0)
SSSA Mode	0.94% (30.1)	1.41% (45.2)
Takewaki	0.90% (28.7)	1.34% (43.0)
Lavan A/R	0.87% (27.7)	1.30% (41.6)

The Uniform and Stiffness Proportional damper schemes produce maximum interstorey drifts within 1% of each other, while the three advanced techniques (SSSA Mode, Takewaki, and Lavan A/R) result in lower peak interstorey drifts, with little disparity between the three schemes. Lavan A/R produces the lowest peak interstorey drift, 3% lower than the Takewaki method, under both ground motion scenarios. Drifts in millimetres particularly highlight the small differences between the methods.

The statistical mean of peak interstorey drifts for the regular building is displayed in Figure 6.24 and Figure 6.25. The standard deviations of drift under the DBE (Figure 6.24) are similar amongst the damper placement methods at each floor (an average of 0.24% maximum standard deviation, with all methods within 8% of the average maximum standard deviation) and greatest for the bare frame (0.40% and 0.84% maximum standard deviations under the DBE and MCE, respectively). A larger dispersion of drifts occurs in the damped frame under the MCE, with an average of 0.39% maximum standard deviation, with all methods within 11% of the average maximum standard deviation (Figure 6.25). The dispersion is largest in the internal floors (2-7) corresponding to the largest peak interstorey drifts in the frame.

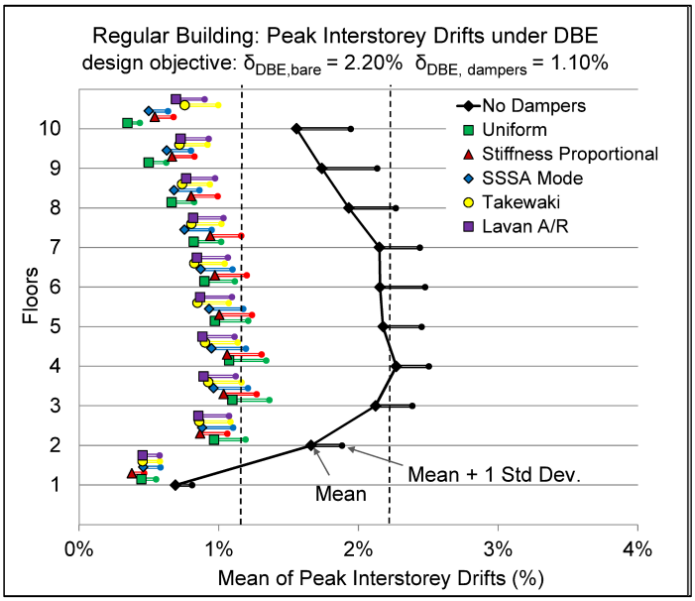

Figure 6.24. Regular Building – Mean and Standard Deviation of Peak Interstorey Drifts - DBE

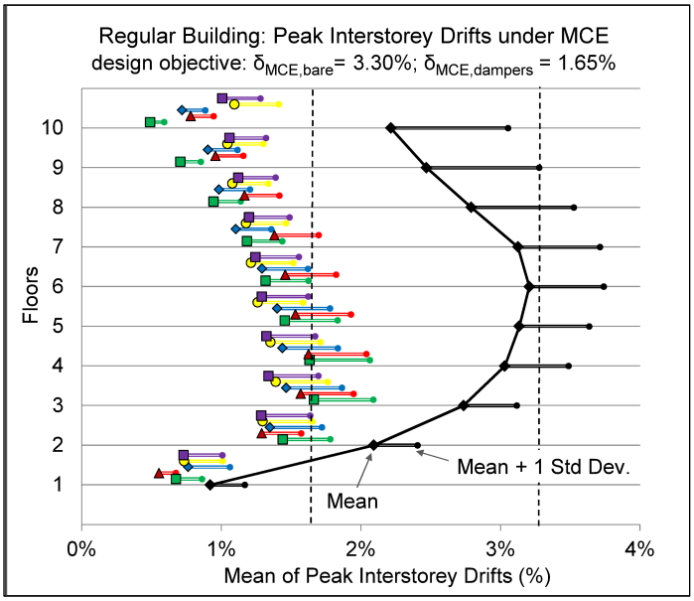

Figure 6.25. Regular Building – Mean and Standard Deviation of Peak Interstorey Drifts – MCE

Figure 6.26 and Figure 6.27 show the peak interstorey drifts amongst all floors for each ground motion under the DBE and MCE scenarios, respectively. The dotted lines indicate the drift design objective. In general, the Lavan A/R scheme achieves the lowest drift values, followed by Takewaki, SSSA Mode, Stiffness Proportional, and the Uniform scheme. A typical drift profile of the damped frames is presented in Figure 6.28, where peak drifts for all damped frames occur at floors 3 or 4. The damped frame typically responds in a first mode shape reflecting the expected design drift of the bare frame (Figure 6.7(A)), with lower interstorey drifts at the upper floors and greater interstorey drifts at floors 2-4. The bare frame

performance in terms of median drifts under the DBE (Figure 6.22) displays the expected design performance, while the bare frame performance under GM 7 yields larger drifts in floors 5-7 (Figure 6.28).

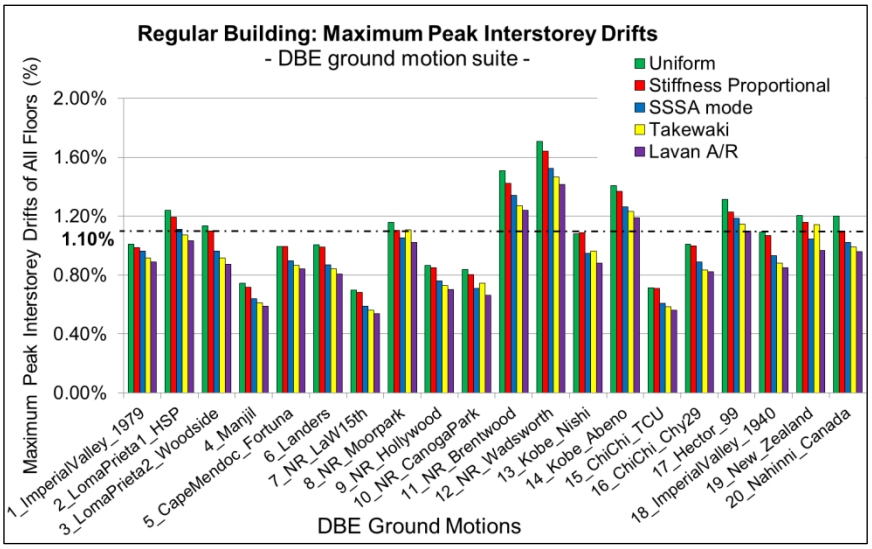

Figure 6.26. Regular Building - Peak Interstorey Drifts for DBE Ground Motions

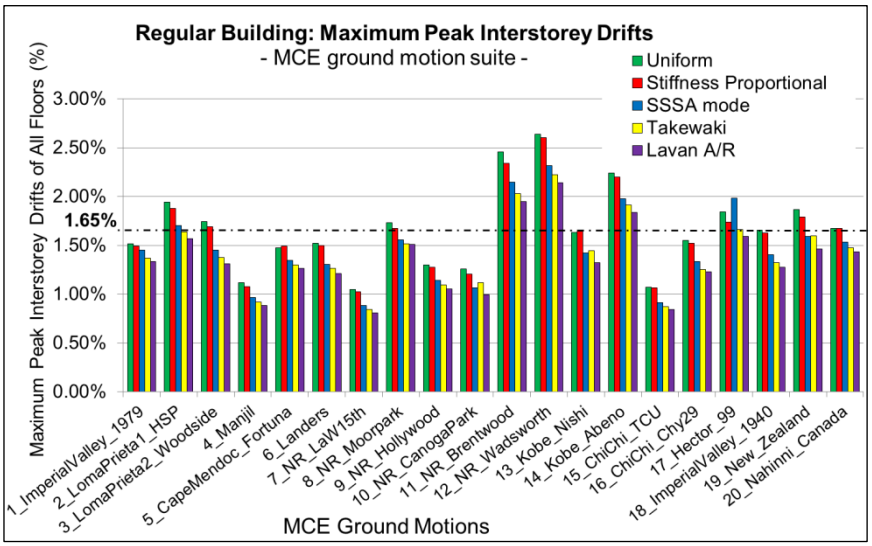

Figure 6.27. Regular Building - Peak Interstorey Drifts for MCE Ground Motions

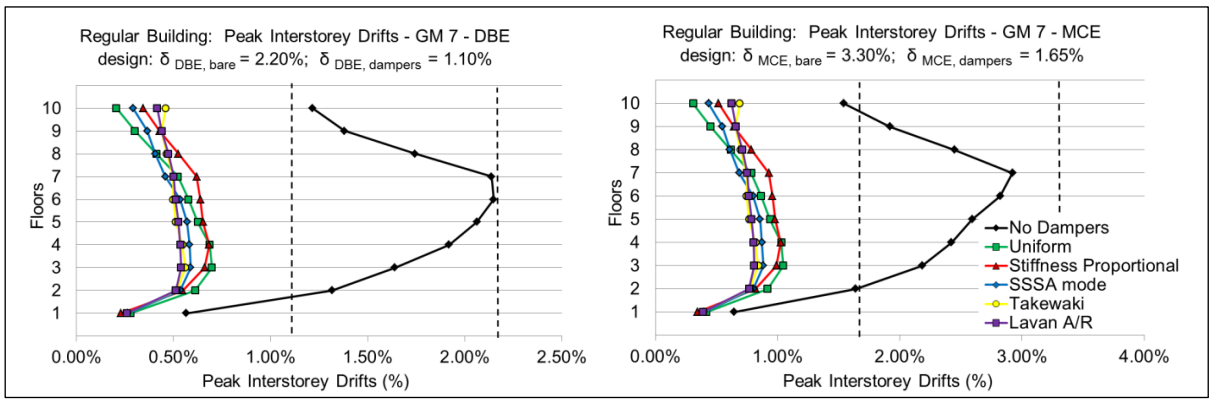

Figure 6.28. Regular Building – Peak Interstorey Drift Profiles – GM 7 – Typical Response Under DBE (Left) and MCE (Right)

The confirmation of mode shape 1 for the bare frame and damped frames in Figure 6.28 is provided by the plots of modal contribution to interstorey drifts. The modal contribution to interstorey drifts for a single ground motion $\delta_{n,GM}$ is calculated using the ground motion spectral displacement $S_{d,GM}$ scaled to the DBE with 5% damping and evaluated at the modal period T_n, the modal participating mass ratio in the lateral direction r_{xn}, and the modal interstorey drifts Δ_n calculated from modal analysis:

$$\delta_{n,GM} = S_{d,GM}(T_n) * r_{xn} * \Delta_n \tag{6.5}$$

This was calculated for four ground motions for the bare frame. The total contribution of modes 1 through 6, which constitute 97% of the total modal mass participation, is approximated with both the square-root of the sum of the squares (SRSS), which represents statistically independent modes, and the conservative absolute sum method, which assumes fully-correlated modes (CSI 2009a). The modal interstorey drifts are presented in Figure 6.29 as a percentage of total floor height.

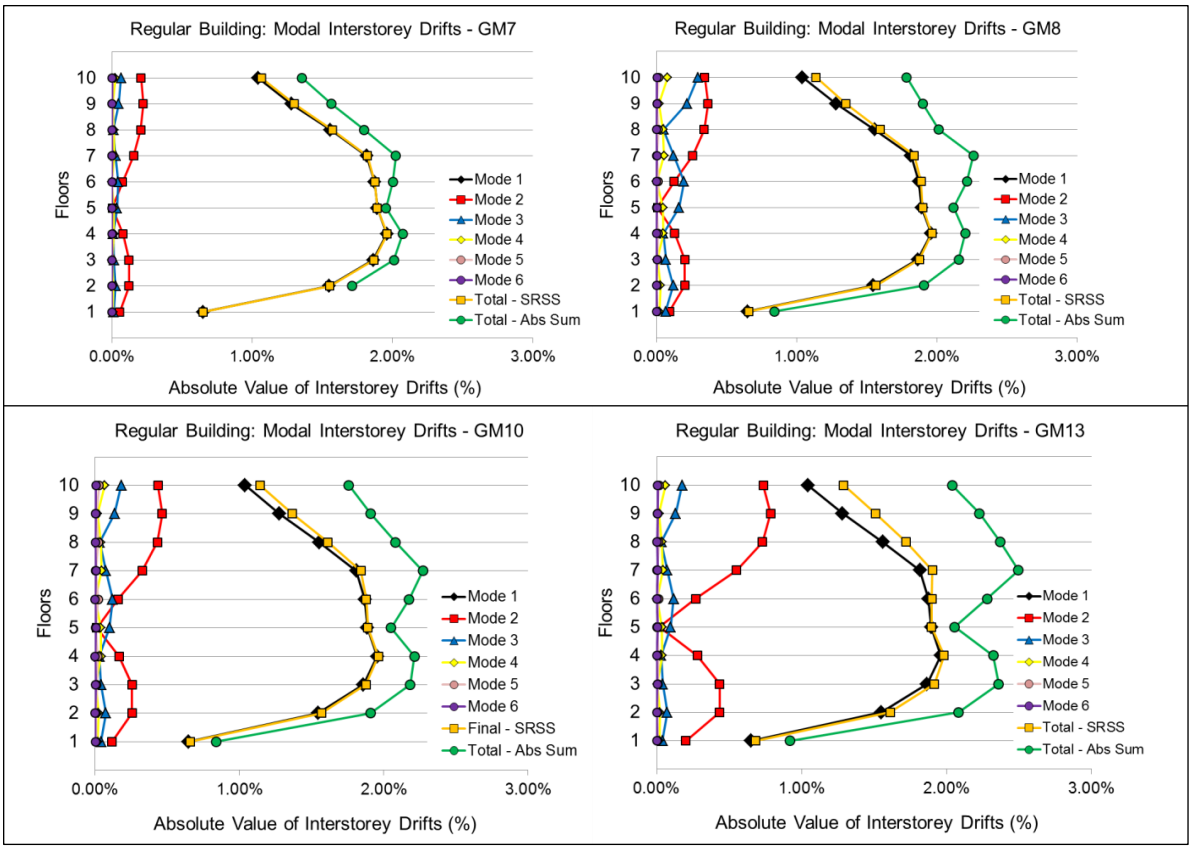

Figure 6.29. Modal Contribution to Interstorey Drifts of the Bare Frame – Regular Building at DBE Scale – GM 7, 8, 10, 13

GM 7 in Figure 6.29 presents the typical drift profile example (confirming first mode response in Figure 6.28), while GM8, 10, 13 represent exceptions to the trend. Note that the bare frame profile assumes linear response of the structure, and is therefore provided here as an estimate of the modal contribution and not a true reflection of the nonlinear response of the bare frame.

Returning to Figure 6.26 and Figure 6.27, there are some exceptions to the typical damped frame trends, including GMs 8, 10, 13 and 19 under the DBE (Figure 6.26) and GMs 8, 13, 17, and 19 under the MCE (Figure 6.27) where the SSSA Mode and Takewaki schemes compete for second-lowest peak interstorey drift. A review of the individual drift profiles of the bare frame reveals an increase in the upper storey drifts under all these ground motions. This results in increased upper storey drifts in the Takewaki distribution (due to zero damping at the roof), occasional increased roof drifts in the Lavan A/R distribution (due to minimal damping at the roof), and the SSSA Mode distribution achieving greater drift reduction than the Takewaki distribution in these cases.

Examples include the increased roof drifts in the Takewaki damped frame and Lavan A/R damped frame under GM 8 (Figure 6.30(A) and (B)) and further amplified drifts under GM 13 (Figure 6.30(C) and (D)), reflecting the second mode response of the bare frame under GM 8 MCE and GM 13 DBE and MCE. The spectral displacements of GM 13 confirms similar displacements at the fundamental and second frequency of the 5% damped regular frame (Appendix A-5.4), thereby suggesting the presence of a large second-mode effect in the bare frame. In addition, the spectral displacements suggest higher mode effects of the regular bare frame with no damping under GM 8, yet GM 10, 17, and 19 do not indicate a large presence of higher mode contributions in the 5% damped frame. Interestingly, the generalised 37% damping spectral displacement curves suggest only first mode response for all of the ground

motions. However, these spectral displacement curves are based on a uniformly damped, single degree-of-freedom structure; results suggest higher modes may alter the profile of the damped frame drift distribution causing increased upper storey drifts.

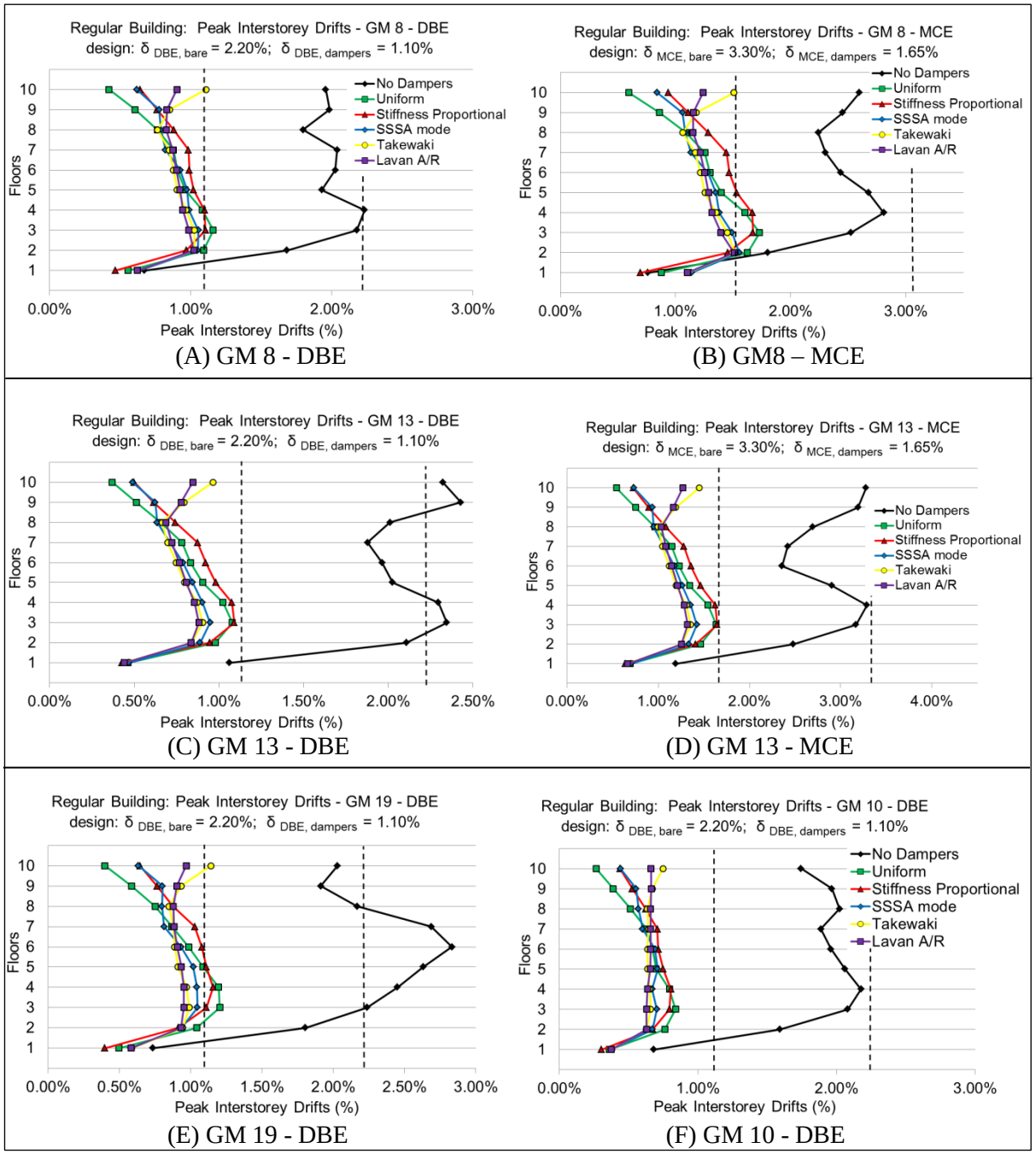

Figure 6.30. Regular Building – Peak Interstorey Drift Profiles – GM 8, 13, 10, 19

Finally, the modal contribution to interstorey drifts (Figure 6.29) highlights the larger presence of the second mode under GM13 compared to GM7, an example of the typical drift profile. Higher modes, such as two and three, reflect increased upper storey peak interstorey

drifts in the bare frame, as seen in the examples of GM8, 10, and 13, while the first mode dominates the overall modal contribution response, confirming calculations in section 6.2.

Under GM 8, GM 13, and GM 19, peak drifts occur at the roof for the Takewaki damped framed, while the Lavan A/R damped frame has peak drifts at either the roof or floors 2 and 3. The bare frame drift profile under GM 19 exhibits a first mode shape with slightly increased drifts at the roof; these increased roof drifts are mirrored in the Takewaki and Lavan A/R drift distributions under the DBE (Figure 6.30(E)). For GM 10 under both hazard levels, the Lavan A/R achieves a fairly uniform drift distribution, while the Takewaki method produces larger roof drifts than the other damping distributions (Figure 6.30(F)).

Another exception to the trend is at GM 17 MCE where SSSA Mode achieves the largest peak interstorey drift, even greater than the conventional methods. Peak drifts of the SSSA Mode distribution occur at floor 3, and floors 1-5 all yield peak drifts greater than the Uniform distribution (Figure 6.31 (A)). The SSSA Mode distribution does not produce the same extreme drift values under the DBE, and a review of the first floor drift time history (Figure 6.31 (B)) revealed that the high MCE demands caused yielding in the form of plastic hinging at the base of the SSSA Mode damped frame. This results in the large first floor interstorey drifts, subsequently large peak interstorey drifts at floors 2-5, and significant residual drifts. This is the only instance where an advanced distribution technique shows nonlinearity greater than the standard distributions for the regular building.

Overall, it may be concluded that both the Takewaki and Lavan A/R distributions for the regular building are sensitive to higher mode effects in the structure, Takewaki more so than the Lavan A/R distribution. This is a result of both distributions removing or minimising the damping at the roof to achieve the best drift profile under first mode response (Takewaki approach) or a uniform drift profile under the active ground motion (Lavan A/R approach).

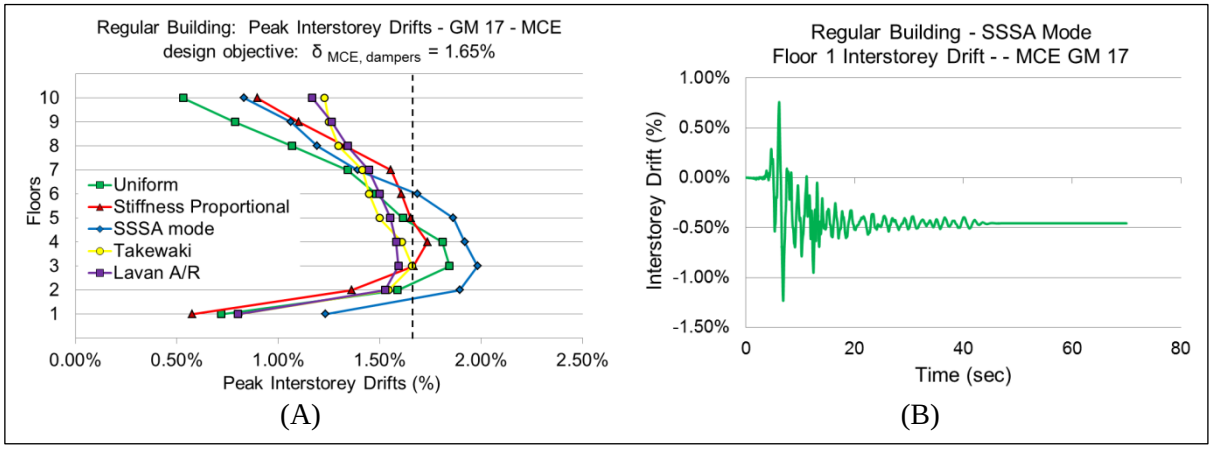

Figure 6.31. Regular Building under GM 17 – MCE -
A) Damped frame distributions B) Interstorey drift time history of SSSA Mode

The damped frame profiles under the Lavan A/R active ground motion GM 21 are presented in Figure 6.32 (A). Despite the expected uniform drift distribution of Lavan A/R under GM 21 (based on the linear analysis), the slight nonlinearities considered during nonlinear analysis yield a less uniformly distributed drift distribution. Because the active ground motion produces a bare frame drift profile of reduced upper storey drifts, the upper stories will likely experience greater drifts when the Lavan A/R distribution is subjected to ground motions with higher mode contributions (such as GM 13). However, the Lavan A/R distribution effectively overdamps the frame such that variations in the drift profile due to higher mode effects still results in Lavan A/R being the most effective distribution amongst the advanced methods and reveals less sensitivity than the Takewaki method to higher mode contributions.

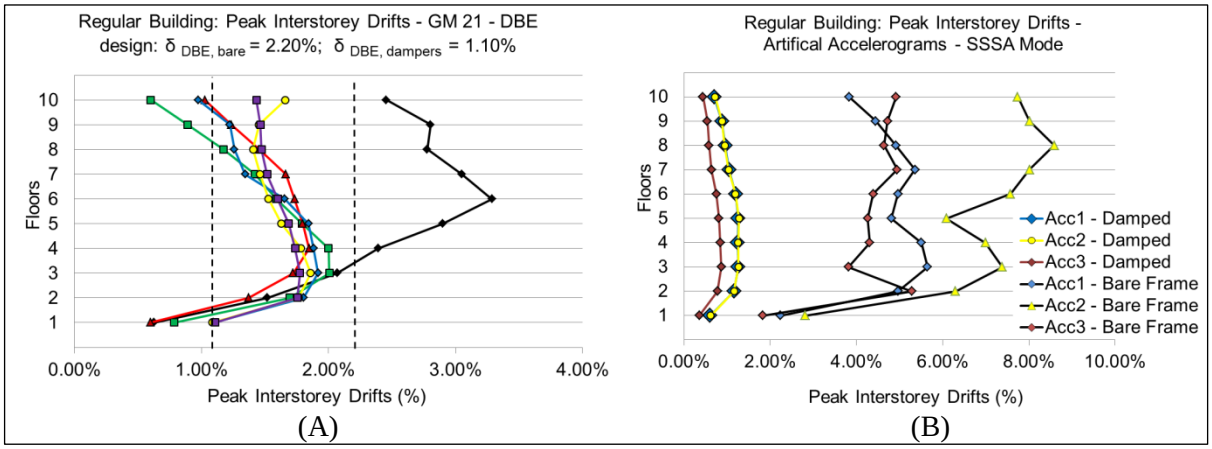

Figure 6.32. Regular Building Design Drift Profiles – A) Lavan A/R and B) SSSA Mode

The SSSA Mode performance under its artificial accelerograms (Acc1-3) based on linear time history analysis and accelerograms scaled to the DBE level is presented in Figure 6.32(B). The drift profiles indicate that the upper stories of the damped frame have been slightly overdamped. This may be advantageous for increased upper storey drifts as seen in the ground motions with higher mode contributions The SSSA mode damped frame response is a product of the selected artificial accelerograms and increased robustness in the design due to the use of three design accelerograms. However, robustness is not guaranteed and is dependent on the characteristics of the selected artificial accelerograms. The bare frame's performance under the artificial accelerograms indicates that the first artificial accelerogram simulates lower upper storey drifts, the second accelerogram a similar profile with amplified drifts, while the third artificial accelerogram yields a different drift profile and potentially larger upper storey drifts.

Finally, to provide insight into the time history behavior of the building, an example of the interstorey drift time history is presented for the regular building. The drift profiles under the GM 6 at DBE scale indicate that peak interstorey drifts occur at the third floor for the majority of the damped frames (Figure 6.33(A)). Thus, the time history of the third floor interstorey drifts is presented for each damping distribution compared to the bare frame drifts (Figure 6.33 (B)-(F)). The peak drift at each floor is the maximum drift over the duration of the ground motion, $\max(\delta(t))$ in Eq. 6.4. Peak interstorey floor drifts for all damping distributions, Uniform (1.00%), Stiffness Proportional (0.96%), SSSA Mode (0.79%), Takewaki (0.78%), and Lavan A/R (0.77%), occur near 20.9 seconds. All damping distributions have largely damped the high interstorey drifts in the bare frame from 20-40 seconds and reach equilibrium near 50 seconds. Note the residual drift in the bare frame is 0.35%, while there are negligible residual drifts in the damped frames under GM 6.

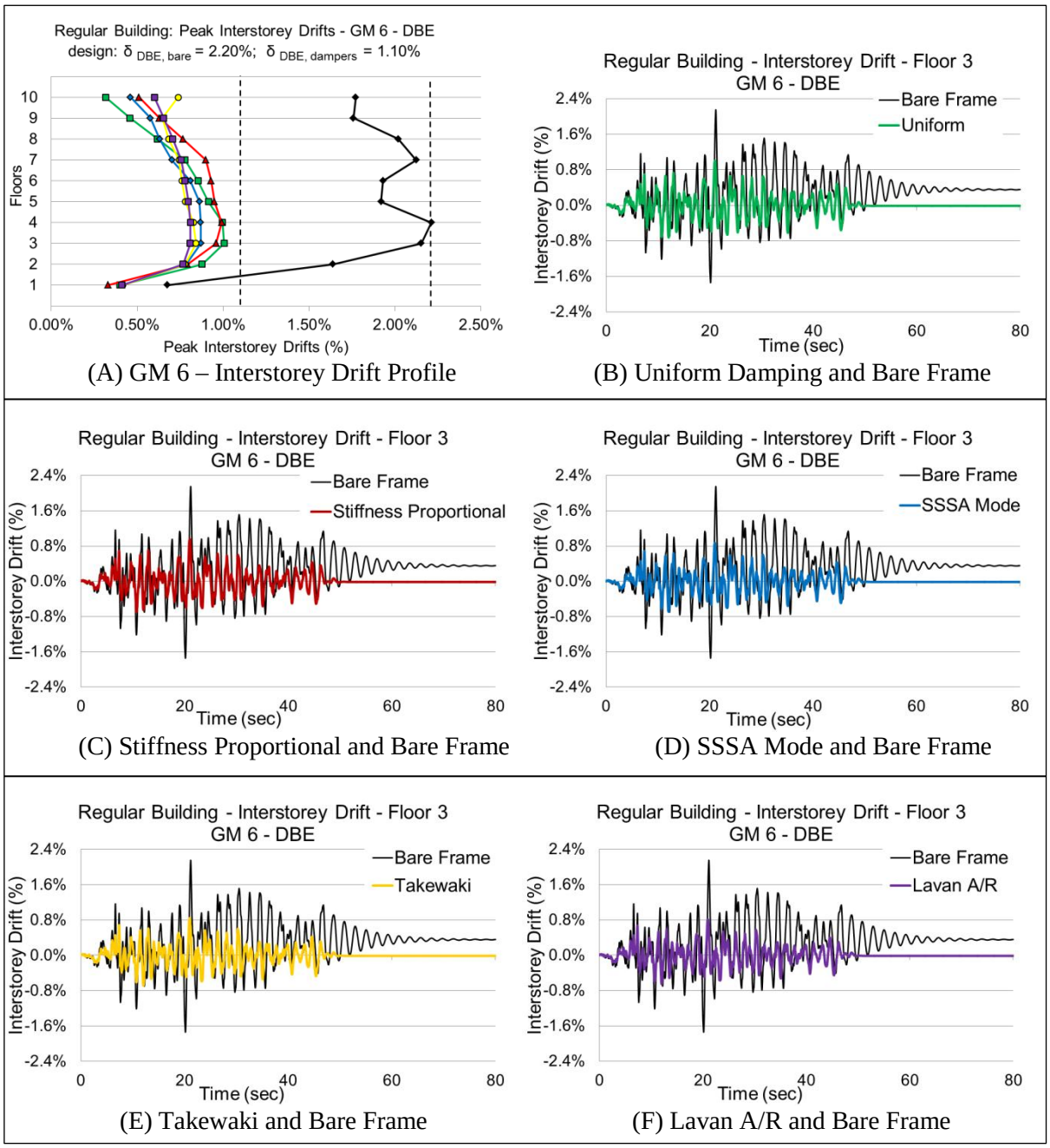

(A) GM 6 – Interstorey Drift Profile

(B) Uniform Damping and Bare Frame

(C) Stiffness Proportional and Bare Frame

(D) SSSA Mode and Bare Frame

(E) Takewaki and Bare Frame

(F) Lavan A/R and Bare Frame

Figure 6.33. Regular Building – GM 6 - DBE
(A) Interstorey Drift Profile; (B) - (F) Interstorey Drift Time Histories at Floor 3

6.3.2. Absolute Accelerations

The second design concern is the reduction of absolute accelerations. Figure 6.34 and Figure 6.35 compare the placement techniques in terms of absolute accelerations of the regular building under the DBE and MCE. All the damper placement schemes reduce the absolute accelerations of the bare frame at all floors except the 1st floor. The large first floor accelerations are a product of the shared ground floor absolute accelerations (denoted as floor zero in Figure 6.34 and Figure 6.35).

In both the DBE and MCE scenarios, the small differences between the accelerations leads to the conclusion that the total added damping controls the reduction of acceleration in the linear-elastic structure, as opposed to the particular damper placement scheme controlling the overall acceleration reduction. Because the damped structure behaves linearly and the viscous dampers are velocity-controlled, the damper reaction forces are out-of-phase with the maximum stressed state of the building (maximum building accelerations and maximum drift). Therefore, the dampers do not contribute substantially to increasing the accelerations of the buildings, as would be likely with highly nonlinear structural behavior or most other dissipative devices.

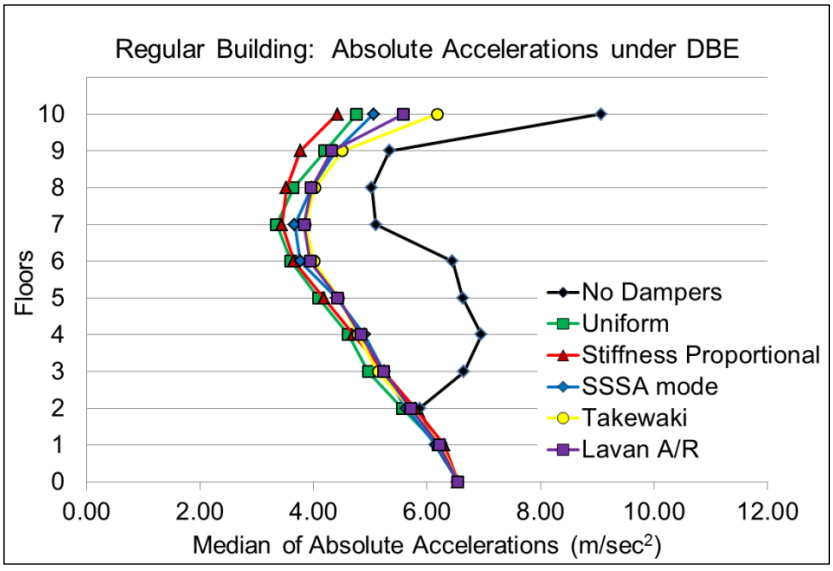

Figure 6.34. Regular Building – Median of Absolute Accelerations under the DBE

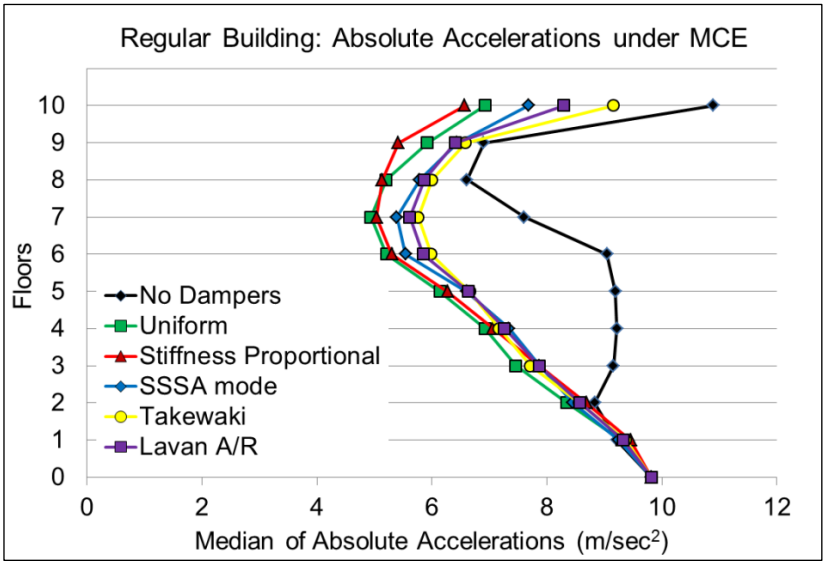

Figure 6.35. Regular Building – Median of Absolute Accelerations under the MCE

Table 6.16 summarises the absolute accelerations values as the peak of all floors (calculated similarly to maximum interstorey drifts, Eq. 6.4). The maximum peak accelerations in the damped frames occur at the first floor and are within a narrow range of 6.17 m/sec^2 to 6.30 m/sec^2 under the DBE. Similar distributions and narrow range of maximum peak accelerations (9.25 m/sec^2 to 9.46 m/sec^2) are exhibited in the damped frame under the MCE. The maximum peak accelerations of the bare frame (at the roof) are reduced by an average of 30% under the DBE and 14% under the MCE with the added dampers (peak at the first floor).

Table 6.16. Regular Building - Maximum Absolute Accelerations

	DBE Ground Motion Suite	MCE Ground Motion Suite
	m/sec^2	m/sec^2
No Dampers	9.07	10.90
Uniform	6.20	9.30
Stiffness Proportional	6.30	9.46
SSSA Mode	6.17	9.25
Takewaki	6.25	9.37
Lavan A/R	6.22	9.33

In terms of overall distribution, the Uniform and Stiffness Proportional schemes are the most effective at reducing accelerations at floors 5-10. For example, under the MCE at the roof, Uniform achieves a 10% reduction and Stiffness Proportional a 14% reduction from the nearest advanced method, SSSA, which may be attributed to the standard methods apportioning large damping at the base and roof of the building.

6.3.3. Residual Drifts

The maximum residual peak interstorey drifts of the regular building are presented in Table 6.17. The building with added dampers experiences negligible residual interstorey drifts under the DBE (confirming linear building performance with dampers), but experiences large residual drifts in the bare frame, 0.42% at floor 6 (Figure 6.36). McCormick, Aburano, Ikenaga, and Nakashima (2008) recommend a permissible residual drift limit of less than 0.5%, based on realistic repair costs and human tolerance of drifts. The bare frame under the MCE (Figure 6.37) achieves peak residual drifts near 0.73% that, according to this

recommendation, would render the building economically unsalvageable after the earthquake. However, the addition of viscous dampers reduces the residual drifts to less than 0.15% for the standard placement methods and less than 0.05% for the advanced placement methods. Overall, the residual drifts confirm the design objective of elastic building performance with dampers in the DBE scenario (Immediate Occupancy) and slight inelastic building performance with dampers in the MCE scenario (Life Safety). It could be argued that the advanced schemes achieve close to an 'Immediate Occupancy' performance level under the MCE scenario.

Table 6.17. Regular Building - Residual Peak Interstorey Drifts

	DBE Ground Motion Suite	MCE Ground Motion Suite
	%	%
No Dampers	0.42 %	0.73%
Uniform	0 %	0.13%
Stiffness Proportional	0 %	0.13%
SSSA Mode	0 %	0.04%
Takewaki	0 %	0.02%
Lavan A/R	0 %	0.02%

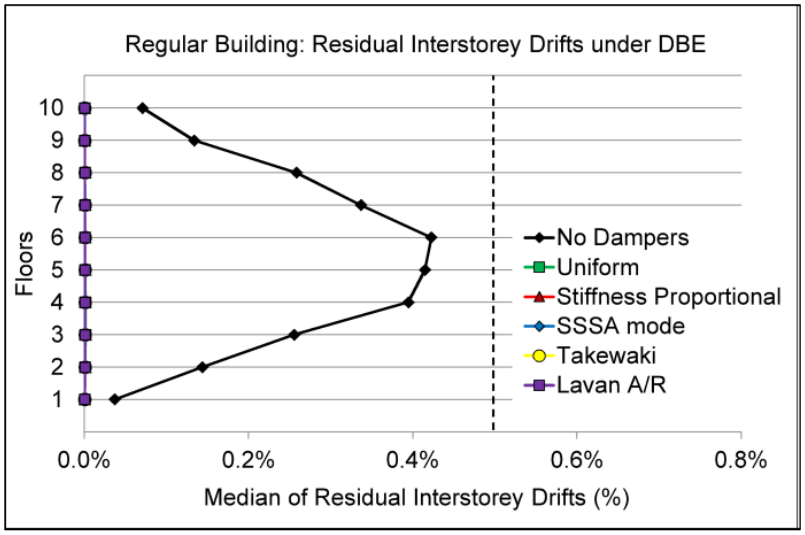

Figure 6.36. Regular Building – Median of Residual Interstorey Drifts under the DBE

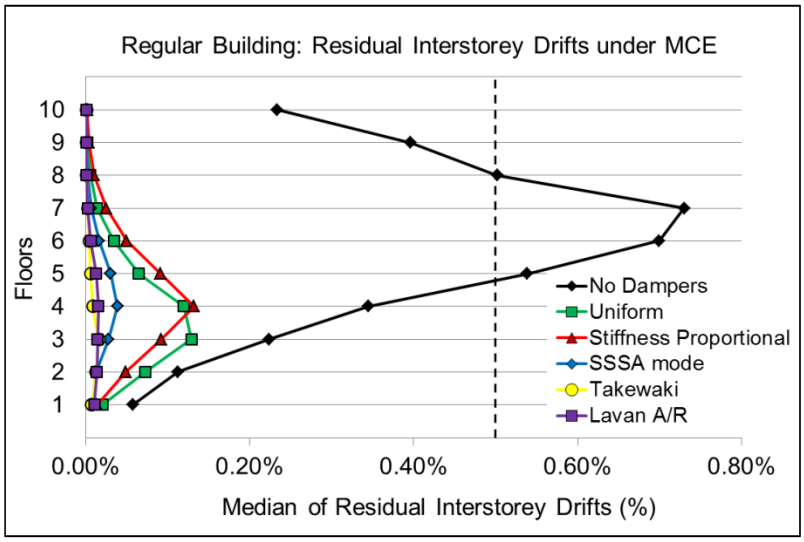

Figure 6.37. Regular Building – Median of Residual Interstorey Drifts under the MCE

6.4. Results and Discussion: Irregular Building

The irregular building performance with the various damper placement schemes is compared in terms of peak interstorey drifts, absolute accelerations, and residual interstorey drifts. All values presented are the median results of the twenty-ground motion suite, unless otherwise noted.

6.4.1. Peak Interstorey Drifts

Figure 6.38 compares the damper placement schemes in terms of median peak interstorey drift distribution under the DBE. The upper tower (floors 7-10) of the bare frame experiences larger drifts than designed, indicating the limitations of response spectrum design for vertical irregularities. All of the added damper schemes achieve less than 1.18% peak interstorey drift, thus meeting the design objective and reducing maximum drifts in the bare frame by 62% in the Uniform case (least reduction, at floor 3) and effectively damping the upper tower of the frame. The Lavan A/R method produces the most uniform drift distribution and the best reduction in the maximum interstorey drift (Table 6.18), more than a 10% improved reduction of the bare frame compared to the Uniform method, closely followed by the SSSA Mode and Takewaki schemes. Uniform damping produces the least uniform drift distributions.

Figure 6.39 compares the distributions under the MCE, where the dashed lines indicate the close correlation of the expected MCE drifts (DBE drift increased by 50%) and achieved MCE drifts. The bare frame produces unrealistic upper-storey interstorey drifts that would be expected to cause collapse, but the damped frame meets the design objective of 1.77% peak drift for every placement configuration. The Uniform scheme very closely meets the design objective, followed secondly by the Stiffness Proportional scheme, which achieves a 10% reduction of the Uniform method peak drifts (Table 6.18). The advanced methods for the irregular building achieve a maximum interstorey drift of all floors ranging from 1.25% to 1.40%, substantially smaller than the drift design objective of 1.77%. In fact, in both buildings, the advanced techniques reduce the drift beyond the design objective. For example, in the best case, the Lavan A/R method reduces the maximum interstorey drift by 21% of the original design objective for the regular building under DBE and MCE and by 29% for the irregular under DBE and MCE.

Unlike the regular building, the Takewaki method is less effective than the SSSA Mode method for reducing the maximum peak interstorey drifts, by more than 5% under the DBE and MCE. However, Takewaki best minimises the sum of the interstorey drifts. This is correlated to meeting its objective function of minimising the sum of the interstorey drifts of the transfer function.

Table 6.18. Irregular Building – Maximum of Peak Interstorey Drifts

	DBE Ground Motion Suite $\delta_{DBE,\ bare}$ = 2.47% $\delta_{DBE,\ dampers}$ = 1.18%	MCE Ground Motion Suite $\delta_{MCE,\ bare}$ = 3.71% $\delta_{MCE,\ dampers}$ = 1.77%
	% (mm)	% (mm)
No Dampers	3.05% (97.5)	5.22% (167.0)
Uniform	1.16% (37.2)	1.75% (55.9)
Stiffness Proportional	1.05% (33.7)	1.58% (50.5)
SSSA Mode	0.88% (28.2)	1.31% (42.0)
Takewaki	0.93% (29.8)	1.40% (44.8)
Lavan A/R	0.84% (26.9)	1.25% (40.0)

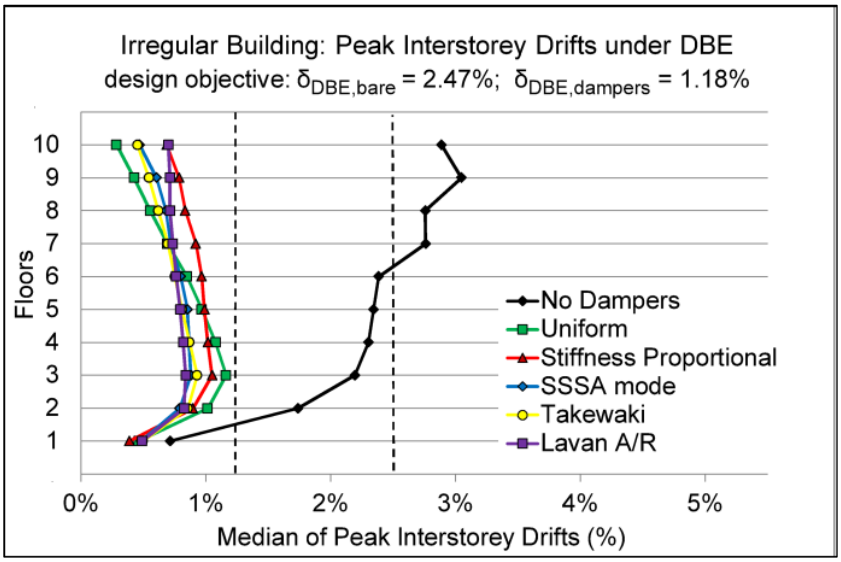

Figure 6.38. Irregular Building – Median of Peak Interstorey Drifts under the DBE

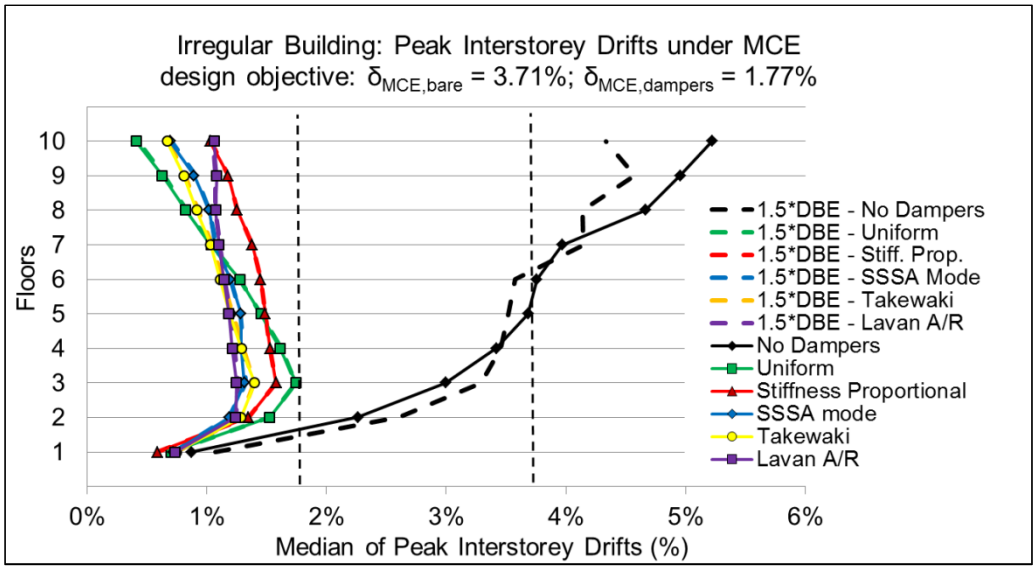

Figure 6.39. Irregular Building – Median of Peak Interstorey Drifts under the MCE

The statistical mean of peak interstorey drifts for the irregular building is displayed in Figure 6.40 and Figure 6.41. The mean drifts of the bare frame accentuate the dispersion and unrealistic drifts in the upper half of the frame, and it can be concluded that the bare frame has inadequate performance under both hazard levels. The dispersion of mean drifts under the DBE and MCE for each damper placement scheme is similar at each floor, apart from the very small standard deviations of the Uniform method at the upper floors. Maximum standard deviation occurs with the Uniform method, 0.33% and 0.51%, under the DBE and MCE, respectively. The dispersion of drifts with added dampers is greater under the MCE than the

DBE by an average of 70% for the maximum standard deviations. Evaluating the design drift objective as the mean plus one standard deviation for both hazard scenarios reveals that only the Lavan A/R method meets this drift limit for the irregular building under the DBE scenario. Note that the *median* of peak interstorey drifts has been selected as the primary drift performance indicator in this research.

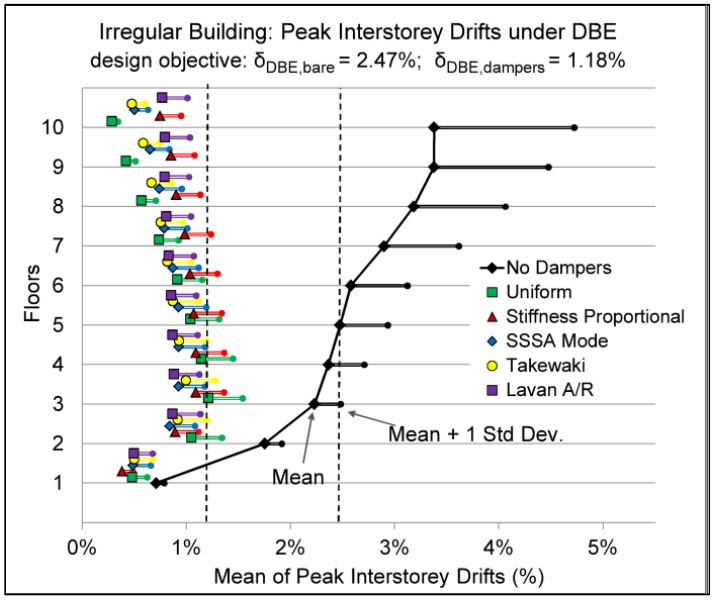

Figure 6.40. Irregular Building – Mean and Standard Deviation of Peak Interstorey Drifts – DBE

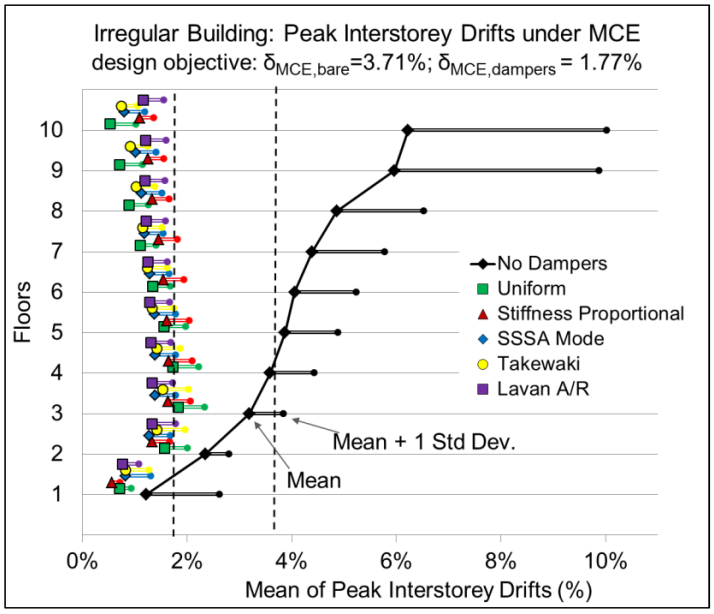

Figure 6.41. Irregular Building – Mean and Standard Deviation of Peak Interstorey Drifts – MCE

Figure 6.42 and Figure 6.43 illustrate the peak interstorey drifts of the irregular building for each ground motion of the DBE and MCE ground motion suite, where the dotted lines

indicate the drift design objective (i.e. 1.18% drift with dampers for the DBE). Peak drifts occur at different floors for each ground motion. Under the DBE and MCE, the Lavan A/R method is generally the best at reducing the peak interstorey drifts, followed by SSSA Mode, Takewaki, Stiffness Proportional, and lastly, the Uniform method. A typical profile of drift distributions is presented in Figure 6.44 under GM 7. Unlike the regular building, SSSA Mode consistently achieves slightly reduced peak interstorey drifts than the Takewaki distribution. While the design objective is achieved when considering a median of interstorey drifts, Figure 6.42 and Figure 6.43 highlight the range of drifts within the ground motion suite.

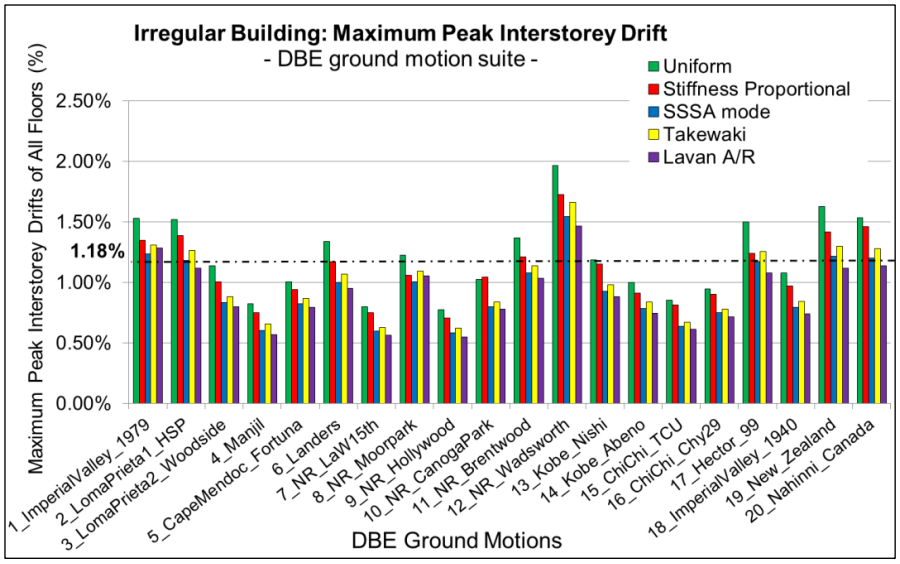

Figure 6.42. Irregular Building - Peak Interstorey Drifts for DBE Ground Motions

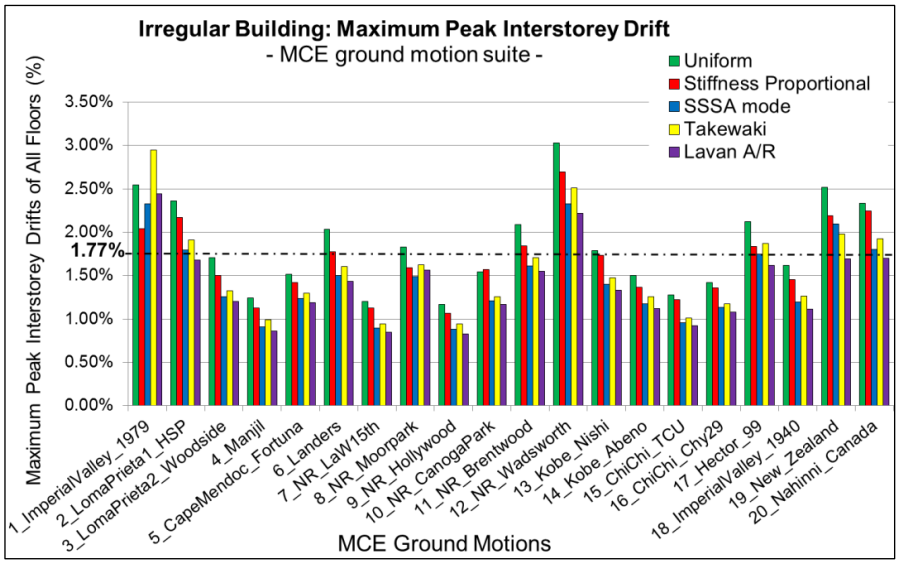

Figure 6.43. Irregular Building - Peak Interstorey Drifts for MCE Ground Motions

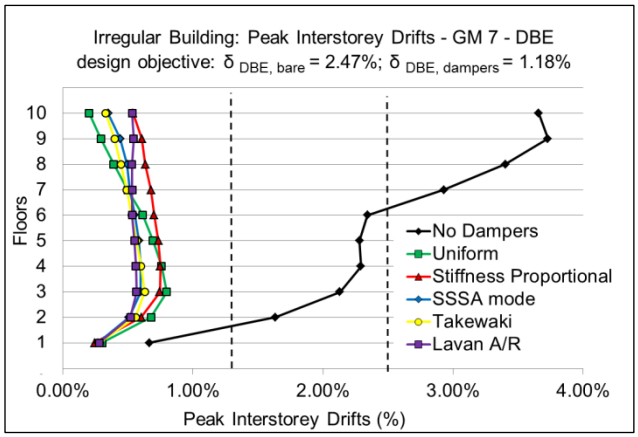

Figure 6.44. Irregular Building – Peak Interstorey Drift Profiles – GM 7 – Typical Response

Linear estimates of the modal interstorey drift contributions of the irregular bare frame building were calculated following the same procedures used for the regular building, and are presented in Figure 6.45. Modes 1 through 6 combine to 95% of the modal participating mass ratio. GM 7 presents the typical drift profile example, while GM8, 10, 17 represent exceptions to the trend, as discussed in the following section.

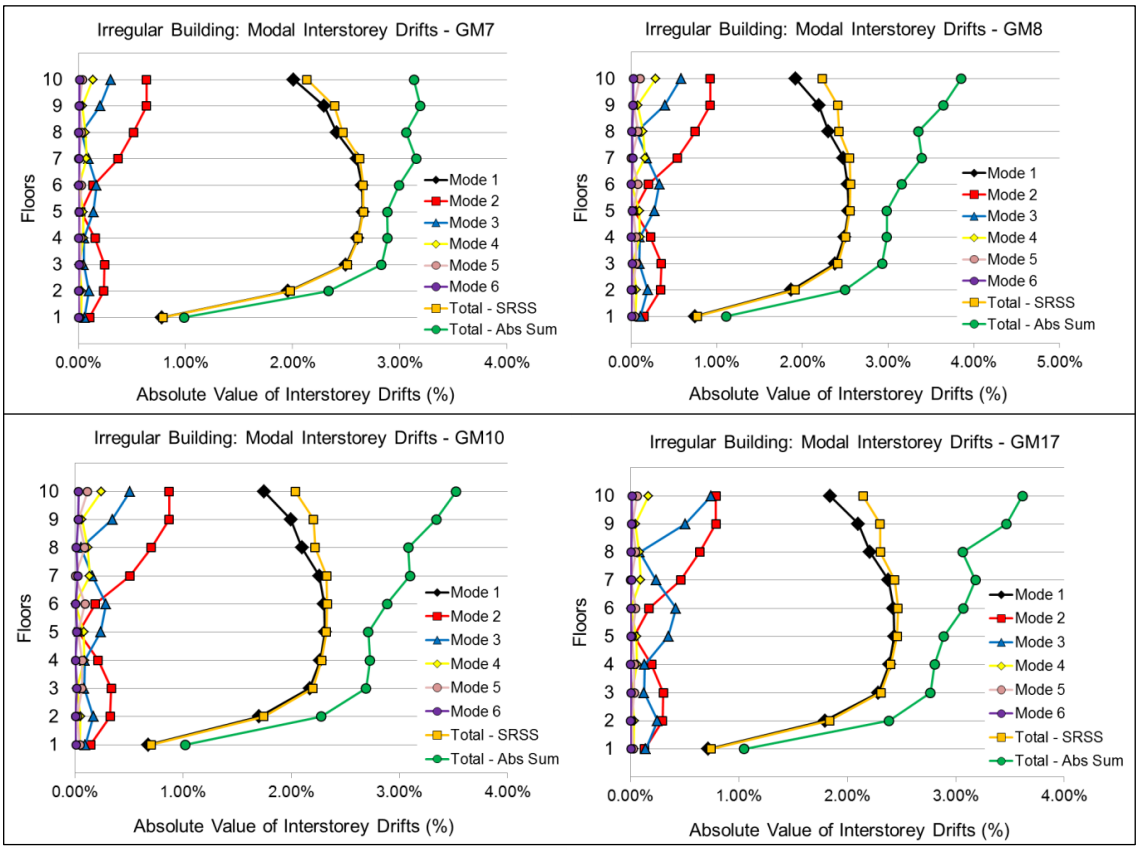

Figure 6.45. Modal Contribution to Interstorey Drifts of the Bare Frame – Irregular Building at DBE Scale – GM 7, 8, 10, 17

Returning to Figure 6.42 and Figure 6.43, exceptions to the typical trend of best to worst drift reduction amongst the damper distributions include GM 1, 8, 10, 17, and 19. Note that GM 8, 10, 17, and 19 were also exceptions to the trend for the regular building. The MCE results exhibit a wider variation in peak interstorey drifts. The SSSA Mode distribution performs better than Lavan A/R distribution under the DBE and MCE for GM 1 and GM 8. The drift profiles are very similar for both ground motions, and the profile for GM 8 is presented in Figure 6.46 (A) and (B), including the bare frame performance and a close-up of the damper distribution profiles. Under both ground motions, Lavan A/R overdamps floor 3 and under-damps floors 2, such that the SSSA Mode distribution yields the lowest maximum interstorey drifts. The Lavan A/R profile yields a distribution profile that differs from the first mode shape present in the other damper distribution profiles.

The spectral displacement curve for GM1 reveals equal first and second mode spectral displacements in the 5% damped frame, while GM 8 shows equal second and third mode spectral displacements in the 0% damped frame (Appendix A-5.4). This suggests higher mode effects in both ground motions for the irregular building. The Stiffness Proportional distribution performs better than the typical trend under GM 1 and 8, likely the result of effectively damping the lower half of the frame for these ground motions and thereby reducing the tendency for greater upper storey drifts. In addition, the Takewaki distribution achieves the worst reduction in drifts under GM 1 at MCE. Review of the drift profile and nonlinear building performance confirms the presence of plastic hinging at the base of the Takewaki damped frame, resulting in large first floor interstorey drifts similar to the behaviour seen in the regular building with SSSA Mode damping under GM 17 at MCE scale.

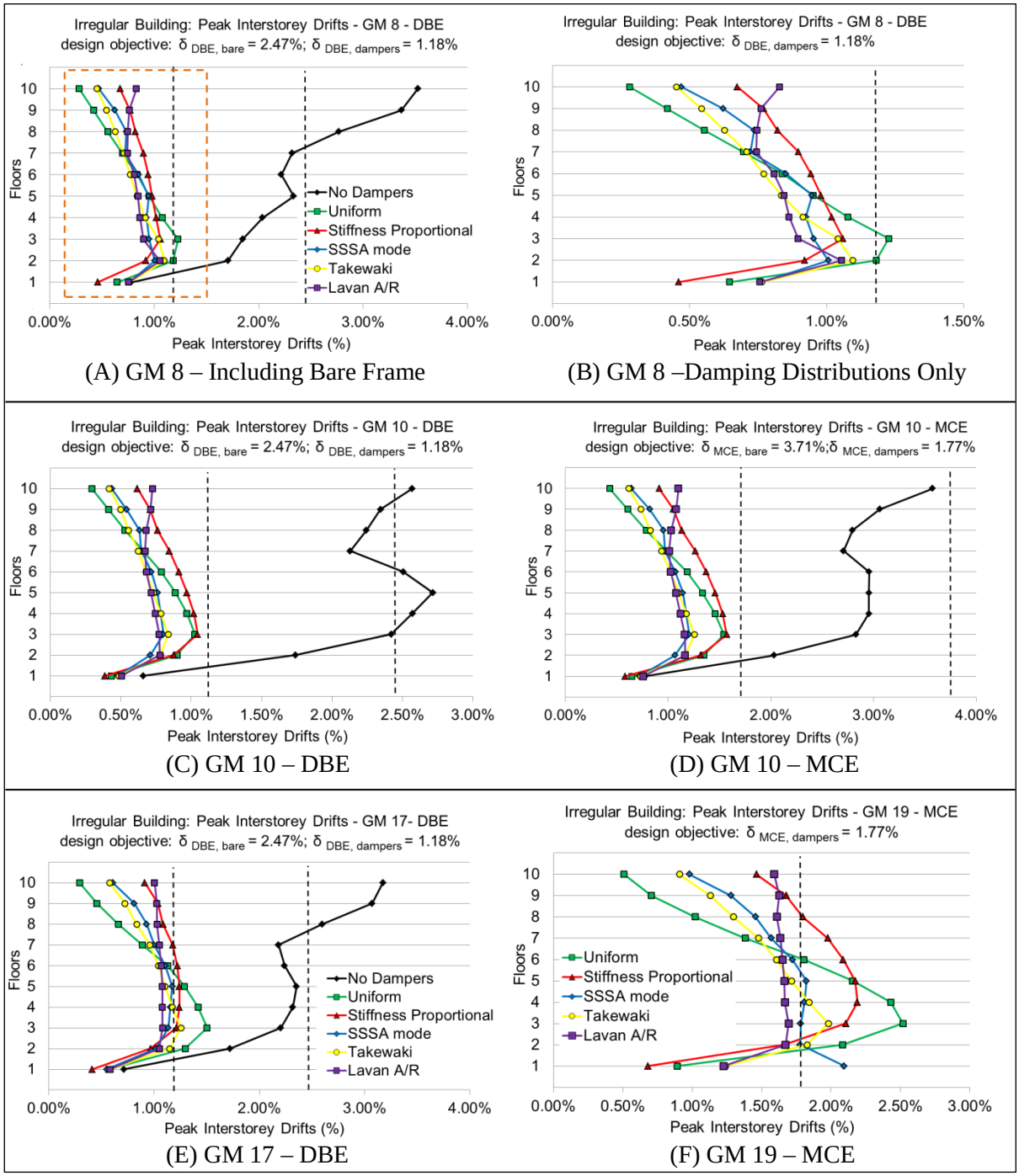

(A) GM 8 – Including Bare Frame

(B) GM 8 –Damping Distributions Only

(C) GM 10 – DBE

(D) GM 10 – MCE

(E) GM 17 – DBE

(F) GM 19 – MCE

Figure 6.46. Irregular Building – Peak Interstorey Drift Profiles – GM 8, 10, 17, 19

Another exception to the trend is the Uniform distribution performing marginally better than Stiffness Proportional distribution under GM 10 and both hazard levels (Figure 6.46(C) and (D)). The spectral displacement curve for GM 10 (Appendix A-5.4) and shape of the bare frame suggest higher mode contributions in the response, which yields an s-shaped profile more effectively damped by the uniform distribution than the typical first mode response.

The linear estimate of modal peak interstorey drifts (Figure 6.45) under GM10 confirms the S-shaped second mode and the increase in the total interstorey drift at the upper storeys caused by modes two and three. Just as under GM 1 and 8, the Lavan A/R distribution most closely resembles the shape of the bare frame profile. The last two exceptions are GM 17, where Stiffness Proportional performs better than the trend (Figure 6.46(E)) and modes two and three have a relatively larger contribution (Figure 6.45), and GM 19 under the MCE where Takewaki performs better than SSSA Mode (Figure 6.46(F)), due to the extreme first floor interstorey drift value of the SSSA Mode distribution. Note that the Lavan A/R distribution achieves a near-uniform damage distribution under the active ground motion (GM 19) as designed (Figure 6.46(F)).

Overall, the Takewaki distribution does not exhibit the same sensitivity to the higher mode effects as shown for the regular building. This is likely a result of damping existing at the roof for the Takewaki distribution and all other damping distributions. Note that the Lavan A/R distribution has the lowest amount of damping at the roof and occasionally responds in a drift profile reflecting the bare frame (i.e. potential higher mode response), unlike the other distribution profiles. This may be explained by the objective of the Lavan A/R method – to achieve a uniform drift distribution – and therefore its profile is likely to be affected by drifts varying from the active ground motion.

The bare frame and Lavan A/R distribution under the active ground motion scaled to the DBE is presented in Figure 6.47(A). The bare frame drift profile confirms that the Lavan A/R distribution is designed based on an active ground motion with a first mode response of increasing interstorey drifts with height. Similar to the regular building, if the damped frame undergoes ground motions prompting large variations in upper storey drifts, the Lavan A/R distribution is likely to reflect similar increases in upper storey drifts. However, in the

majority of ground motions investigated, the overall large drift reductions achieved by the Lavan A/R distribution provides a degree of safety against extreme maximum interstorey values such that the Lavan A/R is generally the most effective at reducing the maximum drift.

Similar to the regular building SSSA Mode distribution, the SSSA Mode damped frame for the irregular building reveals a design of reduced upper storey drifts, as seen in the very similar drift profiles of the SSSA Mode damped frames under linear analysis of the three artificial accelerograms (Acc1, Acc2, Acc3) scaled to the DBE in Figure 6.47(B). The bare frame performance under the artificial accelerograms scaled to the DBE cannot be assessed in terms of drift values (a limitation of using linear analysis not capturing true nonlinear behaviour). However, the drift profiles of the bare frame indicate that the SSSA Mode was designed considering bare frame drift profiles of increasing interstorey drifts per storey, with the exception of the reduced drift at floor 5 in accelerograms 1 and 3.

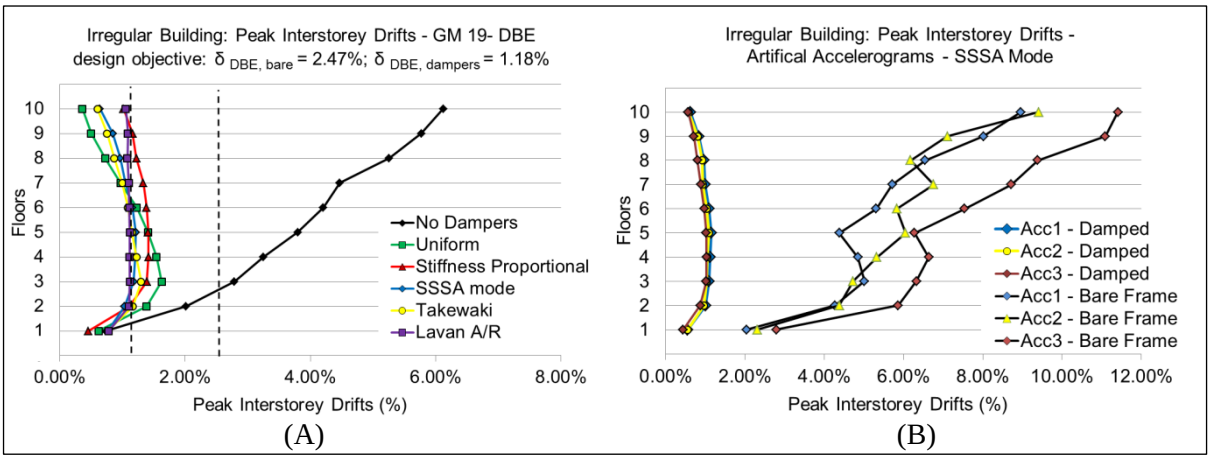

Figure 6.47. Irregular Building Design Drift Profiles – A) Lavan A/R and B) SSSA Mode

Finally, an example of the interstorey drift time history is presented for the irregular building. The drift profiles under GM 3 at MCE scale indicate that peak interstorey drifts occur at the third floor for the majority of the damped frames (Figure 6.48(A)). Thus, the third floor interstorey drift time histories are presented for each damping distribution compared to the bare frame drifts (Figure 6.48(B)-(F)). Peak interstorey floor drift for Uniform damping (1.71%) occurs near 4.3 seconds, while peak drifts of Stiffness Proportional (1.48%), SSSA

Mode (1.25%), Takewaki (1.32%), and Lavan A/R (1.20%), occur near 3.5 seconds. Note the residual drift in the bare frame is 0.45%, while there are negligible residual drifts in the damped frames for this particular ground motion.

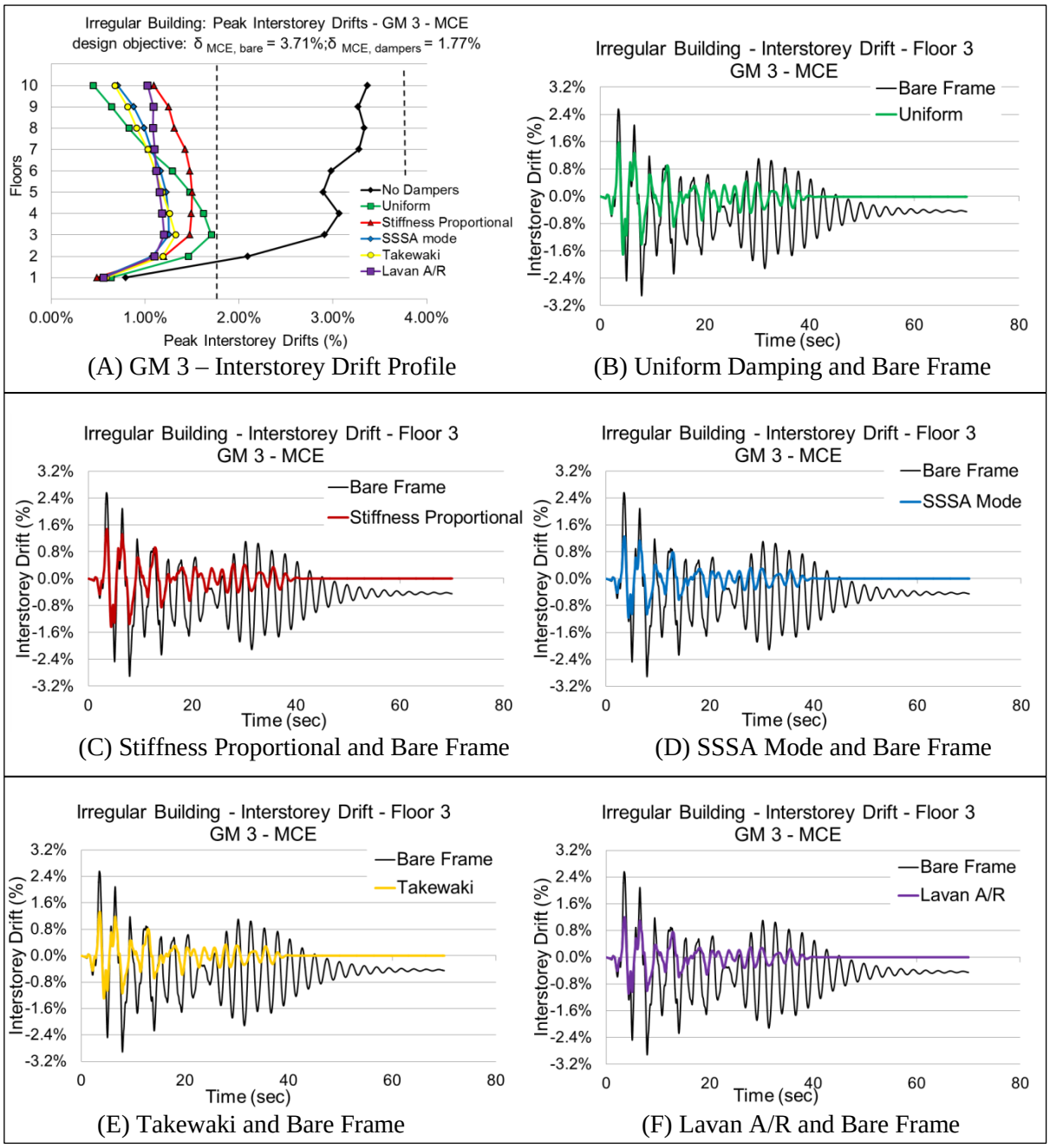

(A) GM 3 – Interstorey Drift Profile

(B) Uniform Damping and Bare Frame

(C) Stiffness Proportional and Bare Frame

(D) SSSA Mode and Bare Frame

(E) Takewaki and Bare Frame

(F) Lavan A/R and Bare Frame

Figure 6.48. Irregular Building – GM 3 - DBE
(A) Interstorey Drift Profile; (B) – (F) Interstorey Drift Time Histories at Floor 3

6.4.2. Absolute Accelerations

Figure 6.49 and Figure 6.50 compare the added damper placement techniques in terms of absolute accelerations of the irregular building under the DBE and MCE. Maximum absolute

accelerations are presented in Table 6.19. All the damper placement schemes reduce the acceleration at all floors except the 1st floor and produced similar maximum absolute accelerations within a small range of 5.40 m/sec^2 to 5.56 m/sec^2, occurring at the first floor. The large first floor accelerations are a product of the shared ground floor absolute accelerations (denoted as floor zero). Similar to the regular building, both the Uniform and Stiffness Proportional schemes result in the lowest overall acceleration distribution, likely attributed to the large damping at the base for both schemes, as compared to the advanced methods (damping is predominantly on floors 2-9). Similar results occurred under the MCE with maximum absolute accelerations of the damped building within a range of 8.11 m/sec^2 to 8.35 m/sec^2.

The acceleration distribution of the added damper schemes is very similar for both hazard scenarios. The MCE absolute accelerations generally fit the 50% increase scaling of the DBE results, which leads to more pronounced discrepancies at each floor between the added damper schemes under the MCE (larger differences due to the scale factor). Performance of the building with added dampers was only slighlty nonlinear (maximum drifts less than 1.77% under the MCE). This may explain why the addition of linear viscous dampers contributed forces that were out-of-phase with the maximum stressed state of the building, thereby not increasing maximum accelerations.

Table 6.19. Irregular Building - Maximum Absolute Accelerations

	DBE Ground Motion Suite	MCE Ground Motion Suite
	m/sec^2	m/sec^2
No Dampers	9.43	12.02
Uniform	5.40	8.11
Stiffness Proportional	5.50	8.25
SSSA Mode	5.56	8.35
Takewaki	5.49	8.23
Lavan A/R	5.52	8.29

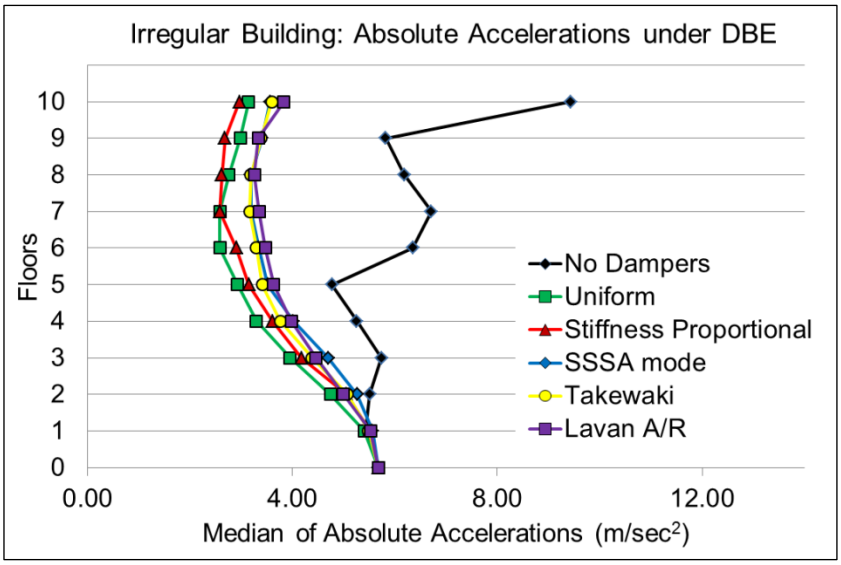

Figure 6.49. Irregular Building – Median of Absolute Accelerations under the DBE

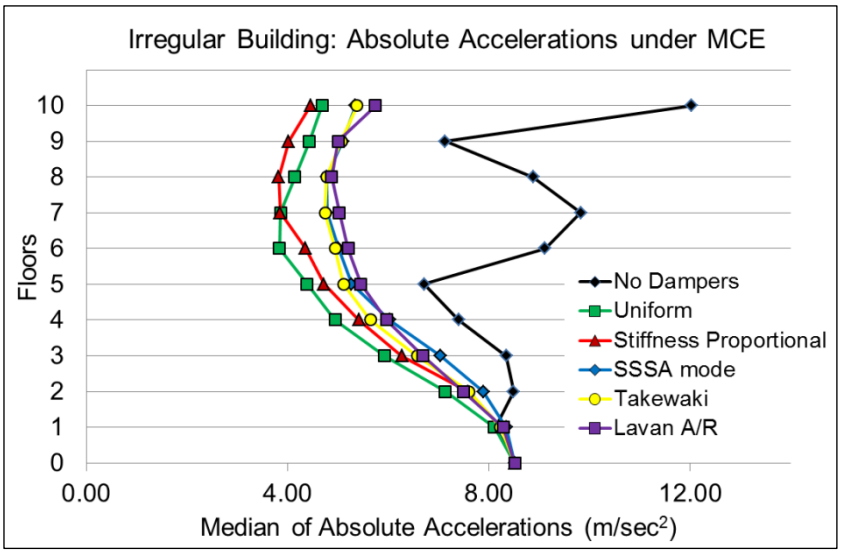

Figure 6.50. Irregular Building – Median of Absolute Accelerations under the MCE

An example of the total acceleration time history is presented for the irregular building. The acceleration profiles under the GM 3 at MCE scale indicate that the maximum absolute acceleration is best reduced at floor 4 for the Uniform damping distribution and floors 5 and 6 for the other damping distribution (Figure 6.51 (A)). The fourth floor total acceleration time histories are presented for each damping distribution compared to the bare frame drifts (Figure 6.51 (B)-(F)). Maximum accelerations occur for most distributions near 4.85 seconds, with the exception of the Uniform damping that produces the lowest maximum acceleration (3.04 m/s^2) at 4.2 seconds. Overall, the damping distributions slightly reduce the extreme

peak values of acceleration in the first ten seconds of the time history and yield very similar acceleration responses.

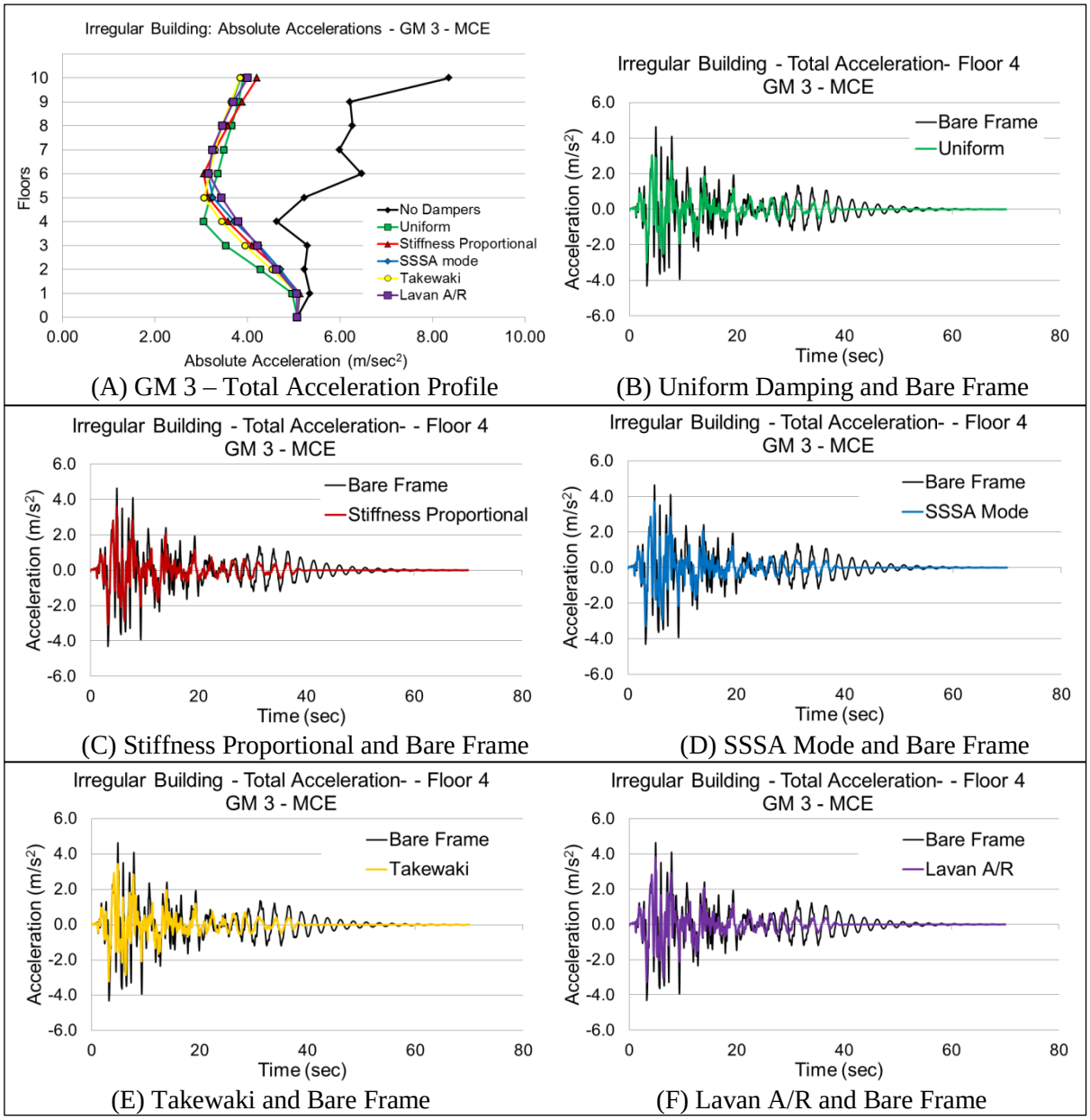

(A) GM 3 – Total Acceleration Profile (B) Uniform Damping and Bare Frame

(C) Stiffness Proportional and Bare Frame (D) SSSA Mode and Bare Frame

(E) Takewaki and Bare Frame (F) Lavan A/R and Bare Frame

Figure 6.51. Irregular Building – GM 3 MCE
(A) Total Acceleration Profile; (B) – (F) Total Acceleration Time Histories at Floor 4

6.4.3. Residual Drifts

The maximum residual peak interstorey drifts of the irregular building are presented in Table 6.20. The bare frame experiences a 0.46% maximum residual drift under the DBE, approaching the residual drift limit for economical repairs (McCormick et al. 2008) (Figure 6.52). The residual drifts under the MCE for the bare frame indicate unrealistic performance

and likely failure under the high hazard level (Figure 6.53). However, under both the DBE and MCE, the added damper placement methods produce negligible residual interstorey drifts.

Due to different ground motion scaling factors, the residual drift values of the regular and irregular buildings cannot be directly compared. For example, the larger residual drifts of the damped regular building compared to the damped irregular building under the MCE does not allow for conclusions about the damper schemes effectiveness in one building compared to the other. However, the overall distributions of performance indicators can be compared, both between the buildings and between the various damping distributions.

Table 6.20. Irregular Building - Residual Peak Interstorey Drifts

	DBE Ground Motion Suite	MCE Ground Motion Suite
	%	%
No Dampers	0.46%	1.81%
Uniform	0.02%	0.04%
Stiffness Proportional	0.02%	0.02%
SSSA Mode	0.02%	0.02%
Takewaki	0.02%	0.02%
Lavan A/R	0.02%	0.02%

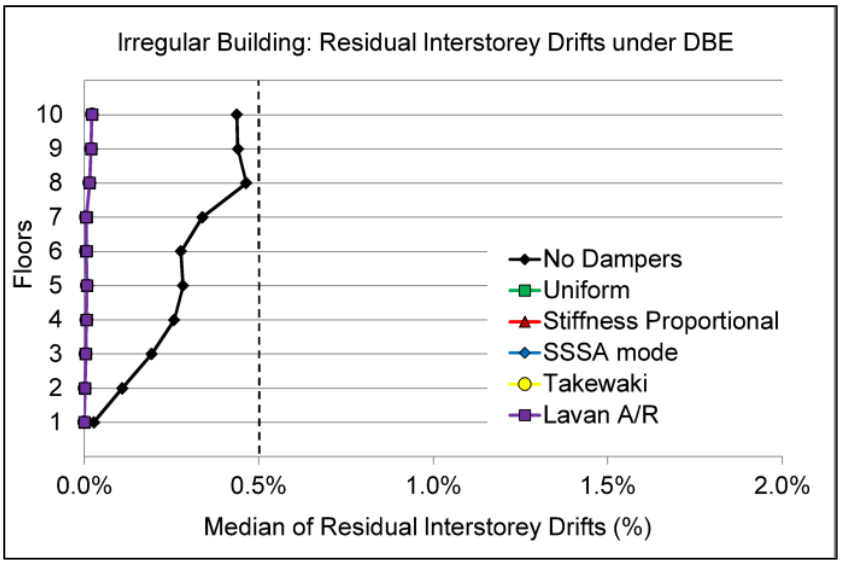

Figure 6.52. Irregular Building – Median of Residual Interstorey Drifts under the DBE

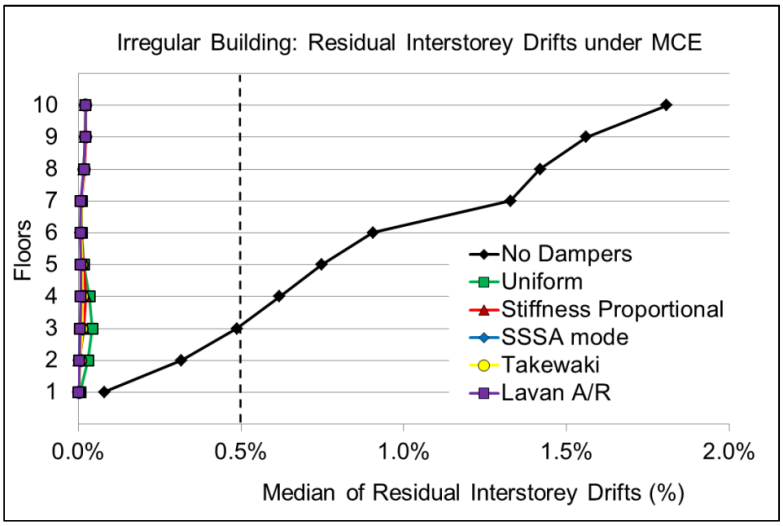

Figure 6.53. Irregular Building – Median of Residual Interstorey Drifts under the MCE

6.5. Results and Discussion: Usability of the Placement Methods

Observations about the usability of the placement methods are presented, based on adherence to the methods' procedures as outlined in literature. The Uniform and Stiffness Proportional methods are the simplest to apply while still achieving the desired drift limit. SSSA Mode is an easily-applied adaptation of the SSSA technique, allowing quicker application to a large number of ground motions. Despite this, SSSA Mode is the most time consuming method because it requires twenty steps for three ground motions (i.e. sixty linear time history analyses). The Takewaki technique is also time-intensive, as it requires creation and iterative application of a programming script. However, once programmed, the method is reasonably efficient, requiring only minimal inputs and operating independently from ground motions. Selection of the correct step-size greatly influences convergence time, and no stringent guidelines for selecting step-size are provided. The Lavan A/R technique is the easiest to implement from scratch, of all three advanced techniques. While it depends on an iterative analysis with specific ground motions, this can be conducted with the same tools used for the SSSA Mode or Takewaki methods and requires fewer ground motions and steps than either method. For both examples presented, convergence occurred in less than 10 iterations.

The Takewaki method, although attractive because of its independence from the ground motion characteristics, is difficult to interpret in a physical sense. In addition, convergence of

the optimal solution is not guaranteed, such as was seen in the variable stiffness frame (1) in Chapter 5. Recent improvements of the Takewaki method have been made to consider peak interstorey drift, as opposed to the sum of peak interstorey drift, as the objective function (Fujita, Yamamoto, & Takewaki 2010), and were not included in this research due to publication in the latter stages of this research project. Although the 2010 Takewaki approach is an improvement of the method, the limitations of the method in terms of complexity of application still apply. On the other hand, the Lavan A/R and SSSA Mode methodologies are more transparent, and the approach towards the optimal solution can be seen in each step, represented by a physical, understandable quantity.

The framework of the *2000 NEHRP Provisions* (BSSC 2001) and Whittaker et al. (2003) in conjunction with damper placement techniques that are not inherently performance-based (i.e. SSSA Mode or Takewaki) allow a final check that the design objectives in terms of drift or modal damping have been met. The ability to adequately employ and assess these techniques with performance-based criteria resolves one of the criticisms of these techniques.

6.6. Results and Discussion: Suggested Guidelines for Engineers

A future aim of supplemental damping placement research is the adoption of a particular method into structural engineering guidelines. Considering the comparable performance of the three advanced techniques compared to standard placement methods, an engineer is advised to select advanced techniques based on usability. The examples presented in this chapter support the Lavan A/R method as the most suitable candidate for recommendation because of its effective limitation of drifts (as per its objective function), familiar approach using fully-stressed analysis/redesign, time efficiency, and usability in application. However, thorough checks of the Lavan A/R distribution under multiple ground motions should be conducted because the method is based on selected active ground motions and has shown sensitivity to ground motions with higher mode effects.

The total damping used in this research uses a conservative uniform damping estimation based on first-mode response; this approach provides a level of safety of the Lavan A/R method against increases in floor drifts corresponding to variations from the active ground motions. Caution is advised when using a more economical reduced total damping to achieve the performance objectives in conjunction with few active ground motions.

In addition, results have suggested the risk of eliminating damping at the roof. Regardless of the advanced damper placement technique selected, adequate damping should be applied at the upper stories as reserve damping capacity for any unforeseen increases in upper storey drifts due to higher mode effects. This is particularly recommended when using the Takewaki method that may remove floor damping abruptly and absolutely. The damping distribution schemes indicate sensitivity to higher mode effects for roof damping less than 25% of the damping at the adjacent floor (i.e. Takewaki and Lavan A/R for the regular building and Lavan A/R for the irregular building, Table 6.13). Thus, it is recommended that adequate roof damping be greater than 50% of the adjacent floor damping. Use of three design accelerograms for the SSSA Mode method resulted in a damping distribution less noticeably affected by large roof drifts and higher mode effects; therefore, if SSSA Mode is employed, it is recommended that selected spectral-compatible accelerograms produce a diversity of bare frame drift profiles.

Because the uniform damping method is quickly and easily implemented, it is recommended that any selected advanced technique be compared against the uniform damping method for a variety of ground motion characteristics, to obtain additional confirmation of the advanced method's effectiveness. This comparison could be quickly conducted with a few nonlinear time history analyses and would provide some redundancy in the damping distribution selection. While not explicitly addressed in this research, selected ground motions should

possess frequency content to potentially excite higher modes in the structure as well as prompt a typical structural response. Simple power spectral density functions are suggested to obtain the major frequency components of ground motions to compare to the structure's natural frequencies; in addition, the modal contribution to interstorey drifts, as presented in this chapter, may be used to illustrate the linear modal contribution of major modes for a specific ground motion. Future work is needed to consider a stringent method for selecting the ground motions. A starting point would be employing the FEMA/SAC ground motion suite, which is standard design practice to cover a wide-range of ground motion characteristics for specific hazard levels (Somerville et al. 1997).

6.7. Conclusions

All of the damper placement methods achieve the desired drift objective for the regular and irregular buildings under the DBE and MCE, evaluated by the median results of 20 ground motions. This indicates that the design performance level of Immediate Occupancy has been met with the dampers, regardless of the placement scheme. In addition, all five placement schemes further reduced the absolute accelerations and residual drifts as compared to the bare frames.

Peak absolute accelerations do not reveal large differences between the added damper schemes, apart from consistently smaller acceleration distributions in the upper floors for the standard placement methods. Residual drifts support the effectiveness of adding viscous damping to limit permanent deformation and suggest minor sensitivity of residual drifts to damper distributions.

Few ground motions excited higher mode effects in the Takewaki and Lavan A/R damping distributions, a result of the minimal damping at the upper floors in both methods. This leads to the design recommendation that minimal or zero roof damping should be employed with caution. Adequate roof damping is suggested as 50% of the adjacent floor damping. Further

work is needed to evaluate if the additional roof damping combined with advanced placement schemes yield effective performance and protection against amplifications in roof drift. SSSA Mode is proposed as a more time efficient, usable adaption of the SSSA method, and strategic selection of the three design accelerograms directly influences the robustness of the SSSA Mode distribution.

Uniform and Stiffness Proportional, the simplest methods to implement, are shown to meet the design drift limits, yet do not achieve an optimal distribution of dampers in terms of best performance reduction or most uniform drift distributions. The three advanced methods show broadly comparable performance. The Lavan A/R technique achieves the best performance with the least complexity and time expended to achieve the damper distribution scheme. Neither the Takewaki nor SSSA Mode method is clearly more effective considering both building results, although the Takewaki damper distribution is achieved more quickly. Overall, the performance differences between the advanced techniques should not be exaggerated, as all three produced similar placement schemes and extremely similar drift and acceleration results.

While controlling the total added damping permits a fair comparison of the placement methods, less damping cost could be used to meet the drift performance objectives, especially for the advanced damper placement schemes, which achieved drifts much smaller than the design drift limit. Further research is needed to conduct thorough comparisons of the existing damper placement methods that consider both the optimal placement of dampers and reduction of total damping to meet specific performance criteria. In addition, investigation of a wider range of effective damping ratios and structural properties would provide additional insight into the efficiency and robustness of the damper placement methods.

Chapter 7

Performance of Structural Members in Supplementally Damped Frames

7.0. Introduction

Examination of the vertical damping distribution in Chapters 5 and 6 revealed that strategic damper placement reduces key performance parameters, and improved levels of performance may be achieved for advanced techniques. However, strategic damping distribution is irrelevant if the supporting structural members cannot sustain the damper reaction forces during seismic events.

Although the damper reaction forces of a fluid viscous damper are ideally out of phase with the peak frame forces (displacement and acceleration being out of phase with velocity), there remains a need to check the capacity of the structural members in the interim phase between peak displacement (maximum member forces) and zero displacement (maximum damper forces). In this phase, the lateral components of the damper reaction forces are additive to the seismic lateral forces. The damper reaction forces also contribute an axial load on the columns, additive to the constant gravity loads. Therefore, the lower storey columns become critical members collecting the axial force of the supported columns and dampers.

Most damper distribution studies avoid this capacity check by relying on the advantageous out-of-phase relationship between viscous dampers and the structural system. Nonetheless, a practical design issue with supplemental damping is the capacity of the structural system to accommodate large levels of damping and associated increased damper reaction forces (Hanson & Soong 2001). Interestingly, seismic retrofits with linear FVDs have shown an increase in the axial loading and sometimes overstressing of columns after added damping.

This chapter addresses the practical issue of structural member capacities with added supplemental dampers. A brief background reviews the influence of axial forces due to dampers and introduces brace arrangements for adding dampers. The impact of the damper reaction forces are assessed with a capacity check of the final stressed state of the structural members with added dampers. While controlling the vertical damping distribution, multiple brace-damper arrangements are explored to improve the load path of the damper reaction forces and reduce the axial load on the columns.

7.1. Background

In previous chapters a vertical damping distribution ('lumped' damping per floor) was investigated, using chevron braces to transfer to damper reaction forces to the frame. All brace-damper sets were placed in the central bay of the regular building and the left exterior bay of the irregular building. The following terms will be used throughout this chapter. Damping distribution refers to the vertical distribution of total damping per floor, while brace-damper arrangements refer to the horizontal distribution of damping in terms of bay location per floor. A review of the effect of dampers on column axial loading and the influence of brace-damper arrangements is presented in this section.

7.1.1. Axial Loading of the Columns

Supplemental devices in an MRF contribute damper reaction forces to the frame, particularly the axial force that must be resisted and transmitted through the columns (Constantinou & Symans 1993b). The horizontal component of the damper reaction force will be resisted by the lateral load-resisting system (i.e. columns constrained by the stiff floor slab), and represents a less-critical design concern (Lee, Ricles, & Sause 2009).

The last step of the performance-based supplemental design procedure (Kim & Choi 2006) is checking that the structural members can resist the axial and shear forces from the supplemental dampers. Investigations of damping distributions for ten- and twenty-storey steel MRFs with linear viscous dampers installed diagonally within interior bays showed an

increase in column axial force for all damping distributions (Figure 7.1) as well as a redistribution of member forces to columns connected to the dampers. The force redistribution may be the result of the added dampers reducing building response and decreasing exterior column loads (Kim & Choi 2006). In all cases, greater than 20% effective damping was added in the form of viscous or viscoelastic dampers.

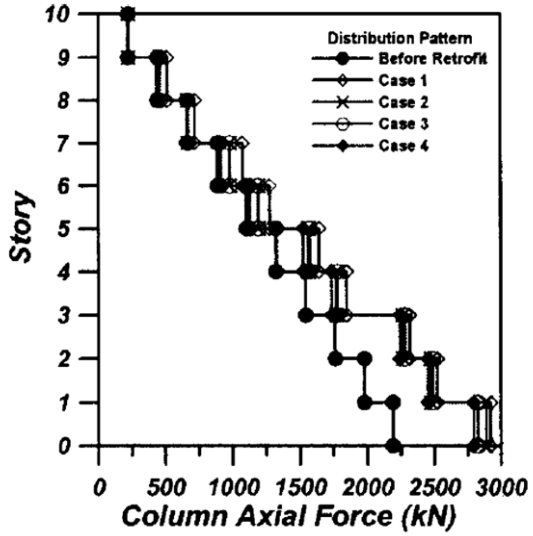

Figure 7.1. Peak Axial Forces of Interior Columns with Added Linear Viscous Dampers (Kim & Choi 2006)

Constantinou and Symans (1993a) experimentally showed the out-of-phase behaviour of a linear fluid viscous damper and based on the results, claimed that column compression failure is not a critical concern with added linear FVDs. In contrast, a retrofit of a three-storey, pre-Northridge, steel MRF building with linear FVDs (at a 40% effective damping ratio) caused substantial increases in column axial forces and base shear, which would require re-strengthening of the base columns (Uriz & Whittaker 2001).

This may be explained by two factors. Although the maximum force of the linear FVD is out of phase with the structure's peak drift, both forces are additive during the interim phase between peak drift and peak velocity. Secondly, the axial forces from the damper add to the static seismic gravity loads. Considering the axial-buckling-bending interactions in column members with large added damping, the axial loads from the dampers combined with the

static loads and bending moments during seismic events may overstress the columns, regardless of the out-of-phase damper and structure relationship.

Lee et al. (2009) investigated the performance of six-storey steel MRFs with elastomeric dampers in chevron braces (Figure 7.2). Axial forces as a result of the added dampers were found to overstress the ground floor columns in two of the MRFs, while an outer MRF with internal pinned beam-column connections greatly reduced the axial loads and permitted smaller ground floor columns. Note that the elastomeric dampers, unlike the FVDs, contribute a stiffness to the structure, and hence, are not out-of-phase with the structural system.

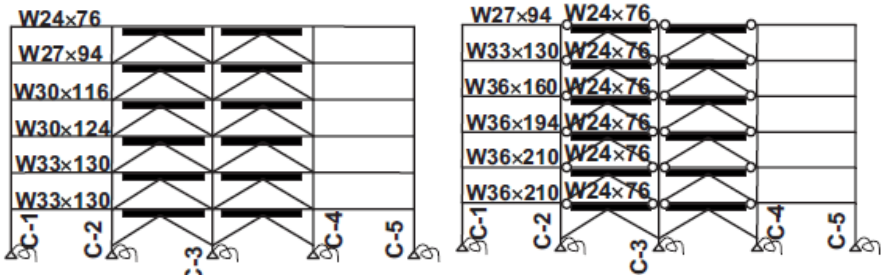

Figure 7.2. Steel Frames with Elastomeric Dampers – Rigid and Pinned Interior Columns (Lee et al. 2009)

The damper reaction force contributes loading to the structural members, whether that loading is out-of-phase, like the FVDs, or not of out-of-phase, like dissipative devices with stiffness components. A few case studies have shown that even with linear FVDs, ground storey columns may experience increased peak axial loads (Kim & Choi 2006) or overstressing (Uriz & Whittaker 2001) when damping ratios are greater than 20% of critical.

7.1.2. Brace-Damper Arrangements

Since brace-damper arrangements control the load path of the damper reaction forces, they may be used to re-route axial forces and reduce the axial loads on critical columns. Both common and innovative brace arrangements are presented for a variety of dissipative devices. Although a conventional approach is to restrict the brace-damper set to only interior or exterior columns (Figure 7.3), Apostolakis and Dargush (2010) found that for friction dampers and buckling-restrained braces installed in steel MRFs, a combination of interior and

exterior columns produced the best structural performance (Figure 7.4). Pekcan, Mander, and Chen (1999) recommend that energy dissipation devices with braces be placed within interior, pinned frames to produce a moment frame-truss configuration and to take advantage of the reserve axial capacity of the interior gravity columns. However, this is not necessarily the case for an *interior* moment-resisting frame, such as the building examples in Chapter 6, where the interior columns carry both bending and axial loads as well as a larger portion of the static gravity loads based on tributary area. Thus, they are not likely to have greater reserve axial capacity than the exterior frames.

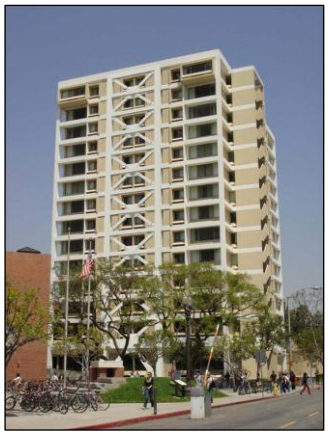

Figure 7.3. Interior Bay Brace-Damper Arrangement with Energy-Dissipating Braces (Islam, Skokan, & Huang 2010)

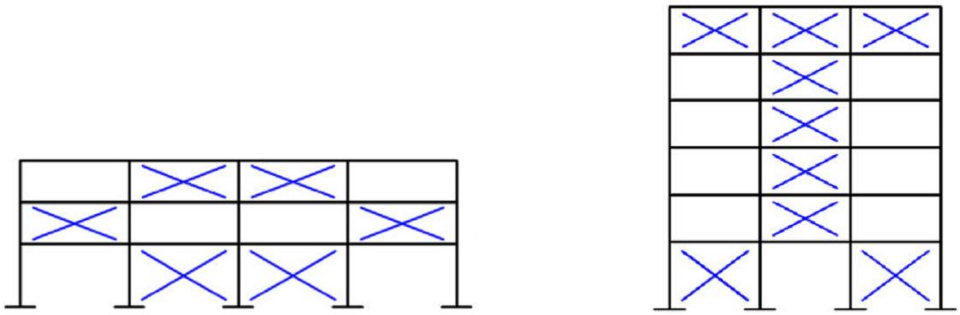

Figure 7.4. Optimal Arrangements of Friction Dampers and Braces (left) and BRBs (right) (Apostolakis & Dargush 2010)

Mezzi (2010) suggests conventional and innovative bracing arrangements for energy-dissipating braces and compares them in terms of interstorey drifts, column bending moments, and column axial loads of an 18-storey reinforced-concrete frame (Figure 7.5). The R1, R2, and R3 bracing arrangements represent random brace locations based on architectural and construction limitations. Two energy-dissipating braces per floor were used in the numerical

analysis and were constrained in terms of yield force per floor for each brace arrangement (Mezzi 2010). Decreased column bending moments occurred in the arrangement of braces directly connected (such as IN, XD, and SP). The SP brace arrangement produced the smallest axial forces of the non-random arrangements (Mezzi 2010).

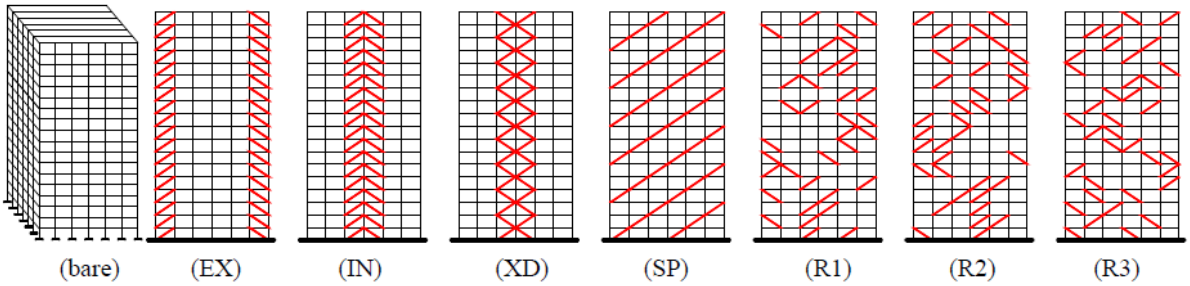

Figure 7.5. Tested Bracing Arrangements of the Perimeter Concrete Frame (Mezzi 2010)

An example of the chevron-braced frame and damper typology used in this thesis is a concrete frame retrofit with fluid viscous dampers in Palo Alto, California (Islam 2001). Figure 7.6 illustrates the schematic of brace-damper arrangements in the exterior bays and a photograph of the installed brace with dampers.

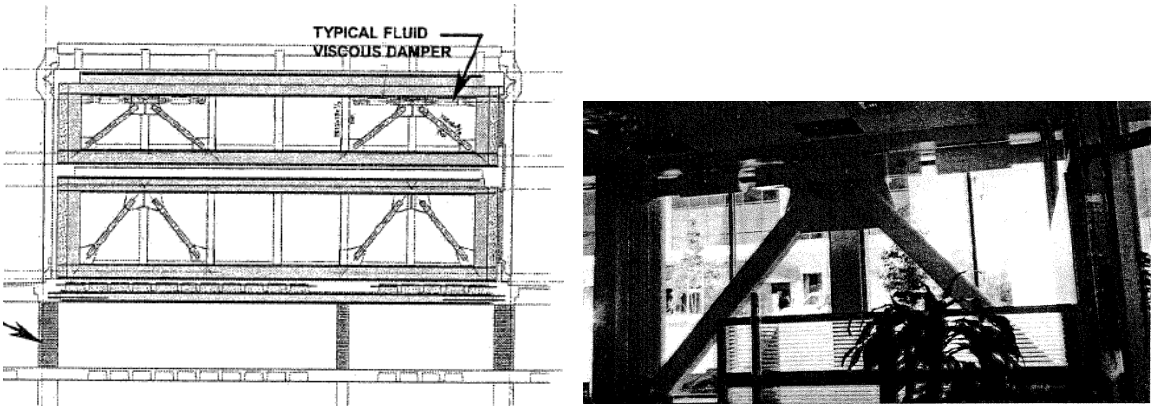

Figure 7.6. FVD and Brace Arrangement - East Frame of Palo Alto Retrofit (Islam 2001)

7.2. Methodology

The methodology includes the damper retrofit scenario, a description of the five brace-damper arrangements, selected ground motions, time history analyses, and the demand/capacity check of structural members.

7.2.1. Damper Retrofit Scenario and Reaction Forces

A retrofit scenario of the regular building design with uniform damping under the design-based earthquake (DBE) was selected. Uniform damping is both a standard distribution and a

worst-case example, in terms of peak damper reaction forces, from amongst the distributions explored in Chapter 6. The uniformly damped regular building performs linearly (without plastic hinging) under the DBE. The damper typology of chevron braces with horizontal FVDs was employed. The pinned braces transfer the damper reaction forces to the columns and have been designed as artificial braces with low-mass, high-stiffness (see Chapter 6). Further design and capacity checks of the braces is beyond the scope of this research. The load combination considered is the same seismic load combination ($G + 0.3Q \pm E$) as used in Chapter 6, based on the full dead load G, partial live load Q, and earthquake load E, applied with time history analysis.

Figure 7.7 illustrates the load path of damper forces in a single bay, in terms of a single damper reaction force (F_D) in one direction of motion. For simplification, this diagram assumes pinned column and beam joints. Damper reaction forces are transferred through the braces in compression (black) and tension (red), and they are resolved into the axial force on columns and the lateral force, producing a bending moment on column members. F_B is the force in the brace. Note that the forces at the beam-column connection represent the damper force (transferred by the brace) and its vertical and horizontal components (dashed arrows) acting on the column. The angle of the chevron brace θ is 38.6 degrees using a damper installation height of 3.19 m and half-bay width of 4 m. As expected, the lateral component on the column is the total damper force F_D, and the axial component of the damper force on the column is $F_D \tan\theta$. The lateral damper reaction forces are resisted by the four columns per floor restrained by the concrete slab diaphragm, while the axial loads from the damper reaction forces are resisted by the individual columns and follow the vertical load path to the base of the structure.

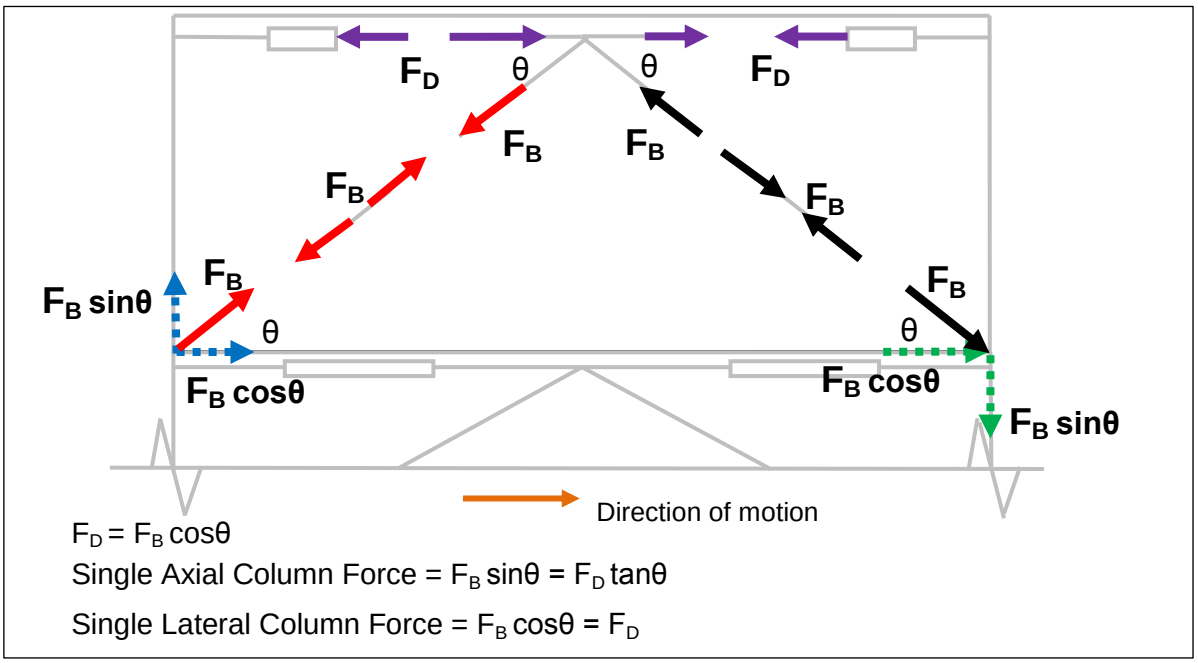

Figure 7.7. Load Path of Damper Reaction Forces in a Single Bay

7.2.2. Brace-damper Arrangements

Five brace-damper arrangements were created with different damper force load paths (Figure 7.8). Some resemble common arrangements or architectural constraints, such as restriction of brace-dampers to either interior or exterior bays (A1 and A5), while A2, A3, and A4 connect brace-damper columns at adjoining floors with a combination of exterior and interior bays. This concept showed promise in Apostolakis and Dargush (2009) and Mezzi (2010). The motivation for selecting A2, A3, and A4 is their potential to counteract the axial compressive force from the damper at one column with the tensile force from another damper at an adjoining floor, thereby reducing the axial loads on the interior columns (Figure 7.9). Figure 7.9 is a simplification of the load path of the damper reaction forces, considering only the damper forces' axial componens on the columns (see Figure 7.7). If all the axial reaction forces from dampers were equivalent, then each brace-damper arrangement could be assessed by the number of unbalanced axial forces collected in the base columns.

For example, for A4 in Figure 7.9, many of the interior column axial loads from dampers would be counteracted due to the brace-damper arrangement, resulting in one unbalanced axial load in each interior column and three unbalanced damper axial forces collected and

resisted by the exterior base columns. Figure 7.8 notes the unbalanced axial forces at the base columns for each arrangement, assuming one reaction force is from a damper with half the floor damping coefficient. However, while the column axial loads from the dampers may be similar at adjoining floors, the damper reaction forces will vary depending on the interstorey velocity at the installation floor, leaving a residual axial force even with force counteraction.

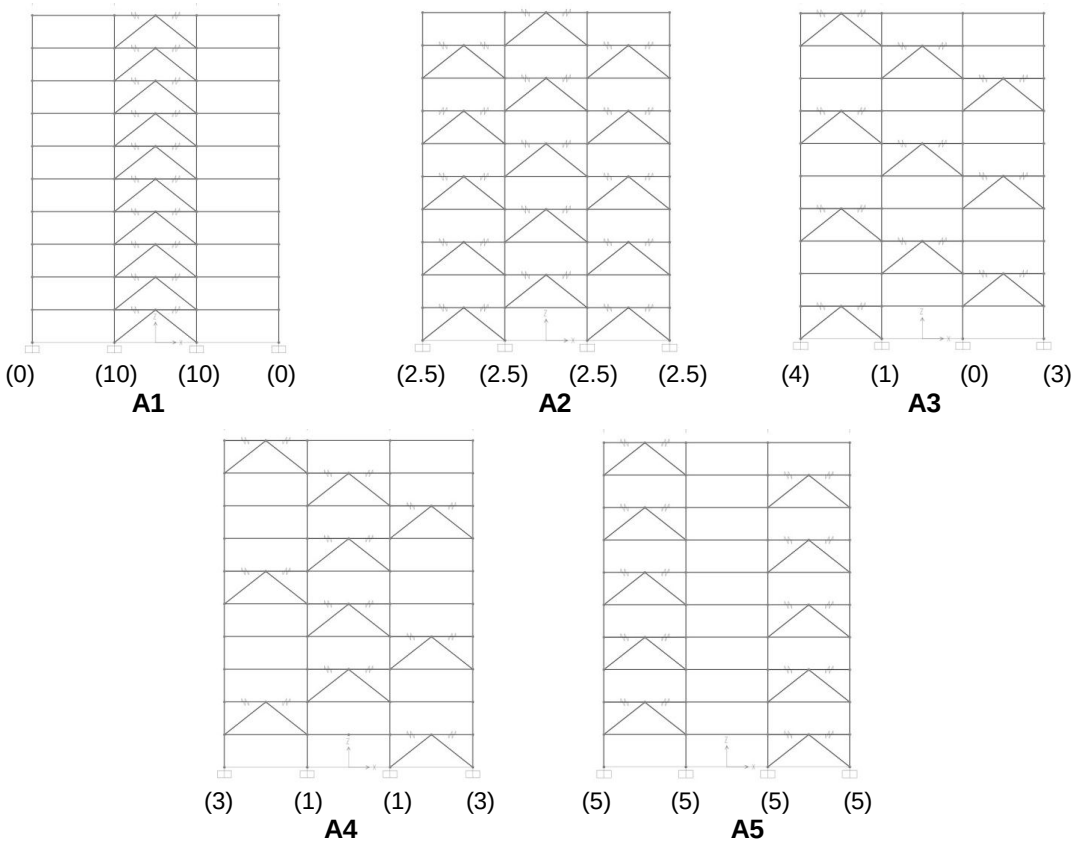

Figure 7.8. Brace-damper Arrangements

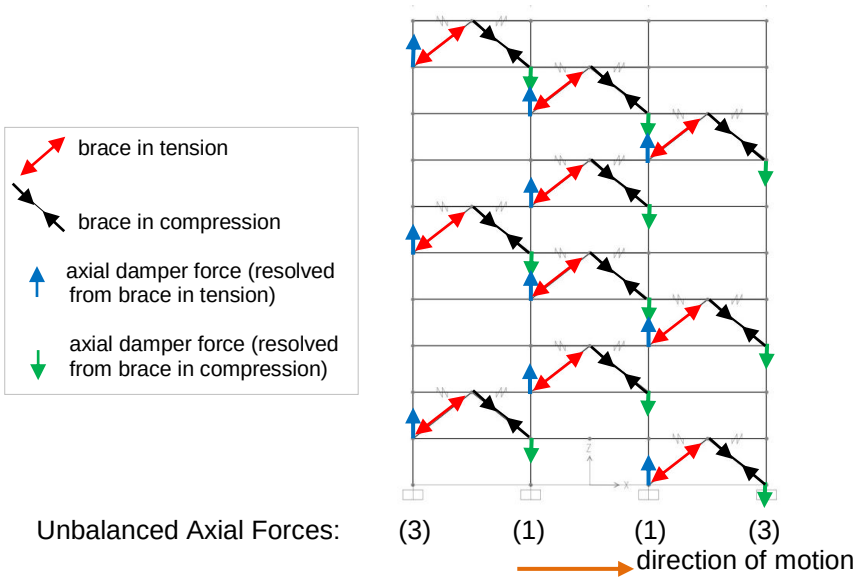

Figure 7.9. Axial Force Counteraction –Unbalanced Damper Reaction Axial Forces for A4

Descriptions of the arrangements and the associated load paths of the damper axial forces are presented in Table 7.1. Note that A1 is the original configuration used in Chapter 6. The assumption of a rigid floor diaphragm eliminates the potential of unsymmetrical brace-damper placement prompting y-axis rotations and torsion. Finally, the uniform damping distribution (81.2 kN-sec/cm per floor) is constrained in each brace-damper arrangement.

Table 7.1. Brace-damper Descriptions

Brace-damper Arrangement	Position	Objective	Load Path of Damper Reaction Axial Forces
A1	Central bay, original	Simplicity, keep dampers aligned and outer bays open	Interior columns resist the damper reaction forces (ten unbalanced damper reaction forces at ground interior columns).
A2	Triangular shape*	Distribute forces to interior and exterior columns	Interior dampers are twice the capacity of exterior dampers. Two and one-half unbalanced damper forces (at 81.2 kN-sec/cm each) in exterior and interior ground columns.
A3	Diagonals	Counteract interior damper forces	Four unbalanced damper forces in left exterior column, three unbalanced in right column, one unbalanced force at interior column. Similar to Mezzi (2010) SP pattern.
A4	Alternating diagonals	Counteract interior damper forces	Single unbalanced force in both interior columns and three unbalanced in exterior columns.
A5	Outer bays	Architectural option of an open central bay with single brace-damper per floor	No force counteraction and five unbalanced damper forces in all base columns.

* Only arrangement including multiple brace-damper sets per floor.

7.2.3. Ground Motions

Two ground motions were selected and scaled to the DBE using the procedure in Chapters 6. The Imperial Valley 1979 ground motion (GM1) and the Manjil 1990 ground motion (GM4) represent average and low demands on the structure, respectively, based on the peak interstorey drifts of the uniformly damped building. The uniformly damped building experienced peak interstorey drifts of 1.01% under the Imperial Valley earthquake and 0.74% under the Manjil earthquake.

7.2.4. Time History Analysis

Nonlinear time history analysis was performed using SAP2000 with each ground motion on the damped frame with various brace arrangements. The nonlinear time history was

performed at the end of the nonlinear static load case, which includes the gravity loads (*G* and 0.3*Q*) and the self-weight of structural members. The time history analysis was applied with a 0.01 sec time step, a larger time step than that used in Chapter 6 to increase speed of the time history analysis and steel design check. Although a time step of 0.005 seconds is ideal for sampling all relevant frequencies (largest lateral mode is 18.5 Hz), additional analyses confirmed that the larger time step of 0.01 seconds yielded equivalent demand/capacity ratios for these frames. Nonlinearity and structural damping assumptions are the same as those used in Chapter 6.

7.2.5. Demand/Capacity Check of Structural Members

The SAP2000 steel member design tool (CSI 2009a) was employed to check the final stressed state of the structural members with added brace-damper arrangements. The step-by-step steel design tool performed design/capacity checks of the structural members at each time step of the nonlinear time history analysis and at three stations on each member. The capacity check includes the following three steps: calculation of factored forces of axial, flexural, and shear forces at each station for the design combination (the nonlinear ground motion time history), calculation of nominal strengths for shear, bending, tension, and compression (based on EC3), and calculation of demand/capacity ratios comparing the factored member forces to the nominal strengths (CSI 2009b). The largest demand/capacity ratios were presented for the members, and it is assumed that the maximum stressed state occurs at different times for each structural member.

The steel demand/capacity check is based on Eurocode 3-1 2005 with default parameters, including the partial factor for resistance of cross-sections γ_{M0} and the partial factor for resistance of members to instability γ_{M1} both equal to 1.1. The critical demand/capacity ratio for members is the bending-compression-buckling ratio (PMM), where Euler and lateral-torsional buckling is considered for columns, following the interaction equations in EC3 6.3.3(4) (BS EN 2005).

The PMM ratios are found to control over the shear demand/capacity ratios; therefore, methodology and results will be restricted to the PMM ratios. The methodology used by SAP2000 for calculating nominal member forces based on EC3 is presented in terms of the demand/capacity ratios for axial force, bending moments, and total combined forces.

7.2.5.1. Axial Force Demand/Capacity Ratios

As per EC3 (BS EN 2005), the axial design capacity of the columns is defined in terms of the axial compressive resistive force $N_{c,Rd}$, the axial tensile resistive force $N_{T,Rd}$, and the axial buckling resistive force $N_{b,Rd}$. Additional parameters include the cross-sectional area A, yield stress of steel f_y, net cross-sectional area A_{net} (equivalent to A for these design checks), and ultimate stress of steel f_u. The partial factor for resistance of cross-sections in tension to fracture γ_{M2} was selected as 1.25, as per EC3 defaults.

$$N_{c,Rd} = \frac{Af_y}{\gamma_{M0}} \tag{7.1}$$

$$N_{T,Rd} = \min\left(N_{c,Rd}, N_{u,Rd} = \frac{0.9A_{net}f_u}{\gamma_{M2}}\right) \tag{7.2}$$

$$N_{b,Rd} = \frac{\chi Af_y}{\gamma_{M1}} \tag{7.3}$$

The reduction factor for buckling resistance χ is calculated based on the elastic critical force N_{cr}, slenderness ratio $\bar{\lambda}$, and imperfection value Φ, selected from tables based on the member cross-section. Elastic critical force depends on the unbraced member length L_{cr}, and the force varies depending on the moment of inertia I, resulting in a strong-axis axial buckling resistance force $N_{b,Rd,strong}$ and weak-axis resistance force $N_{b,Rd,weak}$. Axial buckling is ignored if the slenderness ratio or design/capacity ratio of the critical force and the design axial force N_{SdDsgn} is less than prescribed limits:

$$\chi = f(\bar{\lambda}, \Phi) \tag{7.4}$$

$$\bar{\lambda} = \sqrt{\frac{Af_y}{N_{cr}}} \tag{7.5}$$

$$N_{cr} = \frac{\pi^2 EI}{L_{cr}^2} \tag{7.6}$$

Ignore axial buckling if: $\bar{\lambda} \leq 0.2$ or $\frac{N_{Sd\ Dsgn}}{N_{cr}} \leq 0.04$ (7.7)

The SAP2000 steel design check calculates the resistance force N_{Rd} as the minimum of the axial buckling, axial compression, and axial tension resistance forces. Finally, the total axial force ratio *PRatio* is the quotient of the design axial force N_{SdDsgn} and the minimum axial resistive force N_{Rd}:

$$N_{b,Rd,min} = \min(N_{b,Rd,strong}, N_{b,Rd,weak}) \tag{7.8}$$

$$N_{Rd} = \min(N_{b,Rd,min}, N_{c,Rd}, N_{T,Rd}) \tag{7.9}$$

$$PRatio = \frac{N_{Sd\ Dsgn}}{N_{Rd}} \tag{7.10}$$

7.2.5.2. Bending Moment Demand/Capacity Ratios

The bending capacity of columns is defined by EC3 in terms of the major bending moment resistance $M_{c,Rd}$ and the major bending buckling resistance moment $M_{b,Rd}$. The section modulus W_y is the plastic section modulus W_{pl} for class 1 and 2 sections and the elastic section modulus W_{el} for class 3 sections. The lateral-torsional buckling resistance factor χ_{LT} is based on the non-dimensional slenderness and imperfection factors, as described in EC3 – 6.3.2.

$$M_{c,Rd} = \frac{W_y f_y}{\gamma_{M0}} \tag{7.11}$$

$$M_{b,Rd} = \chi_{LT} W_y \frac{f_y}{\gamma_{M1}} \tag{7.12}$$

The bending moment ratio and buckling bending moment ratio are ratios of previously calculated resistance moments and the design major moment $M_{SdMajDsgn}$. The demand/capacity major moment ratio *MMajRatio* is the maximum of the bending moment ratio multiplied by the major design moment interaction factor k_{Major} and the bending buckling moment ratio multiplied by the major design moment interaction factor k_{LT} for lateral-torsional buckling.

$$MMajRatio = \max \left| \frac{\left(\frac{M_{SdMajDsgn}}{M_{c,RdMaj}}\right) * k_{Major}}{\left(\frac{M_{SdMajDsgn}}{M_{b,RdMaj}}\right) * k_{LT}} \right| \quad (7.13)$$

7.2.5.3. Total PMM Ratio

The demand/capacity ratio *PMM ratio* is the sum of the axial force demand/capacity ratio and the bending moment demand/capacity ratio. A PMM value greater than one will be used here to indicate overstressed members.

$$\text{PMM Ratio} = \text{PRatio} + \text{MMajRatio} <= 1 \quad (7.14)$$

A single HE800B column under ramped, cyclic loading was analysed and the demand/capacity assessed to confirm that the capacity check methodology used by SAP2000 corresponded with EC3 design standards.

7.2.5.4. Output Parameters

Important output parameters from the steel member check included the PMM ratios, the breakdown of PMM ratios (participation of axial, buckling, and bending components), axial forces from gravity loads only, peak interstorey drifts, maximum absolute accelerations, residual drifts, and hinge results, to confirm the state of plastic hinging. A schematic of the frame with PMM ratios and highlighted overstressed members was also plotted. Refer to Appendix A-10 for an example of the steel design check results as produced for each structural member.

7.2.5.5. Member Capacity and Hinge Activation

Upon initial analysis, it was observed that members yielded according to the PMM interaction equations without forming plastic hinges during the same nonlinear ground motion analysis. The difference between the plastic hinge definition and the member yielding interaction equations explains this discrepancy. The hinge definition is a property of the cross-section, while the PMM interaction is a property of the entire member, considering unbraced lengths. Hinges form upon yielding of the extreme fibre of the cross-section, which is based on the effective yield stress and combination of axial forces and bending moments (CSI 2011).

The formation of the PMM hinges for the columns is a deformation-controlled action defined by FEMA 356, Equation 5.2 (ASCE 2000), where the rotation at yield θ_y is a function of the total column length L, plastic section modulus W_{pl}, effective (expected) yield stress F_{ye}, axial force in member at target displacement P, and expected axial force P_{ye}, a function of the gross cross-sectional area A_g and effective yield stress.

$$\theta_y = \frac{W_{pl}F_{ye}L}{6EI}\left(1 - \frac{P}{P_{ye}}\right) \tag{7.15}$$

$$P_{ye} = A_g F_{ye} \tag{7.16}$$

The hinge definition for beams is equivalent to this equation, without the axial load component in parentheses. The design column moment must be less than or equal to the plastic moment capacity to perform without plastic hinging (ASCE 2000):

$$M_{CE} = 1.18W_{pl}F_{ye}\left(1 - \frac{P}{P_{ye}}\right) \leq W_{pl}F_{ye} \tag{7.17}$$

The example of a single HE800B was analysed under ramped cyclic loading to verify the yield rotation definition for the PMM hinges (a value of 0.0028 rads for the single column with 147 kN applied axial force). The PMM interaction equation used by the design tool is a more conservative representation of yielding, based on the actual yield stress value F_y, strength reduction factors γ_{M0}, γ_{M1}, γ_{M2} , and the consideration of global and lateral-torsional buckling effects. The effective yield stress of S355 steel is 3.792 x 10^8 N/m^2, while the actual yield stress is 3.55 x 10^8 N/m^2. Nonlinear structural performance in previous chapters has been defined by the presence of plastic hinging, a standard definition based on FEMA 356. However, the more conservative definition of nonlinear structural performance based on the PMM interaction equations from EC3 will be used in the following sections to denote overstressed members.

7.3. Results and Discussion

The results of the brace-damper arrangements include an overview of the overstressed members for each configuration (total PMM ratio), individual demand/capacity ratios for

axial forces and bending moments, and performance parameters, including drift and accelerations, of the structure with various brace-damper arrangements.

7.3.1. Overstressed Members

The column frame members of the bare MRF and an example of the PMM output are shown in Figure 7.10. The MRF is an interior frame, the same selected for design in Chapter 6. Ground and first floor columns were the only overstressed members, indicated by an exceedance of the demand/capacity (D/C) ratio limit of 1. Columns are assigned a number and letter, based on interior (I) or exterior (E) location in the frame. Table 7.2 and Table 7.3 display the PMM D/C ratios for the ground and first floor columns under GM1 and ground floor columns under GM4. The ground floor columns are the only members to yield under GM4. Red-highlighted PMM ratios designate overstressed columns. A critical parameter is the maximum PMM ratio, which indicates the most stressed column in the system considering both flexural and axial capacity. A lower maximum PMM ratio corresponds to a more desirable brace-damper arrangement. In addition, the PMM ratios under GM1 and GM4 are plotted in Figure 7.11 and Figure 7.12.

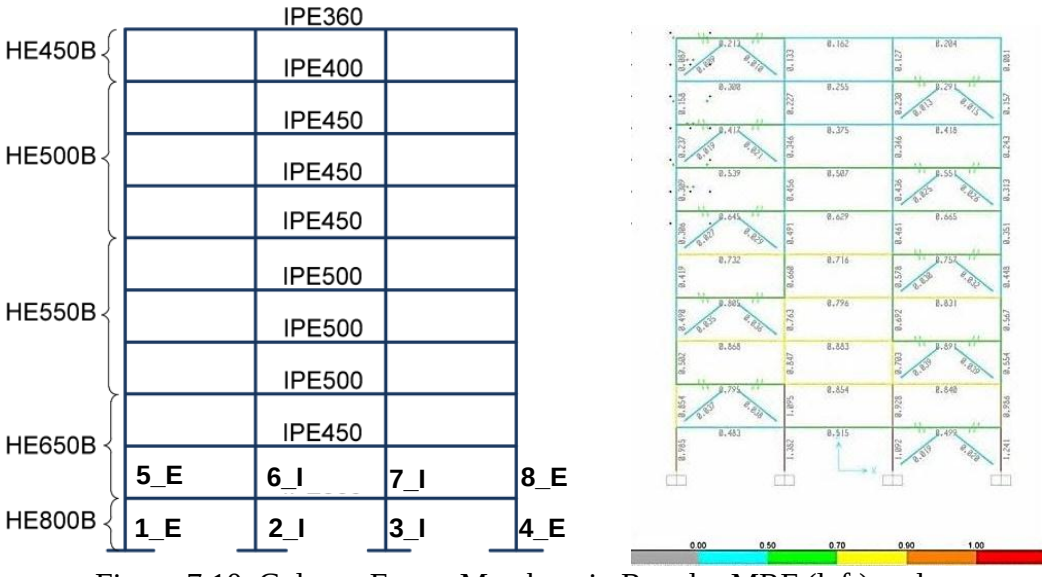

Figure 7.10. Column Frame Members in Regular MRF (left) and PMM Ratio Output for A5 under GM1 (right)

GM1 and GM4 produced PMM ratios similarly distributed amongst the five brace-damper arrangements. For example, arrangement 3 (A3) under both ground motions produces the

lowest value of the maximum PMM ratios, a 22% reduction of the maximum PMM ratio compared to A1 under GM1 and a 20% reduction under GM4. Arrangement 2 and 4 (A2, A4) have similar performance under the respective ground motions, and arrangement 1 (A1) yields the largest PMM ratio under both ground motions. Arrangement 5 (A5) performs better than A1 but worse than A2, A3, and A4 under both ground motions. A3 is the only configuration under GM1 where the maximum PMM ratio occurs at an exterior column. While A2 has the most uniform force distribution at the base (Figure 7.8), A3 achieves a lower maximum PMM value by shifting the loads from the interior columns, which carry greater gravity loads, to the exterior columns.

Table 7.2. Overstressed Columns under GM 1 (Imperial Valley 1979)

Frame Members	Column Location (Floor/Bay)	Brace-Damper Arrangements PMM Ratios, Overstressed (PMM > 1)				
		(A1)	(A2)	(A3)	(A4)	(A5)
1_E	Ground Exterior	0.94	0.88	0.92	0.92	1.01
2_I	Ground Interior	1.28	1.08	1.07	1.08	1.34
3_I	Ground Interior	1.54	1.31	1.09	1.29	1.12
4_E	Ground Exterior	0.97	1.07	1.21	1.07	1.22
5_E	First Exterior	0.77	0.75	0.79	0.83	0.74
6_I	First Interior	1.11	0.88	0.83	0.91	1.02
7_I	First Interior	1.31	0.99	0.89	1.03	0.89
8_E	First Exterior	0.78	0.86	0.98	0.98	0.91
	Maximum PMM Ratio =	1.54	1.31	1.21	1.29	1.34
	Std Dev (Ground Floor) =	0.28	0.18	0.12	0.15	0.14
	Std Dev (1st Floor) =	0.26	0.10	0.08	0.09	0.12
Percent Reduction from A1: Max PMM =		-	15%	22%	16%	13%

Table 7.3. Overstressed Columns under GM 4 (Manjil 1990)

Frame Members	Column Location (Floor/Bay)	Brace-Damper Arrangements PMM Ratios, Overstressed (PMM > 1)				
		(A1)	(A2)	(A3)	(A4)	(A5)
1_E	Ground Exterior	0.71	0.68	0.70	0.71	0.75
2_I	Ground Interior	1.02	0.89	0.84	0.87	0.99
3_I	Ground Interior	1.05	0.94	0.84	0.94	0.93
4_E	Ground Exterior	0.76	0.75	0.77	0.76	0.79
	Maximum PMM Ratio =	1.05	0.94	0.84	0.94	0.99
	Std Dev (1st Floor) =	0.18	0.12	0.07	0.11	0.11
Percent Reduction from A1: Max PMM =			10%	20%	10%	6%

Standard deviation measures the disparity between columm PMM ratios per floor. The arrangements most effective at minimising the maximum PMM ratio distribute the axial forces more uniformly to the columns, indicated by a lower standard deviation of the column PMM ratios per floor. This is the case under GM4, where similar standard deviations correspond with similar maximum PMM ratios for A2 and A4, and the minimum standard deviation corresponds to the lowest value for the maximum PMM ratio at A3. The correlation generally applies for GM1. This is not the case for the A5 ground floor columns, where A5 has the largest PMM ratio amongst A2, A3, A4, and A5, despite the second-lowest standard deviation under both ground motions.

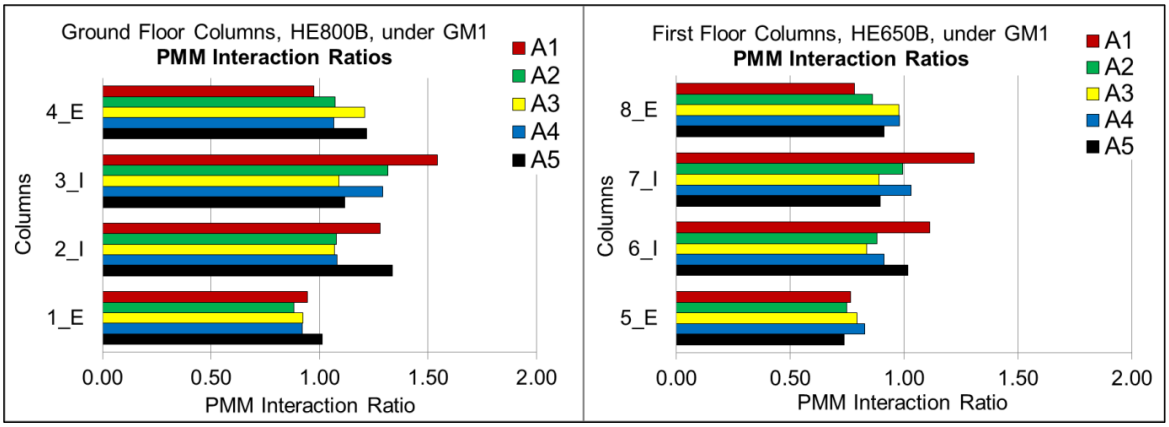

Figure 7.11. PMM Interaction Ratios under GM1 –
Columns at Ground Floor (left) and First Floor (right)

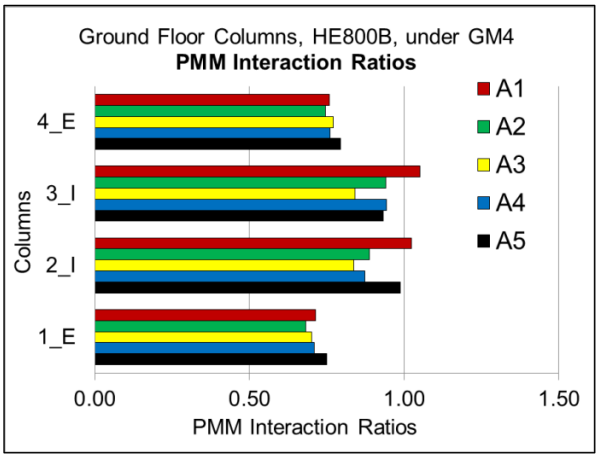

Figure 7.12. PMM Interaction Ratios under GM4 - Ground Floor Columns

7.3.2. Demand/Capacity Ratios

Additional performance of the brace-damper arrangements may be acquired from the individual D/C Ratios, including the total axial force ratio, the bending moment ratio, the

axial force ratio from static loads, and the axial force ratio from added dampers. The total axial force ratio and bending moment ratios reflect the D/C ratios of the members after the static and ground motion time history load cases, while the axial load ratio from static loads (axial static force ratio) reflects the axial force ratio after the static load case only. The axial static force ratios are constant for each member size and location (e.g.. an HE800B interior column) because the static loads were proportioned by tributary areas (twice as large for interior columns). Note that the tributary area for the interior columns of this interior MRF are greater than the exterior columns, and thus, interior columns carry larger axial static forces for this frame.

The axial force ratio from added dampers (axial damper force ratio) neglects the contribution of the static gravity loads to the axial force ratio and emphasizes the relative size of the damper axial forces. Axial damper force ratios are presented as positive values, regardless of tensile or compressive direction; the controlling forces of the total and static axial force ratio are compression forces. The axial damper force ratio $PRatio_{added\ dampers}$ is defined as the difference between the total axial force ratio PRatio and the axial static force ratio $PRatio_{static}$:

$$PRatio_{added\ dampers} = | PRatio - PRatio_{static} | \quad (7.18)$$

7.3.2.1. Ground Motion 1 – Overstressed Ground and 1st Floor Columns

Figure 7.13 presents the D/C ratios for the regular building under GM1, with the ground floor HE800B members in the left column and the first floor HE650B members in the right column. Recall that the PMM ratio is equal to the sum of the total axial force ratio and the bending moment ratio (Figure 7.11). For the ground floor columns under GM1, the bending moment ratio is a larger component of the PMM ratio than the total axial force ratio, with the exception of the A1 2_I column. First floor columns have more comparable bending moment and total axial force ratios, with variation depending on column location. The increase in axial

force ratios from ground floor to first floor is likely attributed to the column size and capacity decreasing at the first floor without a similar decrease in axial force.

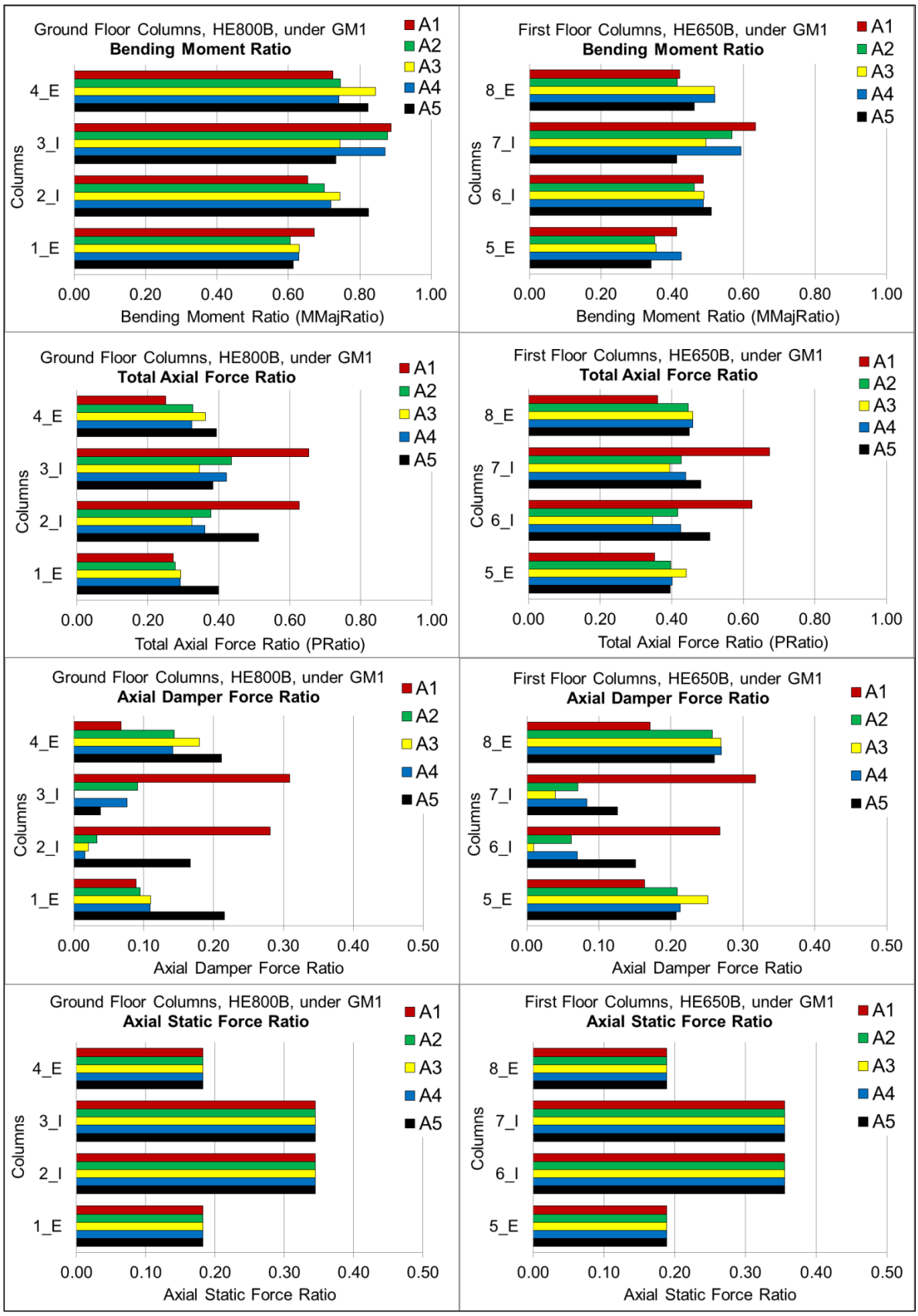

Figure 7.13. D/C Ratios under DBE GM1 – Columns at Ground (left) and First Floor (right)

A comparison of the axial damper force ratio and axial static force ratio shows the merits of the force counteraction concept used in A2, A3, and A4. The interior column axial damper force ratios are much smaller than the axial static force ratios for A2, A3, and A4. The counteraction concept is particularly effective in interior columns of A3, where there is small to negligible axial damper force ratios, and also effective in A2 and A4, where small ratios exist in comparison to A1. In contrast, the axial damper force ratio in A1 is greater than or equal to 75% of the axial static force ratio at the interior columns at both floors. The axial damper force ratios at interior columns of A5 are also improved from the A1 interior columns, a result of distributing the damper reaction forces uniformly to exterior and interior columns. All arrangements except A1 have shifted the damper axial forces to the exterior columns, causing an increase in the axial damper force ratios at these columns compared to A1. Despite the fact that the brace-damper sets are restricted to interior columns in A1, exterior columns are still resisting a portion of the axial damper force.

7.3.2.2. Ground Motion 4 – Overstressed Ground Floor Columns

Figure 7.14 includes the D/C ratios under GM4 for the ground floor HE800B columns. Similar to the GM1 results, bending moment ratios constitute a larger portion of the PMM ratios. Comparisons of the axial static force ratios and axial damper force ratios reveal the low contribution of the damper axial forces to the total axial force ratios for all brace-damper arrangements. Axial damper force ratios are at most 60% of the maximum axial static force ratio at exterior columns and 31% of the maximum axial static ratio at interior columns. A3 yields negligible axial damper force ratios at the interior columns and small contributions of axial force occur with A4, followed by A2 and A5. Note that the reduction in axial damper force ratio at interior columns results in larger exterior column axial force ratios, such that A1 and A5 are comparable in terms of maximum axial damper force ratio. Because GM4 is less-demanding than GM1, interstorey velocities and resulting damper reaction forces are smaller, prompting lower axial force ratios due to dampers.

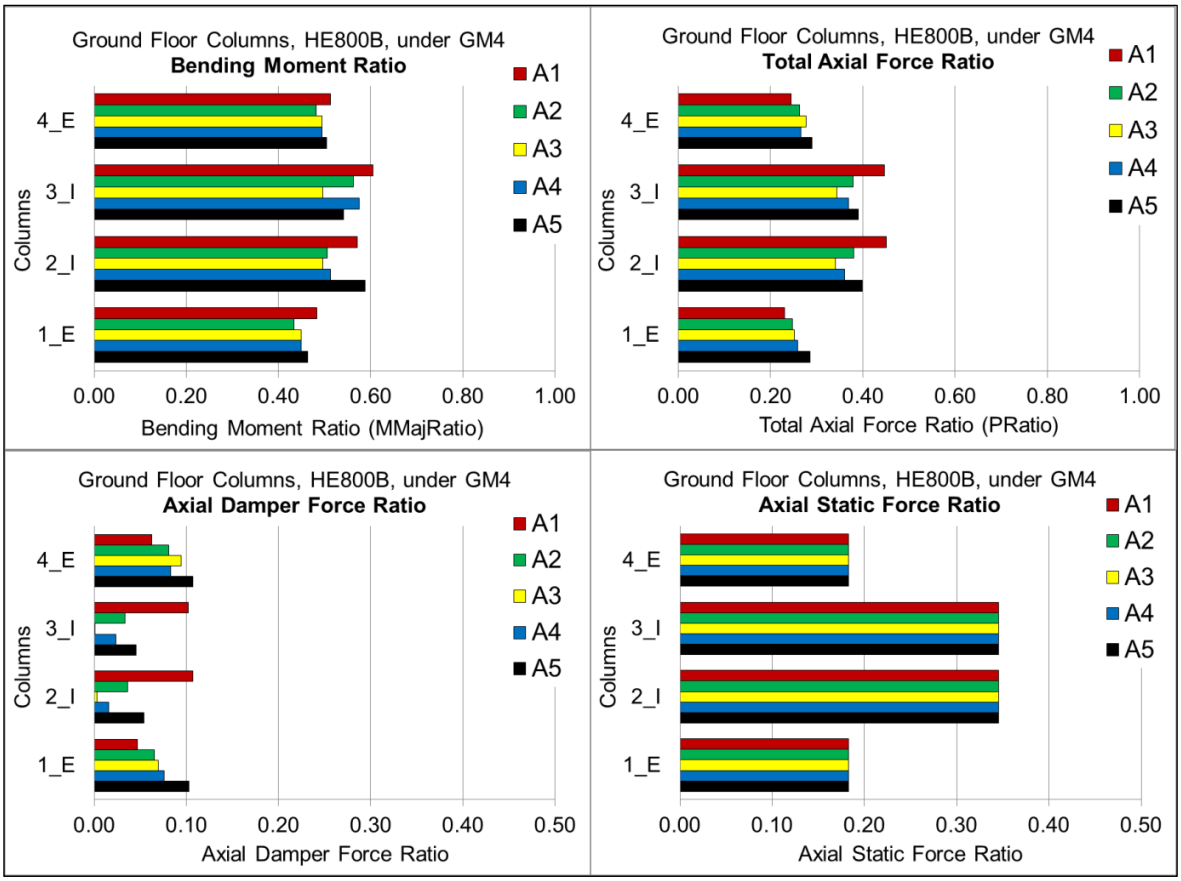

Figure 7.14. D/C Ratios under DBE GM4 – Ground Floor Columns

7.3.2.3. Discussion of Force Paths

The benefits of force counteraction and eliminating axial forces from dampers at the interior columns with A2, A3, and A4 is shown in the reduced axial force ratios from dampers at the interior columns under both ground motions. The level of reduction of axial force demand for various arrangements, in comparison to A1, depends on the seismic hazard level. A low-demanding ground motion (GM4) produced relatively small axial damper force ratios for all columns, at best (A2) a 24% reduction in the maximum axial damper force ratio and at worst (A5), the equivalent maximum axial damper force ratio, as compared to A1. A more demanding ground motion (producing peak drifts of 1%) prompted larger damper reaction forces and at best (A2 and A4) a 54% reduction in the maximum axial damper force ratio at the ground floor and at worst (A5) a 30% reduction in the maximum axial damper force ratio at the ground floor, as compared to A1.

In attempting to divert the axial forces from the internal columns, A5 shifted the load path prompting larger exterior column axial force demands and no improvement in maximum axial damper force ratio under GM4 but a 30% reduction in axial damper force ratio under GM1 at the ground floor as compared to A1. Despite superiority of A2 at reducing maximum axial damper force ratios under both ground motions, it did not reduce the moment demand on the interior members enough to best improve the overall maximum PMM ratios in the structure. The minimal axial damper force ratios at interior columns of A3 confirms that the force counteraction concept produces the expected results by reducing the unresolved forces on the interior columns and producing minimal axial forces from dampers. A3 achieves the lowest maximum PMM ratio in the ground and first floor columns.

7.3.3. Comparison of Performance Parameters

The structural performance of the system with various brace-damper arrangements was assessed in terms of peak interstorey drift and absolute accelerations. It is expected that each system will display equivalent structural performance because identical stiffness, mass, and damping properties were used per floor. Figure 7.15 shows the peak interstorey drifts per floor for each brace-damper arrangement, while Figure 7.16 presents the absolute accelerations per floor. Finally, the maximum performance parameters per brace-damper arrangement are summarised in Table 7.4.

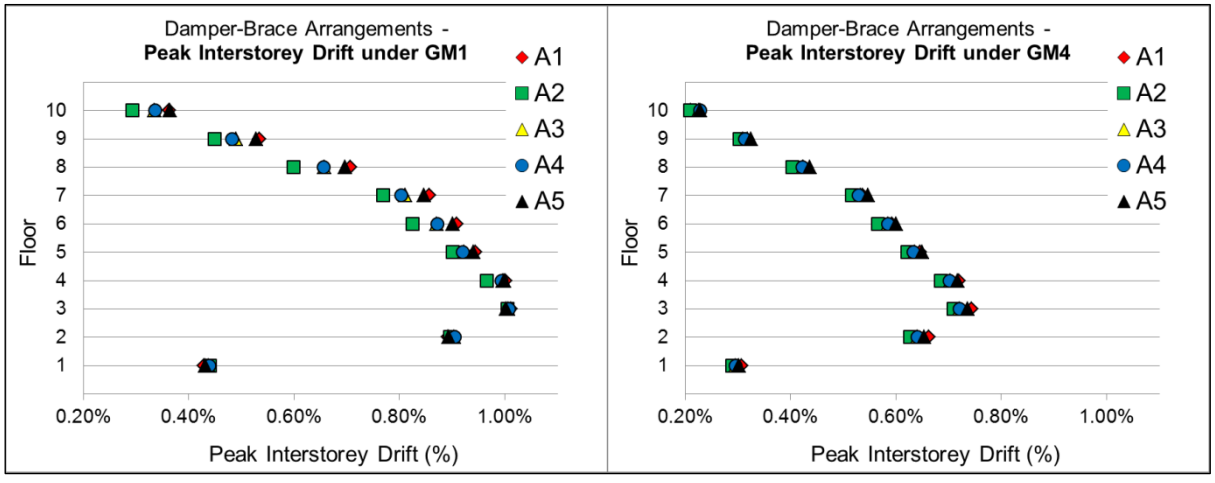

Figure 7.15. Peak Interstorey Drifts under GM1 (left) and GM4 (right)

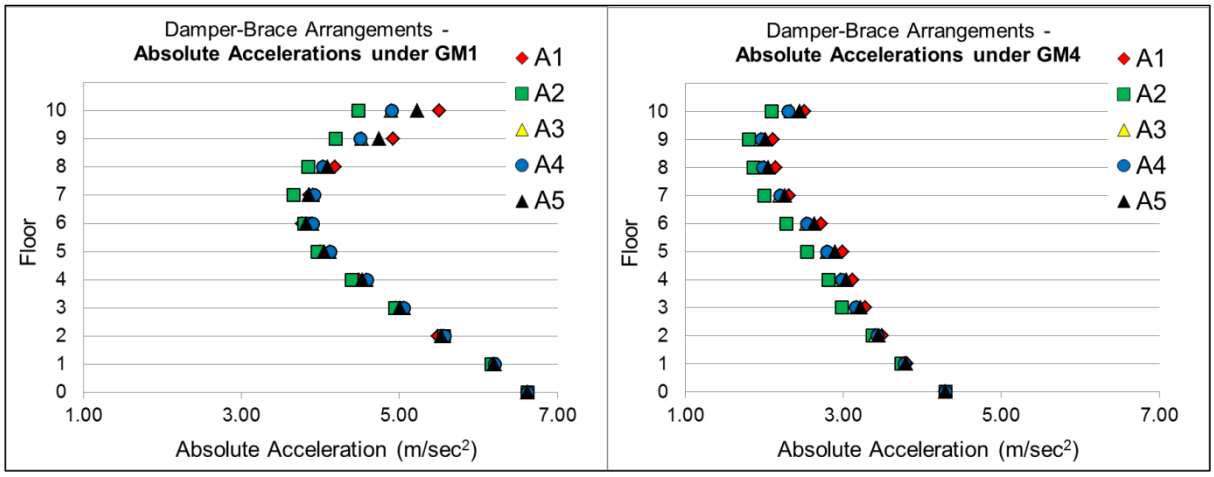

Figure 7.16. Absolute Accelerations under GM1 (left) and GM4 (right)

Table 7.4. Maximum Performance Parameters for Brace-Damper Arrangements

Brace-Damper Arrangements	Max Peak Interstorey Drift (%)		Max Absolute Acceleration (m/sec^2)	
	GM1	**GM4**	**GM1**	**GM4**
A1	1.01%	0.74%	6.18	3.81
A2	1.00%	0.71%	6.17	3.74
A3	1.01%	0.72%	6.21	3.78
A4	1.01%	0.72%	6.21	3.78
A5	1.00%	0.74%	6.20	3.79

The maximum peak drift values are approximately equivalent under GM1 and similar under GM4 with the lowest value at A2 and largest drifts at A1 and A5. In terms of drift distribution, A2 produces smaller drifts at most floors, A3 and A4 average drifts, and A1 and A5 the largest drifts in the distribution, particularly under GM1. Maximum absolute accelerations are very similar for all arrangements, and best minimised by A2 under both ground motions. Similar to the drift distribution, absolute acceleration distribution reveals overall reduced accelerations with A2 and increased accelerations with A1. Marginal differences in interstorey drifts and accelerations amongst the five brace-damper arrangements are due to the horizontal damper locations per floor that prompt slight differences in the stressed state of the structural members.

Residual drifts were negligible for all frame arrangements, which is justified by the linear building performance under this seismic hazard and confirmed by peak interstorey drifts and

absence of hinge formation. A review of the brace-damper arrangements after nonlinear time history analysis showed the absence of hinge formation under both ground motions. The same details used in Chapter 6 for bilinear hinge design were assumed.

Results show similar overall performance in terms of these performance parameters for all brace-damper configurations. Some improvement may be achieved with the triangular floor distribution of A2, where multiple dampers of lower force are introduced in comparison to arrangements with one brace-damper per floor. Overall, the similar performance of brace-damper arrangements in terms of drifts and accelerations confirms that the method of single-bay placement, as used in investigation studies of optimal placement, is acceptable for an initial assessment. However, designers must consider strategic placement of dampers within a floor to avoid overstressing structural members, particularly for such a large total amount of added damping. Finally, a steel design check of supplementally damped frames should be performed in combination with plastic hinge model to ensure that the conservative interaction equations are met and buckling does not pose a risk.

7.4. Conclusions

An assessment of various brace-damper arrangements has shown that strategic placement of dampers horizontally per floor can be used as a design strategy to avoid overstressing structural members. Results of two ground motions and five frame arrangements suggest that linear fluid viscous dampers can contribute critical axial forces to the supporting system, regardless of the out-of-phase trait of viscous dampers. For example, the selection of the standard arrangement A1 under GM4 results in two overstressed ground columns, while strategic selection of any of the alternative arrangements (A2-A5) avoids overstressing the columns.

However, the size of axial damper forces may be small in comparison to the axial static force depending on the ground motion demands. The influence of brace-damper arrangements on

the structural member capacity may be greater when the structural members are approaching the demand/capacity limit (as seen with A1 under GM4 compared to A2-5), when there are large damper forces due to high seismic demands, and when there is a large quantity of viscous damping and therefore, increase damper reaction forces.

The review of the axial damper force ratios confirms the effectiveness of the force counteraction approach for arranging brace-dampers throughout a structure. Brace-damper arrangements may be used as a tool to control force paths and reduce axial force demands from dampers. The PMM ratios serve as the best assessment for the overall performance of the brace-damper system at reducing demands on structural members. The diagonal arrangement A3 provides the most effective damper reaction force path and best reduces the maximum PMM ratios, while the alternating diagonal A4 and triangular arrangements A2 are improvements over the single-bay arrangements of A1 and A5 in terms of best reducing maximum PMM ratios. Slightly enhanced building performance may be achieved with using multiple brace-damper sets per floor, as shown by A2. The interior bay A1 approach yields the highest demands on the interior columns and slightly decreased building performance compared to alternative arrangements. Therefore, restriction of brace-dampers to interior bays should be used with caution of overloading interior columns, as they are carrying a greater proportion of the axial static loads.

In conclusion, the addition of viscous dampers requires that the structural capacity of the supporting members be checked, particularly to assess the axial damper force demands on the columns. Brace-damper arrangements with diagonals and multiple brace-damper sets per floor pose effective means of distributing the axial damper force and protecting the lower-storey columns from overstressing.

Chapter 8

Conclusions

This research leads to final conclusions about viscous damper behaviour and strategic placement of viscous dampers. The background presented in Chapter 2 highlighted the increasing application of supplemental energy dissipation systems with viscous dampers and importance of strategic damping distribution to ensure maximum building performance with minimum cost. Despite the quantity and variety of damper placement techniques in literature, there is a lack of consensus in structural design guidelines for the most effective and usable technique. Thus, common practice relies on damper distribution methods that are not necessarily optimal. Review of current damper placement methods in Chapter 3 summarised the categories for damper placement methods, limitations of these techniques and the comparative studies, and described three advanced placement methods in detail.

Conclusions presented in Chapter 4 concerning viscous device behaviour are limited to nonlinear viscous devices readily available for testing, yet the conclusions also provide insight into general viscous devices and a background for pursuing the strategic placement research for linear fluid viscous devices in Chapters 5, 6, and 7. It was found that the Maxwell model for the FVD and the Kelvin-Voigt-Maxwell (KVM) model for the FSD using the approximate stress relaxation factor better predict the behaviour of the devices compared to the standard dashpot model and Kelvin-Voigt model. Equations for the damper output force as a function of cyclic frequency and amplitude are proposed for the FSD and FVD based on the fitting of behavioural parameters, such as stiffness, the velocity exponent, damping coefficient, and the approximate stress-relaxation factor. The force equations for both devices are shown to perform well and capture the nonlinear behaviour over a range of frequencies and amplitudes.

Energy dissipation calculations of the devices reveal that the standard models over-predict the energy dissipation of the stress-relaxation analytical models by a maximum of 5%. Based on these results, it is recommended that standard device models are adequate for numerically modelling these nonlinear viscous devices in damped structures. Note that the stress relaxation due to the high shear stress zone is controlled by the highly nonlinear velocity exponent and exhibited in the square-shaped hysteresis curve. Therefore, linear fluid viscous devices, which lack this high shear stress zone, may be adequately modelled by standard dashpot models and linear fluid spring devices by KV models.

The conclusions of the damper distribution investigation for shear frames in Chapter 5 confirms the correct application of the three advanced placement methods using the examples presented in literature. This is essential for obtaining reliable damper distributions and accurate representations of the different damper placement methods prior to thorough comparisons for realistic scenarios in Chapter 6. In addition, a framework is created for determining total added damping, applying and improving the techniques, analysing the structures, and comparing the performance of the damped frames, that can be used for further studies with complex structures, larger ground motion suites, and additional performance objectives.

Based on the shear frame examples, the Uniform damping method was shown to perform similarly or slightly less effectively than the advanced methods, while the advanced placement methods of SSSA Mode and Takewaki yielded comparable performance for the second frame example. The results prompt the question of usability versus performance improvements of employing complex advanced placement techniques. Potential susceptibility to higher mode effects is observed in the Takewaki method. The need for more realistic

structures, seismic hazard levels without extreme effects of far-fault ground motions, and realistic total damping supports the in-depth investigation in Chapter 6.

The application and comparison of the five damper placement methods in Chapter 6 for a regular and an irregular building provide the most conclusive results about the effectiveness and usability of the methods. In addition, suggested guidelines for engineers employing damper placement strategies are presented. The main conclusion is the comparable performance observed amongst the advanced placement techniques; while it is expected that the advanced techniques should outperform the standard methods, the similarity amongst the advanced techniques in terms of interstorey drifts, absolute accelerations, and residual drifts is a key conclusion. This is particularly relevant in the field of damper placement research, considering the lack of thorough comparisons and lack of implementing techniques from beginning to end to assess usability.

Maximum absolute accelerations are reduced effectively and similarly by all of the damper placement methods. Absolute acceleration distributions are reduced further at the central floors by the Uniform and Stiffness Proportional damping methods that effectively damp the lower portion of the structure possessing the largest absolute accelerations for these two buildings. Residual drifts are drastically reduced by the addition of damping, including the irregular building under the MCE hazard level. The advanced methods exhibit slightly improved residual drifts in select cases. Overall, the performance-based seismic design objective for added damping to achieve a desired drift response is achieved by all of the damper placement methods. While a conservative total damping value is constrained to allow for comparisons amongst the damper distribution schemes, results indicate the potential for using a reduced quantity of damping for the advanced techniques to achieve the desired response.

In terms of drift distribution and maximum peak interstorey drifts, the Lavan A/R damping scheme consistently achieves the best performance in both the regular and irregular building under both hazard levels. The SSSA Mode is the second most-effective damping scheme for the irregular building, and the Takewaki scheme the second most-effective damping scheme for the regular building. In terms of usability, the Lavan A/R method is the most easily implemented in the shortest duration. The adapted SSSA Mode technique suggested in this research reduces the application time and increases the robustness of the SSSA Mode distribution against high-mode effects.

Overall, the usability of a placement technique is a direct product of the application methodology, and the effectiveness is a direct product of the objective function of the method. For the Lavan A/R method, both the application methodology and objective function are conducive for improved usability and effectiveness in terms of interstorey drifts. Improvements in the Takewaki method to include an objective function of peak interstorey drifts may resolve this limitation of the method but not the limitation of complex application. The SSSA Mode method, on the other hand, is designed such that the objective function cannot be altered, yet the adaptation of using three design accelerograms has slightly increased usability.

All three advanced placement methods are designed toward a fundamental mode response, which is justified by the modal damping results of both buildings. Particular sensitivity to higher mode effects is suggested by the altered drift profile of the Takewaki scheme for the regular building and Lavan A/R scheme for the irregular building excited by ground motions with higher mode effects. Results indicate that a damping distribution with zero or minimal damping at the roof is more easily excited by higher mode effects. This highlights the necessity for engineering judgement to be applied to the final damping distribution, regardless

of the damper placement technique employed. The Takewaki method may be at a particular risk for producing zero damping at upper stories because it does not employ time history analysis, is based on the first-mode response only, and may remove floor damping abruptly and absolutely. Similarly, the Lavan A/R method may be at risk if all active ground motions reflect only a first mode frame response. Results have not shown SSSA Mode to possess the same sensitivity, which may be a reflection of the robustness of using three design accelerograms with diverse characteristics.

Suggested design guidelines include the selection of advanced damper techniques based on usability, particularly amongst these comparable three methods. It is recommended that the Lavan A/R method be used because of its performance reduction and usability. It is shown that the damper distributions achieve the performance objectives even with minimal roof damping and when excited by higher-mode effects; however, this is in part due to the factor of safety associated with the large total damping value. Caution should be advised when using a reduced total damping value and a damping distribution with minimal upper storey damping. A recommended improvement of the Lavan A/R method is the use of more active ground motions based on not only the large spectral displacement values but also the drift profiles excited by a variety of modes.

Finally, Chapter 7 explores strategic placement of dampers horizontally per floor (brace-damper arrangements) as a design strategy to avoid overstressing structural members under axial damper reaction forces. It is found that linear viscous dampers can contribute critical axial forces to the supporting system, regardless of the out-of-phase trait of viscous dampers, which is a common reason for not investigating column capacities with added dampers. The brace-damper arrangements are selected based on architectural appeal or the potential for counteracting axial damper forces within the frame. The most effective brace-damper

arrangement is the diagonal arrangement (A3), which employs the force-counteraction principle, thus diverting axial forces from the interior columns, those columns most heavily loaded axially in the interior MRF, and reducing the maximum PMM ratios. The use of multiple brace-damper arrangements per floor (as seen in the triangular pattern of A2) results in slightly enhanced building performance in terms of peak interstorey drift and accelerations. The main design concern for an interior MRF is overstressing the interior columns at the lower-storeys. Generally, brace-damper arrangements with diagonals and multiple brace-damper sets per floor pose effective means of distributing the axial damper force and protecting the lower-storey columns from overstressing.

Detailed future work suggestions and limitations of this research are discussed at the end of each chapter. In summary, the main areas for future work include the incorporation of nonlinear dampers within structures, particularly the effectiveness of damper placement methods for structures with nonlinear dampers. Future work should also consider a stringent criteria for the selection of ground motions to cover a wide-range of possible building performance, the application of damper placement methods to three-dimensional, torsional structures with recommendations for vertical and horizontal damping distributions, as presented in Chapter 6 and 7, respectively, and finally, an investigation of the recommended 50% adjacent floor damping suggestion when coupled with a damper placement distribution with zero floor damping.

While the structures presented in this work have exhibited some nonlinear performance, the application of damper placement methods for highly nonlinear structures would be another interesting area for future research. More variety in building characteristics, a wide range of total added damping, and an investigation of damping placement methods that both constrain total damping and strategically place dampers should be considered in future work. Finally,

the work presented here has implicitly created a framework for comparing the effectiveness of damper placement schemes; application of this framework to more recent placement methods would provide additional insight towards the goal of determining a commonly accepted damper placement method for structural design guidelines.

In summary, strategic placement of dampers has been investigated from an enhanced performance perspective in terms of effective vertical damping distributions and from a practical perspective of structural capacity in terms of effective horizontal damping distribution. An incorporation of brace-damper arrangements with usable, advanced damper placement techniques will produce a structure that efficiently meets performance objectives while protecting the structural capacity of the primary system.

References

References

Agrawal, A. K., Yang, J. N., & He, W. L. (2003). Applications of some semi active control systems to benchmark cable-stayed bridge. *Journal of Structural Engineering, 129*(7), 884-894.

Ahmadizadeh, M. (2007). On equivalent passive structural control systems for semi-active control using viscous fluid dampers. *Structural Control and Health Monitoring, 14*(6), 858-875.

American Society of Civil Engineers (ASCE). (2006). *ASCE 7-05 - Minimum Design Loads for Buildings and Other Structures*. Reston, Virginia.

American Society of Civil Engineers (ASCE). (2000). *FEMA 356: Prestandard and Commentary for the Seismic Rehabilitation of Buildings.* Washington, D.C.: Federal Emergency Management Agency, FEMA.

Antonucci, R., Balducci, F., Bartera, F., Castellano M., Fuller, K., & Giacchetti, R. (2004). Shaking table testing of an RC frame with dissipative bracings. *Thirteenth World Conference on Earthquake Engineering*, Vancouver, BC, Canada.

Apostolakis, G., & Dargush, G.F. (2010). Optimal seismic design of moment-resisting steel frames with hysteretic passive dampers. *Earthquake Engineering and Structural Dynamics, 39,* 355-376.

Applied Technology Council (ATC). (2005). *FEMA 440: Improvement of Nonlinear Static Seismic Analysis Procedures*. Washington, D.C.: Federal Emergency Management Agency, FEMA.

Ashour, S.A., & Hanson, R.D. (1987). Elastic response of buildings with supplemental damping. *Report UMCE 87-1*, Ann Arbor, Michigan: Dept. of Civil Engineering, University of Michigan.

Aydin, E., Boduroglu, M.H., & Guney, D. (2007). Optimal damper distribution for seismic rehabilitation of planar building structures. *Engineering Structures, 29,* 176-185.

Bird, R.B., Armstrong, R.C., & Hassager, O. (1987). *Dynamics of polymeric liquids*. Chichester, UK: John Wiley & Sons.

Blakeborough, A. (2004). NEFOREEE real time tests. *Report No. OUEL 2274/04,* Oxford, United Kingdom: University of Oxford.

Blakeborough, A., Williams, M.S., Darby, A.P., & Williams, D.M. (2001). The development of real-time substructure testing. *Philosophical Transactions: Mathematical, Physical and Engineering Sciences, 359*(1786), 1869-1891.

BS EN 1993-1-1:2005. (2005). *Eurocode 3: Design of Steel Structures – Part 1-1: General Rules and Rules for Buildings,* British Standards.

BS EN 1998-3:2005. (2005). *Eurocode 8: Design of Structures of Earthquake Resistance- Part 3: Assessment and Retrofitting of Buildings*, British Standards.

BS EN 1998-1:2004. (2004). *Eurocode 8: Design of Structures for Earthquake Resistance – Part 1: General Rules, Seismic Actions and Rules for Buildings*, British Standards.

Building Seismic Safety Council (BSSC). (2004). NEHRP Recommended Provisions for Seismic Regulations for New Buildings and Other Structures, 2003 Edition. *Report No. FEMA 450-1,* Washington, DC: FEMA.

Building Seismic Safety Council (BSSC). (2001). NEHRP Recommended Provisions for Seismic Regulations for New Buildings and Other Structures, 2000 Edition. *Report Nos. FEMA 368 and 369*, Washington, DC: FEMA.

Burton, S., Konstantopoulos, I., Makris, N., & Antsaklis, P. (1995). Modelling the response of a fluid damper: constitutive models and neural networks. *Proceedings of the 3rd IEEE Mediterranean Symposium on Control and Automation*, Cyprus, Retrieved from http://med.ee.nd.edu/MED3/MED95/VI_PDFs/375-379.pdf.

CEN/TC, European Committee for Standardization. (2008). *Draft of prEN15129(E):2008,European Standard for Anti-seismic Devices*.

Cheng, F. Y., & Pantelides, C.P. (1988). Optimal placement of actuators for structural control. *Technical Report NCEER-88-0037*, Buffalo, N.Y.: National Centre for Earthquake Engineering Research, State University of New York.

Christopoulos, C., & Filiatrault, A. (2006). *Principles of Passive Supplemental Damping and Seismic Isolation*. Pavia, Italy: IUSS Press.

Chu, S.Y., Soong, T.T., & Reinhorn, A.M. (2005). *Active Hybrid, and Semi-active Structural Control – A Design and Implementation Handbook*, Chapter 1. London: John Wiley & Sons, Ltd.

Cimellaro, G. P., & Retamales, R. (2007). Optimal softening and damping design of buildings. *Structural Control and Health Monitoring, 14*(1), 831-857.

Constantinou, M.C., Soong, T.T., & Dargush, G.F. (1998). *Passive Energy Dissipation Systems for Structural Design and Retrofit*. Monograph Series 1, Buffalo, NY.: Research Foundation of the State University of New York and Multidisciplinary Center for Earthquake Engineering Research.

Constantinou, M.C., & Symans, M.D. (1993a). Experimental study of seismic response of buildings with supplemental fluid dampers. *The Structural Design of Tall Buildings, 2*, 93-132.

Constantinou, M.C., & Symans, M.D. (1993b). Seismic response of structures with supplemental damping. *The Structural Design of Tall Buildings, 2*, 77-92.

Constantinou, M.C., & Tadjbakhsh, I.G. (1983). Optimum design of a first story damping system. *Computers and Structures, 17*(2), 305-310.

CSI, Computers and Structures, Inc. (2011). Hinge FAQ. Online resource, Accessed May 25, 2011, Retrieved from http://wiki.csiberkeley.com.

CSI, Computers and Structures, Inc. (2009a). *SAP2000, version 14*. Berkeley, CA, USA.

CSI, Computers and Structures, Inc. (2009b). *Steel Frame Design Manual – Eurocode 3-1:2005*. For SAP2000 version 14, Berkeley, CA.: CSI.

Di Paola, M., La Mendola, L., & Navarra, G. (2007). Stochastic seismic analysis of structures with nonlinear viscous dampers. *Journal of Structural Engineering, 133*(10), 1475-1478.

Fujita,K., Yamamoto, K., & Takewaki, I. (2010). Optimal damper placement for minimum transfer function of interstorey drift in shear building. *Proceedings of the First International Conference on Advances in Interaction and Multiscale Mechanics (AIMM)*, 30 May – 4 June 2010 in Jeju, Korea, 291-309.

Gluck, N., Reinhorn, A.M., Gluck, J., & Levy, R. (1996). Design of supplemental dampers for control of structures. *Journal of Structural Engineering, 122*(12), 1394-1399.

Gürgöze, M., and Müller, P.C. (1992). Optimal positioning of dampers in multi-body systems. *Journal of Sound and Vibration, 158*(3), 517-530.

Hahn, G.D., & Sathiavageeswaran, K.R. (1992). Effects of added-damper distribution on the seismic response of buildings. *Computers and Structures, 43*(5), 941-950.

Hanson, R. D., & Soong., T.T. (2001). *Seismic Design with Supplemental Energy Dissipation Devices, Second Monograph Series (MNO-8).*Oakland, CA: Earthquake Engineering Research Institute.

Hart, G. C., & Wong, K. (2000). *Structural Dynamics for Structural Engineers*. New York: John Wiley & Sons.

Haskell, G., & Lee, D. (2002). Fluid viscous damping as an alternative to base isolation. Technical Papers from Taylor Devices, Inc., Retrieved from www.taylor-device.com/fvd_alt1.htm.

Hou, C.Y. (2008). Fluid dynamics and behavior of nonlinear viscous fluid dampers. *Journal of Structural Engineering, 134*(1), 56-63.

Infanti, S. (2009). FIP Industriale device specifications. Personal communication.

Instron Limited. (1997). Performance envelope plot – 100kN actuator. *Instron Manual*, High Wycombe, England.

International Code Council. (2006). *International Building Code*. Country Club Hills, IL, USA: ICC.

Islam, S. (2001). Seismic retrofit of an existing building using energy-dissipation devices. *SEAOC 2001 70th Annual Convention Proceedings*, 287-301, San Diego, CA.

Islam, S., Skokan, M., & Huang, S. (2010). Innovative seismic retrofit of two high-rise buildings with unique challenges. *Proceedings of the 9th U.S. National and 10th Canadian Conference on Earthquake Engineering*, Toronto, Canada.

Karabalis, D.L., Cokkinides, G.J., Rizos, D.C., & Mulliken, J.S. (2000). Simulation of earthquake ground motions by a deterministic approach. *Advances in Engineering Software, 31*, 329-338.

Karabalis, D. L., Cokkinides, G.J., & Rizos, D.C. (1992). *Seismic Record Processing Program (SRP), v.1.03*. Prepared for Westinghouse Savannah River Company, SC, USA.

Key, D. (1998). *Earthquake Design Practice for Buildings*. London: Thomas Telford Limited.

Kim, J., & Choi, H. (2006). Displacement-based design of supplemental dampers for seismic retrofit of a framed structure. *Journal of Structural Engineering, 132*(6), 873-883.

Kramer, S. (1996). *Geotechnial Earthquake Engineering*. New Jersey: Prentice Hall.

Lavan, O., & Dargush, G.F. (2009). Multi-objective evolutionary seismic design with passive energy dissipation systems. *Journal of Earthquake Engineering, 13*(6), 758-790.

Lavan, O., & Levy, R. (2009). Simple iterative use of Lyapunov's solution for the linear optimal seismic design of passive devices in framed buildings. *Journal of Earthquake Engineering, 13,* 650-666.

Lavan, O., & Levy, R. (2006). Optimal peripheral drift control of 3D irregular framed structures using supplemental viscous dampers. *Journal of Earthquake Engineering*, *10*(6), 903-923.

Lee, K., Ricles, J., & Sause, R. (2009). Performance-based seismic design of steel MRFs with elastomeric dampers. *Journal of Structural Engineering*, *135*(5), 489-498.

Levy, R., & Lavan, O. (2009). Quantitative comparison of optimization approaches for the design of supplemental damping in earthquake engineering practice. *Journal of Structural Engineering*, *135*(3), 321-325.

Levy, R., & Lavan, O. (2006). Fully stressed design of passive controllers in framed structures for seismic loadings. *Structural Multidisciplinary Optimisation, 32*(6),485-498.

Liu, W., Tong, M., & Lee, G. (2005). Optimization methodology for damper configuration based on building performance indices. *Journal of Structural Engineering*, *131*(11), 1746-1756.

Lopez-Garcia, D., & Soong, T. T. (2002). Efficiency of a simple approach to damper allocation in MDOF structures. *Journal of Structural Control*, *9*, 19-30.

Lopez-Garcia, D., 2001. "A simple method for the design of optimal damper configurations in MDOF structures," *Earthquake Spectra*, 17(3)**,** 387-398.

Lu, X., Gong, Z., Weng, D., & Ren, X. (2007). The application of a new structural control concept for tall building with large podium structure. *Engineering Structures*, *29*(8), 1833-1844.

Makris, N., & Constantinou, M.C. (1991). Fractional-derivative maxwell model for viscous dampers. *Journal of Structural Engineering*, *117*(9), 2708-2724.

McCormick, J., Aburano, H., Ikenaga, M., & Nakashima, M. (2008). Permissible residual deformation levels for building structures considering both safety and human elements. *Proc. 14th World Conf. Earthquake Engineering*, Paper No. 05-06-0071, Beijing, China.

Mezzi, M. (2010). Innovative configurations and morphologies using dissipating bracing systems. *Proceedings of the 9th U.S. National and 10th Canadian Conference on Earthquake Engineering*, Toronto, Canada.

Molina, F. J., Sorace, S., Terenzi, G., Magonette, G., & Viaccoz, B. (2004). Seismic tests on reinforced concrete and steel frames retrofitted with dissipative braces. *Earthquake Engineering and Structural Dynamics*, *33*(15), 1373-1394.

Movaffaghi, H., & Friberg, O. (2006). Optimal placement of dampers in structure using genetic algorithm. *Engineering Computations: International Journal for Computer-Aided Engineering and Software*, *23*(6), 597-606.

Ojaghi, S.M.M. (2010). *The Development of Real-Time Distributed Hybrid Testing for Earthquake Engineering*. Thesis, University of Oxford, UK.

Ojaghi, S.M.M. (2008). FVD photograph. University of Berkeley, CA.

PEER - Pacific Earthquake Engineering Research Center. (2005). *Next Generation Attenuation Relationships – Strong-motion Database*, Regents of the University of California, USA, Retrieved from http://peer.berkeley.edu/nga.

Pekcan, G., Mander, J.B., & Chen, S.S. (1999). Design and retrofit methodology for building structures with supplemental energy dissipating systems. *Technical Report MCEER-99-0021*, Buffalo, New York: MCEER.

Pekcan, G., Mander, J.B., & Chen, S.S. (1995). The seismic response of a 1:3 scaled model R.C. structure with elastomeric spring dampers. *Earthquake Spectra*, *11*(2), 249-267.

Pintér, J. (2008). Global optimization. From *MathWorld*--A Wolfram Web Resource, Retrieved from http://mathworld.wolfram.com/GlobalOptimization.html.

Pintér, J., & Weisstein, E.W. (2008). Evolution strategies. From *MathWorld*--A Wolfram Web Resource, Retrieved from http://mathworld.wolfram.com/EvolutionStrategies.html.

Post, N. (2003). Latin America's tallest 'sails' through Mexico quake. *Engineering News-Record*, *250*(4), 16-17.

Press, W., Teukolsky, S., Vetterling, W., & Flannery, B. (2007). *Numerical Recipes – The Art of Scientific Computing*. 3rd Ed., Cambridge: Cambridge University Press.

Ramirez, O.M., Constantinou, M.C., Whittaker, A.S., Kircher, C.A., & Chrysostomou, C.Z. (2002). Elastic and inelastic seismic response of buildings with damping systems. *Earthquake Spectra, 18*(3), 531–547.

Shukla, A.K., & Datta, T.K. (1999). Optimal use of viscoelastic dampers in building frames for seismic force. *Journal of Structural Engineering*, *125*(4), 401-409.

Singh, M.P., & Moreschi, L.M. (2002). Optimal placement of dampers for passive response control. *Earthquake Engineering and Structural Dynamics*, *31*, 955-976.

Singh, M.P., & Moreschi, L.M. (2001). Optimal seismic response control with dampers. *Earthquake Engineering and Structural Dynamics*, *30*, 553-572.

Smith, R., & Coates, K. (2009). Arup Design Engineers, Personal Interview, 7 Sept. 2009.

Somerville, P., Smith, N., Punyamurthula, S., & Sun, J. (1997). Development of ground motion histories for phase 2 of the FEMA/SAC steel project. *Report No. SAC/BD-97/04*,Retrieved from: http://nisee.berkeley.edu/data/strong_motion/sacsteel/motions/la10in50yr.html.

Soneji, B. B., & Jangid, R. S. (2007). Passive hybrid systems for earthquake protection of cable-stayed bridge. *Engineering Structures*, *29*(1), 57-70.

Soong, T.T., & Dargush, G.F. (1997). *Passive Energy Dissipation Systems in Structural Engineering*. Chichester, England: John Wiley & Sons Ltd.

Soong, T.T., & Spencer Jr., B.F. (2002). Supplemental energy dissipation: state-of-the-art and state-of-the-practice. *Engineering Structures, 24*, 243-259.

Sorace, S., Terenzi, G., Magonette, G., & Molina, F. (2008). Experimental investigation on a base isolation system incorporating steel-Teflon sliders and pressurized fluid viscous spring dampers. *Earthquake Engineering and Structural Dynamics*, *37*(2), 225-242.

Sorace, S., & Terenzi, G. (2001). Non-linear dynamic modelling and design procedure of FV spring-dampers for base isolation. *Engineering Structures, 23*, 1556-1567.

Symans, M.D., Charney, F.A., Whittaker, A.S., Constantinou, M.C., Kircher, C.A., Johnson, M.W., & McNamara, R.J. (2008). Energy dissipation systems for seismic applications: current practice and recent developments. *Journal of Structural Engineering*, *134*(1), 3-21.

Symans, M.D., & Constantinou, M.C. (1998). Passive fluid viscous damping systems for seismic energy dissipation. *ISET Journal of Earthquake Technology*, Paper No. 382, *35*(4), 185-206.

Takewaki, I. (2009). *Building Control with Passive Dampers – Optimal Performance based Design for Earthquakes*. London, U.K: John Wiley & Sons.

Takewaki, I.. (2000). Optimal damper placement for planar building frames using transfer functions. *Structural and Multidisciplinary Optimization*, *20*(4), 280-287.

Takewaki, I., Yoshitomi, S., Uetani, K. and Tsuji, M. (1999). Non-monotonic optimal damper placement via steepest direction search. *Earthquake Engineering and Structural Dynamics*, *28* (6), 655-670.

Takewaki, I. (1997). Optimal damper placement for minimum transfer functions. *Earthquake Engineering and Structural Dynamics, 26,* 1113-1124.

Taylor. D. P. (2007). Personal interview, 5 November 2007.

Taylor, D. P. (2002a). History, design, and applications of fluid dampers in structural engineering. *Proceedings of the 2002 Passive Control Symposium*, Tokyo, Japan: Tokyo Institute of Technology.

Taylor, D. P. (2002b). Damper retrofit program for the London Millennium Pedestrian Bridge, PowerPoint Presentation, North Tonawanda, NY: Taylor Devices, Incorporated.

Torre Mayor. (2011). Retrieved from http://www.torremayor.com.mx/, 8 May 2011.

Uang, C.M., & Bertero, V.V. (1990). Evaluation of seismic energy in structures. *Earthquake Engineering and Structural Dynamics*, *19*, 77-90.

Uriz, P., & Whittaker, A.S. (2001). Retrofit of pre-Northridge steel moment-resisting frames using fluid viscous dampers. *The Structural Design of Tall Buildings*, *10*, 371-390.

Weisstein, E.W. (2008). Stochastic optimization. From *MathWorld*--A Wolfram Web Resource, Retrieved from http://mathworld.wolfram.com/StochasticOptimization.html.

Whittaker, A.S., Constantinou, M.C., Ramirez, O.M., Johnson, M.W., & Chrysostomou, C.Z. (2003). Equivalent lateral force and modal analysis procedures of the *2000 NEHRP Provisions* for buildings with damping systems. *Earthquake Spectra*, *19*(4), 959-980.

Wu, B., Ou, J.P., & Soong, T.T. (1997). Optimal placement of energy dissipation devices for three dimensional structures. *Engineering Structures*, *19*(2), 113-125.

Zhang, R., & Soong, T.T. (1992). Seismic design of viscoelastic dampers for structural applications. *Journal of Structural Engineering*, *118*(5), 1375-1392.

Appendix

Appendix

A-1. FVD Schematic

(FIP Industriale 2009)

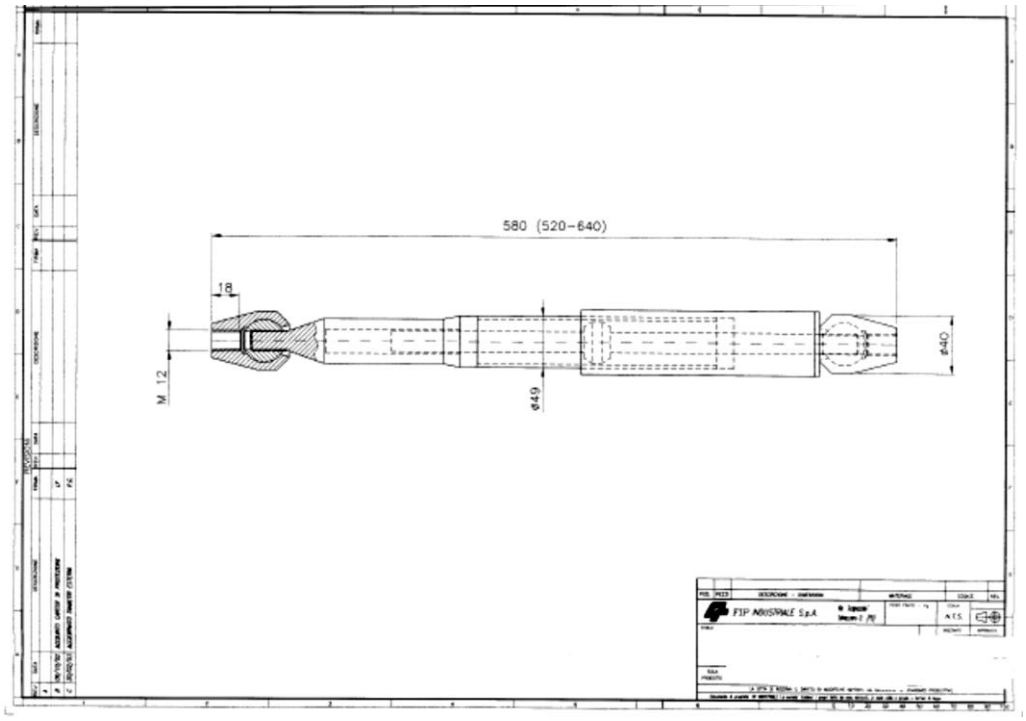

A-2. Notes for Operating in the Structural Dynamics Laboratory

Using the Pump Equipment:

1) Sign the log book.
2) Turn on main red dial.
3) Turn on large red pump dial 1 and large red pump dial 2, depending on desired pump. (Note: Pump 1 must always be on)
4) Turn on small green button – "Pump start 1"
5) Turn on small green button – "Pump start 2"
6) Heat the oil reservoir
7) Possibly work the actuators a bit (move them back and forth)
8) When the red button lights are on – press "Pump 1 On" and "Pump 2 On"
9) At end of testing…
    a. Ensure hydraulics are turned off (grey Instron box on mezzanine)
    b. Follow the same procedure in reverse
        i. Pump 1 off (red button-push)
        ii. Pump 2 off
        iii. Wait for an audible click. Turn off the large red pump knobs, first 2, then 1.
        iv. Turn off main Red Knob
        v. Complete log book.

* Turn on Instron box BEFORE starting RS Plus (switch on side of Instron)

***** For device testing = AXIS 2; Dspace channel board – Axis 2X and 2Y

Using RSPlus *located on older PC*

1) Select "RS Plus" from the Windows start-up Menu
2) Select the 1st and 3rd buttons on the vertical start-up menu
3) Calibration of Load Cell (*complete prior to starting the pumps*)
    3.1) "Transducer Setup"
    3.2) Axis→ Calibrate → Auto →wait → Done
    3.3) Lock
4) Turn on the Pumps (follow instructions included previously)
5) Position Calibration
    5.1) Set Displacement and Force Limits (green hourglass, right of "status monitor")
    5.2) Max/Min (ARM)
    5.3) Currently: +- 20 mm, +- 100 kN

5.4) Action – "actuator off"

6) Cyclic Waveform (or Ramp)
   6.1) Note that the actuators are on a 10 volt system
   6.2) Set max Amplitude
   - Either force or displacement controlled
   - Currently, use 40mm displacement controlled
   - Check analog output (implies a 4mm/V to achieve 40 mm amplitude on 10 volt system)
   - Waveform – select "Ext-Aux" if using dspace to control the motion

7) Control Loop
   7.1) To use the fPIDL – outer loop controller; Instron – inner-loop controller
   7.2) Set the RSPlus limits as PG = 33.39 dB; IG = 1; DG (and all others) = 0

8) Analog Outputs
   - load = 10 kN/V (Selected for a load = 100 kN)
   - typically, we don't use position "B" on the analog outputs

9) Confirm "Control Loop" is set properly (displacement or force)
   For Jarret FSD: 4mm/V @10 volts = 40mm stroke
   5 kN/V @10 volts = 50 kN
   For FIP FVD: 10 mm/V @10 volts = 100 mm stroke
   5 kN/V @10 volts = 50 kN

RESET - will return device to its original position
FINISH – device stops at current location

Using the Hydraulic Substation

1) Max pressure on one substation = 3000 psi (needle at 12 o'clock)
2) Using the grey box on mezzanine –
   a. Pilot (wait at least 10 seconds to warm up the oil)
   b. Low (wait)
   c. High
   d. Keep hand on the emergency stop during testing

Shutting Down

1) Turn off RS Plus software and older PC
2) Logout of Vulpecula (leave computer running for remote access).
3) Turn off Instron box
4) Complete pump shutdown as outlined earlier

A-3. Takewaki Script : Irregular Building

Applying the Takewaki Technique to the Irregular Building - 2.47% DBE, 0.99% FOE

```
IrregBldg_TAKEWAKI.m  Jessica Whittle  last updated: July 2, 2011
NT=300;   % total number of iterations
N=1;      %  N = current iteration
Ni=3;     % denominator of the delta_y value, which equals (yF-yo)/(Ni)
n=10;     % degrees of freedom, number of floors
```

Step 1: Define Known Values

```
Transfer function - to convert total drifts to interstorey drifts, where Interstory Drift (id) = T * drift(U)
CONSTANTS
T = diag(ones(n,1));  %construct transfer function
for d=1:1:n-1
    T(d+1,d)=-1;
end
k1=469E5; %N/m – Known lateral floor stiffnesses
k2=182E5; k3=137E5; k4=121e5; k5=106e5; k6=90e5;k7=73e5; k8=61e5; k9=44e5; k10=26e5;
m1=90031; %kg - Known masses (total in lateral direction)
m2=60020; m3=m2; m4=m2; m5=m2; m6=m2; m7=30010; m8=m7; m9=m7; m10=m7;
```

Step 2: Determine the undamped fundamental natural frequency (w)

```
Determined based on M and K
w = 2.7224; % rad/sec (fundamental period is 2.308 sec, freq = 0.433 Hz)
```

Step 3: Define Unknown Values (Variables_C)

```
Set a symbolic set of damping values for ease of partial differentiation of the "A" matrix later on.
% lumped damping per floor, c1 = first floor damping coefficient (N-sec/m)
syms c1 c2 c3 c4 c5 c6 c7 c8 c9 c10;
% Create Matrices: K, C, M
K =[(k1 + k2) -k2 0 0 0 0 0 0 0 0; (-k2) (k2+k3) -k3 0 0 0 0 0 0 0; 0 -k3 (k3+k4) -k4 0 0 0 0 0 0; 0 0 -k4 (k4+k5) -k5 0 0 0 0 0; 0 0 0 -k5
(k5+k6) -k6 0 0 0 0; 0 0 0 0 -k6 (k6+k7) -k7 0 0 0; 0 0 0 0 0 -k7 (k7+k8) -k8 0 0; 0 0 0 0 0 0 -k8 (k8+k9) -k9 0; 0 0 0 0 0 0 0 -k9 (k9+k10) -
k10; 0 0 0 0 0 0 0 0 -k10 k10];
C =[(c1 + c2) -c2 0 0 0 0 0 0 0 0; (-c2) (c2+c3) -c3 0 0 0 0 0 0 0; 0 -c3 (c3+c4) -c4 0 0 0 0 0 0; 0 0 -c4 (c4+c5) -c5 0 0 0 0 0; 0 0 0 -c5 (c5+c6) -
c6 0 0 0 0; 0 0 0 0 -c6 (c6+c7) -c7 0 0 0; 0 0 0 0 0 -c7 (c7+c8) -c8 0 0; 0 0 0 0 0 0 -c8 (c8+c9) -c9 0; 0 0 0 0 0 0 0 -c9 (c9+c10) -c10; 0 0 0 0 0 0
0 0 -c10 c10];
m = [m1;m2;m3;m4;m5;m6;m7;m8;m9;m10]; % column vector of the Mass Matrix
M = diag(m);
```

Step 4: Define the matrix A. A * U_ = -M

```
Ug is the ground acceleration; U_ and id_ are true drifts;
U and id are normalised by the ground acceleration.
Therefore, the ground motion is never specifically used for this method.
U = U_/Ug;            id = id_/Ug;          Define A as A* U = -M
A = K + ((1i*w).*C)-((w^2).*M); %C is still symbolic
%A differentiated with respect to C values (symbolic differentiation)
A_c1 = diff(A,c1);   A_c2 = diff(A,c2);   A_c3 = diff(A,c3);   A_c4 = diff(A,c4);   A_c5 = diff(A,c5);
A_c6 = diff(A,c6);   A_c7 = diff(A,c7);   A_c8 = diff(A,c8);   A_c9 = diff(A,c9);
A_c10 = diff(A,c10);
```

Step 5: Assign "c" values per floor

```
In order to more quickly calculate the inv(A), use the assumed c values...
W = 33700000; %Ns/m, vTotal added viscous damping ==> known in advance
% Initial Values of damping - UNIFORM DAMPING
Wi = W/n;
c = Wi.*(ones(n,1));%Ns/m
c_v=0; %index of damping values = 0
V_total=zeros(NT,1);
c1f=zeros(NT,1);  c2f=zeros(NT,1);  c3f=zeros(NT,1);  c4f=zeros(NT,1);  c5f=zeros(NT,1);
c6f=zeros(NT,1);  c7f=zeros(NT,1);  c8f=zeros(NT,1);  c9f=zeros(NT,1);  c10f=zeros(NT,1);
c1f(1)=c(1);  c2f(1)=c(2);  c3f(1)=c(3);  c4f(1)=c(4);  c5f(1)=c(5);
c6f(1)=c(6);  c7f(1)=c(7);  c8f(1)=c(8);  c9f(1)=c(9);  c10f(1)=c(10);
y1f=zeros(NT,1); y2f=zeros(NT,1); y3f=zeros(NT,1); y4f=zeros(NT,1); y5f=zeros(NT,1);
y6f=zeros(NT,1); y7f=zeros(NT,1); y8f=zeros(NT,1); y9f=zeros(NT,1);
```

START ITERATIONS

```
for N=1:1:NT
syms c1 c2 c3 c4 c5 c6 c7 c8 c9 c10
A = K + ((i*w).*C)-((w^2).*M); %C is still symbolic
%A differentiated with respect to C values (symbolic differentiation)
A_c1 = diff(A,c1); A_c2 = diff(A,c2);  A_c3 = diff(A,c3); A_c4 = diff(A,c4); A_c5 = diff(A,c5);
A_c6 = diff(A,c6); A_c7 = diff(A,c7);  A_c8 = diff(A,c8); A_c9 = diff(A,c9); A_c10 = diff(A,c10);
c1=c(1);subs(A); c2=c(2);subs(A); c3=c(3);subs(A); c4=c(4);subs(A); c5=c(5);subs(A);
c6=c(6);subs(A); c7=c(7);subs(A); c8=c(8);subs(A); c9=c(9);subs(A); c10=c(10);subs(A);
A = subs(A);
IA = inv(A);
iT = inv(T);
A_c = [A_c1;A_c2;A_c3;A_c4;A_c5;A_c6;A_c7;A_c8;A_c9;A_c10];
c1=c(1);subs(A_c); c2=c(2);subs(A_c); c3=c(3);subs(A_c); c4=c(4);subs(A_c); c5=c(5);subs(A_c);
c6=c(6);subs(A_c); c7=c(7);subs(A_c); c8=c(8);subs(A_c); c9=c(9);subs(A_c); c10=c(10);subs(A_c);
A_c = subs(A_c);
```

Step 6: Determine the Fourier Transforms of the Interstorey Drifts based on new C values

```
Interstorey drifts - determined from analysis at the undamped fundamental natural frequency
U = A\-m;  %floor drifts...at undamped fundamental frequency..A*U = -m .. U = Ureal/Uaccelground
id = T*U;   %interstorey drifts...normalised  id = idreal/Uaccelground = id_/Ug
for p=1:1:n
   id_abs(p,1)=sqrt((real(id(p))^2)+((imag(id(p)))^2));
end
id_abs;  %absolute value of the interstorey drifts at each floor
```

Step 7: Determine first-order sensitivities of interstory drift

```
id_x = zeros(n,n);   % First-order sensitivities of id (id differentiated wrt to j = id_j)
s = -(n-1);
for f=1:1:n
   s=s+n;  %index for A_c start (100x10 matrix)
   e=n*f;  %index for A_c end (100x10 matrix)
   id_x(:,f)=-T*(IA)*(A_c(s:e,:))*iT*id;
end
idj_abs_j = zeros(n,n);
Bj = zeros(n,1);  % Bj = [sum_idj_1; sum_idj_2;sum_idj_3; sum_idj_4; …; sum_idj_10];
for f=1:1:n
   for z=1:1:n
   idj_abs_j(z,f)=((1/(id_abs(z)))*(((real(id(z))*real(id_x(z,f)))+((imag(id(z))*(imag(id_x(z,f)))))));
   end
   Bj(f,1) = sum(idj_abs_j(:,f));
end
```

Step 8: Determine the Optimalitiy Criteria gamma (yo) (without lambda)

```
yo = sum of interstorey drifts differentiated wrt to cj / sum of..wrt c1
% Bj = vector of the sum of interstorey drifts of all floor differentiated wrt cj
% For example: sum_idj_1 = sum of interstorey drifts of all floors differentiated wrt to c1.
% Initially assume denominator in yo ratio = B1, yet if c(1)=0, must use next largest Bj value as the denominator in the yo ratio.
if c(1)==0
   r1 = find(Bj== max(abs(Bj)));
   r2 = find(Bj == -max(abs(Bj)));
   if r1 > 0 % if it exists
```

```
      maxBj = Bj(r1);
   end
   if r2 > 0
      maxBj = Bj(r2);
   else
      pause;
   end
else
   maxBj = Bj(1); %default.
end
yo = [Bj(2)/maxBj; Bj(3)/maxBj; Bj(4)/maxBj; Bj(5)/maxBj; Bj(6)/maxBj; Bj(7)/maxBj; Bj(8)/maxBj; Bj(9)/maxBj; Bj(10)/maxBj];
y1f(N)=yo(1); y2f(N)=yo(2); y3f(N)=yo(3); y4f(N)=yo(4); y5f(N)=yo(5);
y6f(N)=yo(6); y7f(N)=yo(7); y8f(N)=yo(8); y9f(N)=yo(9);
```

Step 9: Determine Additional Values, yF,delta_y,Bj,id_x

```
yF = ones(n-1,1); %[1;1;1;1;1]; Desired final values
% delta_y = the difference in the desired value(yF)and the current value(yo)
for h=1:1:(n-1)
  delta_y(h,1) = (yF(h)-yo(h))/(Ni); %Ni = step size; N = step of the current iteration, NT = total steps
end
delta_y(n) = 0;
```

Step 10: Check Optimality Criteria (from the previous iteration's "c")

Let 'no'=0 and 'yes'= very near 1 (optimality criteria met)
At this point - the 'c' array has only positive values (been altered by the last loop in the script... negative c-values = 0 and rest of the total C is distributed equally among the remaining floors).

```
Z=zeros(n,1);
for g=2:1:n
   if c(1)>0 && c(g)>0 && (yo(g-1)<=1.10 && yo(g-1)>=0.9999)
      Z(g)=1;
   end
   if c(1)>0 && c(g)==0 && yo(g-1)<=1
      Z(g)=1;
   end
   if c(1)==0 && c(g)>0 && (yo(g-1)<=1.10 && yo(g-1)>=1.0)
      Z(g)=1;
   end
end
if Z(2:n)==1
   X='OPTIMALITY REACHED'
   pause
end
```

Step 11: Define the second differentiation of interstory drift (idf_jk)

id_x differentiated with respect to "j" and "k" - creates 100 x 10 matrix of values (each idf_jk vector is 10x1 column); The ten rows of the 100 x 10 matrix represent differentiation wrt to j=1, k=1-10;

```
% J = row;  K = column;
idf_jk = zeros(n*n,n);
s=-(n-1);
for j=1:1:n
   s=s+n; %index for A_c start
   e=n*j; %index for A_c end
   b=-(n-1);
   for k=1:1:n
      b = b+n;
      q = n*k;
      idf_jk(s:e,k)=(T*IA*A_c(b:q,:)*IA*A_c((s:e),:)*iT*id)-(T*IA*A_c((s:e),:)*iT*id_x(:,k));
   end
end
idf_jk_abs = zeros(n*n,n);
for j=1:1:n
    for k=1:1:n
      for e=1:1:n
      g =e+(n*(j-1));
idf_jk_abs(g,k)=(1/((id_abs(e))^2))*((id_abs(e)*((real(id_x(e,k))*real(id_x(e,j)))+(real(id(e))*real(idf_jk(e+(n*(j-
1)),k)))+(imag(id_x(e,k))*imag(id_x(e,j)))+(imag(id(e))*imag(idf_jk(g,k)))))- idj_abs_j(e,k)*((real(id(e))*real(id_x(e,j)))+
(imag(id(e))*imag(id_x(e,j))));
      end
   end
end
```

Step 12: Define partial derivatives dBj/dc

```
%Bj = [sum_idj_1; sum_idj_2;, sum_idj_3; sum_idj_4; sum_idj_5; sum_idj_6…sum_idj_10];
dB_dc=zeros(n,n);
s=-(n-1);
for j=1:1:n
   s=s+n;
   s2=n*j;
```

```
   for k=1:1:n
      dB_dc(j,k)=sum(idf_jk_abs(s:s2,k));
   end
end
% Determine the B matrix ... B* delta C = delta y
if c(1)==0
   r1 = find(Bj== max(abs(Bj)));
   r2 = find(Bj == -max(abs(Bj)));
   if r1 > 0 %if it's real
      maxBj = Bj(r1);
   elseif r2 > 0
      maxBj = Bj(r2);
   else
      pause;
   end
else
   maxBj = Bj(1);
end
B = ones(n,n); % 10 x 10 matrix
for t=1:1:(n-1)
     B(t,:)=(1/maxBj).*(dB_dc(t+1,:)-(dB_dc(1,:).*yo(t)));
end
% Modify the B (coefficient) Matrix and delta_y Matrix - remove jth column and j-1 row corresponding to cj=0
%c_v; = previous iteration value;  %determine which index {rows and columns} corresponds to zero
if N >1
for g=length(cv):-1:1
    if cv(g)>1 %follow this if-statement for c(2)-c(n)
         row=cv(g)-1;%limit of the row ...
         col=cv(g);
         B(row,:) = [];
         B(:,col) = [];
         delta_y (row) = [];
    end
    if cv(g)==1  %% for c(1)=0; .. DELETE COLUMN 1
        B(:,1) = [];
    end
end
end
```

Step 13: Solve for delta_c

```
B * delta_c = delta_y   (where delta_c = increment to increase or decrease each floor "c" value)
%yo(N) will change each time (N), as will delta_y as new damping coefficients are added per floor...
delta_c = B\delta_y;
```

RECONSTRUCT delta_c_add function:

```
delta_c_add = zeros(n,1);
z_=length(delta_c);
r=find(c==0);
rw = find(c~=0);
if c(1)== 0
   delta_c_add(1) = 0;
else
   delta_c_add(1) = delta_c(1);
end
for g=1:1:length(rw)
     delta_c_add(rw(g)) = delta_c(g);
end
for g=1:1:length(r)
   delta_c_add(r(g))=0;
end
```

Step 14: Solve for c

```
New c vector = old c vector + delta_c; note that delta_c = 0 when c = 0
c_old = c;
c = c_old + delta_c_add;  % actual c values
c_real = c;
```

Step 15: Solve for the Objective function (sum of interstorey drifts of transfer function)

```
V = sum(id_abs);
V_total(N)=V;
```

Step 16: Check Objective Function and Constraints

```
sum_c = sum(c_real);
```

Step 17: Prepare for Next Iteration

```
c_v = 0;          % reset the c_v value for this iteration
c_v_new = 0; % this value is cumulative, for every new vanishing number
cv=0;             %c_v =  number of c_values that "vanish"
```

```
cv=find(c<=0);
for k=1:1:n
   if c(k)==0
     c_v=c_v+1;  % this has already "vanished" in previous iterations... hence = 0;
   end
   if c(k)< 0
      c_v = c_v+1;
      c_v_new = c_v_new+1;
      c(k)=0;
   end
 end
cd = W/(n-c_v);
% cd = damping of other floors = total damping redistributed, assuming certain floors=0;
% redistribute c values ONLY IF there are numbers that vanish (floors have zero damping coefficients)
if c_v_new > 0
   for p=1:1:n
      if c(p)>0
         c(p)= cd;
      end
   end
end
sum2=sum(c);
c1f(N+1)=c(1); c2f(N+1)=c(2); c3f(N+1)=c(3); c4f(N+1)=c(4); c5f(N+1)=c(5);
c6f(N+1)=c(6); c7f(N+1)=c(7); c8f(N+1)=c(8); c9f(N+1)=c(9); c10f(N+1)=c(10);
end
```

Step 18: Plot Final Values

```
t=1:1:NT;
figure;
plot(t,V_total(1:NT));
title('Objective Function vs Step');
figure;
            subplot(2,3,1); plot(t,c1f(1:NT)); title('C1 versus Step');
            subplot(2,3,2); plot(t,c2f(1:NT)); title('C2 versus Step');
            subplot(2,3,3); plot(t,c3f(1:NT)); title('C3 versus Step');
            subplot(2,3,4); plot(t,c4f(1:NT)); title('C4 versus Step');
            subplot(2,3,5); plot(t,c5f(1:NT)); title('C5 versus Step');
            subplot(2,3,6); plot(t,c6f(1:NT)); title('C6 versus Step');
figure;
            subplot(2,3,1); plot(t,c7f(1:NT)); title('C7 versus Step');
            subplot(2,3,2); plot(t,c8f(1:NT)); title('C8 versus Step');
            subplot(2,3,3);plot(t,c9f(1:NT)); title('C9 versus Step');
            subplot(2,3,4);plot(t,c10f(1:NT));title('C10 versus Step');
figure;
            subplot(2,3,1); plot(t,y1f(1:NT)); title('Y1 versus Step');
            subplot(2,3,2); plot(t,y2f(1:NT)); title('Y2 versus Step');
            subplot(2,3,3); plot(t,y3f(1:NT)); title('Y3 versus Step');
            subplot(2,3,4); plot(t,y4f(1:NT)); title('Y4 versus Step');
            subplot(2,3,5); plot(t,y5f(1:NT)); title('Y5 versus Step');
            subplot(2,3,6); plot(t,y6f(1:NT)); title('Y6 versus Step');
figure;
            subplot(2,3,1);plot(t,y7f(1:NT));title('Y7 versus Step');
            subplot(2,3,2);plot(t,y8f(1:NT));title('Y8 versus Step');
            subplot(2,3,3);plot(t,y9f(1:NT));title('Y9 versus Step');
```

A-4. Ground Motion Set (7) - Chapter 5: Shear Frames

A-4.1. Acceleration Time Histories

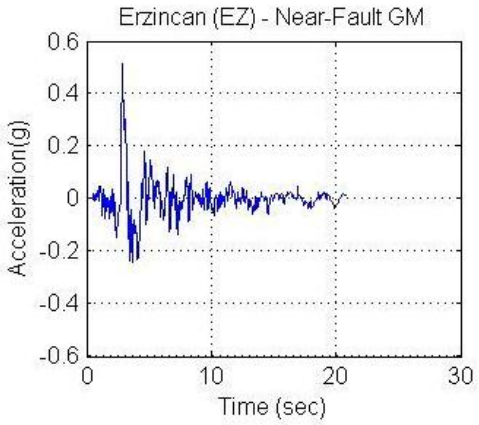

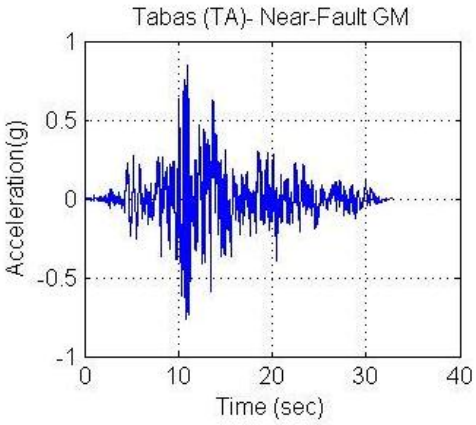

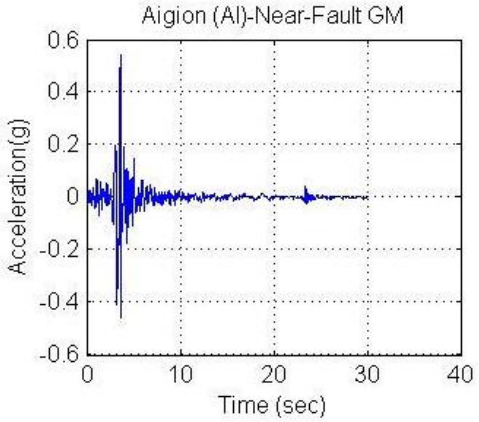

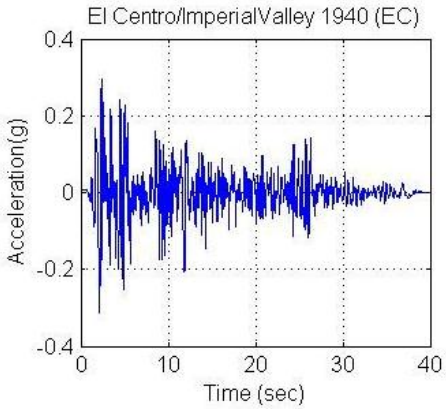

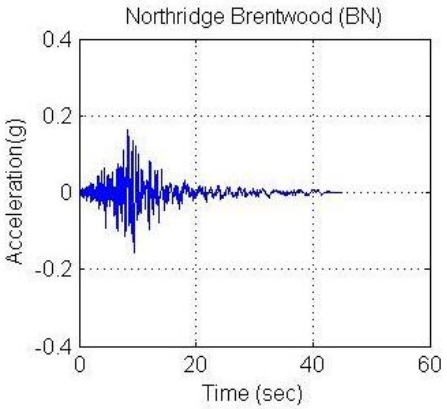

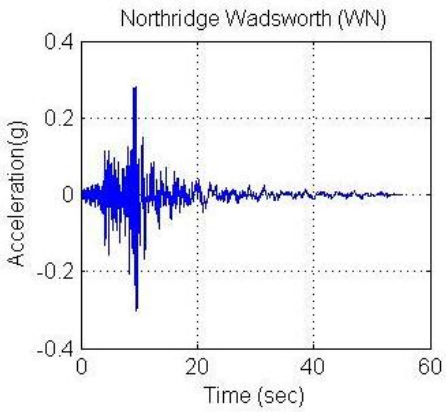

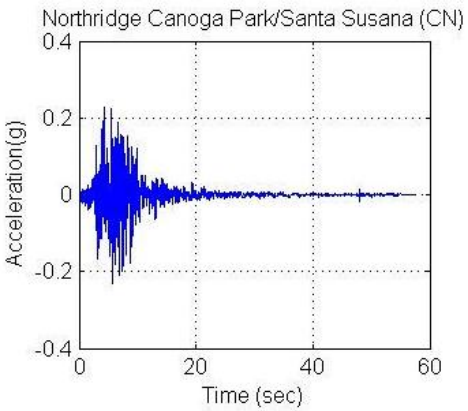

A-4.2. Velocity Time Histories

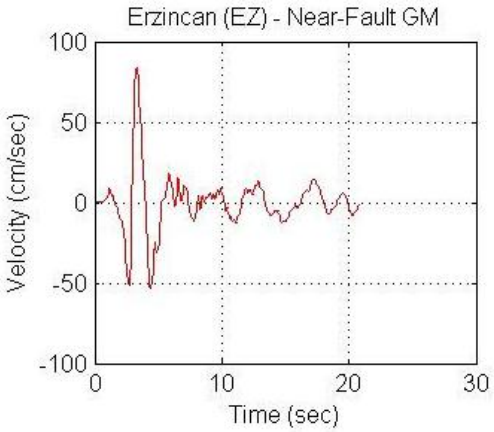

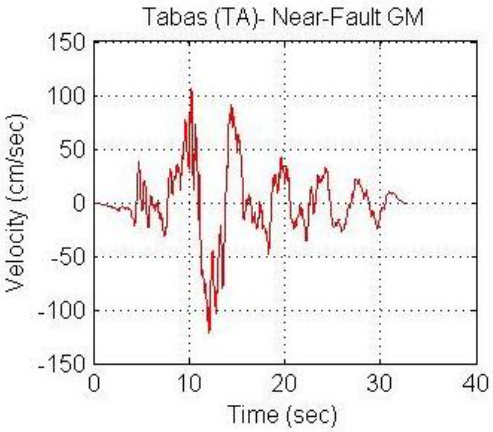

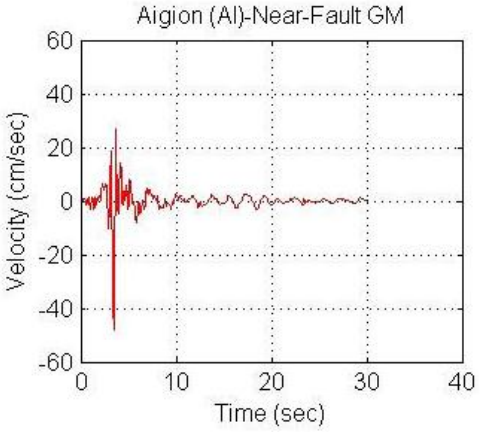

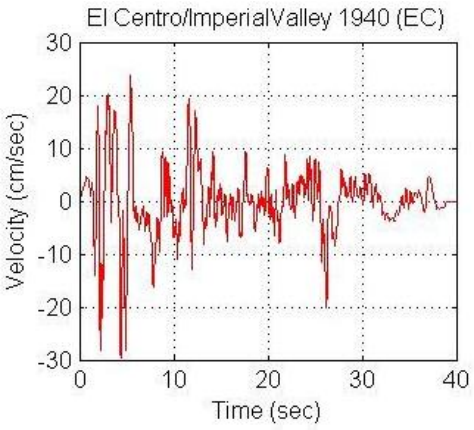

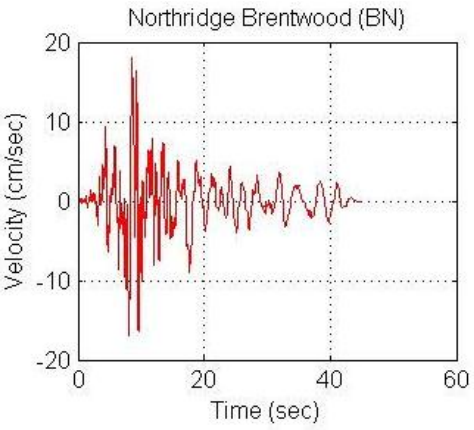

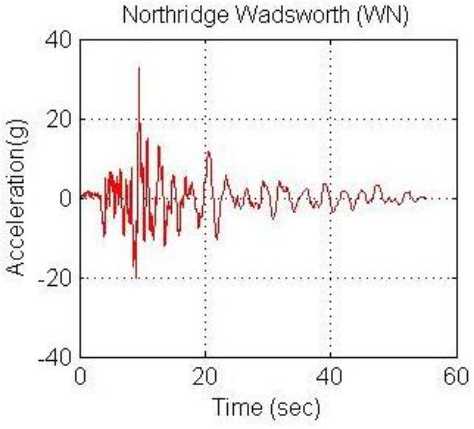

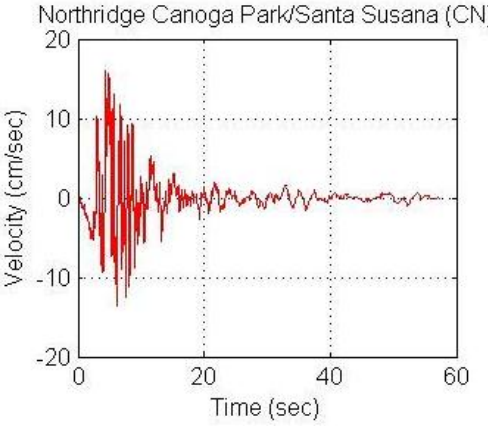

A-4.3. Pseudo-spectral Acceleration Plots

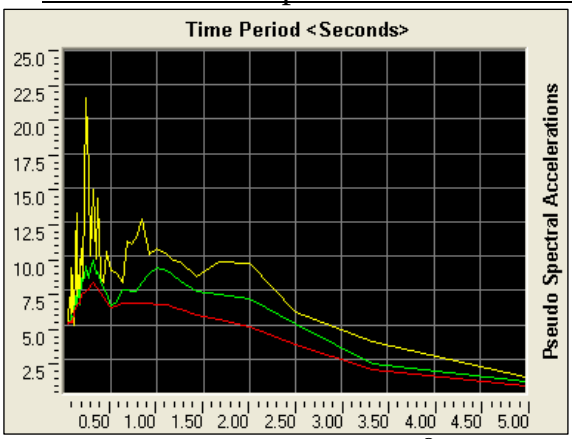

Erzincan (EZ) – PSA (m/sec^2)

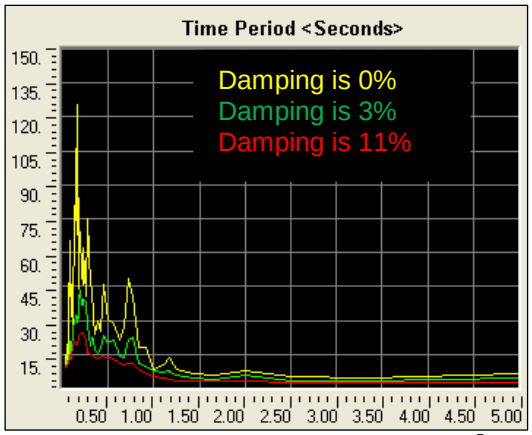

Tabas (TA) – PSA (m/sec^2)

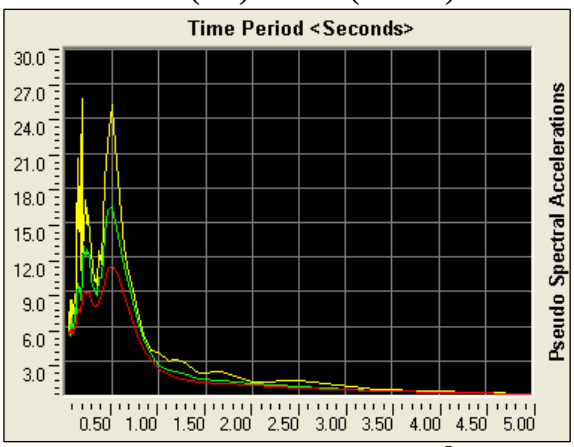

Aigion (AI) – PSA (m/sec^2)

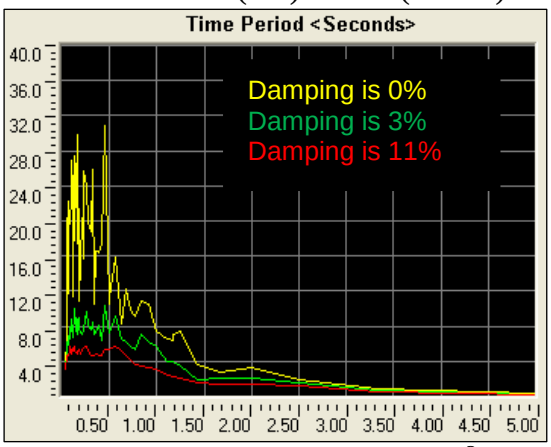

El Centro (EC) – PSA (m/sec^2)

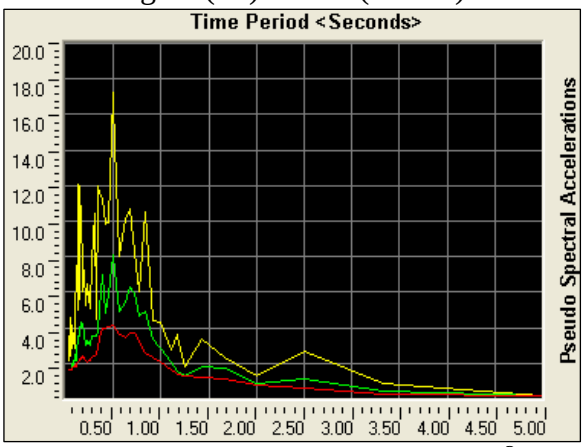

Brentwood NR (BN) – PSA (m/sec^2)

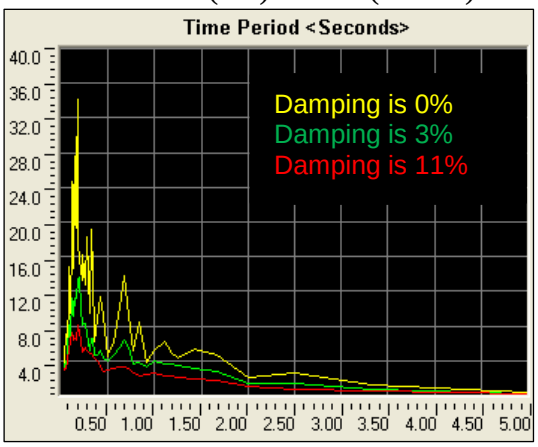

Wadsworth – NR (WN) – PSA(m/sec^2)

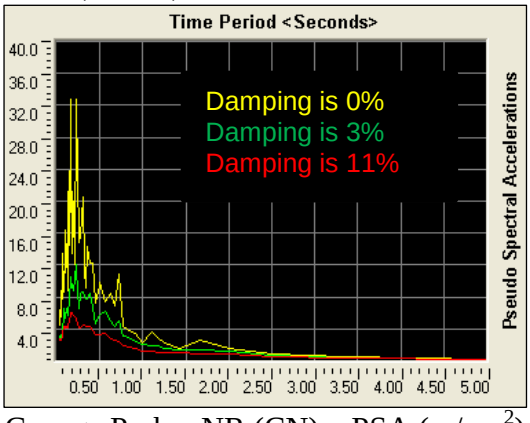

Canoga Park – NR (CN) – PSA (m/sec^2)

A-4.4. Spectral Displacement Plots

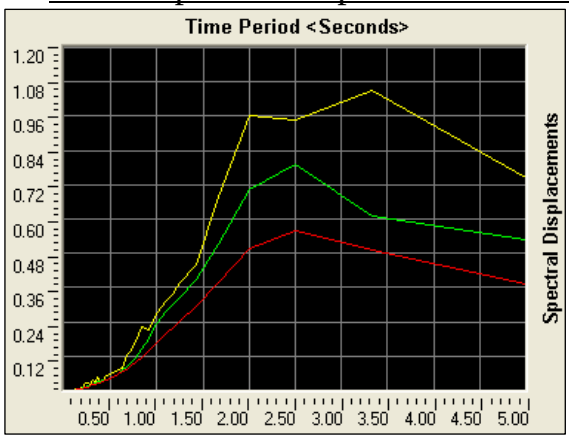

Erzincan (EZ) – S_D (m)

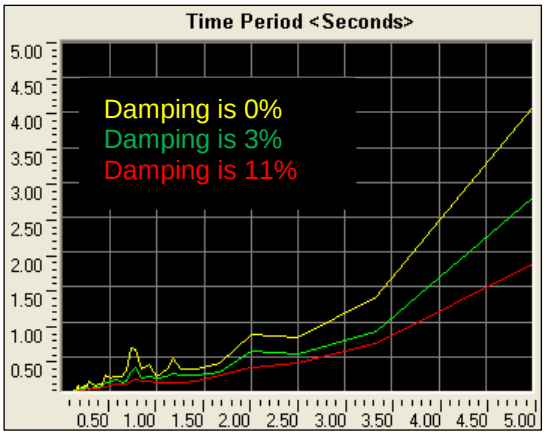

Tabas (TA) – S_D (m)

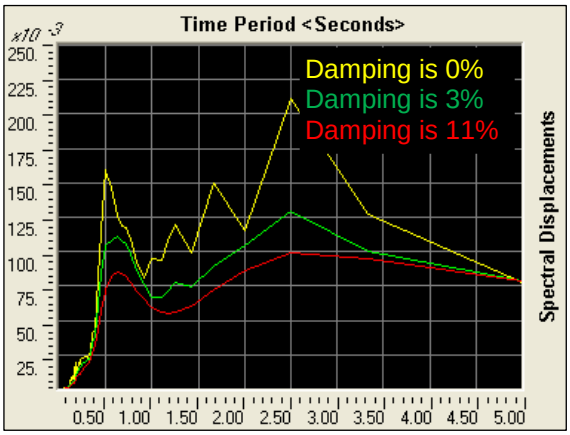

Aigion (AI) – S_D (m)

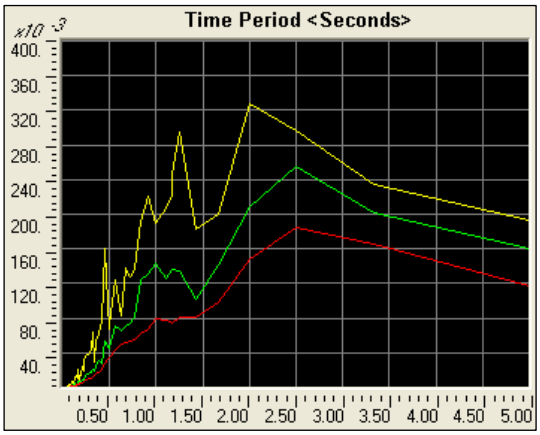

El Centro (EC) – S_D (m)

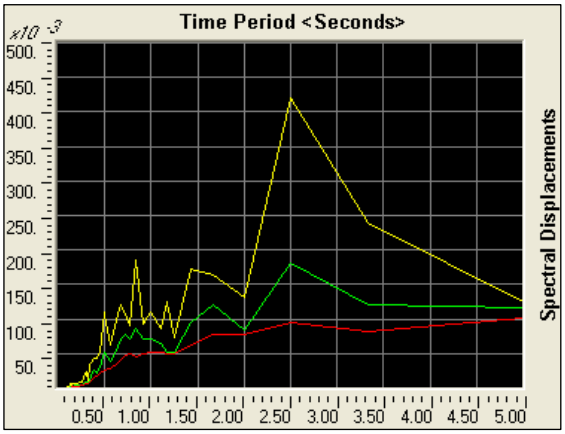

Brentwood NR (BN) – S_D (m)

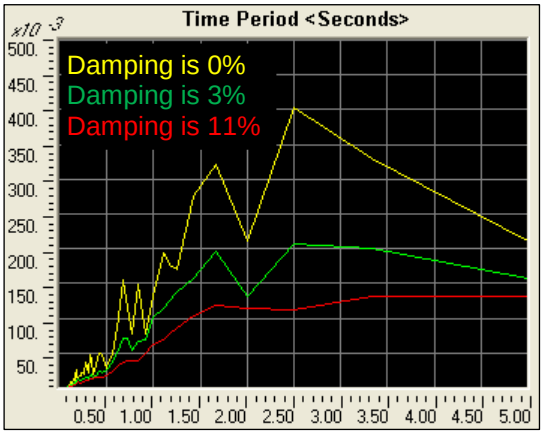

Wadsworth NR (WN) – S_D (m)

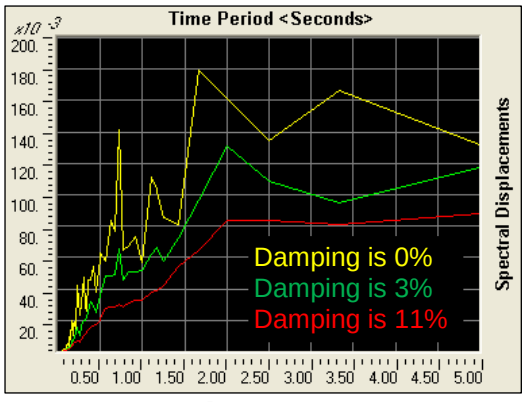

Canoga Park NR (CN) – S_D (m)

A-4.5. Power Spectral Density Plots

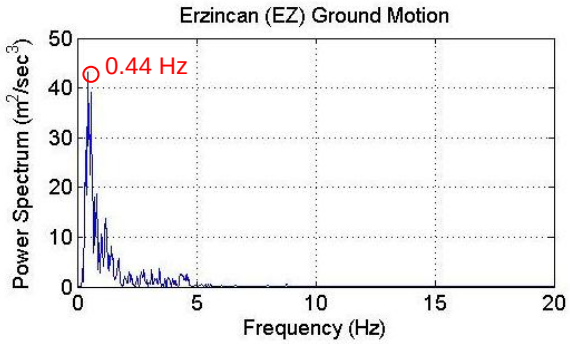

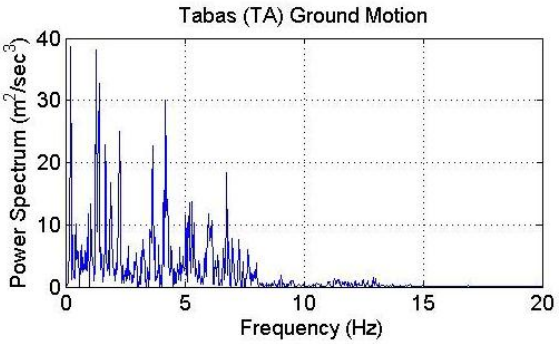

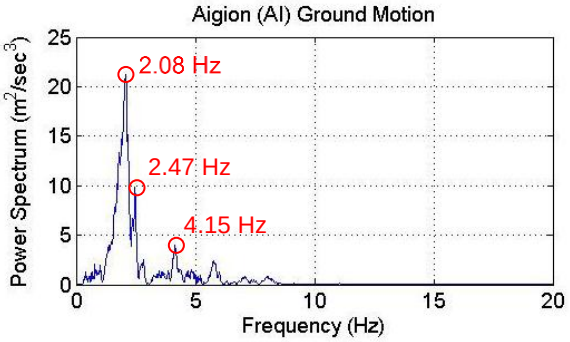

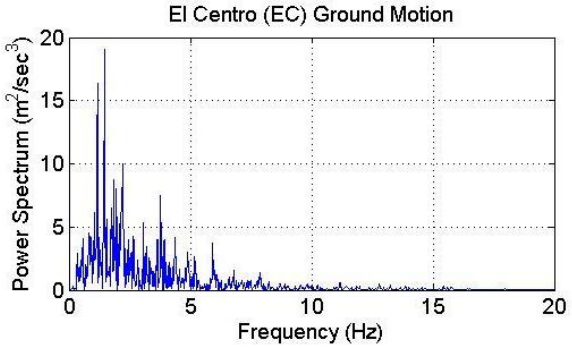

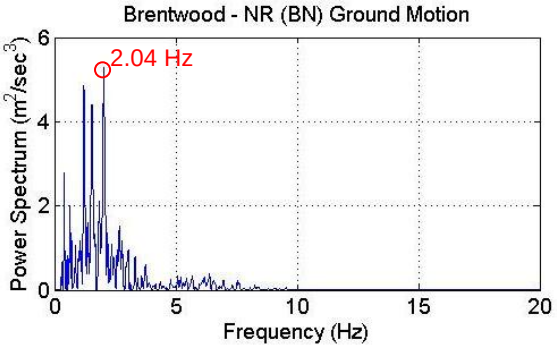

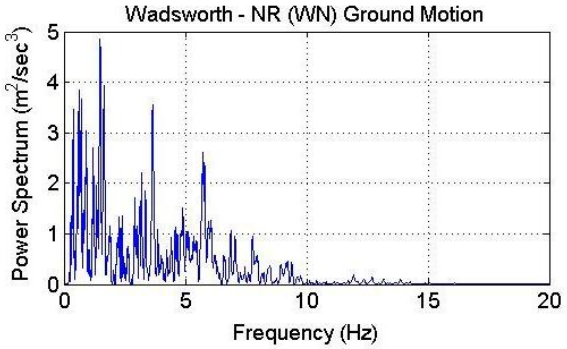

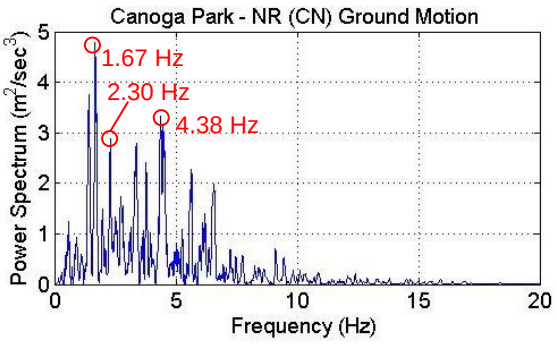

Major Frequency Components of the Ground Motion Set – Based on Power Spectral Density Plots

Ground Motion	Major Frequency Components (Hz) (corresponding periods (s))				
EZ	0.44 Hz (2.27 s)	0.56 Hz (1.78 s)	0.80 Hz (1.25 s)	1.20 Hz (0.83 s)	-
TA	0.22 Hz (4.55 s)	1.27 Hz (0.79 s)	1.42 Hz (0.70 s)	2.27 Hz (0.44 s)	4.20 Hz (0.24 s)
AI	2.08 Hz (0.48 s)	2.47 Hz (0.40 s)	4.2 Hz (0.24 s)	-	-
EC	1.17 Hz (0.85 s)	1.45 Hz (0.69 s)	2.20 Hz (0.45 s)	3.78 Hz (0.26 s)	-
BN	0.40 Hz (2.5 s)	1.21 Hz (0.83 s)	1.55 Hz (0.65 s)	2.04 Hz (0.49 s)	-
WN	0.38 Hz (2.63 s)	0.63 Hz (1.59 s)	1.46 Hz (0.68 s)	3.66 Hz (0.27 s)	5.74 Hz (0.17 s)
CN	1.40 Hz (0.71 s)	1.67 Hz (0.60 s)	2.30 Hz (0.43 s)	3.39 Hz (0.29s)	4.38 Hz (0.23 s)

A-5. Ground Motion Suite (21) – Chapter 6: Buildings

A-5.1. Acceleration Time Histories

Ground motions are unscaled in the acceleration and velocity time histories.

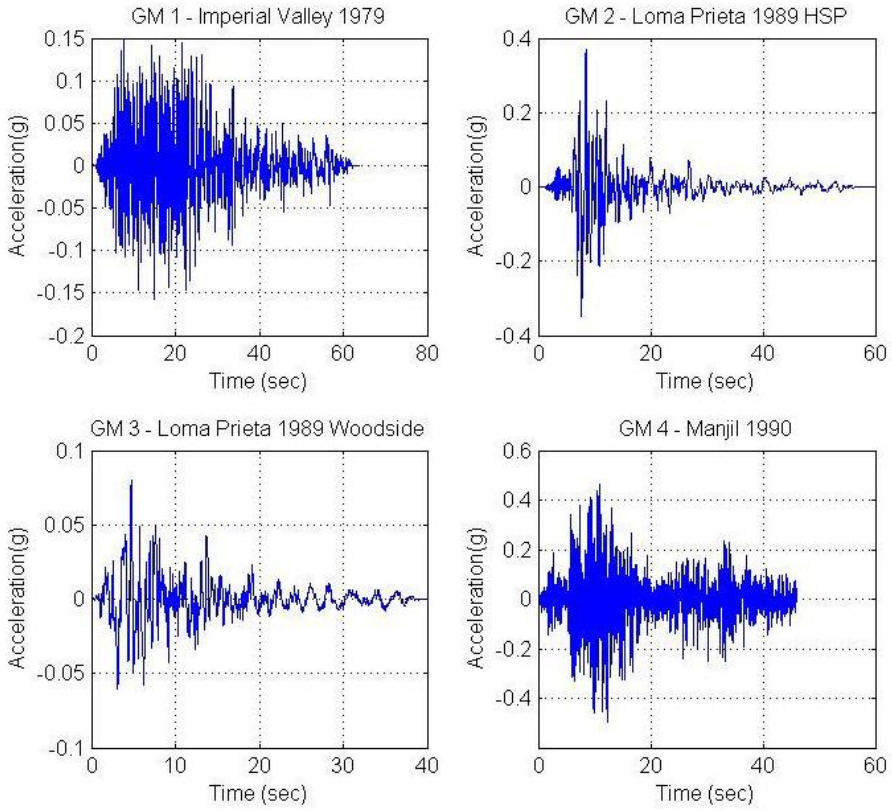

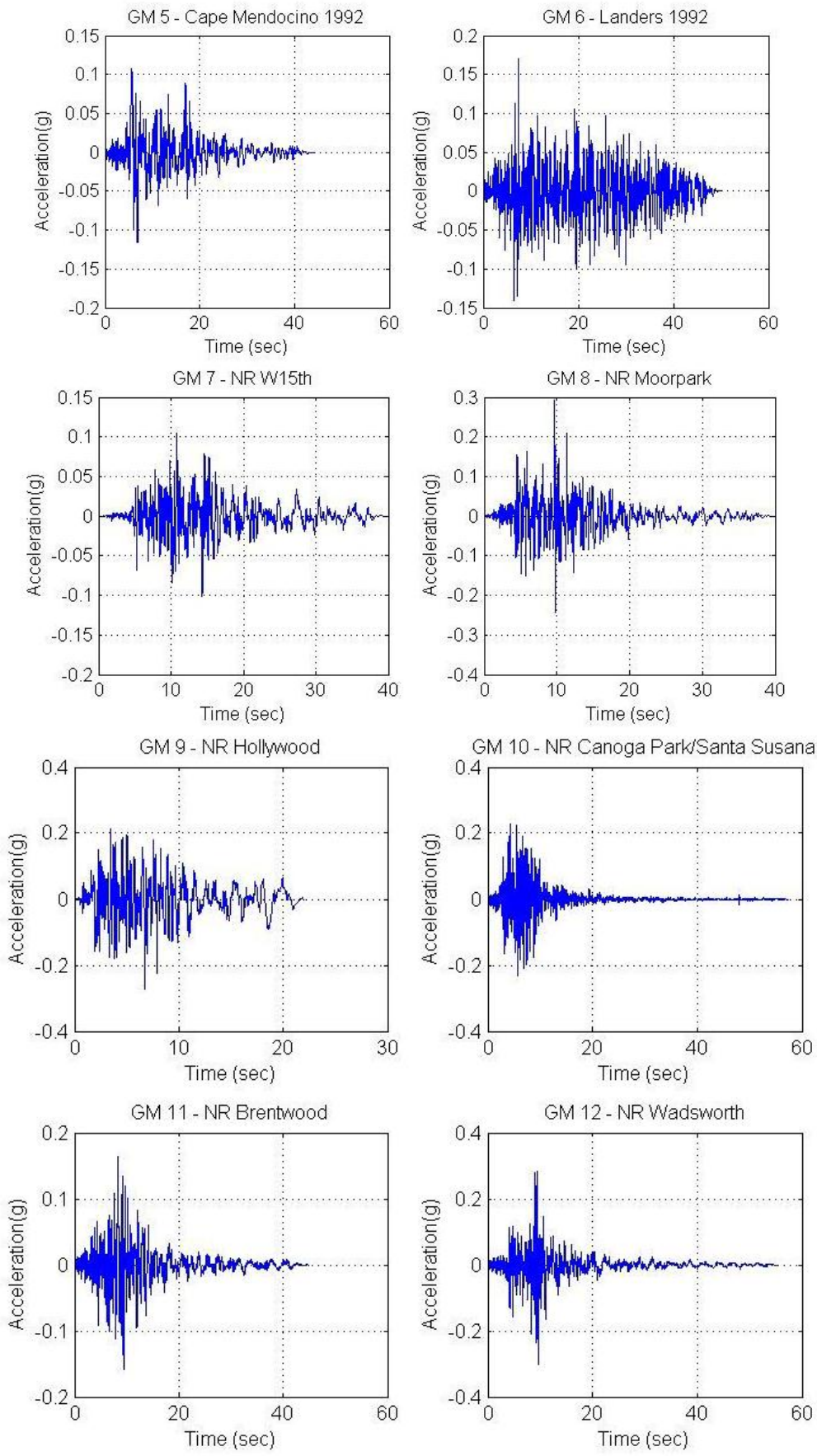
GM 5 - Cape Mendocino 1992
GM 6 - Landers 1992
GM 7 - NR W15th
GM 8 - NR Moorpark
GM 9 - NR Hollywood
GM 10 - NR Canoga Park/Santa Susana
GM 11 - NR Brentwood
GM 12 - NR Wadsworth
Acceleration(g)
Time (sec)

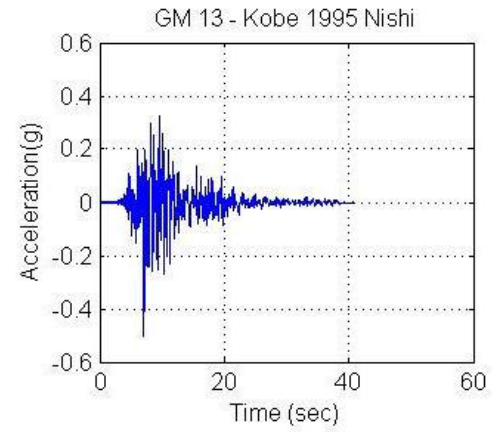
GM 13 - Kobe 1995 Nishi
Acceleration(g)
Time (sec)

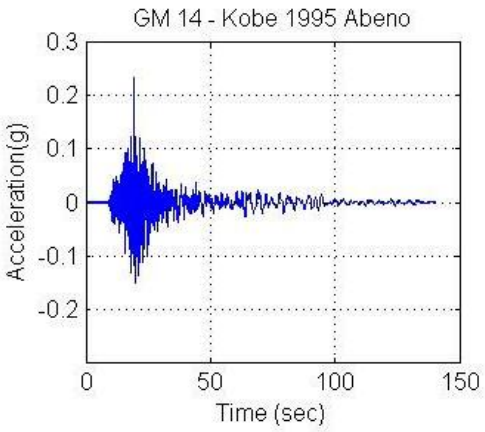
GM 14 - Kobe 1995 Abeno
Acceleration(g)
Time (sec)

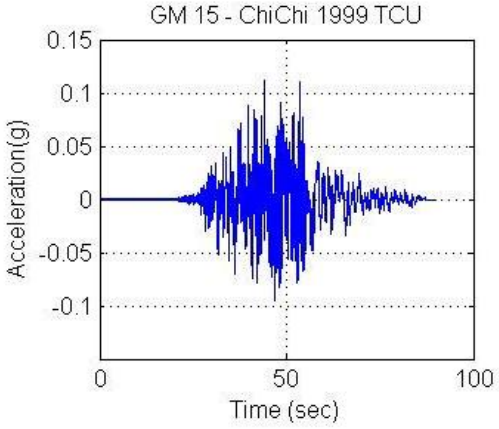
GM 15 - ChiChi 1999 TCU
Acceleration(g)
Time (sec)

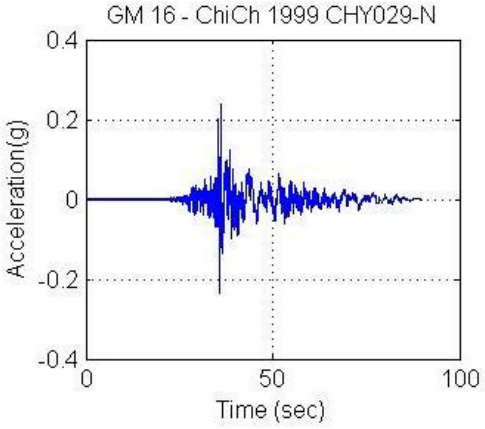
GM 16 - ChiCh 1999 CHY029-N
Acceleration(g)
Time (sec)

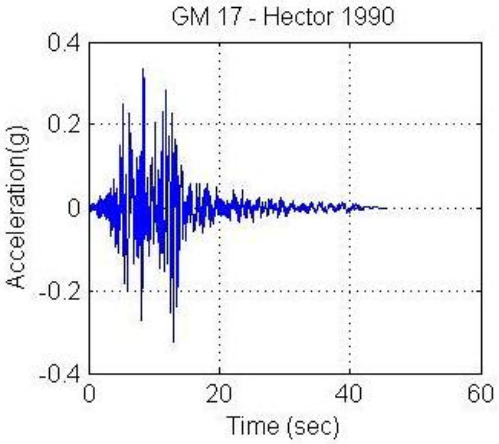
GM 17 - Hector 1990
Acceleration(g)
Time (sec)

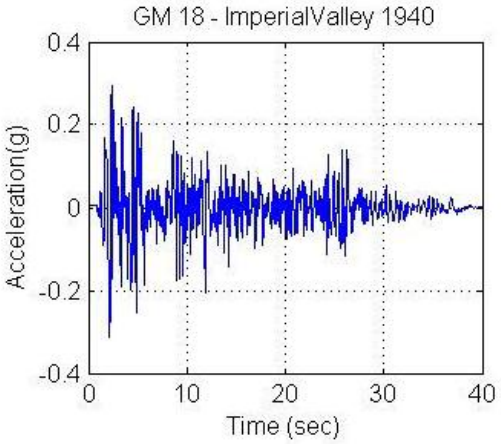
GM 18 - ImperialValley 1940
Acceleration(g)
Time (sec)

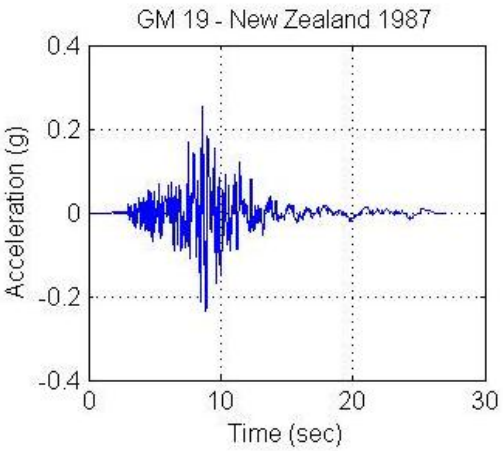
GM 19 - New Zealand 1987
Acceleration (g)
Time (sec)

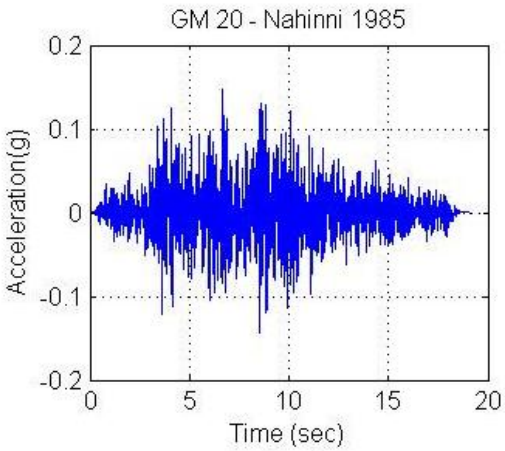
GM 20 - Nahinni 1985
Acceleration(g)
Time (sec)

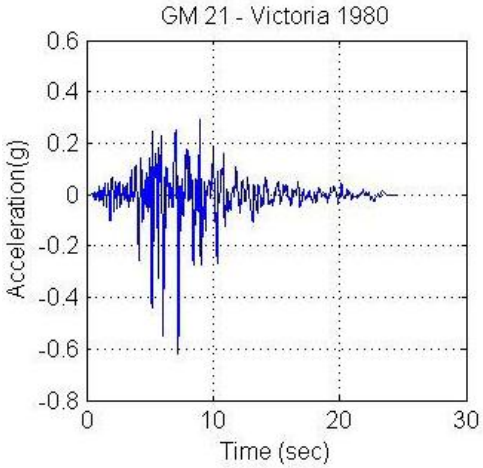

A-5.2. Velocity Time Histories

Ground motions are unscaled in the acceleration and velocity time histories.

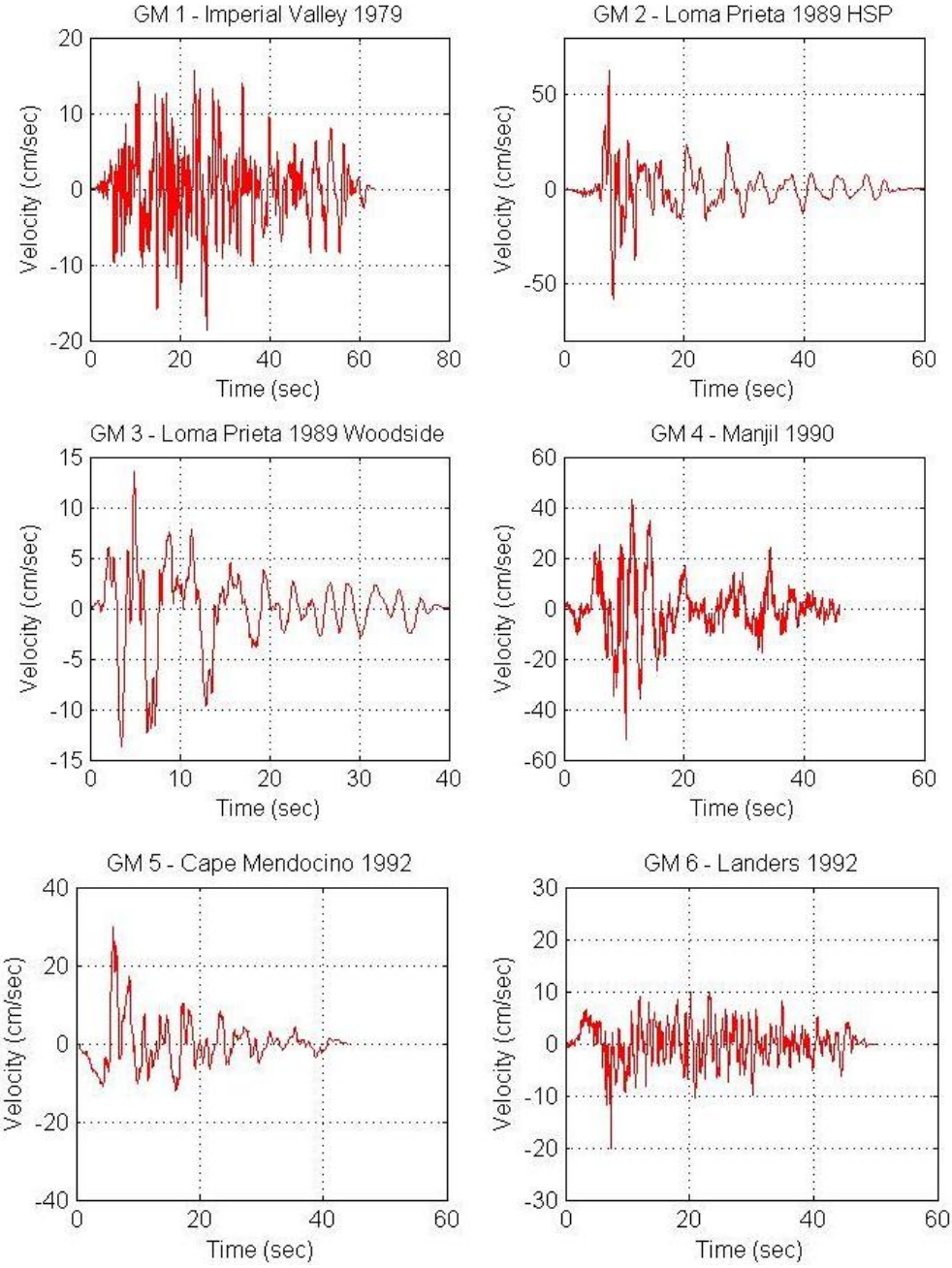

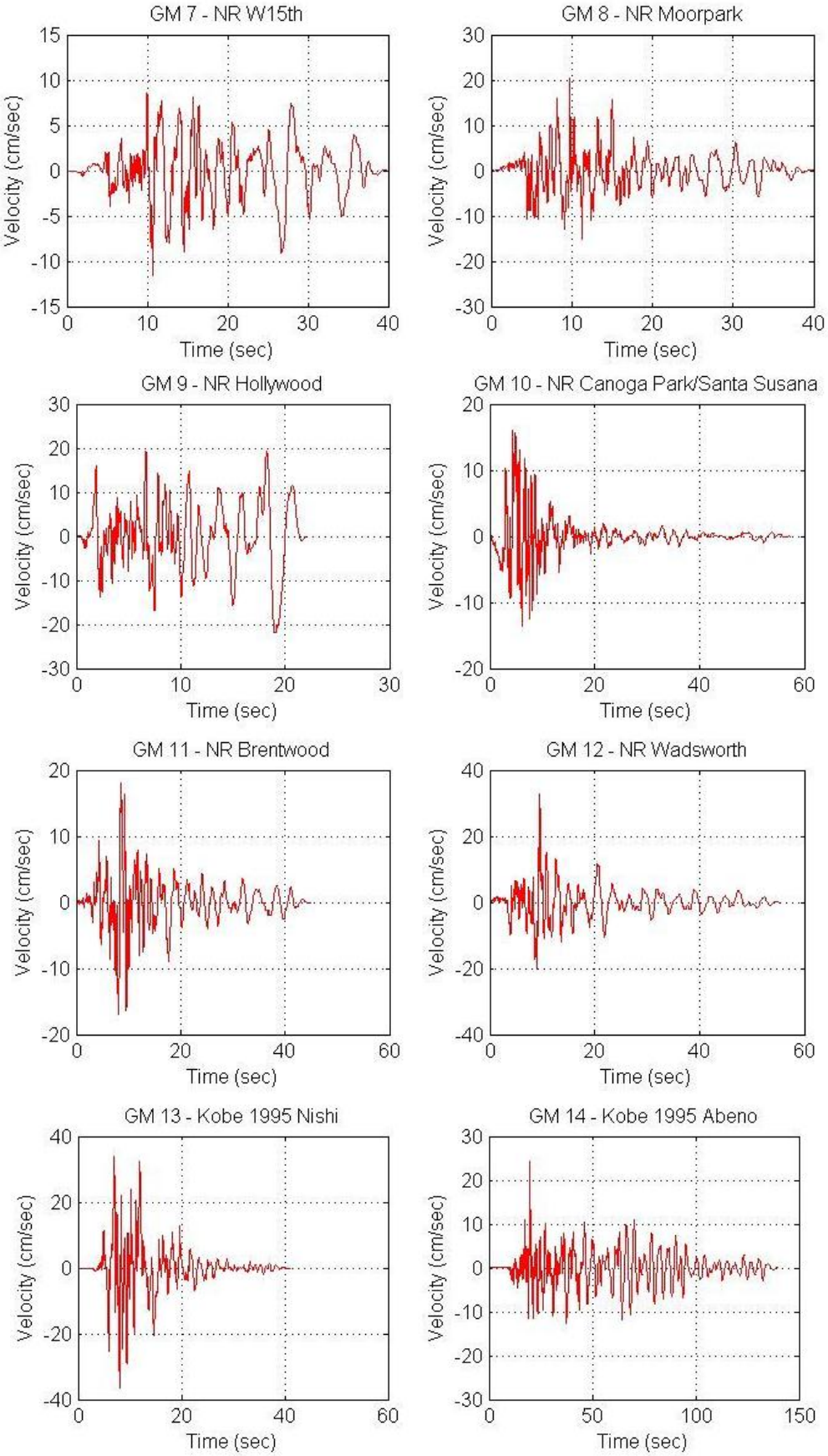
GM 7 - NR W15th
Velocity (cm/sec)
Time (sec)
GM 8 - NR Moorpark
Velocity (cm/sec)
Time (sec)
GM 9 - NR Hollywood
Velocity (cm/sec)
Time (sec)
GM 10 - NR Canoga Park/Santa Susana
Velocity (cm/sec)
Time (sec)
GM 11 - NR Brentwood
Velocity (cm/sec)
Time (sec)
GM 12 - NR Wadsworth
Velocity (cm/sec)
Time (sec)
GM 13 - Kobe 1995 Nishi
Velocity (cm/sec)
Time (sec)
GM 14 - Kobe 1995 Abeno
Velocity (cm/sec)
Time (sec)

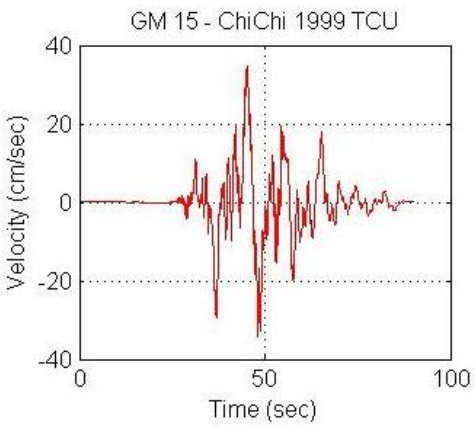
GM 15 - ChiChi 1999 TCU
Velocity (cm/sec)
Time (sec)

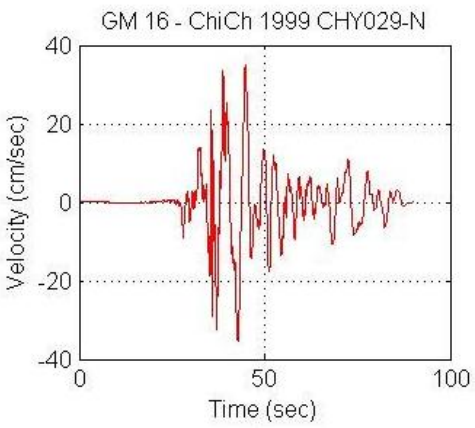
GM 16 - ChiCh 1999 CHY029-N
Velocity (cm/sec)
Time (sec)

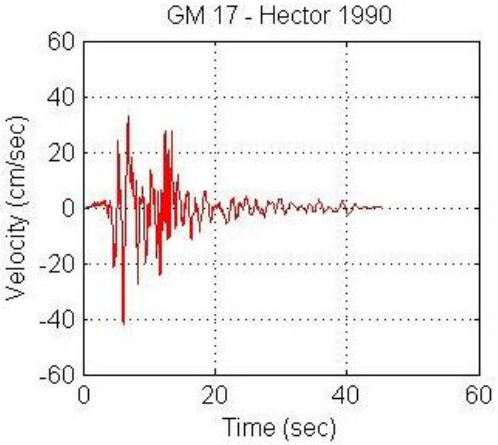
GM 17 - Hector 1990
Velocity (cm/sec)
Time (sec)

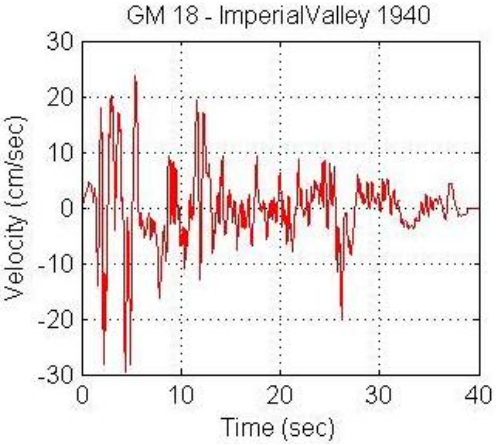
GM 18 - ImperialValley 1940
Velocity (cm/sec)
Time (sec)

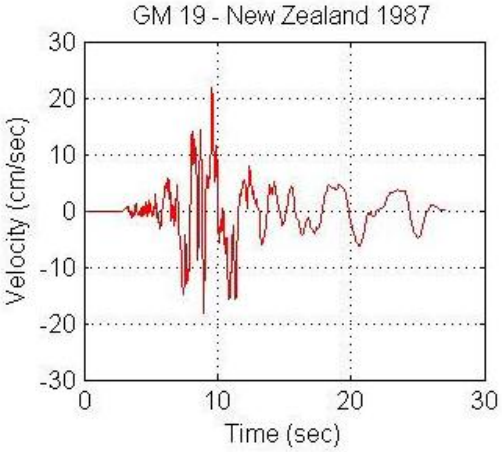
GM 19 - New Zealand 1987
Velocity (cm/sec)
Time (sec)

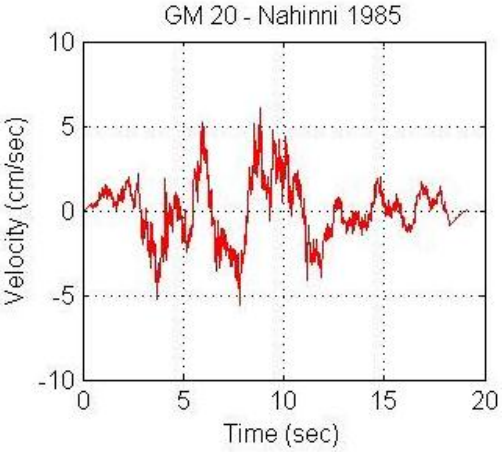
GM 20 - Nahinni 1985
Velocity (cm/sec)
Time (sec)

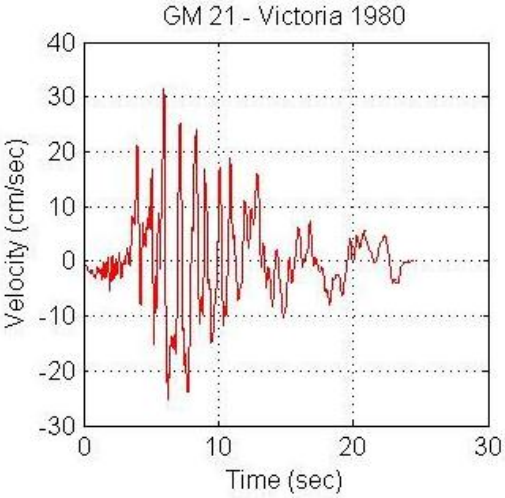
GM 21 - Victoria 1980
Velocity (cm/sec)
Time (sec)

A-5.3. Pseudo-spectral Acceleration Plots

GMs scaled to the DBE hazard level based on the fundamental period of the regular building.

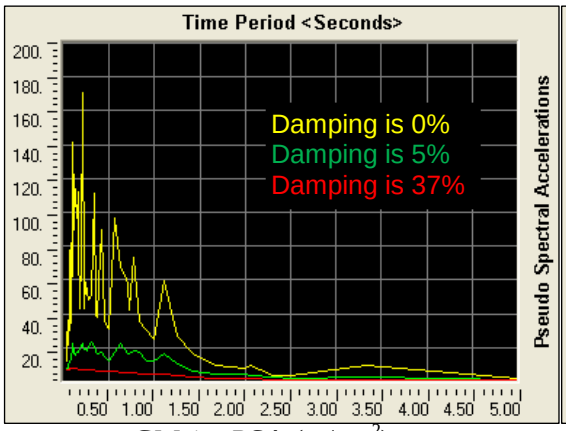

GM 1 – PSA (m/sec^2)

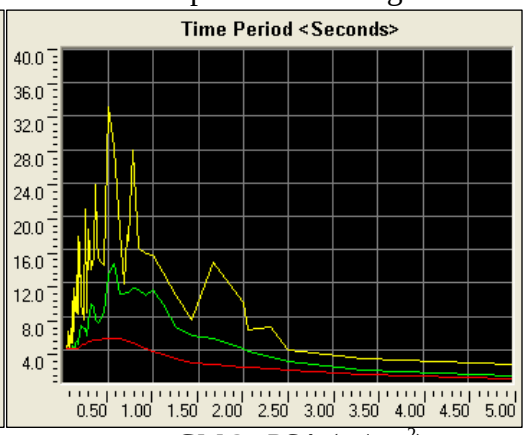

GM 2– PSA (m/sec^2)

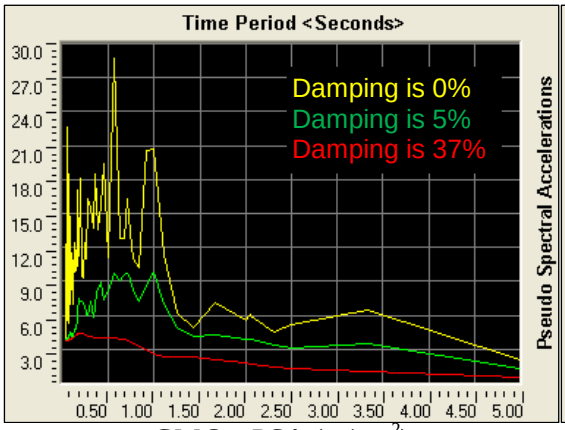

GM 3 – PSA (m/sec^2)

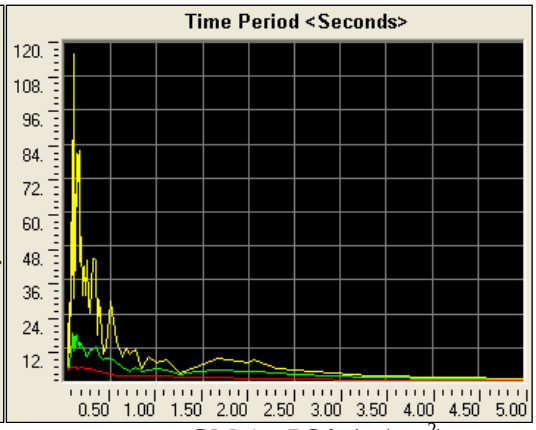

GM 4 – PSA (m/sec^2)

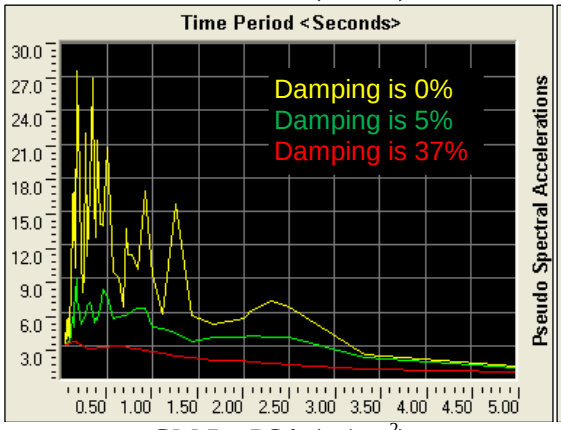

GM 5 – PSA (m/sec^2)

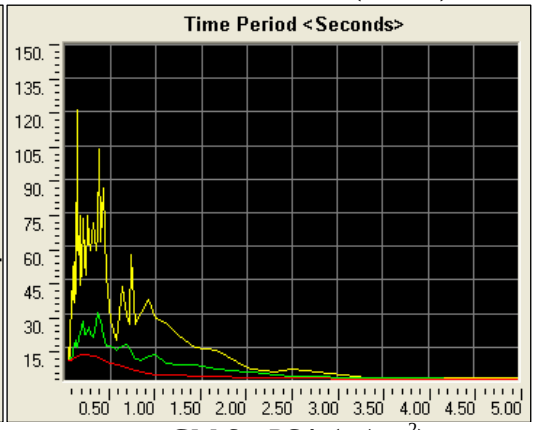

GM 6 – PSA (m/sec^2)

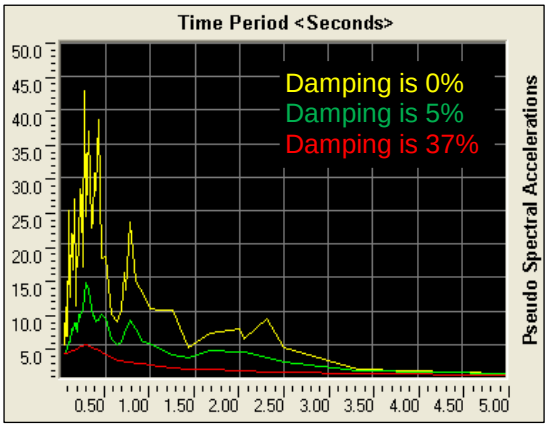

GM 7 – PSA (m/sec^2)

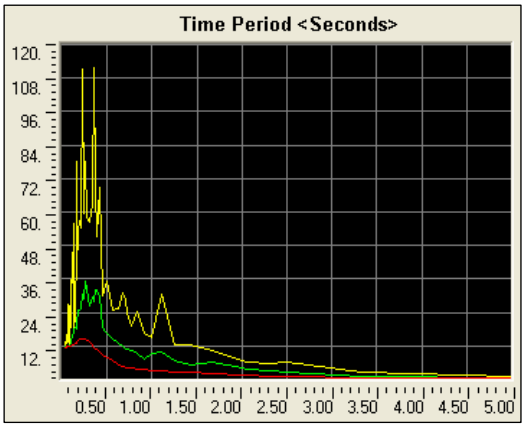

GM 8 – PSA (m/sec^2)

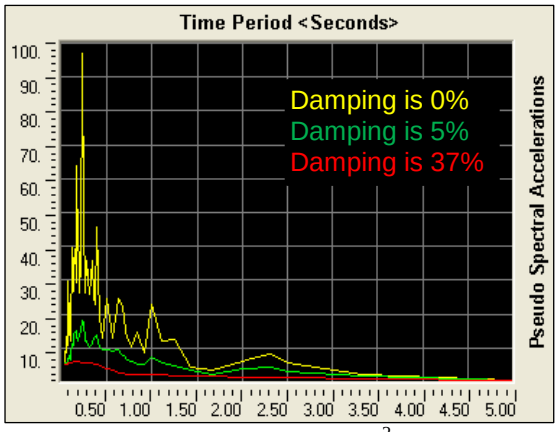

GM 9 – PSA (m/sec^2)

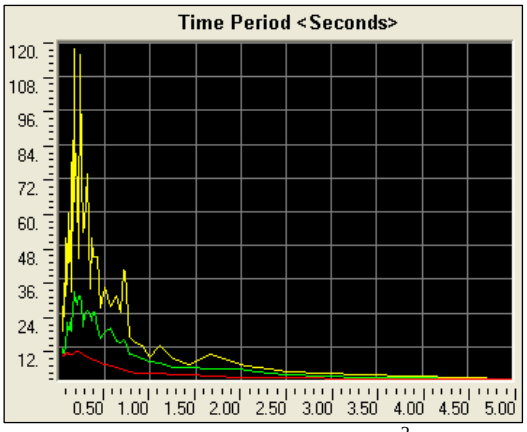

GM 10– PSA (m/sec^2)

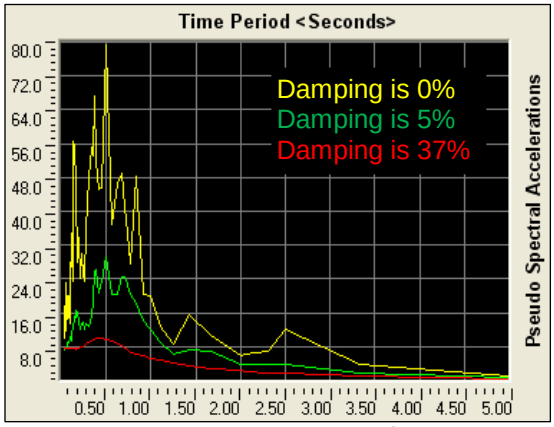

GM 11 – PSA (m/sec^2)

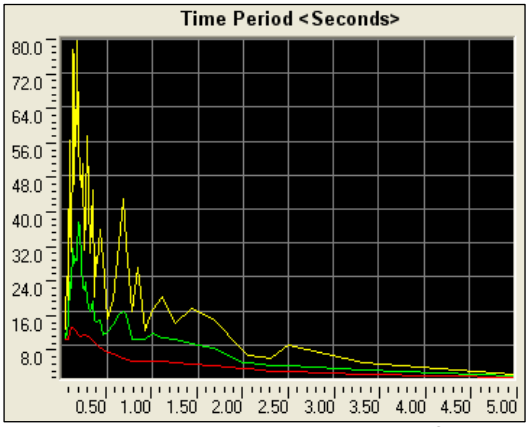

GM 12 – PSA (m/sec^2)

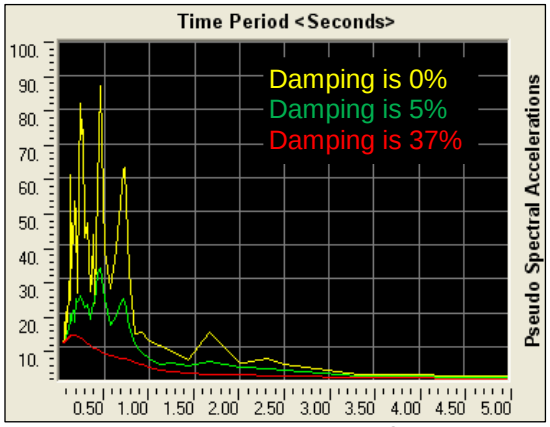

GM 13 – PSA (m/sec^2)

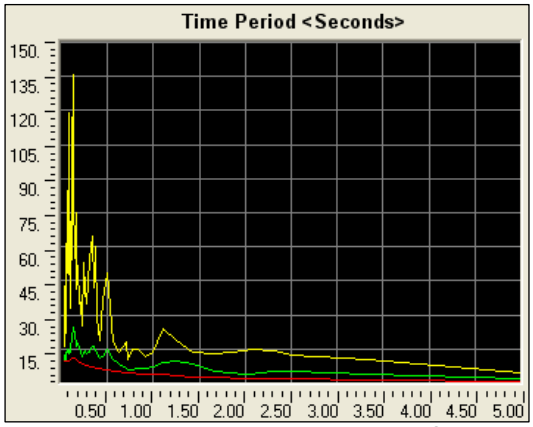

GM 14 – PSA (m/sec^2)

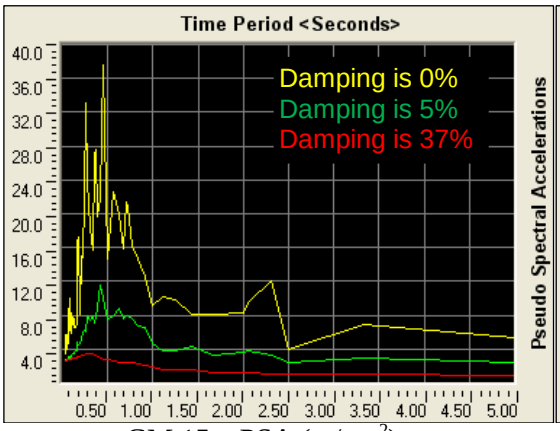

GM 15 – PSA (m/sec^2)

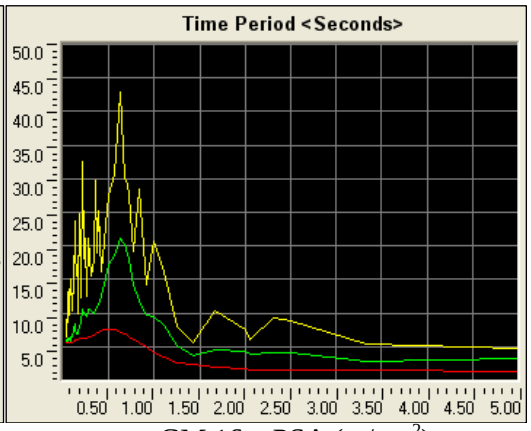

GM 16 – PSA (m/sec^2)

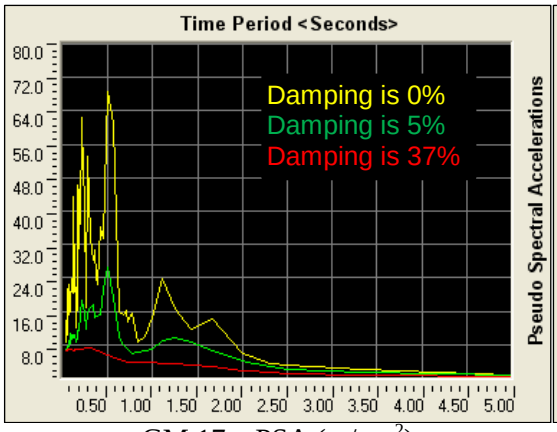

GM 17 – PSA (m/sec^2)

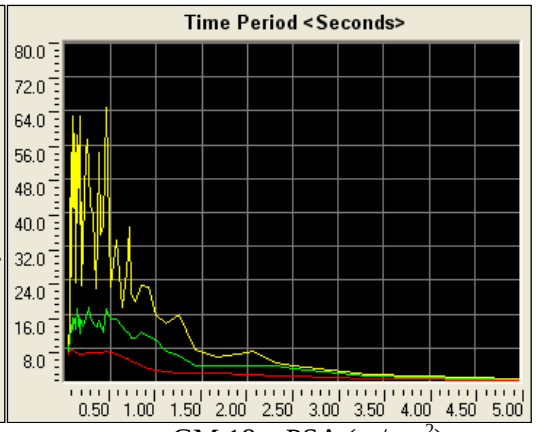

GM 18 – PSA (m/sec^2)

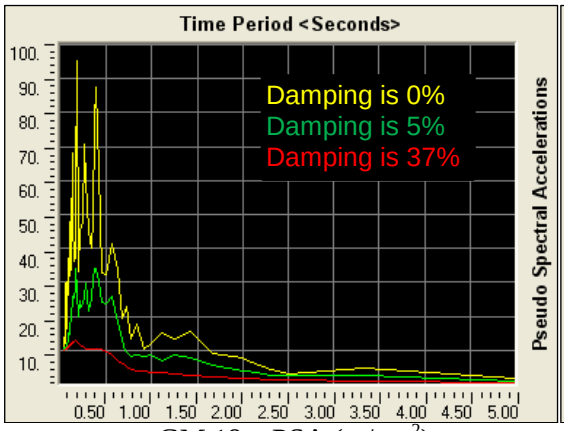

GM 19 – PSA (m/sec^2)

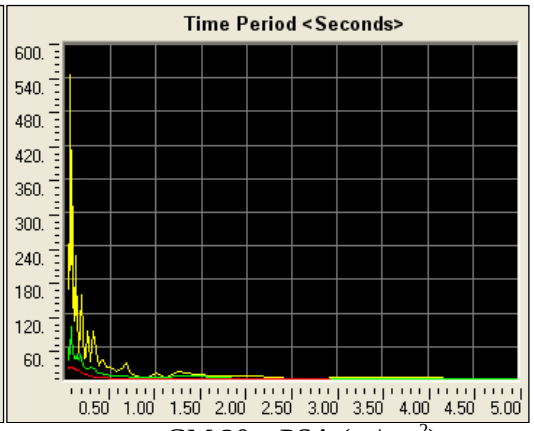

GM 20 – PSA (m/sec^2)

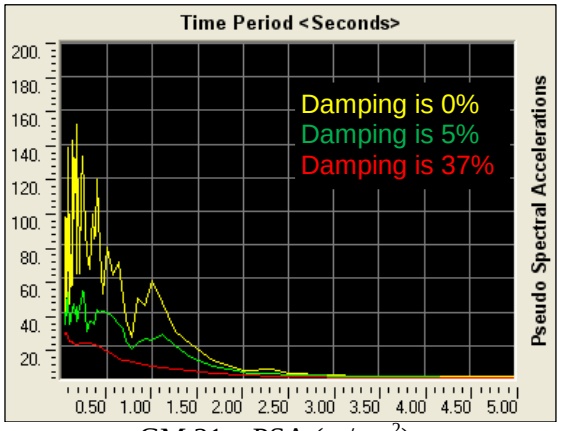

GM 21 – PSA (m/sec^2)

A-5.4. Spectral Displacement Plots

GMs scaled to the DBE hazard level based on the fundamental period of the regular building.

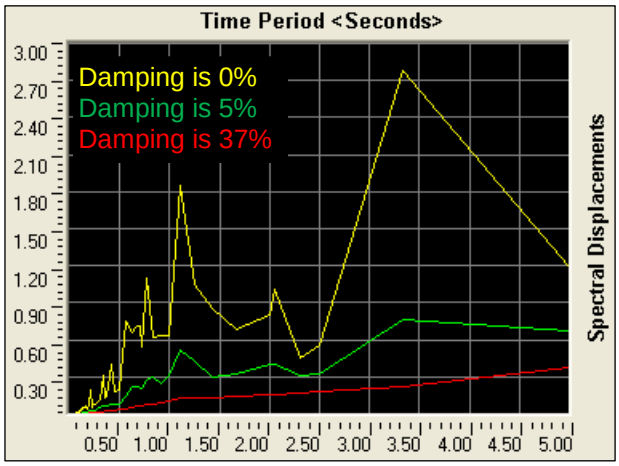

GM 1 – S_D (m)

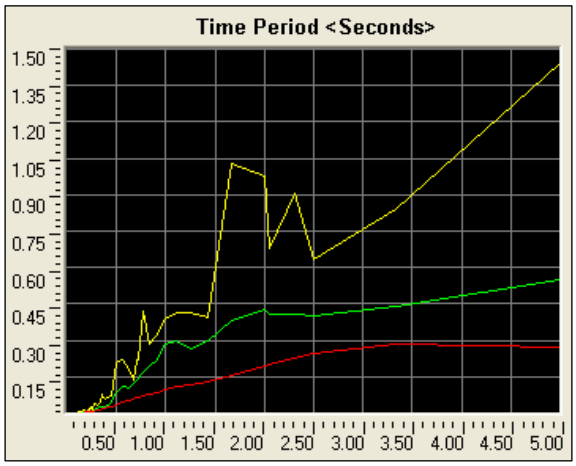

GM 2 – S_D (m)

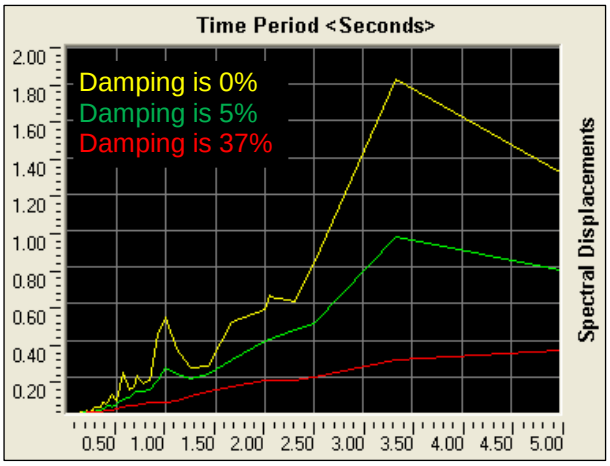

GM 3 – S_D (m)

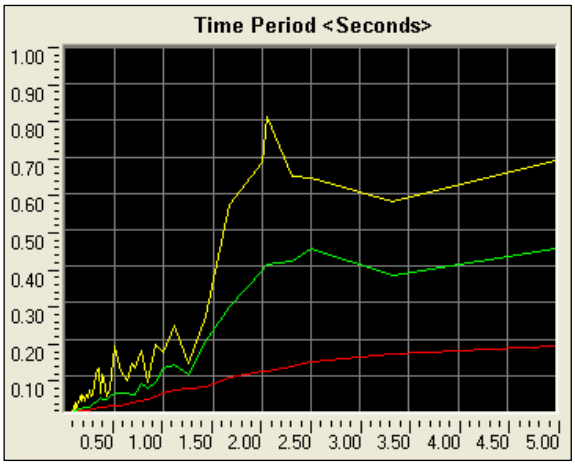

GM 4 – S_D (m)

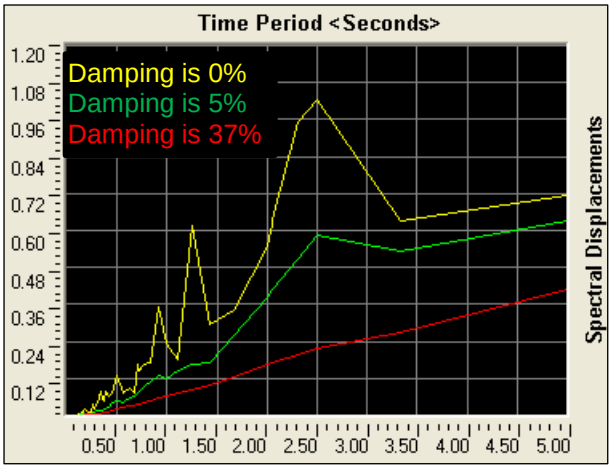

GM 5 – S_D (m)

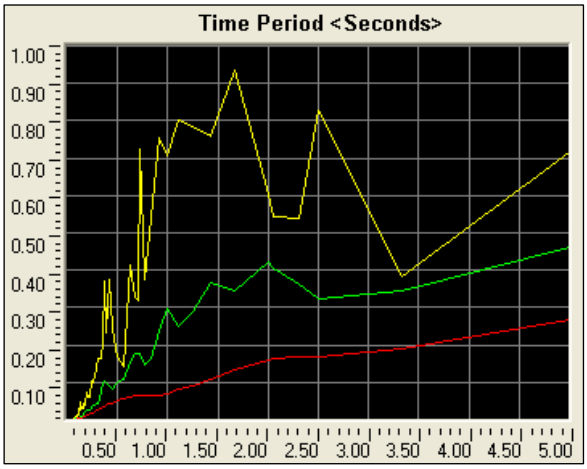

GM 6 – S_D (m)

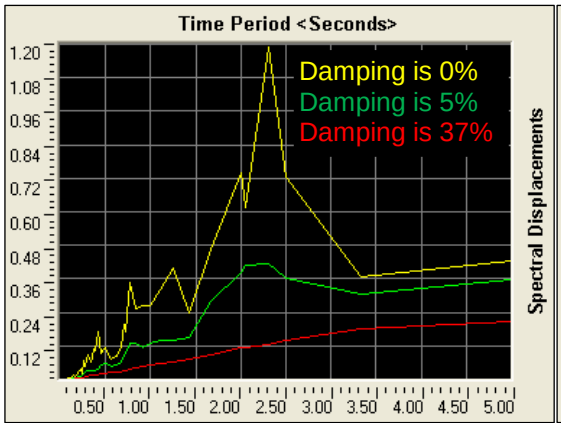

GM 7 – S_D (m)

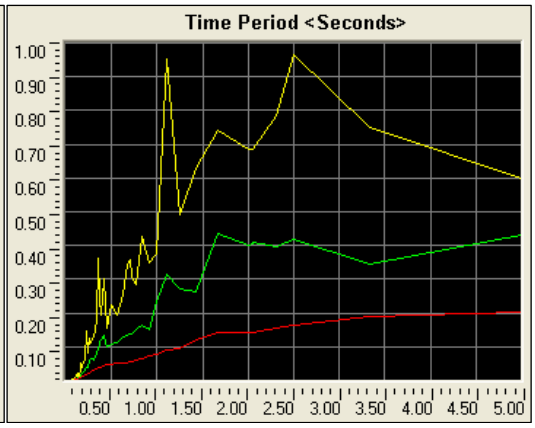

GM 8 – S_D (m)

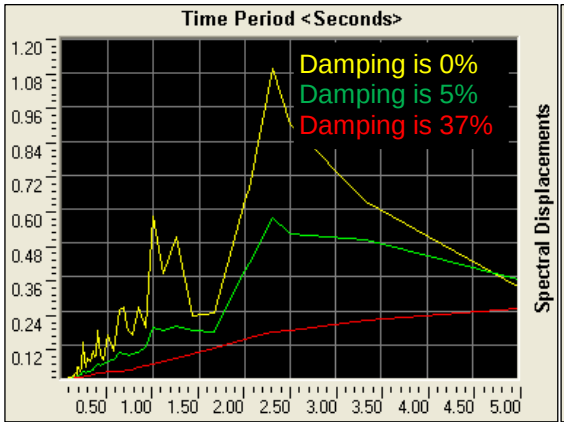

GM 9 – S_D (m)

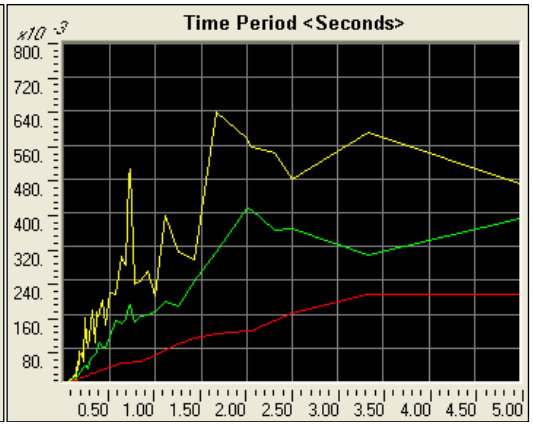

GM 10 – S_D (m)

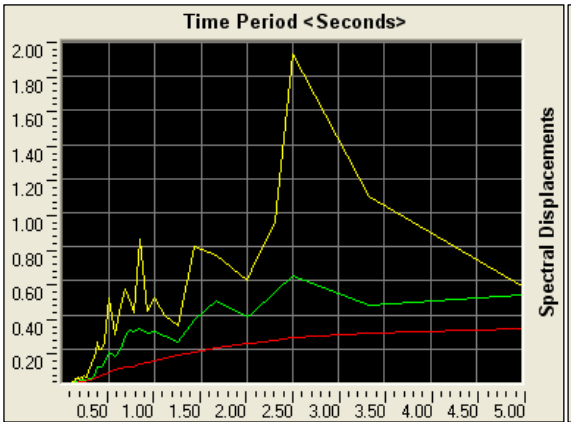

GM 11 – S_D (m)

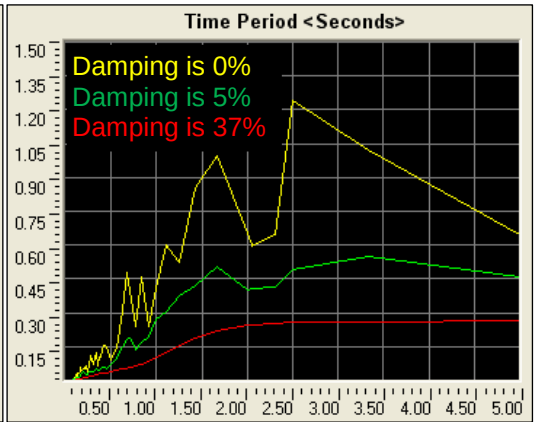

GM 12– S_D (m)

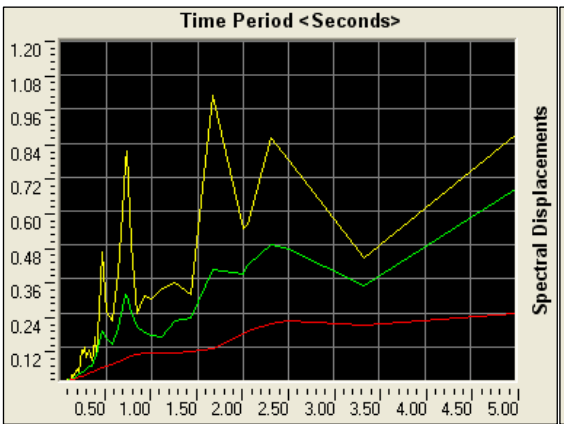

GM 13– S_D (m)

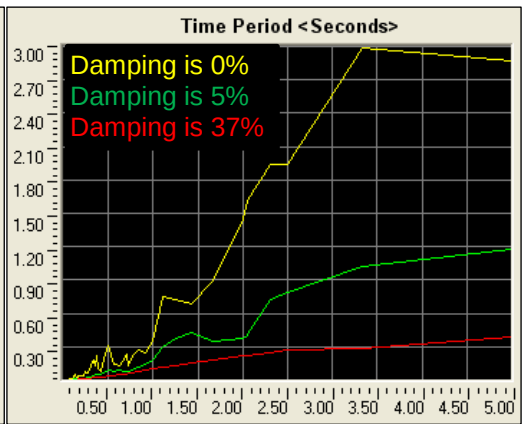

GM 14 – S_D (m)

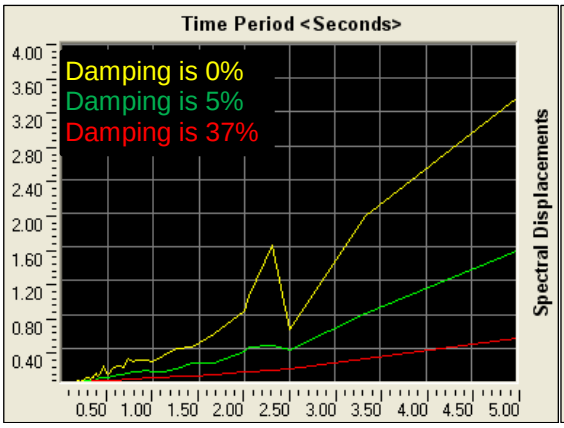

GM 15 – S_D (m)

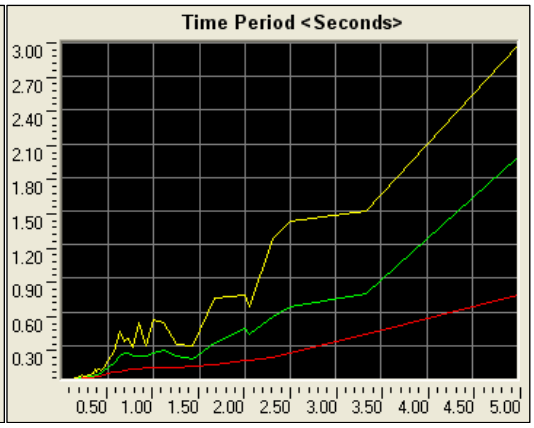

GM 16 – S_D (m)

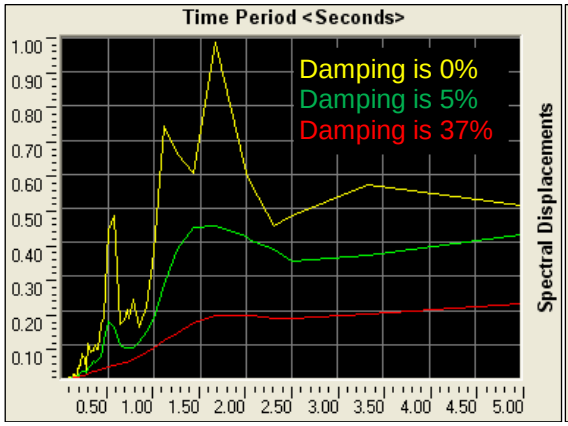

GM 17 – S_D (m)

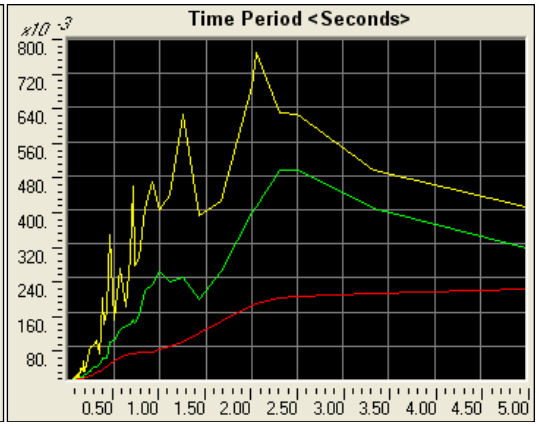

GM 18 – S_D (m)

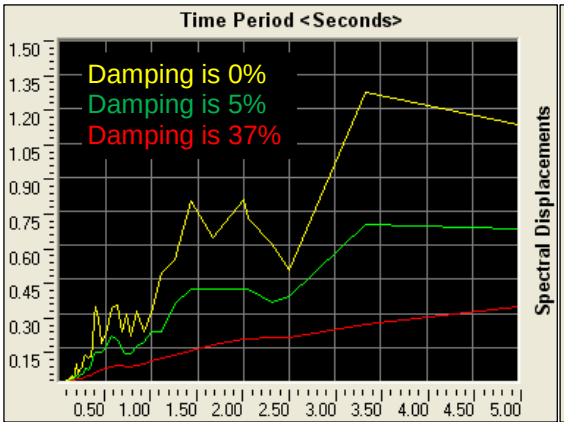

GM 19 – S_D (m)

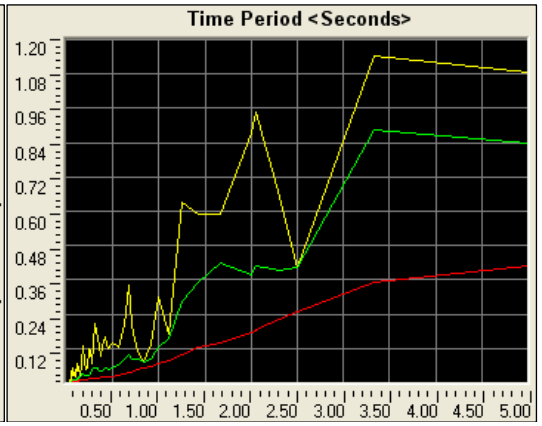

GM 20– S_D (m)

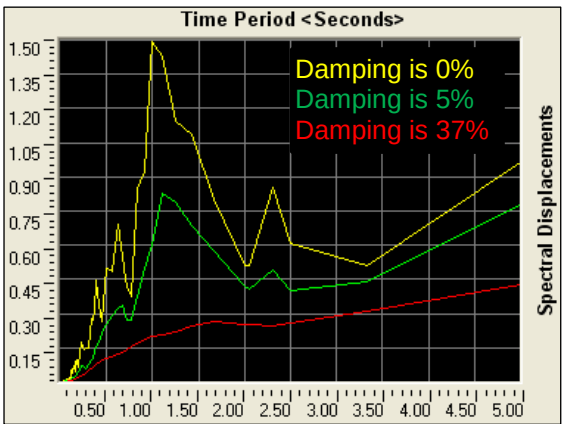

GM 21– S_D (m)

A-6. Artificial Acceleration Set (3) - Chapter 6: Buildings –Time Histories

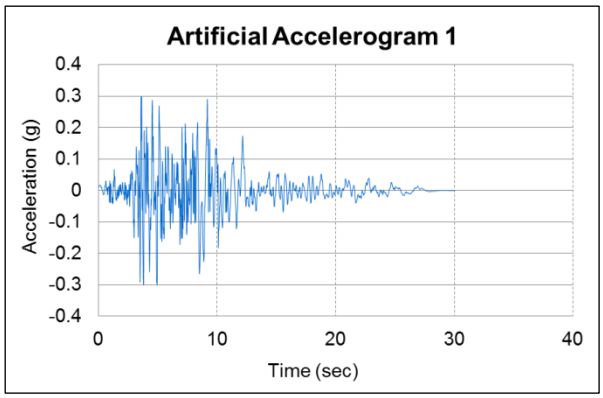

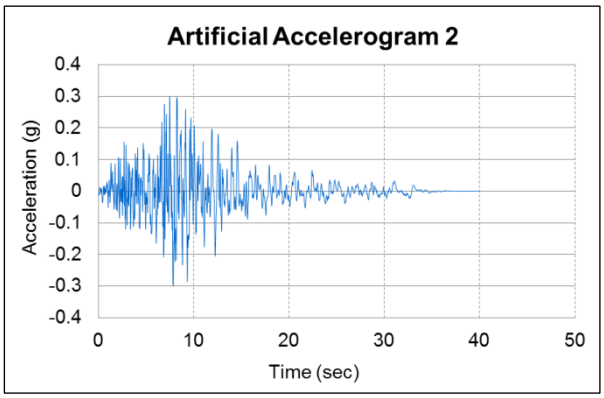

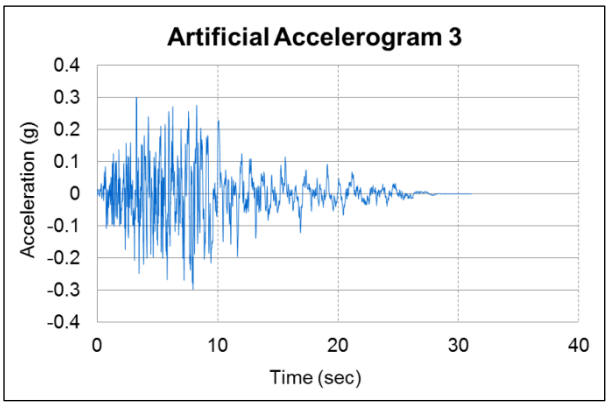

A-7. Mode Details – Chapter 5: Shear Frames

A-7.1. Period, Frequency, and Modal Participating Mass Ratios

Mode	Period (s)	Frequency (Hz)	Modal Participating Mass Ratios	
			UX	RY
Frame 1				
1	1.17	0.86	79 %	100 %
2	0.50	1.99	12 %	0.1 %
3	0.31	3.19	5 %	0 %
4	0.22	4.48	2.3 %	0 %
5	0.17	5.77	1.2 %	0 %
6	0.14	7.06	0.6 %	0 %
Frame 2				
1	1.17	0.86	87 %	99.0%
2	0.40	2.52	8.9 %	1.2%
3	0.25	4.04	2.7 %	0.1%
4	0.19	5.33	1.0 %	0 %
5	0.16	6.30	0.4 %	0 %
6	0.14	6.91	0.1 %	0 %

A-7.2. Mode Shapes –Frame 1 (Variable Stiffness)

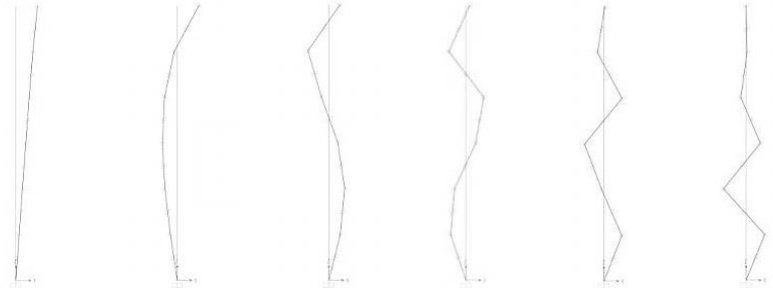

(1) (2) (3) (4) (5) (6)

A-7.3. Mode Shapes –Frame 2 (Uniform Stiffness)

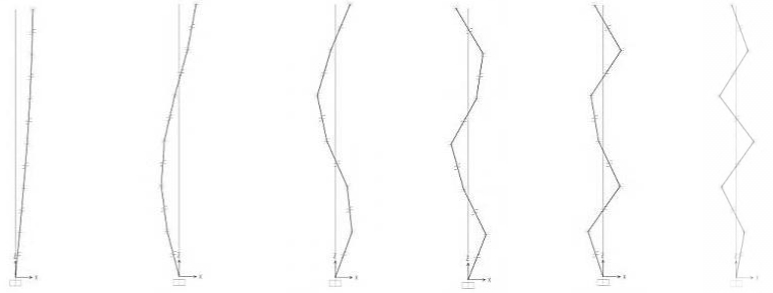

(1) (2) (3) (4) (5) (6)

A-8. Mode Details – Chapter 6: Regular Building

A-8.1. Period, Frequency, and Modal Participating Mass Ratios

Mode	Period (s)	Frequency (Hz)	Modal Participating Mass Ratios		
			UX	UZ	RY
1	2.05	0.49	75 %	0 %	99 %
2	0.70	1.43	11 %	0 %	0 %
3	0.38	2.66	4.5 %	0 %	0.2 %
4	0.23	4.29	2.9 %	0 %	0 %
5	0.16	6.27	1.9 %	0 %	0 %
6	0.12	8.53	1.4 %	0 %	0 %
7	0.09	10.98	1.0 %	0 %	0 %
8	0.08	13.22	0.7 %	0 %	0 %
9	0.07	15.30	0.4 %	0 %	0 %
10	0.05	18.53	1.0 %	0 %	0 %
11	0.03	29.70	0 %	56 %	0 %
12	0.03	30.70	0 %	0 %	0.2 %

A-8.2. Mode Shapes

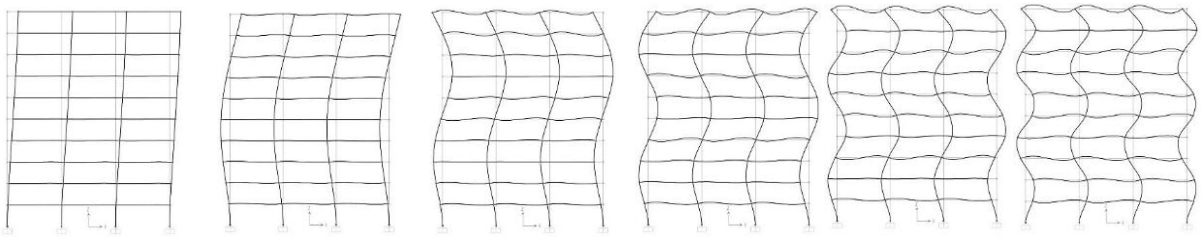

Mode 1 Mode 2 Mode 3 Mode 4 Mode 5 Mode 6

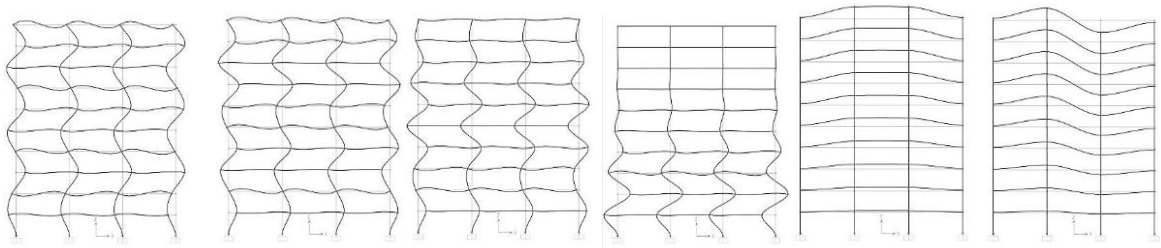

Mode 7 Mode 8 Mode 9 Mode 10 Mode 11 Mode 12

A-9. Mode Details – Chapter 6: Irregular Building

A-9.1. Period, Frequency, and Modal Participating Mass Ratios

Mode	Period (s)	Frequency (Hz)	Modal Participating Mass Ratios		
			UX	UZ	RY
1	2.31	0.43	65 %	0 %	98 %
2	0.93	1.08	13 %	0 %	0.3 %
3	0.47	2.15	7.3 %	0 %	0.3 %
4	0.29	3.42	3.9 %	0 %	0.1 %
5	0.19	5.14	4.5 %	0 %	0.1 %
6	0.14	7.21	2.3 %	0 %	0 %
7	0.11	8.84	1.9 %	0 %	0 %
8	0.09	11.52	1.1 %	0 %	0 %
9	0.08	13.14	0.3 %	0 %	0 %
10	0.07	15.13	0.3 %	0 %	0 %
11	0.03	33.43	0 %	47 %	0.2 %
12	0.03	35.26	0 %	17 %	0.5 %

A-9.2. Mode Shapes

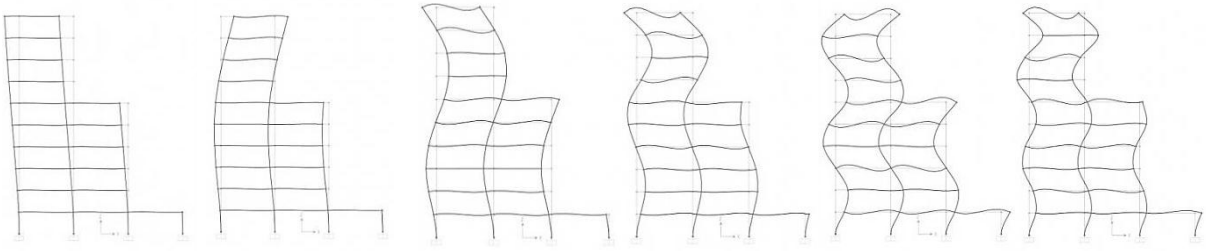

Mode 1 Mode 2 Mode 3 Mode 4 Mode 5 Mode 6

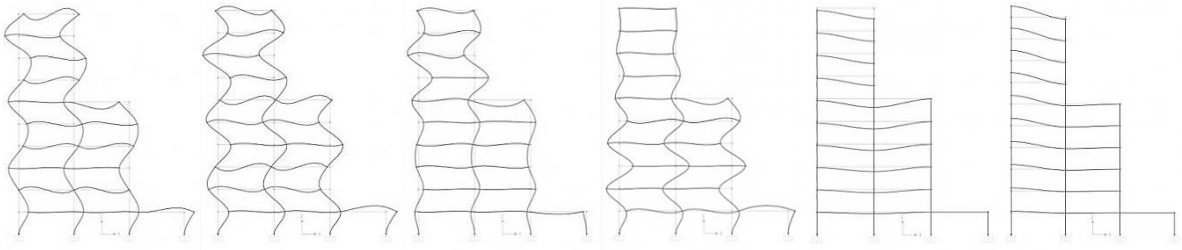

Mode 7 Mode 8 Mode 9 Mode 10 Mode 11 Mode 12

A-10. Steel Design Demand/Capacity Form

Arrangement A3 under GM1 (Imperial Valley) – HE800B Ground Column

SAP2000 Steel Design

Project _____

Job Number _____

Engineer _____

EUROCODE 3-1993 STEEL SECTION CHECK
Combo : timehistory_gm1
Units : N, m, C

Frame : 11 Design Sect: HE800B
X Mid : -4.000 Design Type: Column
Y Mid : 0.000 Frame Type : Moment Resisting Frame
Z Mid : 1.600 Sect Class : Class 2
Length : 3.200 Major Axis : 0.000 degrees counterclockwise from local 3
Loc : 0.000 RLLF : 1.000

Area : 0.033 SMajor : 0.009 rMajor : 0.328 AVMajor: 0.014
IMajor : 0.004 SMinor : 9.933E-04 rMinor : 0.067 AVMinor: 0.017
IMinor : 1.490E-04 ZMajor : 0.010 E : 1.999E+11
Ixy : 0.000 ZMinor : 0.002 Fy : 355000000.0

DESIGN MESSAGES
Error: Section overstressed

STRESS CHECK FORCES & MOMENTS

Location	P	M33	M22	V2	V3	T
0.000	-2846280.47	2311743.196	0.000	526531.002	0.000	0.000

PMM DEMAND/CAPACITY RATIO

Governing Equation	Total Ratio		P Ratio		MMajor Ratio		MMinor Ratio	Ratio Limit	Status Check
(5.5.4)	1.068	=	0.324	+	0.744	+	0.000	0.950	Overstress

AXIAL FORCE DESIGN

	Fc or Ft Force	Nc.Rd Capacity	Nt.Rd Capacity	Nb33.Rd Major	Nb22.Rd Minor
Axial	-2846280.47	8786153.845	10779090.91	10568632.59	8786153.845

MOMENT DESIGN

	M.Sd Moment	Mc.Rd Capacity	Mv.Rd Capacity	Mb.Rd Capacity
Major Moment	2311743.196	3301500.000	3301500.000	3107871.353
Minor Moment	0.000	501195.455	501195.455	

	K Factor	L Factor	k Factor	klt Factor	C1 Factor
Major Moment	2.194	1.000	1.036	1.000	1.557
Minor Moment	1.000	1.000	1.175		

SHEAR DESIGN

	V.Sd Force	V.Rd Capacity	Stress Ratio	Status Check	Tu Torsion
Major Shear	550153.179	2608573.489	0.211	OK	0.000
Minor Shear	0.000	3074390.183	0.000	OK	0.000

SAP2000 v14.0.0 - File:C:\Documents and Settings\labjw\Desktop\thom computer lab\final\Full GM Suite_NONLINEAR\...